Mesoscopic lattice Boltzmann nemato-dynamics.

GOOD, Kevin.

REFERENCE

Mesoscopic Lattice Boltzmann Nemato-dynamics

KEVIN GOOD, BSc (Hons.), Grad.Inst.Phys.

A thesis submitted in partial fulfilment of the requirements

of Sheffield Hallam University for the degree of

Doctor of Philosophy

20th February 2001

Materials Research Institute, Sheffield Hallam University

in collaboration with DERA Malvern.

Abstract

In this thesis we have developed an anisotropic lattice Boltzmann (LB) model that recovers the incompressible isentropic Ericksen-Leslie-Parodi (ELP) equations of continuum nemato-dynamics in two dimensions with the director confined to the plane. Suitable validations of the developed model against known solutions of the continuum theory are undertaken as well as investigations into nematic flow in interesting geometries.

The model is based upon two coupled LBE schemes, the standard momentum density distribution and a new link angle distribution. To achieve evolution, the link angle distribution undergoes a Bhatnagar-Gross-Krook (BGK) collision step and advects (propagates) in unit time with the momentum densities. Anisotropy is introduced into the momentum density evolution scheme through a linearized Lattice Boltzmann (lLB) collision process which is made anisotropic. Correctly to capture the macroscopic dynamics, 6^{th} order isotropy of the underlying lattice structure is required, accordingly we introduce a new variant on the standard lLB scheme : a two-dimensional thirteen link (D2Q13) model. Chapmann-Enskog expansions of the momentum and angle evolution schemes are shown, through a suitable selection of equilibrium distribution functions and forcing terms, correctly to map onto the target macroscopic ELP equations of continuum nemato-dynamics.

Results are presented which validate the new scheme against known analytical solutions of the governing equations to a high degree of accuracy. The validated scheme is subsequently applied to nemato-dynamic behavior in an applied magnetic field, i.e the Fréedericksz transition and velocity back-flow with director kick-back. Finally we simulate the geometrically complex Zenithly Bi-stable Display (ZBD) device to illustrate some of the advantages of the LB schemes.

The continuum is that which is divisible into indivisibles that are infinitely divisible,

Aristotle.

Acknowledgements

I would like to express my thanks to the following people who have helped and influenced me during my research.

Firstly, my supervisors Dr. I.Halliday, Prof. C.M.Care and Dr D.J.Cleaver, who's guidance has proved invaluable. I also acknowledge the financial support of the MRI at Sheffield Hallam University and my sponsors, DERA (Malvern) and all the MRI administrative staff.

It also gives me pleasure to thank all the friends and acquaintances whom I have made during my time as a PhD student. To Martin, Stu, Steve, Tom, Daz, Ian and Richard, for having, *been there and done that,* before me and whose help was crucial. To Gav, Lloyd and Lee for their assistance in developing my social skills (down the pub). Richard W, for all his graphics help, Greg and Kev for been understanding system administrators and last but not least Viktor, Dymtro, Fatima and Fred.

I would like to reserve my biggest thanks, however, firstly to my family for their support and understanding during my under-graduate and post-graduate studies, without which none of this would have been possible and finally to Nip, for being there throughout.

Advanced Studies

As part of the course of study a number of postgraduate courses within the MRI at Sheffield Hallam University were attended. These included the topics - Fluid Dynamics, Molecular Simulation techniques and Polymers and Liquid Crystals

Also a number of relevant conferences were attended, including :

- Modelling of liquid crystals at interfaces - one day workshop, Sheffield Hallam University (November 1997)

- LGA 98 International Symposium on the Discrete Simulation of Fluid Dynamics, Oxford University (July 1998) - Contributed to oral presentation.

- Faraday Discussion (April 1999) - poster presentation, *Lattice Boltzmann Nemato-dynamics - a first approach.*

- LGA 99 International Symposium on the Discrete Simulation of Fluid Dynamics, Tokyo University (July 1999) - Oral and poster presentation, *Towards Lattice Boltzmann Incompressible Isentropic Nemato-dynamics In Two Dimensions.*

- CCP5, Sheffield Hallam University (September 2000) - poster presentation, *Lattice Boltzmann Incompressible Isentropic Nemato-dynamics In Two Dimensions.*

Finally the work has produced a number of refereed articles [1, 2].

Contents

List of Figures

List of Tables

Chapter 1

Introduction

1.1 Overview

The scientific study of fluid dynamics impacts on virtually every aspect of modern life. The field has its origins in antiquity but it was not until the late 18^{th} century that a mathematical continuum description of a fluid was laid down. Until the advent of computers in the latter half of the 20^{th} century almost all of the research into fluid dynamics was performed by either experimentation or simplified analytical solutions of a theoretical model. But since the foundation of the field of Computational Fluid Dynamics (CFD), a new and immensely valuable tool has being brought to bear on the task of obtaining an exact solution of the equations of fluid dynamics.

Modern day computational techniques such as Finite Difference (FD) methods have had great success in modelling fluid dynamics and can be applied to a variety of

different flow phenomena. It is a measure of the success of these models that CFD models are today viewed as a complementary tool to the more traditional methods of experimental fluid dynamics with certain advantages.

The ability in CFD to change the configurational details of the system under study with relative ease as well as the potential for full data point recovery are major advantages where experimental solutions are becoming increasingly more complex and expensive and CFD models have been developed to tackle a variety of different types of flows including incompressible, compressible, thermal, immiscible and turbulent.

Whereas CFD treats a fluid at the continuum level, molecular dynamics (MD) is a computational tool to model the motions and interactions of individual molecules. Current MD and Monte-Carlo (MC) models have had great success, however, the models are by their very nature microscopic in origin. Although it is theoretically possible to use them to do macroscopic fluid dynamics, the computational requirements to do so are well beyond the capabilities of today's computers.

This leads us onto the relatively recent development of the lattice models whose most recent and widely used incarnations are the Lattice Gas (LG) and Lattice Boltzmann (LB) models. Mapping onto the macroscopic equations of fluid dynamics the LG and LB models essentially describe particle populations propagating on a lattice of velocity vectors, undergoing simplified "collision" rules at the lattice nodes.

These models approximate (coarse grain) the molecular dynamics occurring on the microscale and use a statistical expansion process to tailor the emergent macroscopic dynamics of the lattice fluid, as defined by its governing partial differential equations (pde's).

For many simulators the LG and LB models operate in the grey area between molecular dynamics and continuum dynamics called the "mesoscale". It is this ability to access the best parts from the microscopic and macroscopic models that places the modern day lattice models in a unique position within the modelling community.

Although still in their infancy, mesoscale models have shown that they can offer some advantages over more traditional CFD techniques in certain areas of fluid dynamics. LG and LB algorithms are relatively easy to implement (code) as is bounding the flows in complex geometries. The models implicit parallisability also allows large scale simulations on massively large parallel processors. Possibly most importantly though, algorithmic extensions for e.g. diphasic flow can be devised by appealing directly to the physics transparently captured by the simple underlying evolution rules.

These are just a few of the advantages of the LG and LB techniques which have been developed in recent years. This is apparent from the growing body of literature on the subject of lattice models, which many believe ultimately should prove to be an invaluable tool, complementing the more traditional CFD, theoretical and experimental methods of investigating fluid dynamics.

All the CFD methods discussed above have been widely used in the modelling of isotropic fluid dynamics which, whilst it has received much interest over the latter part of the century, is still far from a completely solved problem. The situation is more extreme when we turn to modelling anisotropic fluid dynamics which is still a relatively new area of science. The increasing domination of liquid crystals in the display industry, however, has motivated a lot of interest in the subject over the last few decades, since Ericksen, Leslie and Parodi (ELP) developed a continuum description of a nematic liquid crystal. However, relatively little work has been carried out in attempting numerical solutions of the fully coupled equations of nemato-dynamics at the continuum scale.

Historically, microscopic models have been mostly used to simulate liquid crystals and there is a large literature on this subject, as is the case for experimental work carried out on liquid crystals. A lot of this work deals with the phase transitions which a liquid crystal undergoes. There are drawbacks such as those that infect isotropic fluid mechanics. Namely experimental work is by nature expensive and complicated : MD techniques are for all practical purposes confined to the microscale for the foreseeable future. Current analytical solutions of the ELP equations of nemato-dynamics all have to make substantial approximations and/or regime limitations.

1.2 Aims

The work presented in this thesis essentially entails a proof of concept. The main aim involves extending a Lattice Boltzmann (LB) model of fluid dynamics to recover the anisotropic ELP equations of nemato-dynamics.

Having obtained a clear strategy based upon a second scalar distribution, the scheme is to be implemented into an LB model and validated against known theoretical results. It is hoped that this process of development and implementation/validation would produce feed-back and contribute to maturing and refining the model over the course of the work.

In order to produce an LB scheme for nemato-dynamics it is necessary to clarify certain fundamental issues within what one might term the core LB methodology: namely a correct and consistent treatment of forcing.

In the next section we review the overall structure of this thesis describing the work undertaken to meet the aims stated above.

1.3 Outline of thesis

The field of continuum anisotropic fluid dynamics is introduced in chapter 2. A brief overview is followed by a word about the notation used in this thesis. The appropriate governing equations for *isotropic* hydrodynamics, namely the mass continuity equation and the Navier-Stokes equations are subsequently derived. In the next section we introduce the field of liquid crystals before reviewing the generalized continuum equations of anisotropic fluid dynamics (nemato-dynamics) in terms of the Ericksen-Leslie-Parodi (ELP) presentation . Importantly, we then take the vectorial equation of motion for the nematic and reduce it to a scalar angle equation of motion in two dimensions where the director is confined to the plane $(2 \oplus 2)$. This reduced form lends itself more conveniently to the methodology employed in later chapters to generate our models director dynamics.

Having set-out the "target" macroscopic continuum equations, we proceed in chapter 3 to introduce mesoscopic Lattice Gas (LG) and Lattice Boltzmann (LB) lattice models. Starting from a historical point of view, we cover the seminal work by Frisch *et al* [8] on LGs through to the conception of the two main LB models - the linearized Lattice Boltzmann (lLB) and the single relaxation Lattice Boltzmann (BGK) model. In particular a short review of the mapping of an LG model onto isotropic hydrodynamics is presented along with a literature review of pertinent LG and LB papers.

In this section we also present the development of the LB models and provide a full derivation of the particular variant, an isotropic D2Q13 lLB model, used in

this thesis. The derivation takes the mesoscopic evolution equation of the D2Q13 lLB model and performs the customary Chapman-Enskog expansion procedure to tune the model onto the equations of isotropic hydrodynamics. Subsequently a brief overview of the methodologies involved in bounding and forcing LG and LB models is provided.

In chapter 4 we develop the algorithmic extensions to the isotropic D2Q13 lLB scheme derived in the chapter 3, which recovers the equations of nemato-dynamics. A coupled D2Q13 LBGK evolution scheme is devised to recover the scalar director equation of motion. This extra degree of freedom is then coupled to the existing isotropic D2Q13 lLB model to produce anisotropic flow. The result is a fully coupled mesoscopic model of anisotropic fluid dynamics (nemato-dynamics).

The initial aim of the thesis is a proof of concept and so chapter 5 contains a validation of the underlying isotropic D2Q13 lLB against a rigorous analytical test case (duct flow) and then the fully coupled anisotropic model. The validation of the anisotropic model takes place in two phases, first the response of the director field to an induced (controlled) steady state flow field is tested and second the response of flow properties (viscosity) to different director fields is considered. All results presented are discussed in relation to the expected theoretical results.

Having validated the model for steady state simulations, chapter 6 progresses to investigate induced transient director and flow fields in simple geometries. Firstly the well established magnetic Fréedericksz transition is investigated and the results are compared to the theory. Secondly the nematic effect of velocity "back-flow" with

director "kick-back", upon release from a confining magnetic field, is considered. Results for the back-flow experiments utilize the Fréedericksz aligned nematics from the earlier computer experiments, qualitatively to shed new light on the origins of back-flow.

Finally we present in chapter 7, qualitative results from a system with more complex boundary conditions, namely the Zenithly Bi-stable Display (ZBD) device. This incipient device has promising implications in the liquid crystal display industry and so there is interest in the use of our model to simulate the fully coupled nematic ZBD cell. In this chapter, results are presented not only for steady state simulations in a variety of geometrical configurations, which demonstrate the flexibility and ease inherent in the lLB model to change the system configuration but also for dynamical simulations.

A general conclusion and suggestions for further work are presented in chapter 8.

Chapter 2

Continuum Isentropic Nemato-dynamics

2.1 Overview

Fluid mechanics is the study of the motion of liquids and gases, which on the macroscale are regarded as continuous media. The governing equations of hydrodynamics, derived in the late 18^{th} century are therefore sets of partial differential equations describing the conserved properties of mass, momentum and energy. Unfortunately, due to their complexity, these equations at present have not been solved analytically, except in a few simple cases.

In Computational Fluids Dynamics (CFD), discrete models are used that attempt to map onto the governing equations of hydrodynamics. Since in this thesis we extend

the isotropic Lattice Boltzmann (LB) method to simulate anisotropic fluids it is prudent to cover the governing equations of anisotropic fluid dynamics, onto which we aim to manipulate the macroscopic dynamics of our model. Clearly we cannot discuss all aspects of the theory of anisotropic fluid dynamics, and the interested reader is directed to [9] for a comprehensive review of isotropic fluid dynamics and to [3] for the theory of anisotropic fluid dynamics.

2.2 Brief Note on Notation

Throughout this thesis we shall employ two types of mathematical notation, cartesian vector (e.g. $\nabla \cdot \mathbf{u}$) or the tensorial equivalent (e.g. $\partial_\alpha u_\alpha$, where $\alpha = x, y, z$). At any point during an algebraic derivation we employ the notation that is best adapted to the problem.

When using tensor notation we shall assume that where a repeated subscript occurs, then the Einstein summation principle is implied. For the example given above, the repeated subscript is α so we imply a summation over the subscript :

$$\partial_\alpha u_\alpha = \partial_x u_x + \partial_y u_y + \partial_z u_z.$$

Derivatives are also written in a shorthand manner, with the following meanings

$$\partial_\alpha \equiv \frac{\partial}{\partial x_\alpha} \quad , \quad \partial_t \equiv \frac{\partial}{\partial t} \quad , \quad \partial_{t_0} \equiv \frac{\partial}{\partial t_0} \quad \text{etc.}$$

2.3 Isotropic Fluid Dynamics

2.3.1 Introduction

Completely to describe an isotropic fluid in three dimensions a set of five equations are required. These are:

- The continuity (mass conservation) equation,
- The Navier-Stokes equations (one for each dimension),
- The energy equation.

These conservation laws of fluid dynamics arise intrinsically at the microscale from the molecular dynamics of the fluid molecules. However they are equally as valid at the macroscale through consideration of a volume element (defined below). This universality across scales has allowed the macroscopic conservation laws to be derived by the averaging of conserved microscopic dynamics. This method is known as the kinetic theory approach [4] and it is a kinetic theory technique called the Chapman-Enskog expansion that is traditionally used by Lattice Gas Cellular Automata (LGCAs) to map their dynamics onto macroscopic fluid dynamics. However at present our review of isotropic fluids will deal solely with the derivation of the target macroscopic conservation laws and so we need to define the term volume element.

Any small *volume element* in the fluid is always supposed so large that it still contains a very great number of molecules. Accordingly, when we speak of infinitely small

elements of volume, we shall always mean those which are very small compared with the volume of the body under consideration, but large compared with the distances between the molecules.

In deriving the macroscopic equations of hydrodynamics there are two different but equally valid approaches. The first is to consider the conservation of mass, momentum and energy of an individual fluid element as it moves along with the flow. This method does not employ a fixed co-ordinate system and is thus known as the Lagrangian description. The second method introduces flow variables (density, velocity and temperature) which are functions of space and time which are defined on a fixed coordinate system and so the method is know as the Eulerian description. Integration of the flow variables with respect to a volume element in a sufficiently small time step results in the Lagrangian properties of mass, momentum and energy. Although to some the Eulerian approach may be viewed as more intuitive, I have chosen in this section to follow the Lagrangian approach taken by [9]. Since this section, however, only aims briefly to overview the governing equations and not raise any issues between the two approaches, either method would have sufficed.

In a continuous medium, the continuity equation describes the fact that within the volume element there are no fluid sinks or sources - 'what flows in, flows out'. A flow regime that does not satisfy the mass continuity equation for example is one where bubbles develop within the fluid element. However within the regimes under discussion here, the continuity equation is a paramount requisite.

Euler's equations of motion for an inviscid (ideal) fluid take no account of energy dissipation processes which may occur within the fluid due to internal friction (viscosity) or other processes such as heat transfer. Therefore Euler's equations describe only the reversible mechanical transport of the fluid particles and the pressure forces acting on the fluid. Extending Euler's equations to include viscous dissipation results in the Navier-Stokes equations of fluid flow, one for each dimension so in 3D flow there will be three coupled partial differential equations. Although all results presented in this thesis are for 2D flow, the review of the governing equations will describe the full 3D set of equations.

To include processes such as heat transfer in the fluid, the equation of energy is required, however in the absence of such heat exchanges between different parts of the fluid or any adjoining bodies the fluid flow is said to be adiabatic. Within an adiabatic flow the entropy of any fluid particle remains constant as the particle moves around in space, i.e. the fluid is isentropic. The flow regimes we are interested in are all assumed to be isentropic and temperature variation is neglected, so we can discard the equation of energy and fully describe our isotropic fluid using just the mass continuity equation and the Navier-Stokes equations.

Within the concept of an isentropic flow regime we can also assume that the flow is incompressible (constant density). This simplifies the governing equations and is valid within what is known as the *hydrodynamic limit* of low frequency and long spatial wavelength.

2.3.2 Continuity Equation (Mass Conservation)

Consider some volume V_0 of space, i.e. figure (2.1),

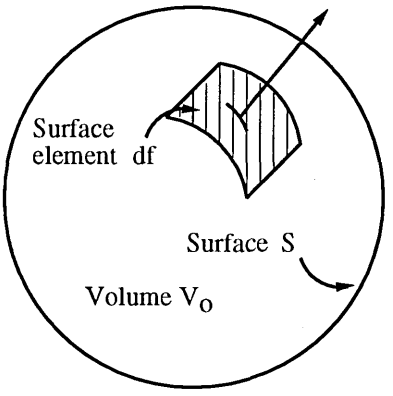

Figure 2.1: Fluid element of volume V_o with a bounding surface S. The magnitude of the surface element $d\mathbf{f}$ is its area and the direction is along the outward normal.

the mass of the fluid in this volume is

$$\int \rho \, dV \tag{2.1}$$

where ρ is the fluid density and the integration is over the volume V_0.

The mass of fluid flowing in unit time through an element $\mathrm{df} = \hat{\mathrm{n}}\,\mathrm{dA}$ of the surface S bounding the volume V_0 is $\rho\mathbf{u}\cdot\mathrm{df}$ where the magnitude of the vector $d\mathbf{f}$ is the area of the surface element and its direction is along the outward normal to the surface.

Therefore the total mass flowing out of the surface element in unit time is

$$\oint \rho \mathbf{u} \cdot \mathrm{d}\mathbf{f} \tag{2.2}$$

where the integration this time is over the whole of the closed surface S surrounding the volume V_0.

Within the volume element V_0 the decrease in mass per unit time is

$$-\partial_t \int \rho \, dV \tag{2.3}$$

Conservation of mass requires that the last two equations must balance, therefore

$$\partial_t \int \rho \, dV = -\oint \rho \mathbf{u} \cdot \mathrm{d}\mathbf{f}. \tag{2.4}$$

The surface integral can be transformed into a volume integral by Greens theorem (also known as the divergence theorem) [9]

$$\oint \rho \mathbf{u} \cdot \mathrm{d}\mathbf{f} \equiv \int \nabla \cdot (\rho \mathbf{u}) \; dV \tag{2.5}$$

Thus equation (2.4) becomes

$$\int \{\partial_t \rho + \nabla \cdot (\rho \mathbf{u})\} \; dV = 0 \tag{2.6}$$

which, since it is true for any volume, must have a vanishing integrand :

$$\partial_t \rho + \nabla \cdot (\rho \mathbf{u}) = 0, \tag{2.7}$$

which is the so-called Continuity equation and expresses the principle of mass conservation.

In the incompressible steady state fluid flow regime, the density ρ of the fluid is constant. This leaves us with the incompressible steady state mass conservation rule

$$\nabla \cdot \mathbf{u} = 0 \tag{2.8}$$

2.3.3 Euler's Equations (Inviscid flow)

Again let us refer to some volume element V_0 in the fluid, figure (2.1). The total force acting on the element is

$$\oint P \mathrm{df} \tag{2.9}$$

where P is the pressure and the integration is over the entire surface S bounding the volume V_0. We can use Green's theorem again to transform the surface integral into a volume integral,

$$\oint P \mathrm{df} = -\int \nabla P \, \mathrm{d}V \tag{2.10}$$

Hence we can say that the force acting on unit volume of the fluid is equivalent to -∇P and so we can write down the equation of motion for the fluid as

$$\rho D_t \mathbf{u} = -\nabla P \tag{2.11}$$

where the mass per unit volume is the fluid density ρ and $D_t\mathbf{u}$ represents the acceleration. $D_t\mathbf{u}$ is actually the rate of change of the velocity of a given fluid particle as it moves about in space which in conventional CFD is termed the *substantive derivative*, which may be written in terms of partial derivatives :

$$D_t\mathbf{u} = \partial_t\mathbf{u} + (\mathbf{u} \cdot \nabla)\,\mathbf{u}. \tag{2.12}$$

Substituting the substantive derivative into (2.11) we obtain the Euler equation for inviscid flow

$$\rho\,\partial_t \mathbf{u} + \rho\,(\mathbf{u}\cdot\nabla)\,\mathbf{u} = -\nabla P \tag{2.13}$$

Assuming the the fluid is incompressible we can write equation (2.13), in tensor notation

$$\partial_t(\rho u_\alpha) = -\partial_\beta \Pi_{\alpha\beta} \tag{2.14}$$

where we have assumed the Einstein summation convention applies and $\Pi_{\alpha\beta}$ is defined as the second rank momentum flux tensor

$$\Pi_{\alpha\beta} = P\delta_{\alpha\beta} + \rho u_\alpha u_\beta \tag{2.15}$$

so-called because it is easy to show from equation (2.14) that the surface integration

$$\oint \Pi_{\alpha\beta}\,\mathrm{d}f_\beta \tag{2.16}$$

gives $-\partial_t \int \rho u_\alpha d^3\mathbf{r}$, the rate of change of the α component of momentum associated with the fluid inside the control volume.

2.3.4 Navier-Stokes Equations (Viscous flow)

However, in order to obtain the equations describing the motion of a viscous fluid, we have to include some additional terms into equation (2.14). The momentum flux tensor described in (2.15) represents a completely reversible transfer of momentum due to simple mechanical transport of the fluid particles and the pressure forces acting on the fluid. In viscous fluids there is a dissipative momentum transfer, this time irreversible, from points where the velocity is large to those where it is small. We model the effect of this process by introducing a term to the momentum flux tensor to account for irreversible 'viscous' transfer of momentum in the fluid.

$$\Pi_{\alpha\beta} \rightarrow \Pi_{\alpha\beta} - \sigma'_{\alpha\beta} \, , \tag{2.17}$$

where $\sigma'_{\alpha\beta}$ is the viscous stress tensor, thus:

$$\Pi_{\alpha\beta} = P \, \delta_{\alpha\beta} + \rho u_\alpha u_\beta - \sigma'_{\alpha\beta}. \tag{2.18}$$

It is useful to rewrite $\Pi_{\alpha\beta}$ in terms of the components that are due to the direct mass transport ($\rho u_\alpha u_\beta$) and those that are not $\left(P \, \delta_{\alpha\beta} - \sigma'_{\alpha\beta}\right)$

$$\Pi_{\alpha\beta} = -\sigma_{\alpha\beta} + \rho u_\alpha u_\beta \tag{2.19}$$

we define the stress tensor

$$\sigma_{\alpha\beta} = -P \, \delta_{\alpha\beta} + \sigma'_{\alpha\beta} \tag{2.20}$$

and with this definition of stress, the momentum equation (2.14) assumes a form which we shall find useful

$$D_t \, \rho u_\alpha = \partial_\beta \sigma_{\alpha\beta} \tag{2.21}$$

The general form for the viscosity stress tensor depends on spatial velocity gradients which are supposed to be small so that the viscosity stress tensor depends only upon the first velocity gradients, i.e that $\sigma'_{\alpha\beta}$ is a linear function of these gradients [9]. In uniform flow or uniform rotation the viscosity stress tensor clearly needs to be zero. The most general second rank tensor that satisfies these conditions is [9]

$$\sigma'_{\alpha\beta} = a(\partial_\alpha u_\beta + \partial_\beta u_\alpha) + b\partial_\gamma u_\gamma \delta_{\alpha\beta} \tag{2.22}$$

in which the terms may be re-grouped as

$$\sigma'_{\alpha\beta} = \eta(\partial_\alpha u_\beta + \partial_\beta u_\alpha - \frac{2}{3}\partial_\gamma u_\gamma \delta_{\alpha\beta}) + \xi\partial_\gamma u_\gamma \delta_{\alpha\beta} \tag{2.23}$$

So now we can write the viscous form of the momentum flux tensor as

$$\Pi_{\alpha\beta} = P\,\delta_{\alpha\beta} + \rho u_\alpha u_\beta - \eta(\partial_\alpha u_\beta + \partial_\beta u_\alpha - \frac{2}{3}\partial_\gamma u_\gamma \delta_{\alpha\beta}) - \xi\partial_\gamma u_\gamma \delta_{\alpha\beta} \tag{2.24}$$

Which can then be substituted back into equation (2.14) to give

$$\rho(\partial_t u_\alpha + u_\beta \partial_\beta u_\alpha) = -\partial_\beta\, P\delta_{\alpha\beta} + \eta\,\partial_\beta(\partial_\alpha u_\beta + \partial_\beta u_\alpha - \frac{2}{3}\partial_\gamma u_\gamma \delta_{\alpha\beta}) + \xi\,\partial_\beta\partial_\gamma u_\gamma \delta_{\alpha\beta} \tag{2.25}$$

which, on invoking the continuity equation reduces straightforwardly to,

$$\partial_t u_\alpha + u_\beta \partial_\beta u_\alpha = -\frac{1}{\rho}\partial_\alpha\, P + \nu\partial_\beta\partial_\beta u_\alpha + \frac{1}{\rho}(\xi + \frac{1}{3}\eta)\partial_\alpha\partial_\beta u_\beta \tag{2.26}$$

see reference [9].

Here $\nu = \eta/\rho$ is the kinematic viscosity of the fluid.

We can further simplify the Navier-Stokes equation if we assume the fluid is incompressible ($\nabla \cdot \mathbf{u} = 0$), the final term vanishes and so equation (2.26) reduces to

$$\partial_t u_\alpha + u_\beta \partial_\beta u_\alpha = -\frac{1}{\rho}\partial_\alpha\, P + \nu\partial_\beta\partial_\beta u_\alpha \tag{2.27}$$

2.4 Anisotropic Fluid Dynamics

The term *liquid crystal* signifies a state of aggregation that is intermediate between the crystalline solid and the amorphous liquid. As a rule, a substance in this state is strongly anisotropic in some of its properties and yet exhibits a certain degree of fluidity, which in some cases may be comparable to that of an ordinary liquid with similar sized molecules. The first observations of liquid crystalline (*mesomorphic*) behavior were made towards the end of the 18^{th} century by Reinitzer [10] and Lehmann [11]. Several thousand organic compounds are now known to form liquid crystals. An essential requirement for the mesomorphism to occur is that the molecule must be highly anisotropic in shape, like a rod or a disc.

Depending on the detailed molecular structure, the system may pass through one or more mesophases before it is transformed into the isotropic liquid. Transitions to these intermediate states may be brought about by purely thermal processes (thermotropic mesomorphism) or by the influence of solvents (lyotropic mesomorphism).

The vast majority of thermotropic liquid crystals are composed of rod-like molecules. Following the nomenclature proposed originally by Friedel [12], liquid crystals are classified broadly into three types: *nematic*,*cholesteric* and *smectic*. It is the *nematic* phase that concerns us in this thesis. The nematic liquid crystal has a high degree of long-range orientational order of the molecules but no long-range translational order, see figure (2.2 b).

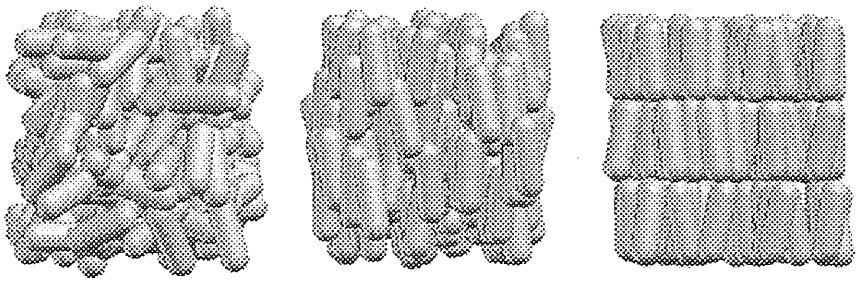

(a) Isotropic (b) Nematic (c) Smectic-A

Figure 2.2: Representation of molecular ordering in the isotropic,nematic and smectic-A phases.

Thus a nematic differs from an isotropic liquid in that the molecules are spontaneously orientated with their long axes approximately parallel. The fluidity of the nematic is due to the ease with which the molecules slide past one another while still retaining their parallelism and clearly their relative orientation must affect their ability to "shear".

The interest in nematic liquid crystals over the last century has increased enormously, due mainly to their applicability to display technology. There is now an extensive literature discussing the physical properties of nematics and their applications, with new technology utilizing nematic liquid crystals appearing continuously. However, until relatively recently, the mathematical models describing nematics were incomplete and most modeling of liquid crystals was performed using MD or MC techniques [13].

The foundations of the continuum model were laid in the late 1920's by Oseen [14] and Zöcher [15] who developed a successful static theory. The subject lay dormant

for nearly thirty years afterwards until Frank [16] re-examined Oseen's treatment and presented it as a theory of curvature elasticity. Dynamical theories were put forward by Anzelius [17] and Oseen [14] but the formulation of the general conservation laws and constitutive equations describing the mechanical behavior of the nematic state are credited to Ericksen [18, 19] and Leslie [20–22]. Other continuum theories have been proposed [23–27] but it turns out that the eponymous ELP presentation (P = Parodi) is the one that is most widely used in discussing the nematic state.

In this chapter we shall review the ELP continuum theory of nematic liquid crystals which captures many important physical phenomena exhibited by the nematic phase, such as its unusual flow properties and its response to bulk external fields. Fully to cover the constitutive mechanical equations of a continuum nematic fluid is rather non-trivial and beyond the scope of the work presented here. Unfortunately most treatments in the literature (e.g de Gennes [3]) are rather fragmented and (we suggest) difficult to piece together. Clearly however, there is a need to appreciate the physics behind the continuum equations and as such we attempt here to give an abbreviated but coherent derivation of the continuum description of a flowing nematic. The interested reader is directed to [3, 4, 13, 28] for a full review of continuum nemato-dynamics, from which a complete and rigorous account can no doubt be derived.

2.4.1 Static Nematic Theory

In a nematic liquid crystal the molecules are aligned around an average direction $\mathbf{n}$ called the director. The director is apolar (so that the same state of alignment may be characterized by $+\mathbf{n}$ or by $-\mathbf{n}$) and varies as a function of position in the nematic $\mathbf{n} \rightarrow \mathbf{n}(\mathbf{r})$ but it has unit magnitude $|\mathbf{n}| = 1$. The length scales of the variations in the director, l, are very large compared to the intermolecular distances of the nematic liquid crystal, a, and so $\mathbf{n}(\mathbf{r})$ can be described by a continuum theory.

Restricting ourselves to nematics below their critical transition temperature T_c (T_{NI}) we can make the assumption that the local properties of a weakly distorted system $a/l \ll 1$ are still those of a uniaxial crystal, with the director orientation able to rotate.

Accordingly, let us now impose on our bulk nematic some state of distortion described through the field $\mathbf{n}(\mathbf{r})$ where the distortion is constrained to have the following properties

1. $\mathbf{n}(\mathbf{r})$ is of fixed unit length but with variable orientation.

2. $\mathbf{n}(\mathbf{r})$ varies slowly and smoothly with $\mathbf{r}$, i.e. $a\nabla\mathbf{n} \ll 1$.

The distortion of $\mathbf{n}(\mathbf{r})$ introduces a new degree of freedom, a distortion free energy F_d in the system, which vanishes if $\nabla\mathbf{n} = 0$. We may expand F_d in terms of $\nabla\mathbf{n}$ within the constraints given above, always ensuring that F_d has the following properties [3]

:

1. F_d must be an even function of $\mathbf{n}(\mathbf{r})$ and its spatial gradients $\partial_\alpha n_\beta$ (since $\mathbf{n}(\mathbf{r})$ is apolar).

2. Terms in F_d which are of the form $\nabla \cdot \mathbf{u}$ where $\mathbf{u}$ is an arbitrary vector field contribute (through the divergence theorem) to surface (not bulk) energies only and so may be discarded.

To construct F_d consider the spatial derivatives of $\mathbf{n}$. They form a second rank tensor $g_{\alpha\beta}$ of the form $\partial_\alpha n_\beta$ which we can deconstruct into its symmetric components

$$e^s_{\alpha\beta} = \frac{1}{2}(\partial_\alpha n_\beta + \partial_\beta n_\alpha) \tag{2.28}$$

and anti-symmetric components.

$$e^a_\gamma = \frac{1}{2}\mathcal{E}_{\gamma\alpha\beta}\partial_\alpha n_\beta \tag{2.29}$$

Now referring back to the first requirement for the distortion free energy F_d will be a quadratic function of the symmetric and anti-symmetric components. Therefore we can separate the contributions to F_d as follows

$$F_d = F_s + F_a + F_{as}$$

where the contributions are from symmetric, anti-symmetric and cross-terms respectively.

Under the conditions imposed on the free energy, the most general forms for F_s, F_a

and F_{as} can be written respectively as [3] :

$$\begin{aligned} F_s &= \lambda_1 (\nabla \cdot \mathbf{n})^2 + \lambda_2 (\mathbf{n} \cdot \nabla \times \mathbf{n})^2 + \lambda_3 (\mathbf{n} \times \nabla \times \mathbf{n})^2 \\ F_a &= \mu_1 (\mathbf{n} \cdot \nabla \times \mathbf{n})^2 + \mu_2 (\mathbf{n} \times \nabla \times \mathbf{n})^2 \\ F_{as} &= \nu (\mathbf{n} \times \nabla \times \mathbf{n})^2 \end{aligned}$$

Regrouping the equations in (2.4.1) we may write the distortion free energy in the well known form :

$$F_d = \frac{1}{2} K_1 (\nabla \cdot \mathbf{n})^2 + \frac{1}{2} K_2 (\mathbf{n} \cdot \nabla \times \mathbf{n})^2 + \frac{1}{2} K_3 (\mathbf{n} \times \nabla \times \mathbf{n})^2 \qquad (2.30)$$

which is the fundamental formula of the continuum theory for nematics [3].

2.4.1.1 Three elastic constants, K_i

The three constants K_i in equation (2.30) are associated with the three basic types of deformations, see figure (2.3), that can occur in a nematic liquid crystal.

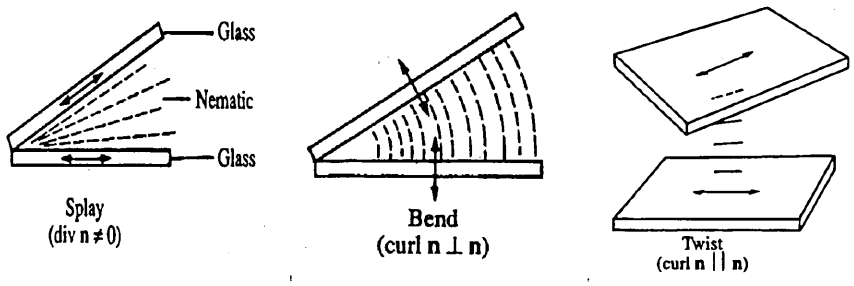

(a) (b) (c)

Figure 2.3: Schematic representation of the three basic types of elastic deformations that can occur in a nematic, reproduced from [3].

$$K_1 : \text{conformations with } \nabla \cdot \mathbf{n} \neq 0 \text{ (splay)}$$

$$K_2 : \text{conformations with } \mathbf{n} \cdot \nabla \times \mathbf{n} \neq 0 \text{ (twist)}$$

$$K_3 : \text{conformations with } \mathbf{n} \times \nabla \times \mathbf{n} \neq 0 \text{ (bend)}$$

All three deformations can be created individually and thus each constant K_i must be *positive* if not, the undistorted nematic conformation would not correspond to a minimum of the distortion free energy F_d.

2.4.1.2 The One Constant Approximation

The full form of equation (2.30) in many cases is too complex to be of practical use, either because the relative values of the three constants K_i are unknown or the equilibrium equations derived are prohibitively difficult to solve. Therefore it is often more practical to make a further approximation which assumes all three constants are equal, i.e.

$$K_1 = K_2 = K_3 = K$$

The distortion free energy (free energy density) then takes the form

$$\mathrm{F}_d \approx \frac{1}{2} K \left((\nabla \cdot \mathbf{n})^2 + (\nabla \times \mathbf{n})^2 \right) \tag{2.31}$$

which ignoring surface terms becomes

$$\mathrm{F}_d \approx K \nabla^2 \mathbf{n} \tag{2.32}$$

If we compare some typical values of the three elastic constants from the nematic material MBBA at 25°C [7].

K_1 (splay)	6.4×10^{-7} dyn
K_2 (twist)	3.8×10^{-7} dyn
K_3 (bend)	8.11×10^{-7} dyn

Table 2.1: Three elastic constants K_1 (splay), K_2 (twist) and K_3 (bend) for MBBA at 25°C. The dimensions of the elastic constants (dyn) is defined as energy/cm^2 [7].

we can see that the above approximation cannot be quantitatively correct however the simpler form of equation (2.32) makes it a valuable tool to reach a qualitative insight into distortions in nematics.

For a two dimensional nematic where the orientation of the director is restricted to lie within the plane $(2 \oplus 2)$ then there can be no contribution from the K_3 (bend) elasticity, since it contains gradients in $\mathbf{n}_z$. The remaining distortions (splay and twist) are about the same and so the distortion free energy in the one constant approximation can be considered to be an accurate representation of the actual distortion free energy.

2.4.1.3 Equilibrium Conditions: Molecular Field

In this subsection we shall introduce the central concept of the molecular field $\mathbf{h}$ essentially as an undetermined multiplier, to frame an equilibrium condition.

Following de Gennes [3], we work at present in the absence of any external fields, and obtain bulk equilibrium conditions by minimizing the total distortion free energy,

$$\mathcal{F}_d = \int F_d \, d^3\mathbf{r} \tag{2.33}$$

with respect to director variations. Any variation in the director field is constrained by the requirement that $\mathbf{n}(\mathbf{r})^2 = 1$ everywhere. Thus we appeal to Lagrange and write

$$\delta \mathcal{F}_d - \int \frac{1}{2} \lambda(\mathbf{r}) \, \delta\left(\mathbf{n}(\mathbf{r})^2\right) \, d^3\mathbf{r} = 0 \tag{2.34}$$

in which $\frac{1}{2}\lambda(\mathbf{r})$ is an undetermined scalar function. The above equation can be written as

$$\delta \mathcal{F}_d = \int \lambda(\mathbf{r}) \, n(\mathbf{r}) \, \delta \mathbf{n}(\mathbf{r}) \, d^3\mathbf{r} \tag{2.35}$$

Now the distortion free energy density F_d given in equation (2.30) is a function of density gradients $g_{\alpha\beta} = \partial_\alpha n_\beta$ and the director itself n_β so

$$\begin{aligned} \delta\mathcal{F}_d &= \delta\left\{\int F_d\left(\mathbf{n}, \underline{\underline{g}}\right)\, d^3\mathbf{r}\right\} \\ &= \int F_d\left(\mathbf{n}+\delta\mathbf{n}, \underline{\underline{g}}+\delta\underline{\underline{g}}\right)\, d^3\mathbf{r} - \int F_d\left(\mathbf{n}, \underline{\underline{g}}\right)\, d^3\mathbf{r} \\ &= \int\left\{\frac{\partial F_d}{\partial n_\beta}\delta n_\beta + \frac{\partial F_d}{\partial g_{\alpha\beta}}\delta g_{\alpha\beta}\right\}\, d^3\mathbf{r} \end{aligned} \tag{2.36}$$

now making the association $\delta\left(g_{\alpha\beta}\right) = \delta\left(\partial_\alpha n_\beta\right) = \partial_\alpha \delta n_\beta$, then we can write the last equation as :

$$\delta\mathcal{F}_d = \int\left\{\frac{\partial F_d}{\partial n_\beta}\delta n_\beta + \frac{\partial F_d}{\partial g_{\alpha\beta}}\partial_\alpha\left(\partial n_\beta\right)\right\}\, d^3\mathbf{r}. \tag{2.37}$$

Applying integration by parts, we can transform the second term in the above integrand

$$\int \frac{\partial F_d}{\partial g_{\alpha\beta}}\partial_\alpha\left(\partial n_\beta\right)\, d^3\mathbf{r} = \oint \frac{\partial F_d}{\partial g_{\alpha\beta}}\delta n_\beta\, \mathrm{d}s_\alpha - \int \partial_\alpha \frac{\partial F_d}{\partial g_{\alpha\beta}}\delta n_\beta \mathrm{d}^3\mathbf{r} \tag{2.38}$$

which can be written as :

$$\int \frac{\partial F_d}{\partial g_{\alpha\beta}}\partial_\alpha\left(\partial n_\beta\right)\, d^3\mathbf{r} = \oint \pi_{\alpha\beta}\, \delta n_\beta\, \mathrm{d}s_\alpha - \int \partial_\alpha \pi_{\alpha\beta}\, \delta n_\beta\, \mathrm{d}^3\mathbf{r} \tag{2.39}$$

and we have defined

$$\pi_{\alpha\beta} = \frac{\partial F_d}{\partial g_{\alpha\beta}} = \frac{\delta F_d}{\delta\left(\partial_\alpha n_\beta\right)}. \tag{2.40}$$

Inserting equation (2.39) into equation (2.37) and neglecting the surface terms :

$$\oint \pi_{\alpha\beta}\, \delta n_\beta\, \mathrm{d}s_\alpha \tag{2.41}$$

we obtain

$$\delta\mathcal{F}_d = \int\left\{\frac{\partial F_d}{\partial n_\beta}\delta n_\beta - \partial_\alpha\left(\frac{\partial F_d}{\partial g_{\alpha\beta}}\right)\delta n_\beta\right\}\, d^3\mathbf{r} \tag{2.42}$$

Comparing the integrals in equations (2.35) and (2.42) we obtain the general equilibrium condition of :

$$\frac{\partial F_d}{\partial n_\beta} - \partial_\alpha \pi_{\alpha\beta} = \lambda n_\beta. \tag{2.43}$$

It is customary to define the molecular field $\mathbf{h}$

$$h_\beta = -\frac{\partial F_d}{\partial n_\beta} + \partial_\alpha \pi_{\alpha\beta} \tag{2.44}$$

whereupon equation (2.43) now gives

$$h_\beta = -\lambda n_\beta, \tag{2.45}$$

from which it is apparent that in equilibrium, the director $\mathbf{n}$ at each point must lie parallel to the molecular field $\mathbf{h}$.

Now, we have an explicit expression for the distortion free energy F_d given by equation (2.30) and so we can find expressions for $\partial_{n_\beta} F_d$ and $\partial_\alpha \pi_{\alpha\beta}$ in the r.h.s of equation (2.44).

$$\partial_{n_\beta} F_d = \partial_{n_\beta} \left\{ K_1 \left(g_{ii}\right)^2 + K_2 \left(n_i \mathcal{E}_{ijk} g_{jk}\right)^2 + K_3 \left(\mathcal{E}_{ijk} n_j \mathcal{E}_{klm} g_{lm}\right)^2 \right\} \tag{2.46}$$

with $\mathcal{E}_{ijk}$ the unit antisymmetric tensor. Performing the differentiations w.r.t n_β we obtain

$$\partial_{n_\beta} F_d = K_2 \, \mathrm{A} \, \nabla \times \mathbf{n}|_\beta + K_3 \, \mathbf{n} \times (\nabla \times \mathbf{n}) \times (\nabla \times \mathbf{n}) \, |_\beta \tag{2.47}$$

where $\mathrm{A} \equiv (\mathbf{n} \cdot \nabla \times \mathbf{n})$. The triple product in the K_3 term expands to zero and so we finally obtain

$$\partial_{n_\beta} F_d = K_2 \, \mathrm{A} \, \nabla \times \mathbf{n}|_\beta \tag{2.48}$$

A similar expression for $\partial_\alpha \pi_{\alpha\beta}$ may be obtained from the explicit form of F_d in equation (2.30), which, when inserted along with equation (2.48) into equation (2.44) for the molecular field yields the result

$$\mathbf{h} = \mathbf{h}_s + \mathbf{h}_t + \mathbf{h}_b \tag{2.49}$$

where

$$\begin{aligned} \mathbf{h}_s &= K_1 \nabla (\nabla \cdot \mathbf{n}) \\ \mathbf{h}_t &= -K_2 \{\mathrm{A}\nabla \times \mathbf{n} + \nabla \times (\mathrm{An})\} \\ \mathbf{h}_b &= K_3 \{\mathrm{B} \times \nabla \mathbf{n} + \nabla \times (\mathbf{n} \times \mathrm{B})\} \end{aligned} \tag{2.50}$$

with A defined above and $\mathrm{B} = \mathbf{n} \times \nabla \times \mathbf{n}$.

In the one-constant approximation $\mathbf{h}$ takes a much simpler form

$$\mathbf{h} = K \nabla^2 \mathbf{n} \tag{2.51}$$

2.4.1.4 External Fields

We now have a definition of the molecular field $\mathbf{h}$ for a nematic in the one constant approximation in the absence of any external fields. However most liquid crystals react strongly to magnetic, electric, flexo-electric and gravitational bulk forces. In fact the di-electric coupling between the nematic and an external electric field is in many cases very complex [13]. However, along with flexo-electric and gravitational forces these shall not be considered here. The coupling for a single nematic liquid crystal molecule to an homogeneous bulk magnetic field $\mathbf{H}$ is very small. However, on the macroscopic scale a nematic element contains many millions of particles which

can rotate in unison. Therefore upon application of a magnetic field the director orientations will tend to align parallel to the applied field in competition with any imposed wall alignment. Quantitatively we can express the effect of a magnetic field on a nematic director by the induced magnetization **M**.

$$\begin{aligned} \mathbf{M} &= \chi_{\parallel}\mathbf{H} \qquad \text{if, } \mathbf{H}\text{, is parallel to } \mathbf{n} \\ \mathbf{M} &= \chi_{\perp}\mathbf{H} \qquad \text{if, } \mathbf{H}\text{, is perpendicular to } \mathbf{n} \end{aligned} \tag{2.52}$$

where $\chi_{\parallel}$ and $\chi_{\perp}$ are the nematic magnetic susceptibilities for parallel and perpendicular magnetic field applications respectively.

If **H** makes an arbitrary angle with **n** then the induced magnetization becomes

$$\mathbf{M} = \chi_{\perp}\mathbf{H} + \chi_a\,(\mathbf{H}\cdot\mathbf{n})\,\mathbf{H} \tag{2.53}$$

where χ_a is referred to as the overall magnetic susceptibility (magnetic anisotropy) of the nematic, defined by

$$\chi_a = \chi_{\parallel} - \chi_{\perp} \tag{2.54}$$

Since the first term in equation (2.53) is independent of the molecular orientation we can omit it from our description of the magnetic coupling to the nematic. Note that the second term in equation (2.53) will be minimized when **n** is collinear with **H** which is the requirement for equilibrium. The free energy of the nematic at equilibrium now entails a magnetic field contribution of

$$F_m = \chi_a\,(\mathbf{H}\cdot\mathbf{n})\,\mathbf{H} \tag{2.55}$$

which results in the molecular field given in equation (2.51) being expanded to

include a magnetic term of the form

$$\mathbf{h}_m = \chi_a \left(\mathbf{H} \cdot \mathbf{n}\right) \mathbf{H} \tag{2.56}$$

2.4.2 Equilibrium Hydrostatics

Let us re-write our expression for the molecular field, in the presence of an external magnetic field.

For our purposes, as we are simulating in a gravitational equi-potential, we can write the molecular field simply as the sum of the contributions from equations (2.44) and (2.56),

$$h_\beta = \partial_\alpha \pi_{\alpha\beta} - \frac{\partial F_d}{\partial n_\beta} + \chi_a \left(\mathbf{H} \cdot \mathbf{n}\right) \mathbf{H} \tag{2.57}$$

where, recalling equation (2.40),

$$\pi_{\alpha\beta} = \frac{\partial F_d}{\partial g_{\alpha\beta}} = \frac{\delta F_d}{\delta \left(\partial_\alpha n_\beta\right)}.$$

With the molecular field defined as above, the equilibrium condition is simply that $\mathbf{h}$ and the director $\mathbf{n}$ be parallel, i.e equation (2.45)

$$h_\beta = -\lambda \left(\mathbf{r}\right) n_\beta$$

Suppose that a director $\mathbf{n}\left(\mathbf{r}\right)$ is displaced without change of orientation to $\mathbf{r}' = \mathbf{r} + \mathbf{u}\left(\mathbf{r}\right)$ so that

$$\mathbf{n}'\left(\mathbf{r}'\right) = \mathbf{n}'\left(\mathbf{r} + \mathbf{u}\left(\mathbf{r}\right)\right) = \mathbf{n}\left(\mathbf{r}\right). \tag{2.58}$$

(We shall consider changes in the director orientation $\mathbf{n} \rightarrow \mathbf{n} + \delta\mathbf{n}$ below.)

Now,

$$\frac{\partial n_\gamma^{'}}{\partial r_\beta^{'}} = \frac{\partial n_\gamma^{'}}{\partial r_\alpha}\frac{\partial r_\alpha}{\partial r_\beta^{'}} \tag{2.59}$$

in which it should be noted that the summation convention applies. Substituting from equation (2.58) into equation (2.59) we obtain

$$\frac{\partial n_\gamma^{'}}{\partial r_\beta^{'}} = \frac{\partial r_\alpha}{\partial r_\beta^{'}}\frac{\partial n_\gamma}{\partial r_\alpha} \tag{2.60}$$

and noting that, to first order in derivatives,

$$\frac{\partial r_\alpha}{\partial r_\beta^{'}} = \frac{\partial}{\partial r_\beta^{'}}\left(r_\alpha^{'} - u_\alpha\left(\mathbf{r}\right)\right) = \delta_{\alpha\beta} - \frac{\partial}{\partial r_\beta^{'}}u_\alpha \tag{2.61}$$

we substitute into equation (2.60) to obtain

$$\frac{\partial n_\gamma^{'}}{\partial r_\beta^{'}} = \frac{\partial n_\gamma}{\partial r_\beta} - \frac{\partial n_\gamma}{\partial r_\alpha}\frac{\partial u_\alpha}{\partial r_\beta^{'}} \tag{2.62}$$

which is re-arranged to give

$$\frac{\partial n_\gamma^{'}}{\partial r_\beta^{'}} - \frac{\partial n_\gamma}{\partial r_\beta} = -\frac{\partial n_\gamma}{\partial r_\alpha}\frac{\partial u_\alpha}{\partial r_\beta^{'}}\,. \tag{2.63}$$

Now the change in the distortion free energy of an incompressible fluid element originally at position $\mathbf{r}$, when displaced to position $\mathbf{r}^{'}$, may be obtained by approximating equation (2.40) as $\Delta F_d \approx \pi_{\gamma\alpha}\left(\Delta g_{\gamma\alpha}\right)$, whereupon we obtain

$$\Delta F_d = \pi_{\gamma\alpha}\left\{\Delta\left[\partial_\gamma n_\alpha\right]\right\}. \tag{2.64}$$

Expanding the braces gives

$$\Delta F_d = \pi_{\gamma\alpha}\left\{\frac{\partial n_\alpha^{'}}{\partial r_\gamma^{'}} - \frac{\partial n_\alpha}{\partial r_\gamma}\right\}, \tag{2.65}$$

which on appeal to equation (2.63) yields the following expression for the change in the distortion free energy of the incompressible fluid element,

$$\Delta F_d = \pi_{\gamma\alpha}\left(\partial_\beta n_\gamma\right)\left(\partial_\gamma u_\beta\right) d^3\mathbf{r} \tag{2.66}$$

and for the change in the distortion free energy of the fluid as a whole

$$\delta F_d = \int \sigma^d_{\beta\alpha} \partial_\beta u_\alpha d^3\mathbf{r} \tag{2.67}$$

with the *distortion stress tensor* defined as

$$\sigma^d_{\beta\alpha} = -\pi_{\beta\gamma} \partial_\alpha n_\gamma. \tag{2.68}$$

In fact the distortion stress tensor, defined above, is not in general symmetric [3,4]. However, for the particular case of the one constant approximation the distortion stress tensor becomes symmetric.

Remembering that we are working in an incompressible regime, to write an equilibrium condition we must seek the minimum change in the total distortion free energy resulting from the displacement field (strain) $\mathbf{u}(\mathbf{r})$ *where* $\nabla \cdot \mathbf{u} = 0$; that is from the condition

$$\delta F_d - \int p(\mathbf{r}) \nabla \cdot \mathbf{u} \, d^3\mathbf{r} = 0 \tag{2.69}$$

where $p(\mathbf{r})$ is again a generalized Lagrange multiplier. Substituting for δF_d from equation (2.67) and expressing the divergence in tensor notation, we obtain an expression for the strain-induced variation in a revised distortion free energy, the minimum of which will coincide with the minimum of F_d for strains which leave the density constant

$$\delta F_d \equiv \int \left(\sigma^d_{\alpha\beta} - p(\mathbf{r}) \delta_{\alpha\beta}\right) \partial_\alpha u_\beta \, d^3\mathbf{r}. \tag{2.70}$$

The form of equation (2.70) motivates the definition of the Ericksen stress $\sigma^e_{\alpha\beta}$ as

$$\sigma^e_{\alpha\beta} = \sigma^d_{\alpha\beta} - p\delta_{\alpha\beta}. \tag{2.71}$$

We need now to consider fluctuations in director orientation $\mathbf{n} \rightarrow \mathbf{n} + \delta\mathbf{n}$. These are accounted for in equation (2.42) which we reproduce below for convenience, but including the surface terms from equation (2.41)

$$\delta F_d = \int \left\{ \frac{\partial F_d}{\partial n_\beta} \delta n_\beta - \partial_\alpha \left(\frac{\partial F_d}{\partial g_{\alpha\beta}} \right) \delta n_\beta \right\} d^3\mathbf{r} + \oint \pi_{\alpha\beta}\, \delta n_\beta \, \mathrm{d}s_\alpha .$$

Replacing the terms inside the braces in the first integrand using the definition of the molecular field in equation (2.44), we obtain a contribution to the free energy from director fluctuations

$$\delta F_d = - \int h_\beta \, \delta n_\beta \, d^3\mathbf{r} + \oint \pi_{\alpha\beta} \, \delta n_\beta \, \mathrm{d}s_\alpha \tag{2.72}$$

adding the above contribution to the free energy to that in equation (2.70) we derive an expression for the complete variation in the free energy

$$\delta f_d = \int \left\{ \sigma^e_{\alpha\gamma} \partial_\alpha u_\gamma - h_\beta \, \delta n_\beta \right\} \mathrm{d}^3\mathbf{r} + \oint \pi_{\alpha\beta} \delta n_\beta \mathrm{d}s_\alpha \tag{2.73}$$

From the last equation we can develop an identity which will prove useful in the next section.

Clearly any deformation that corresponds to a rotation of both the molecular centres and their directors by the same angle should leave F_d invariant. Let the vector Ω define a rotation then such a transformation of the director field is $\mathbf{u}(\mathbf{r}) = \Omega \times \mathbf{r}$ and $\delta\mathbf{n}(\mathbf{r}) = \Omega \times \mathbf{n}$, which in tensor notation yields the identities

$$\begin{aligned} \partial_\beta u_\alpha &= \mathcal{E}_{\alpha\mu\beta}\Omega_\mu \\ \delta n_\gamma &= \mathcal{E}_{\gamma\mu\rho} n_\rho \Omega_\mu . \end{aligned} \tag{2.74}$$

Substituting the identities in equation (2.74) into equation (2.73) we obtain an expression for the corresponding change in total distortion free energy, which we

know to be zero :

$$\delta f_d = \Omega_\mu \int \left\{ \mathcal{E}_{\alpha\mu\beta}\ \sigma^d_{\beta\alpha} + \frac{\partial \mathrm{F}_d}{\partial n_\gamma} \mathcal{E}_{\gamma\mu\rho} n_\rho + \mathcal{E}_{\gamma\mu\rho} \pi_{\beta\gamma} \partial_\beta n_\rho \right\}\ \mathrm{d}^3\mathbf{r} = 0. \tag{2.75}$$

Transforming the second term in the above equation by parts we obtain :

$$\int \mathcal{E}_{\alpha\mu\beta}\ \sigma^d_{\beta\alpha}\ \mathrm{d}^3\mathbf{r} - \int \mathcal{E}_{\gamma\mu\rho}\ (-h_\gamma n_\rho + n_\rho \partial_\beta \pi_{\beta\gamma} + \mathrm{M} \times \mathrm{H} + \pi_{\beta\gamma} \partial_\beta n_\rho)\ \mathrm{d}^3\mathbf{r} = 0 \tag{2.76}$$

where we have used the definition of induced magnetization in equation (2.53). We shall return to use this equation in the next section.

Using the product rule (in reverse) on the terms in $\pi_{\beta\gamma}$ and integrating by parts, it can be shown

$$\int \mathcal{E}_{\mu\alpha\beta}\ \sigma^d_{\beta\alpha} = \int (\mathbf{h} \times \mathbf{n}|_\mu + \mathrm{M} \times \mathrm{H}|_\mu)\ \mathrm{d}^3\mathbf{r} - \oint \mathcal{E}_{\mu\gamma\rho} \pi_{\beta\gamma} n_\rho\ \mathrm{d}s_\beta \tag{2.77}$$

to which equation we shall again return in the next section.

2.4.3 Nemato-dynamics

To derive the governing equations for variables $\mathbf{u}$ and $\mathbf{n}$, subject to the usual limitations of low spatial and temporal gradients, in the isothermal regime, is the principal objective of this section. We follow the usual route of identifying dissipative losses [3] which derives ultimately from a treatment based in non-equilibrium thermo-dynamics by de Groot and Mazur [29].

We introduce the nematic fluid's momentum stress tensor $\sigma_{\alpha\beta}$ in order to write its acceleration (momentum) equation as in equation (2.21)

$$\mathrm{D}_t\ \rho u_\beta = \partial_\alpha \sigma_{\alpha\beta}$$

For an isothermal process, dissipation $\mathrm{D}_t\mathrm{Q} = \mathrm{T}\ \mathrm{D}_t\mathrm{S}$ is equal to the decrease in stored free energy;

$$\mathrm{T}\ \mathrm{D}_t\mathrm{S} = -\mathrm{D}_t \int \{\frac{1}{2}\rho u^2 + F_o + F_d + F_m\} d^3\mathbf{r} \tag{2.78}$$

where the second term F_o is a density dependent internal free energy, and all other terms have their usual meaning. Performing the time differentiation on the first term in the integrand; $\int \mathrm{D}_t \left(\frac{1}{2}\rho u_\beta u_\beta\right) \mathrm{d}^3\mathrm{r} = \int \rho u_\beta \mathrm{D}_t u_\beta \mathrm{d}^3\mathrm{r}$

$$\int \mathrm{D}_t \left(\frac{1}{2}\rho u_\beta u_\beta\right) \mathrm{d}^3\mathrm{r} = \int \rho u_\beta \mathrm{D}_t u_\beta \mathrm{d}^3\mathrm{r} \tag{2.79}$$

and using equation (2.21) we obtain

$$\int \mathrm{D}_t \left(\frac{1}{2}\rho u_\beta u_\beta\right) \mathrm{d}^3\mathrm{r} = \rho \int u_\beta\ \partial_\alpha \sigma_{\alpha\beta}\ \mathrm{d}^3\mathrm{r}. \tag{2.80}$$

Using parts and the divergence theorem, the r.h.s may be transformed to

$$\int \mathrm{D}_t \left(\frac{1}{2}\rho u_\beta u_\beta\right) \mathrm{d}^3\mathrm{r} = \int \sigma_{\alpha\beta}\partial_\alpha u_\beta\ \mathrm{d}^3\mathrm{r}\ +\ \text{surface terms} \tag{2.81}$$

Consider now the time differentiation of the remaining free energy terms in the integrand of equation (2.78). The material (substantive) derivative of a strain field is the velocity field. Accordingly, from the arguments around equations (2.70) and (2.71), we can see that for *flow* there is a contribution to the material derivative of $\int \mathrm{F}_d\ d^3\mathbf{r}$, of the form :

$$\int -\sigma^e_{\alpha\beta}\partial_\alpha u_\beta d^3\mathbf{r}, \tag{2.82}$$

and for *rotation*, from equation (2.72), the contribution to material derivative of $\int \mathrm{F}_d\ d^3\mathbf{r}$, is

$$-\int h_\beta\ \mathrm{D}_t n_\beta\ d^3\mathrm{r}\ +\ \text{surface terms} \tag{2.83}$$

whereupon we can write for the material derivative of $\int \mathrm{F}_d \, d^3\mathbf{r}$

$$-\mathrm{D}_t \int \mathrm{F}_d \, d^3\mathbf{r} = \int \left\{ -\sigma^e_{\alpha\beta} \partial_\alpha u_\beta + h_\beta \, \mathrm{D}_t n_\beta \right\} d^3\mathbf{r} \; + \; \text{surface terms} \tag{2.84}$$

combining the various contributions in equation (2.78) from (2.81) and (2.84) we can write

$$\mathrm{T} \, \mathrm{D}_t \mathrm{S} = \int \left\{ \sigma'_{\alpha\beta} \partial_\alpha u_\beta + h_\beta \, \mathrm{D}_t n_\beta \right\} \; + \; \text{surface terms} \tag{2.85}$$

where

$$\sigma'_{\alpha\beta} = \sigma_{\alpha\beta} - \sigma^e_{\alpha\beta} \tag{2.86}$$

and, of course the material derivative of $\mathbf{n}$ is given by

$$\mathrm{D}_t n_\beta = \partial_t n_\beta + u_\alpha \partial_\alpha n_\beta. \tag{2.87}$$

We resolve the viscous stress into symmetric and anti-symmetric parts

$$\underline{\underline{\sigma}}' = \underline{\underline{\sigma}}^s + \frac{1}{2} \underline{\underline{\Gamma}} \tag{2.88}$$

where $\underline{\underline{\Gamma}}$ is a pseudo-tensor :

$$\Gamma_\alpha = \mathcal{E}_{\alpha\beta\gamma} \sigma'_{\gamma\beta} \tag{2.89}$$

and

$$\sigma^s_{\alpha\beta} = \frac{1}{2} \left(\sigma'_{\alpha\beta} + \sigma'_{\beta\alpha} \right). \tag{2.90}$$

Considering equations (2.89) and (2.90) in order, the torque, Γ_α, can be found by considering the angular momentum of the sample [3] :

$$\begin{aligned} \mathrm{D}_t \mathrm{L}_\alpha &= \mathrm{D}_t \int \mathrm{d}^3\mathbf{r} \; (\mathbf{r} \times \rho \mathbf{u}) \\ &= \int \mathrm{d}^3\mathbf{r} \; (\mathbf{r} \times \mathrm{D}_t \rho \mathbf{u} + \mathrm{D}_t \mathbf{r} \times \rho \mathbf{u}) \, . \end{aligned} \tag{2.91}$$

Therefore

$$D_t L_\alpha = \int d^3\mathbf{r}\,(\mathcal{E}_{\alpha\beta\gamma} r_\beta\,(\partial_\theta \sigma_{\theta\gamma})) \tag{2.92}$$

where we have used the acceleration equation (2.21) and the fact that $D_t\mathbf{r} \times \rho\mathbf{u} = \mathbf{u} \times \rho\mathbf{u} = 0$ and where $\mathcal{E}_{\alpha\beta\gamma}$ is the unit anti-symmetric tensor. Applying parts now, with $\alpha = z$, it can be shown (see appendix (D)) that :

$$D_t L_z = \int d^3\mathbf{r}\,(\sigma_{yx} - \sigma_{xy}) + \oint \mathbf{r} \times (d\mathbf{s} : \underline{\underline{\sigma}}) \tag{2.93}$$

where $d\mathbf{s} : \underline{\underline{\sigma}} \equiv ds_\beta \sigma_{\beta\alpha}$.

Now the rate of change of the total angular momentum of the liquid (the total torque) derives from the magnetic torque, torques due to external stresses at the wall and torques on the director at the boundary [3] :

$$\Gamma_z = \int d^3\mathbf{r}\,(\mathrm{M} \times \mathrm{H})\,|_z + \oint \mathbf{r} \times (d\mathbf{s} : \underline{\underline{\sigma}})\,|_z + \oint \mathbf{r} \times (d\mathbf{s} : \underline{\underline{\pi}})\,|_z \tag{2.94}$$

with the r.h.s terms in the order discussed above. Accordingly we equate (2.93) and (2.94), cancel the terms $\int \mathbf{r} \times (d\mathbf{s} : \underline{\underline{\sigma}})$ and obtain :

$$\int d^3\mathbf{r}\,(\sigma_{yx} - \sigma_{xy}) = \int d^3\mathbf{r}\,(\mathrm{M} \times \mathrm{H})\,|_z + \oint \mathbf{r} \times (d\mathbf{s} : \underline{\underline{\pi}})\,|_z \tag{2.95}$$

writing the total stress as $\sigma_{\alpha\beta} = \sigma'_{\alpha\beta} + \sigma^e_{\alpha\beta}$ and substituting for the Ericksen stress in terms of the distortion stress, the integrand of the l.h.s becomes

$$\left(\sigma'_{yx} - \sigma'_{xy}\right) + \left(\sigma^d_{yx} - \sigma^d_{xy}\right). \tag{2.96}$$

We obtained equation (2.77) in the previous section which may now be used straightforwardly in the form

$$\int \left(\sigma^d_{yx} - \sigma^d_{xy}\right) d^3\mathbf{r} = \int \{\mathbf{M} \times \mathbf{H} - \mathbf{n} \times \mathbf{h}\}\,|_z\, d^3\mathbf{r} + \int \{\mathbf{n} \times (ds_\beta \pi_{\alpha\beta})\}\,|_z. \tag{2.97}$$

Using expression (2.96) in the argument of the l.h.s integrand of equation (2.95) and equation (2.97), and the definition of the torque Γ_α in equation (2.89), we obtain the beautifully simple result

$$\int \{\Gamma - \mathbf{n} \times \mathbf{h}\} \, \mathrm{d}^3\mathbf{r} = 0 \tag{2.98}$$

which must be true for any region, whence we see that the torque exerted by the director on the flow is given by

$$\Gamma = \mathbf{n} \times \mathbf{h}. \tag{2.99}$$

Let us know return to the dissipation equation (2.85), we proceed by separating the velocity gradient tensor into symmetric

$$A_{\alpha\beta} = \frac{1}{2} \left(\partial_\alpha u_\beta + \partial_\beta u_\alpha \right) \tag{2.100}$$

and antisymmetric parts

$$\omega = \frac{1}{2} \nabla \times \mathbf{u}. \tag{2.101}$$

We can write the dissipation as

$$\mathrm{T} \, \mathrm{D}_t \mathrm{S} = \int \left\{ A_{\alpha\beta} \, \sigma^s_{\alpha\beta} - \Gamma \cdot \omega + \mathbf{h} \cdot \mathrm{D}_t \mathbf{n} \right\} \mathrm{d}^3\mathbf{r} \tag{2.102}$$

where $\sigma^s_{\alpha\beta}$ is the symmetric part of the viscous stress $\sigma'_{\alpha\beta}$. Substituting equation (2.99) into equation (2.102), we obtain initially, an equation regarded by many as the fundamental equation of nemato-dynamics,

$$\mathrm{T} \, \mathrm{D}_t \mathrm{S} = \int \left\{ A_{\alpha\beta} \, \sigma^s_{\alpha\beta} + \mathbf{h} \cdot \mathbf{N} \right\} \mathrm{d}^3\mathbf{r} \tag{2.103}$$

where

$$\mathbf{N} = \mathrm{D}_t \mathbf{n} - \omega \times \mathbf{n} \tag{2.104}$$

represents the rate of change of the director with respect to the background fluid [3].

In non-equilibrium thermodynamics, entropy sources are regarded as products (contractions) of fluxes and *conjugate* forces [29], in the sense that the force conjugate to a flux, when contracted with that flux yields a contribution to the entropy source. Accordingly, a glance at equation (2.103) enables us to make a choice of such fluxes and conjugate forces :

$$\begin{aligned} \sigma^s_{xx} &\text{ is the force conjugate to } A_{xx} \\ 2\sigma^s_{xy} &\text{ is the force conjugate to } A_{xy} \quad \text{etc.} \\ h_\alpha &\text{ is the force conjugate to } N_\alpha. \end{aligned} \tag{2.105}$$

(The factor of 2 occurring in the non-diagonal elements expresses the fact that the terms such as $\sigma^s_{xy}A_{xy}$ appear twice in the entropy source equation (2.103) [3]). In the limit of weak fluxes, the forces will be linear functions of the fluxes :

$$\sigma^s_{\alpha\beta} = \mathrm{L}_{\alpha\beta\gamma\delta}A_{\gamma\delta} + \mathrm{M}_{\alpha\beta\gamma}N_\gamma \tag{2.106}$$

$$h_\gamma = M'_{\alpha\beta\gamma}A_{\alpha\beta} + \mathrm{P}_{\gamma\delta}N_\delta. \tag{2.107}$$

The magnetic field effects on the friction constants of the nematic are negligible which along with the Onsager theorem :

$$\mathrm{M}_{\alpha\beta\gamma} = M'_{\alpha\beta\gamma}, \tag{2.108}$$

simplifies the situation considerably. Moreover, we can state that the only vector that may appear in the definition of L, M and P is the local director $\mathbf{n}$. Also, since all measurable properties must be invariant when we change $\mathbf{n}$ to $-\mathbf{n}$ then $\underline{\underline{A}}$ and $\underline{\underline{\sigma}}^s$ are invariant, while $\mathbf{N}$ and $\mathbf{h}$ are odd [3].

The most general structures for equations (2.106) and (2.107) that satisfy the above requirements are [3],

$$\begin{aligned}\sigma^s_{\alpha\beta} &= \rho_1\delta_{\alpha\beta}A_{\mu\mu} + \rho_2 n_\alpha n_\beta A_{\mu\mu} + \rho_3\delta_{\alpha\beta}n_\gamma n_\mu A_{\gamma\mu} + \\ &\quad \alpha_1 n_\alpha n_\beta n_\mu n_\rho A_{\mu\rho} + \alpha_4 A_{\alpha\beta} + \\ &\quad \frac{1}{2}(\alpha_5+\alpha_6)(n_\alpha A_{\mu\beta} + n_\beta A_{\mu\alpha})n_\mu + \frac{\gamma_2}{2}(n_\alpha N_\beta + n_\beta N_\alpha) \qquad (2.109)\\ h_\mu &= \gamma_2' n_\alpha A_{\alpha\mu} + \gamma_1 N_\mu \qquad (2.110)\end{aligned}$$

where the Onsager relation in equation (2.108) imposes that

$$\gamma_2' = \gamma_2 \qquad (2.111)$$

In the incompressible limit the trace of the tensor $\underline{\underline{A}}$ vanishes and the terms with coefficients ρ_1 and ρ_2 drop out of equation (2.109). The term with the ρ_3 coefficient in equation (2.109) reduces to three diagonal components which we take to be similar and so can be lumped into the scalar pressure P and are therefore omitted.

The symmetric form for the total stress tensor in equation (2.109) can now be transformed into an equation for the complete viscous stress $\underline{\underline{\sigma'}}$. The antisymmetric part of $\underline{\underline{\sigma'}}$ is given explicitly in terms of the molecular field $\mathbf{h}$ by equations (2.89) and (2.99), and the molecular field is given by equation (2.110).

Regrouping these terms allows us to write the equations for the total viscous stress tensor and the molecular field respectively as

$$\begin{aligned} \sigma'_{\alpha\beta} &= \alpha_1 n_\alpha n_\beta n_\mu n_\rho A_{\mu\rho} + \alpha_4 A_{\alpha\beta} + \alpha_5 n_\alpha n_\mu A_{\mu\beta} + \\ &\quad \alpha_6 n_\beta n_\mu A_{\mu\alpha} + \alpha_2 n_\alpha N_\beta + \alpha_3 n_\beta N_\alpha \qquad (2.112) \\ h_\mu &= \gamma_1 N_\mu + \gamma_2 n_\alpha A_{\alpha\mu} \qquad (2.113) \end{aligned}$$

along with the relations

$$\begin{aligned} \gamma_1 &= \alpha_3 - \alpha_2 \qquad (2.114) \\ \gamma_2 &= \alpha_2 + \alpha_3 = \alpha_6 - \alpha_5 \qquad (2.115) \end{aligned}$$

2.5 Reduction to the scalar angle, θ

In this section we shall present the method of reducing equation (2.113), the vector equation of motion for the director $\mathbf{n}$ to an equation of motion of a scalar variable θ. We shall also discuss the consequences and reasons behind such an approach.

2.5.1 The scalar director evolution equation

We start by expressing the director equation of motion given in equation (2.113) in the form

$$D_t n_\mu = \frac{K}{\gamma_1}\partial_\gamma\partial_\gamma n_\mu + \frac{\chi_a}{\gamma_1}n_\gamma H_\gamma H_\mu + (\omega \times \mathbf{n})|_\mu - \frac{\gamma_2}{\gamma_1}n_\nu A_{\nu\mu} \tag{2.116}$$

which in two dimensions has two components,

$$D_t n_x = \frac{K}{\gamma_1}\partial_\gamma\partial_\gamma n_x + \frac{\chi_a}{\gamma_1}n_\gamma H_\gamma H_x + (\omega \times \mathbf{n})|_x - \frac{\gamma_2}{\gamma_1}n_\nu A_{\nu x} \tag{2.117}$$

$$D_t n_y = \frac{K}{\gamma_1}\partial_\gamma\partial_\gamma n_y + \frac{\chi_a}{\gamma_1}n_\gamma H_\gamma H_y + (\omega \times \mathbf{n})|_y - \frac{\gamma_2}{\gamma_1}n_\nu A_{\nu y} \tag{2.118}$$

Curling $D_t n_\mu$ with n_μ, effectively couples the two components of the director evolution equation,

$$\begin{aligned} n_x D_t n_y - n_y D_t n_x = & \tfrac{K}{\gamma_1}\left(n_x\partial_\gamma\partial_\gamma n_y - n_y\partial_\gamma\partial_\gamma n_x\right) + \\ & \tfrac{\chi_a}{\gamma_1}n_y\left(n_x n_\gamma H_\gamma H_y - n_\gamma H_\gamma H_x\right) + \\ & n_x(\omega \times \mathbf{n})|_y - n_y(\omega \times \mathbf{n})|_x + \\ & \tfrac{\gamma_2}{\gamma_1}\left(n_x n_\nu A_{\nu y} + n_y n_\nu A_{\nu x}\right) \end{aligned} \tag{2.119}$$

The next step is explicitly to replace the vectorial components of $\mathbf{n}$ with their scaler θ equivalence, i.e.

$$\begin{aligned} n_x &= +\cos(\theta) \\ n_y &= +\sin(\theta) \\ D_t n_x &= -\sin(\theta)\, D_t\theta \\ D_t n_y &= +\cos(\theta)\, D_t\theta \\ \partial_\gamma\partial_\gamma n_x &= -\sin(\theta)\,\partial_\gamma\partial_\gamma\theta - \cos(\theta)\,\{\partial_x\theta^2 + \partial_y\theta^2\} \\ \partial_\gamma\partial_\gamma n_y &= +\cos(\theta)\,\partial_\gamma\partial_\gamma\theta - \sin(\theta)\,\{\partial_x\theta^2 + \partial_y\theta^2\} \end{aligned} \tag{2.120}$$

After application of some standard trigonometric identities we can write the new equation of motion of the director in terms of the scalar angle,θ.

$$D_t\theta = \frac{K}{\gamma_1}\partial_\gamma\partial_\gamma\theta + \frac{\chi_a}{\gamma_1}\mathrm{M} + \Omega + \frac{\gamma_2}{\gamma_1}n_\gamma \mathrm{A}_{\gamma\beta} \tag{2.121}$$

where, M, is the magnetic field contribution, Ω, is the fluid vorticity and, $n_\gamma \mathrm{A}_{\gamma\beta}$, is designated the source term. These terms are defined respectively as

$$\begin{aligned} \mathrm{M} &= \tfrac{1}{2}\left[\,2\cos(2\theta)\,H_x H_y + \sin\{2\theta\}\left(H_y^2 - H_x^2\right\}\,\right] \\ \Omega &= \tfrac{1}{2}\left(\partial_x u_y - \partial_y u_x\right) \\ n_\gamma \mathrm{A}_{\gamma\beta} &= \tfrac{1}{2}\left[\sin(2\theta)\,\{\partial_x u_x - \partial_y u_y\} - \cos(2\theta)\,\{\partial_x u_y + \partial_y u_x\}\,\right] \end{aligned} \tag{2.122}$$

2.5.2 Advantages of the method

To model an anisotropic fluid we intend to enhance a standard isotropic Lattice Boltzmann (LB) model. In our model a link density distribution function f_i is collided and propagated on the mesoscale and produces macroscopic observables of density and momentum. Reducing the director equation of motion to the scalar

angle variable θ allows us to introduce a link angular distribution function θ_i on the mesoscale that produces the director angle as a macroscopic observable. Since we are attempting, in the spirit of LB, to remain as close to the methodology used in the isotropic algorithm, recovering a scalar angle equation of motion is the favoured scheme.

The director equation (2.119) is not in a conservative form: only certain terms contain derivatives of the angle θ. Other terms (the vorticity Ω, the magnetic term M and the designated source term $n_\gamma A_{\gamma\beta}$) do not and must be added into our LB scheme for the θ macroscopic observable as "forcing" to control the attending error. The introduction of a new class of terms into the director evolution equation must be done with considerable care.

2.6 Summary of Isentropic Nemato-dynamics

In this chapter we have reviewed the essential arguments of continuum isentropic nemato-dynamics and introduced the assumptions used to simplify the governing equations. As the concepts of isotropic and anisotropic fluid dynamics are introduced, brief historical reviews are presented to develop a framework for the origins of the governing equations.

We began with a cursory glance at the well established equations of isotropic fluid dynamics, namely the continuity and the Navier-Stokes equations. We assume that the flow regimes we wish to consider in this thesis are isentropic (no temperature effects) and justifiably omit the equation of energy from our fluid description. Within this framework the lattice fluid is further assumed to be incompressible (no density gradients) and suitably reduced the mass continuity and Navier-Stokes equations to their incompressible forms.

Having reviewed isotropic fluid dynamics we then proceeded to overview the Ericksen-Leslie-Parodi (ELP) governing equation of anisotropic fluid dynamics. The continuity equations remained unaffected since the nematic fluid cannot possess any mass sinks or sources. A reduced form of the director equation of motion was introduced, linking the evolution of the director to a molecular field and velocity gradients. Finally to complete the coupling, the isotropic viscous stress tensor was enhanced to represent the six director dependent Leslie viscosity coefficients, $\alpha_1 ... \alpha_6$.

Several important simplifications/observations were made: which we summarize below

- working in the incompressible nematic regime, i.e. $T < T_c$ and $\nabla \cdot \mathbf{u} = 0$.
- the director is apolar, state of alignment can be characterized by $+\mathbf{n}$ or $-\mathbf{n}$.
- the director has unit magnitude $|\mathbf{n}| = 1$.
- working within the one constant approximation of the elastic field.
- no bulk gravitational, electric or flexo-electric field effects.
- the system is reduced to two dimensions with the director being confined to the plane $(2 \oplus 2)$. Accordingly, the vectorial director equation of motion is reduced to a scaler equation for the angle θ.

In the upcoming chapters we shall recover the ELP equations of nemato-dynamics from a mesoscopic Lattice Boltzmann fluid dynamics model.

Chapter 3

Foundations of the lattice models

3.1 Introduction - an overview

In this chapter we shall introduce Lattice Gas Cellular Automata (LGCAs) and the key developments over the last two decades that have led to the Lattice Boltzmann (LB) models used in this thesis.

Although LB models evolved from the earlier work on Lattice Gases, they are today viewed as separate models of computational fluid dynamics. Indeed, He *et al* [30] showed that the LB algorithm can be obtained directly from the continuum Boltzmann equation of kinetic theory.

Historically cellular automata were introduced by von Neumann and Ulam [31]. They consisted of a lattice where each site contained a finite number of states (usually represented by boolean variables). The automata evolved in discrete steps, with the

states "colliding" according to certain deterministic or non-deterministic rules, and then were propagated (streamed) on the lattice.

Modern LG models emerged from attempts to construct discrete models of fluids along the lines of the Ising model of magnetic materials. Pre-cursor Molecular dynamics (MD) models actually simulate the real fluid micro-world in order to recover transport coefficients. They also use discrete particles but with continuous time, positions and velocities and arbitrary interactions [13]. Broadwell [32] introduced discrete velocity models to simulate rarefied gases but the space and time variables were still continuous and the evolution was probabilistic, being governed by scattering rules based on Boltzmann's equation. The first fully deterministic LG model with discrete time, positions and velocities was introduced by Hardy, de Pazzis and Pomeau (HPP) [33, 34] who managed to simulate certain physical phenomena such as sound waves (the HPP model).

However the HPP model lacked fluid isotropy and had spurious conservation quantities which resulted in an inability to recover the full incompressible Navier-Stokes equations at the macroscale. The successor to the HPP model was the Frisch, Hasslacher and Pomeau (FHP) [8] model, whose lattice possessed sufficient isotropy to recover incompressible Navier-Stokes hydrodynamics, although specific rescaling of variables was necessary to obtain Galilean invariance. LB models [35] arose due to a need to overcome the statistical noise inherent in the boolean particle LG models, with the disadvantage that they required more computational power, due to the non-integer arithmetic.

3.2 The Lattice Gas (LG) models

3.2.1 The HPP model

We will begin by describing the HPP model [33,34]. Consider a 2 dimensional 4 link square lattice (D2Q4) with unit lattice spacing as shown in figure (3.1). At integer time steps, particles of unit mass and speed reside on each node of the lattice. The particles obey an exclusion principle which states that not more than one particle is to be found at a given time and node moving in a given direction. If two particles arrive at a node from opposite directions (head-on collision), they leave the node in the two other previously unoccupied directions, see figure (3.2). This deterministic collision law conserves mass and momentum and has the same discrete invariance group as the lattice. Furthermore it is the only non-trivial HPP collision law with these properties.

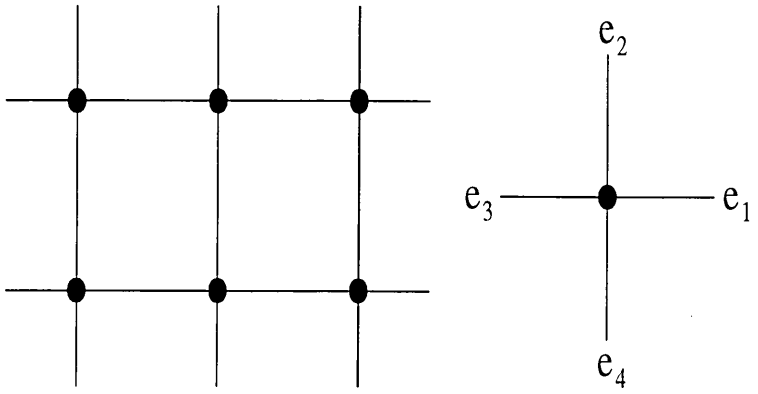

Figure 3.1: (a) The HPP repeating square lattice and (b) the unit cell showing the link speed indexing, e_i $\{i = 1 \cdots 4\}$.

We take the 2D HPP lattice shown above and initially specify a square $L \times L$ lattice that for now we assume to be periodic in both directions. Label each node by a discrete vector $\mathbf{r}$ and state that each node of the lattice is joined to its nearest neighbours by velocity vectors, referred to as lattice links $\mathbf{e}_i$ where $i = 0 \cdots 4$. Each cell has two possible integer states $n_i(\mathbf{r}, t) = 1$ for occupied and $n_i(\mathbf{r}, t) = 0$ for unoccupied. We define a two step cellular automata updating rule on the boolean field $n = \{n_i(\mathbf{r}, t), i = 1 \cdots 4, \mathbf{r} \in \text{Lattice}\}$ in unit time. Step one is a local collision where the four-bit states $(1, 0, 1, 0)$ and $(0, 1, 0, 1)$ are interchanged and all other states are left alone. The second step is propagation $n_i(\mathbf{r}, t) \rightarrow n_i(\mathbf{r} + \mathbf{e}_i, t + 1)$ where the particles are moved around the lattice.

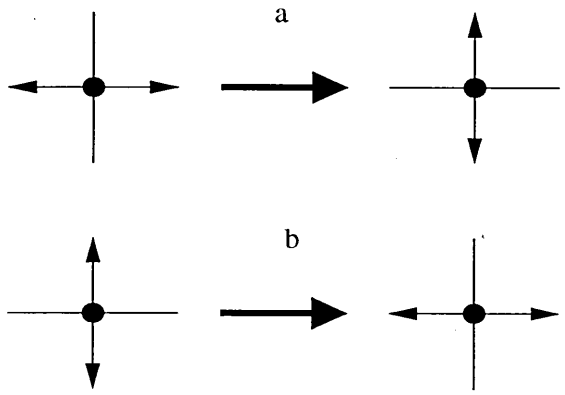

Figure 3.2: Non-trivial collision rule for the HPP models. (a) Four bit state $(1, 0, 1, 0)$ changes to $(0, 1, 0, 1)$. (b) Four bit state $(0, 1, 0, 1)$ changes to $(1, 0, 1, 0)$.

Notably the collision step conserves mass and momentum locally whilst the propagation step conserves them globally. The dynamics of the HPP model is invariant under all discrete transformations that conserve the square lattice, discrete translations, mirror symmetries and rotations by $\pi/2$. Furthermore the dynamics is invariant

under *duality*, which is exchange of 1's and 0' (particles and holes) and importantly momentum in the model is actually conserved along each horizontal and vertical line, resulting in spurious conservation quantities unrealistic for physical modeling.

3.2.2 The FHP model

In 1986 Frisch, Hasslacher and Pomeau [8] matured the HPP model. The lattice in FHP models is 2 dimensional with a minimum of 6 links (D2Q6) but still possesses a single lattice speed unit, see figure (3.3). Each node is again connected to its nearest neighbours but now by six unit vectors $\mathbf{e}_i$ where $i = 0 \cdots b$ and thus, without rest links each node has a minimum six bit state.

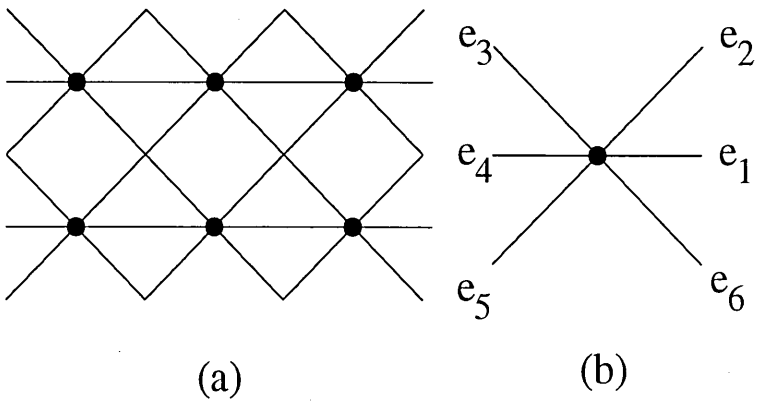

Figure 3.3: (a) The FHP repeating hexagonal lattice and (b) the unit cell showing link speed indexing, e_i $\{i = 1 \cdots 6\}$.

Updating for the FHP models is as in the HPP model, collision and then propagation. For a hexagonal lattice, the construction of the collision rules is not as straightforward as in the HPP model. We must consider both *deterministic* and

non-deterministic rules. This is because for head-on collisions with occupied input-channels $(i, i+3)$ there are two possible pairs of occupied output-channels which conserve mass and momenta, namely $(i+1, i+4)$ and $(i-1, i-4)$, see figure (3.4).

If we choose always to use one of these channels we have a fully deterministic model which is *chiral*, i.e. not invariant under mirror symmetry. Or we can randomly choose a channel in which case we have a non-deterministic model and the mirror symmetry is restored. Finally we can can choose to have a pseudo-random choice of channel, dependent, for example of the parity of a time or space index.

The FHP models also have spurious conservation laws. Head-on collisions conserve not only the total particle number but also the difference of particle numbers in any pair of opposite directions $(i, i+3)$. These additional conservations mean that as well as conserving mass and momenta, two other scalar quantities are conserved with the result that the FHP models macro-dynamical behaviour will differ from physical hydrodynamics. By introducing triple collisions $(i, i+2, i+4) \rightarrow (i+1, i+3, i+5)$ the superfluous conservation law can be removed, resulting in the physical macroscopic hydrodynamics, see figure (3.4).

3.2.2.1 FHP I,II and III models

The FHP-I model [36] is the simplest lattice gas model that has no spurious conservation laws and so can be used to recover macroscopic hydrodynamics. The FHP-I collision rules involve both (pseudo-random) binary head-on collisions and triple collisions [37]. As a rule FHP-I is not invariant under duality but can be made so

by inclusion of duals of the head-on collisions. The set of collision rules can also be saturated (exhausted) by the inclusion of collisions with a spectator particle which remains unaffected by the collision.

The FHP-II model [36] is a variant of the FHP-I (unsaturated) model that includes a rest particle and so requires a seven-bit state fully to describe it. The FHP-II model has all the collision rules of the FHP-I model described above as well as additional collisions with the 'rest-particle'. Binary collisions involving rest particles remove the spurious conservations, and do so more efficiently at low densities than triple collisions.

Finally the FHP-III model is a collision saturated variant of the FHP-II model and contains not only a rest particle, but also a spectator particle [36, 38].

The dynamics of the FHP models are invariant under all discrete transformations that conserve the triangular lattice, discrete translations, rotations by $\pi/3$ and mirror symmetries with respect to a lattice line (except chiral variants).

Although the FHP I,II and III models are most commonly used, it is possible to construct other variants. The FHP-III model for example has 76 possible collisions which conserve mass and momentum, allowing a wide choice of collision laws.

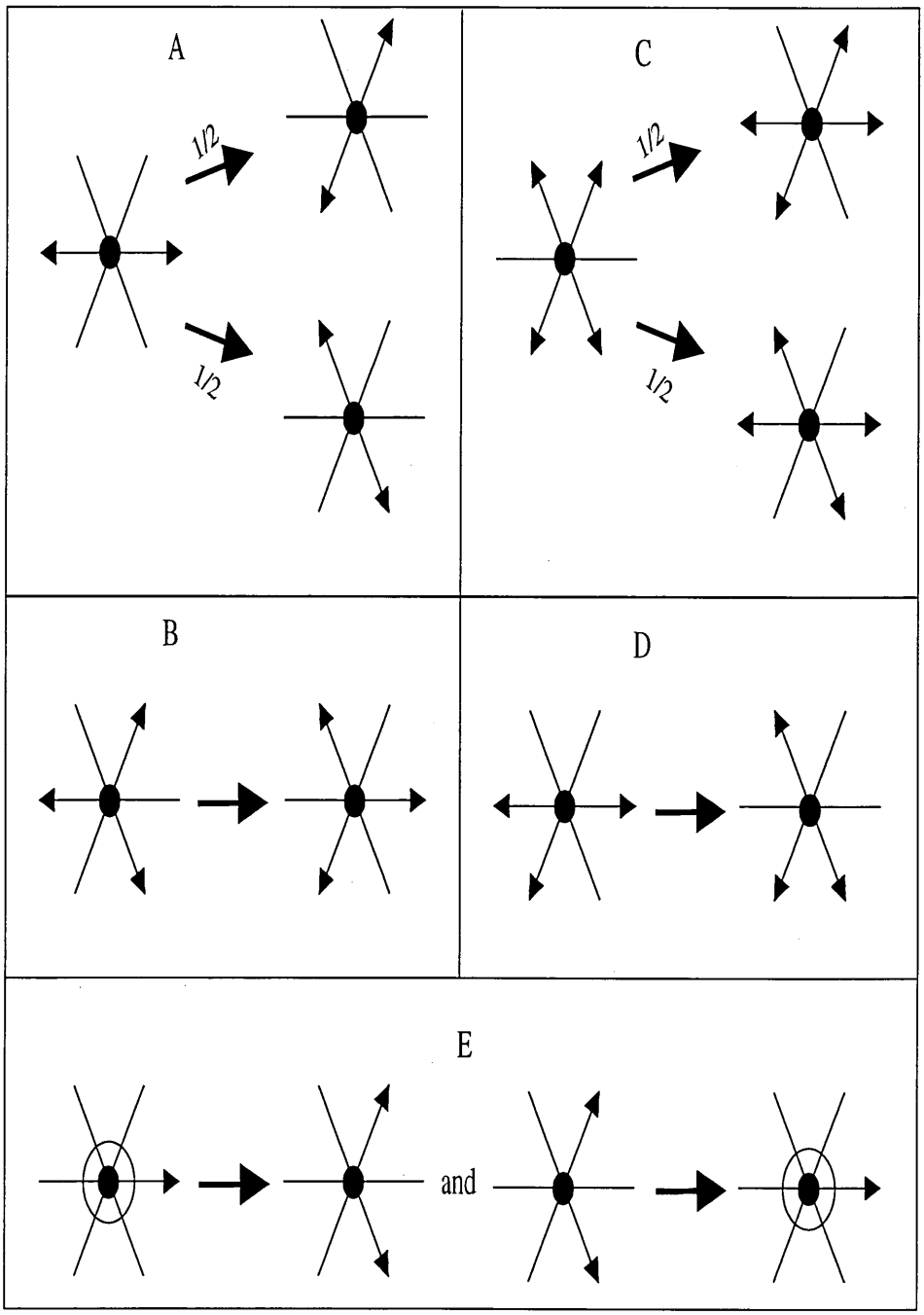

Figure 3.4: Collision rules for the FHP models: (a) head on collision with two output channels given equal weight; (b) triple collision; (c) dual of head-on collision under particle-hole exchange; (d) head-on collision with spectator; (e) binary collision involving one rest particle (represented by a circle).

3.2.3 The FCHC model

The essential requirement for a LG to recover hydrodynamical macroscopic equations is that the underlying lattice needs to have sufficient symmetry to ensure macroscopic isotropy. In 2D, a hexagonal lattice suffices, however, the situation changes when we try to model 3D flow with a lattice gas. It was found that 3D lattices do not posses sufficient symmetry to ensure macroscopic isotropy [8, 39, 40]. To overcome this a pseudo 3D lattice based upon a multi-speed 4D Face Centered Hyper Cubic (FCHC) lattice, with one of its dimensions set to unity (see figure (3.5)) was introduced by d'Humiéres *et al* [39].

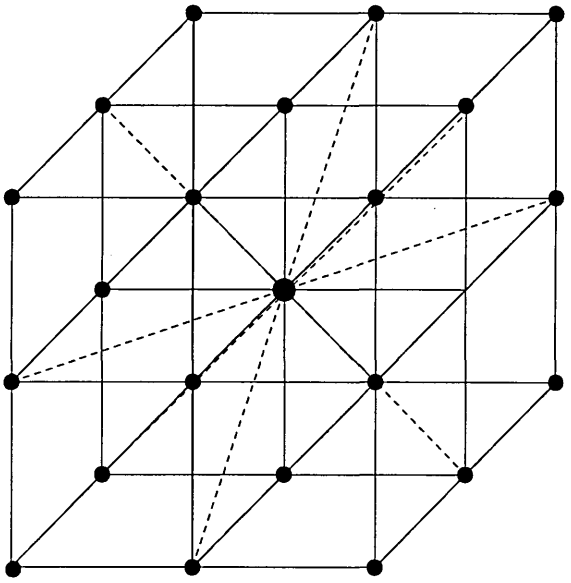

Figure 3.5: The pseudo-4D FCHC model. Only the neighbourhood of one node is shown. Along the dotted lines only one particle can propagate. Along the solid lines, up to two particles can propagate.

The model entails a three speed (0,1 and $\sqrt{2}$) regular cubic lattice with collision rules that conserve mass and four momenta. Non-deterministic collision rules are needed to ensure the collisions have the same invariance group as the lattice. The

link velocity vectors $\mathbf{e}_i$ are connected to 24 nearest and next-nearest neighbours (D3Q24) and so the 3D FCHC model has a minimum 24-bit state. For a more detailed review of the 3D FCHC model we refer the interested reader to [39, 41, 42].

We defer further discussion on Lattice Gases until after the following section.

3.2.4 Navier-Stokes hydrodynamics from LG's

Our analysis, presented for the sake of completeness, follows closely that of Frisch *et al* [8]. Taking a D dimensional lattice we label each node by a discrete vector $\mathbf{r}$ and state that it has b distinct links. Any particle moving on a link has a velocity $\mathbf{e}_i$ where $i = 0 \ldots b$. We define a boolean occupation of the links

$$n_i(\mathbf{r}, t) = \begin{cases} 1 & \text{if } \mathbf{e}_i \text{ occupied} \\ 0 & \text{if } \mathbf{e}_i \text{ unoccupied} \end{cases} \tag{3.1}$$

and use the following equation to evolve the system in unit time

$$n_i(\mathbf{r} + \mathbf{e}_i\delta, t + \delta) = n_i(\mathbf{r}, t) + \Delta_i(n) \tag{3.2}$$

where δ is defined as the shortest time step in the model. The collision function $\Delta_i(n)$ describes the change in $n_i(\mathbf{r}, t)$ during collision in unit time, defined as

$$\Delta_i(n) = \begin{cases} +1 & \text{upon addition of a particle on link } \mathbf{e}_i \\ 0 & \text{if link } \mathbf{e}_i \text{ is unchanged} \\ -1 & \text{upon removal of a particle on link } \mathbf{e}_i \end{cases} \tag{3.3}$$

The collision operator $\Delta_i(n)$ relies upon 'look-up-tables' of a normalized probability A such that an input state $s = (s_i, i = 1 \ldots b)$ will be collided into an output state

$s' = (s'_i, i = 1...b)$. The collision rules are said to satisfy detailed balance if

$$A(s \rightarrow s') = A(s' \rightarrow s) \tag{3.4}$$

and semi-detailed balance if

$$\sum_s A(s \rightarrow s') = 1, \quad \forall s' \tag{3.5}$$

From the boolean particles $n_i(\mathbf{r}, t)$ we can derive [8] the ensemble average over both space and time, defined as the mean population given by,

$$N_i(\mathbf{r}, t) = \langle n_i(\mathbf{r}, t) \rangle$$

At each lattice node we can define two macroscopic variables from the mean population to establish the link to fluid hydro-dynamics. The zeroth order velocity moment defines the fluid density, at a lattice site

$$\rho = \sum_i N_i(\mathbf{r}, t) \tag{3.6}$$

and the first order velocity moment gives the fluid momentum, at the same site

$$\rho \mathbf{u} = \sum_i N_i(\mathbf{r}, t)\, \mathbf{e}_i \tag{3.7}$$

Due to the particle exclusion principle, enforced in the lattice gas models there results a steady state equilibrium solution $N_i^{eqm}(\rho, \mathbf{u})$ of the mean link population $N_i(\mathbf{r}, t)$ based on a Fermi-Dirac distribution function. Under the assumption that the actual mean population does not vary far from the equilibrium population, then the mean population can be expanded around the equilibrium population in powers of a small spatial expansion parameter which is explicitly associated with the shortest time step δ.

Performing zero and first order velocity summations on the first and second order extractions of the velocity moments of the Taylor expanded evolution equation, utilizing equations (3.6) and (3.7) and after substantial algebra, two partial differential equations for the macroscopic observable ρ and $\rho\mathbf{u}$ (equations (3.6) and (3.7) respectively), are derived.

$$\partial_t \rho + \partial_\beta (\rho u_\beta) = 0 \tag{3.8}$$

and

$$\partial_t(\rho u_\alpha) + \partial_\beta \left(\frac{c^2}{D} \rho \delta_{\alpha\beta} + \rho G(\rho) T_{\alpha\beta\gamma\delta} u_\gamma u_\delta \right) = -\partial_\beta \left[\left(\psi(\rho) + \frac{D}{2c^2 b} \right) T_{\alpha\beta\gamma\delta} \, \partial_\gamma (\rho u_\delta) \right] \tag{3.9}$$

where

$$G(\rho) = \frac{D^2}{2c^4 b} \frac{b - 2\rho}{b - \rho} \quad \text{and} \quad T_{\alpha\beta\gamma\delta} = \sum_i e_{i\alpha} e_{i\beta} \left(e_{i\gamma} e_{i\delta} - \frac{c^2}{D} \delta_{\gamma\delta} \right) \tag{3.10}$$

and c is the particle (link) speed and $\psi(\rho)$ is as yet undefined [8].

3.2.4.1 Recovering Isotropy

Equation (3.9) still feels the underlying lattice through the 4^{th} rank tensor $T_{\alpha\beta\gamma\delta}$ which appears in both the nonlinear and the diffusive terms. In order eventually to obtain the Navier-Stokes equations, the tensor $T_{\alpha\beta\gamma\delta}$ given by the second term in equation (3.10) must be isotropic (invariant under the full orthogonal group of the lattice: for general group-theory material concerning the isotropy of tensors with discrete symmetries see Wolfram [40]).

$T_{\alpha\beta\gamma\delta}$ is isotropic if it has the following form.

$$T_{\alpha\beta\gamma\delta} = \frac{bc^4}{D\,(D+2)}\left(\delta_{\alpha\gamma}\delta_{\beta\delta} + \delta_{\alpha\delta}\delta_{\beta\gamma} - \frac{2}{D}\delta_{\alpha\beta}\delta_{\gamma\delta}\right) \tag{3.11}$$

Substituting equation (3.11) into equation (3.9) we obtain

$$\begin{aligned} \partial_t\left(\rho u_\beta\right) + \;\; & \partial_\beta\left(\rho g(\rho) u_\alpha u_\beta\right) + \partial_\alpha\left[c_s^2\rho\left(1 - g(\rho)\tfrac{u^2}{c^2}\right)\right] = \\ & \partial_\beta\left[\left(\nu_c(\rho) + \nu_p\right)\left(\partial_\alpha\left(\rho u_\beta\right) + \partial_\beta\left(\rho u_\alpha\right) - \tfrac{2}{D}\partial_\gamma\left(\rho u_\gamma\right)\delta_{\alpha\beta}\right)\right] \end{aligned} \tag{3.12}$$

with

$$\begin{aligned} g(\rho) &= \tfrac{D}{D+2}\tfrac{b-2\rho}{b-\rho} \quad , \quad c_s^2 = \tfrac{c^2}{D} \\ \nu_c(\rho) &= -\tfrac{bc^4}{D(D+2)}\psi(\rho) \quad , \quad \nu_p = -\tfrac{c^2}{2(D+2)} \end{aligned} \tag{3.13}$$

A couple of things to note here are that $g(\rho) \neq G(\rho)$ and c_s^2 is the sound speed of the fluid. We have in equation (3.12) a macroscopic momentum equation that is very closely related to the Navier-Stokes equations of hydrodynamics.

At this stage we can re-express equation (3.12) to bring out its similarity to the Navier-Stokes equation for viscous hydrodynamics (2.26)

$$\partial_t\left(\rho u_\alpha\right) + \partial_\beta \Pi_{\alpha\beta} = \partial_\beta \sigma'_{\alpha\beta} \tag{3.14}$$

where the momentum flux tensor $\Pi_{\alpha\beta}$ and the viscous stress tensor $\sigma'_{\alpha\beta}$ respectively are equivalent to

$$\Pi_{\alpha\beta} = cs^2\rho\left(1 - g(\rho)\frac{u^2}{c^2}\right)\delta_{\alpha\beta} + g(\rho)\rho u_\alpha u_\beta \tag{3.15}$$

$$\sigma'_{\alpha\beta} = \nu(\rho)\left[\partial_\alpha(\rho u_\beta) + \partial_\beta(\rho u_\alpha) - \frac{2}{D}\partial_\gamma(\rho u_\gamma)\delta_{\alpha\beta}\right] \tag{3.16}$$

and $\nu(\rho)$ is now the kinematic viscosity,

$$\nu(\rho) = \nu_c(\rho) + \nu_p \tag{3.17}$$

The kinematic viscosity can be calculated and is found to be not only a function of the density ρ but model dependent through the constants $\psi(\rho)$ and c_s^2 [8,41].

A few remarks are now in order. Equation (3.14) bears a strong similarity to the Navier-Stokes equations for viscous hydrodynamic flow. However, there are a couple of significant differences.

1. The form of the momentum flux tensor is $\Pi_{\alpha\beta} = P\delta_{\alpha\beta} + \rho u_\alpha u_\beta$ for the Navier-Stokes equations. The scalar pressure term in the LG momentum flux tensor, equation (3.15), contains an extra additive density-dependent contribution $g(\rho)$ that is of second order in velocity. In the low Mach number regime this term vanishes and the term reduces to the expected diagonal pressure term $P\delta_{\alpha\beta}$ where P is the scalar pressure which is given here as $c_s^2\rho$. Even in the low Mach number regime the LG momentum flux tensor contains the multiplicative density-dependent factor $g(\rho)$ in the advection (nonlinear) term which destroys Galilean invariance in the lattice fluid.

2. The kinematic viscosity ν describes the stress-strain relation for a Newtonian fluid with vanishing bulk viscosity [9]. The kinematic viscosity in the LG model, defined in equation (3.17), however, is not only a function of density but of the LG model used. In fact if the LG model includes a rest particle then the traceless property of the stress tensor $\sigma_{\alpha\beta}$ (which is responsible for the vanishing of the bulk viscosity) is broken.

In order to recover Galilean invariance and hence the proper form of the Navier-Stokes equations from the LG momentum conservation equation (3.14), a rescaling

of the space, time and velocity variables needs to be performed. The rescaling forces the undesirable terms to vanish as the small spatial expansion parameter tends to zero.

3.2.4.2 Advantages and disadvantages of Lattice Gas simulation

Like most modeling methods LG's have advantages and disadvantages. Due to their integer arithmetic on the underlying basis in direct simulation, there is no round-off error and so the models are unconditionally stable as well as been highly suited to parallel implementation. The integer nature of the model also means that computer memory can be optimally used, allowing larger scale simulations. Moreover, inclusion of geometrically complex boundary conditions can be realised with relative ease, compared to other modeling techniques such as Finite Difference.* Note however, that the problem of closing a simulation lattice so as to replicate Dirichlet boundary conditions to second order accuracy is unsolved.

Aside from the above considerations, the other main disadvantages of LG's is the statistical noise inherent in the method. To extract the macroscopic flow observables, averaging has to be performed over many different initial configurations, which is computationally expensive. Finally, depending on the number of dimensions and the model used, the size of the collision matrix can become computationally demanding, for example a 3D FCHC model has 2^{24} possible collisions.

*See the end of this chapter for a discussion of boundary conditions in LG and LB models

3.3 Brief Review of the Lattice Gas models

Since the seminal paper by Frisch *et al* [8], LG models have been investigated by many groups and there are currently several comprehensive review articles on the subject, most notably [36, 40, 43, 44]. The particular issues of stability, time/length scales, conservation laws and generalized hydrodynamics of LG's are discussed in [45–49]. De los Santos *et al* [50] have reported on the properties of driven LG's, Cornubert *et al* [51] have discussed bounding issues within LG's, whilst Gunstensen *et al* [52] introduced a Galilean invariant LG satisfying semi-detailed balance. For work covering the introduction of lattice Boltzmann (LB) models from the parent LG models, see Higuera *et al* [47, 53], whilst Esposito *et al* [48] is recommended for rigour.

In terms of applications of the LG model (rather than fundamental statistical mechanics), there is a rich variety of problems that can be simulated using a suitably adjusted cellular automata, including applications outside fluid dynamics, e.g. granular flow [54, 55]. Within the class of fluid dynamics we shall quickly review a few interesting applications.

Simple two-dimensional Poiseuille (channel) flow in an infinite aspect ratio duct, driven by a uniform body force was simulated using a FHP model by Kadanoff *et al* [56, 57]. Quantitative results were in agreement with theoretical predications as well as reproducing earlier LG work by d'Humiéres *et al* [38]. Work has also been carried out investigating flow around solid fixed objects: for general comments see Hasslacher *et al* [44].

Binary fluid mixtures have been simulated extensively using LG models: the work by McNamara [58] measured diffusion coefficients; recently Boghosian *et al* [59], derived the immiscible LG from a particulate basis. Suggested reference material on LG immiscible fluids is the work by Rothman and Keller [60] who first introduced the technique.

In the context of the present work, there have been a few attempts to use of LG's so far to recover anisotropic fluid flow. Vives *et al* [61] introduced a two-dimensional square LG with an extra degree of freedom θ_i. This new variable was allowed to take one of the four possible orientations corresponding to the link directions of the square lattice. The model produced a smectic-nematic like transition and a nematic-isotropic like transition. The authors used Monte-Carlo simulations and mean-field results as comparisons to investigate this first approximation to a real anisotropic system. The model produced a rich variety of structures for the available parameter space and whilst the order of the transitions could not be determined unambiguously, qualitatively they were comparable to experimental data. Angelescu *et al* [62] used the LG technique to investigate long-range ordering of nematics in one and two dimensions. Results show an orientational ordering transition occurring at finite temperature, which the author noted was absent in certain continuum nematic models, although predicted by theory.

3.4 The Lattice Boltzmann (LB) models

Motivated by the inherent problems in the LG models, McNamara *et al* [35] developed the first Lattice Boltzmann (LB) model which utilized the Boltzmann approximation of molecular chaos to terminate the hierarchy of high order moments of the expanded N_i leading to a closed kinetic evolution equation [35]. The molecular chaos assumption for low density gases assumes that the mean free path of a particle is so large that particles entering a collision come mostly from distant uncorrelated regions. Consequences of this assumption include

1. an irreversible approach to equilibrium.

2. explicit evaluation of the transport coefficients in the limit of weak departures from local equilibrium (so called Chapman-Enskog limit).

The boolean link occupation states $n_i(\mathbf{r}, t)$ were replaced by a single-particle distribution function $f_i(\mathbf{r}, t)$ representing the ensemble averages of the n_i over a conceptually infinite number of equivalent systems, in effect,

$$f_i(\mathbf{r}, t) \equiv N_i(\mathbf{r}, t) \equiv \langle n_i(\mathbf{r}, t) \rangle$$

The $f_i(\mathbf{r}, t)$ are now real (non-boolean) continuous functions in the range $0 \leq f_i \leq 1$ and the macroscopic variables of density and momentum are now defined as

$$\rho(\mathbf{r}, t) = \sum_i f_i(\mathbf{r}, t) \tag{3.18}$$

$$\rho \mathbf{u}(\mathbf{r}, t) = \sum_i f_i(\mathbf{r}, t) \mathbf{e}_i \tag{3.19}$$

And by ensemble averaging the LG evolution equation (3.2) we can derive the evolution equation of the distribution function f_i

$$f_i(\mathbf{r}+\mathbf{e}_i, t+1) = f_i(\mathbf{r}, t) + \langle \Delta_i(n) \rangle \tag{3.20}$$

We now replace the ensemble average of the boolean collision operator with an operator dependent only upon the single particle distribution function, i.e.

$$\langle \Delta_i(n) \rangle \Leftrightarrow \Omega(f) \tag{3.21}$$

So, to have a microscopic Lattice Boltzmann model giving macroscopic hydrodynamics, a correct form for the collision function $\Omega(f)$ needs to be found. No subsequent averaging of densities is required, since the distribution functions are the averages themselves : this removes the noise due to statistical fluctuations that plagued LG techniques. However the technique still acquires the complex collision function dependent on the probabilities $A(s \rightarrow s^{'})$. Like the LG models the collision operator has 2^m input and output states, where m is the number of links on the underlying lattice plus any rest particles. Therefore for a 2D FHP model with one rest particle $\Omega(f)$ is a $2^7 \times 2^7$ matrix and for a 3D FCHC model is a $2^{24} \times 2^{24}$ matrix. Obviously the size of these matrices makes the computational memory requirements quite intensive, rendering the method inefficient. However in [35], McNamara and Zanetti showed that the method accurately predicted (within 5%) the decay of shear and sound waves.

In early LBE approaches to hydrodynamics $\Omega(f)$ was derived by considering some underlying CA's collision rules, and was, in general, non-linear. However, if one recognizes that the densities f_i should be close to equilibrium the collision operator

can be considerably simplified.

3.4.1 The linear collision operator

In 1989 Higuera *et al* [47] linearized the collision operator by assuming the distribution function f_i is never far away from equilibrium, thus allowing the distribution function to be expanded around an equilibrium distribution function

$$f_i = f_i^{eqm} + f_i^{neqm} \tag{3.22}$$

where f_i^{eqm} is the equilibrium part of the distribution function, which is dependent only upon the local values of ρ and $\mathbf{u}$, i.e.

$$f_i^{eqm} \rightarrow f_i^{eqm}(\rho, \mathbf{u})$$

and f_i^{neqm} where ($f_i^{neqm} \ll f_i^{eqm}$) is the non equilibrium part which can be expanded in powers of velocity gradients

$$f_i^{neqm} = \epsilon f_i^{(1)} + \epsilon^{(2)} f_i^2 + \mathrm{O}(|u|^3) \tag{3.23}$$

where the labelling parameter ϵ can be considered as playing an identical role as the small spatial expansion δ introduced in the previous section. The superscripts refer to the higher order derivatives of $\mathbf{u}$ and for non-linear hydrodynamics, contributions from f_i^{neqm} are at most of order $\mathrm{O}(f_i^{(2)})$. Expanding the collision operator in equation (3.21) about the equilibrium distribution gives

$$\Omega_i(f) = \Omega_i(f_j^{eqm}) + \sum_j f_j^{neqm} \Omega_{ij} + \mathrm{O}((f_i^{neqm})^2) \tag{3.24}$$

where

$$\Omega_{ij} = \left.\frac{\partial \Omega_i}{\partial f_j}\right|_{f_j = f_j^{eqm}} \tag{3.25}$$

Invoking the requirement that [63],

$$\Omega_i(f_i^{eqm}) = 0 \tag{3.26}$$

reduces equation (3.24) to

$$\begin{aligned} \Omega_i(f) &= \textstyle\sum_j \Omega_{ij} f_j^{neqm} \\ &= \textstyle\sum_j \Omega_{ij}(f_j - f_j^{eqm}) \end{aligned} \tag{3.27}$$

The evolution equation for the linearized Lattice Boltzmann model can now be written as

$$f_i(\mathbf{r} + \mathbf{e}_i\delta, t + \delta) = f_i(\mathbf{r}, t) + \sum_j \Omega_{ij}(f_j - f_j^{eqm}) \tag{3.28}$$

As mentioned earlier the collision operator Ω_{ij} is defined by the underlying boolean micro-dynamics through the transition probabilities $A(s \rightarrow s')$ and so suffers from the same constraints as the LGCA models as well as having the same resultant macrodynamics. In [47] a full form for the collision operator is given, as well as a general discussion between the linearized Lattice Boltzmann form and the full (non-linear) collision operator form for LBE simulation. However the linearized collision operator is now a $m \times m$ matrix, which is clearly a considerable simplification over the previous $2^m \times 2^m$ form. This allows the linearized Lattice Boltzmann scheme to be a more practical method for 2D and especially 3D simulations.

3.4.2 The enhanced collision operator

In [53] Higuera *et al* proposed that the collision operator could be simplified even further by changing its form. Instead of obeying an underlying set of LGCA collision rules, the form of the collision operator was "reversed engineered" from the target macroscopic equations whilst being constrained by the requirements of isotropy. If we consider the collision operator Ω_{ij} its elements $(i, j = 1...b)$ describe the change in the distribution function f_i induced by a change in f_j during a collision. Isotropy dictates that the elements of the collision matrix are dependent only upon the angle between the colliding links $\mathbf{e}_i$ and $\mathbf{e}_j$ and can be tuned to ensure a positive viscosity.

For an D2Q7 FHP hexagonal lattice these angles can take four possible angles 0°, 60°, 120° and 180°. If we include a rest particle $i = 0$ we must include the influence of the rest particles on themselves Ω_{00} and on the moving particles Ω_{i0} and Ω_{0j} (symmetry requires $\Omega_{i0} = b$, and detailed balance, $\Omega_{0j} = b$) where $i, j \neq 0$. On general grounds, we can therefore write the entire collision operator for the FHP hexagonal lattice with one rest particle as a circulant matrix :

$$\Omega_{ij} = \begin{bmatrix} c & b & b & b & b & b & b \\ b & a_0 & a_{60} & a_{120} & a_{180} & a_{120} & a_{60} \\ b & a_{60} & a_0 & a_{60} & a_{120} & a_{180} & a_{120} \\ b & a_{120} & a_{60} & a_0 & a_{60} & a_{120} & a_{180} \\ b & a_{180} & a_{120} & a_{60} & a_0 & a_{60} & a_{120} \\ b & a_{120} & a_{180} & a_{120} & a_{60} & a_0 & a_{60} \\ b & a_{60} & a_{120} & a_{180} & a_{120} & a_{60} & a_0 \end{bmatrix} \tag{3.29}$$

Mass and momenta must still be conserved, which imposes the following constraints upon the elements of Ω_{ij}

$$\sum_i \Omega_{ij} = 0 \quad \text{and} \quad \sum_i \Omega_{ij} \mathbf{e}_{i\alpha} = 0 \tag{3.30}$$

which lead to the following constraints

$$\begin{aligned} 6b + c &= 0 \\ a_0 + 2a_{60} + 2a_{120} + a_{180} + b &= 0 \\ a_0 + a_{60} - a_{120} - a_{180} &= 0 \end{aligned} \tag{3.31}$$

Consequently, the zero-eigenvalue eigenvectors for the collision matrix can be calculated taking into account the imposed constraints in equation (3.31) and there are three distinct non-zero eigenvalues

$$\begin{aligned} \lambda &= 6(a_0 + a_{60}) + 2b \\ \sigma &= -6(a_0 + 2a_{60}) - 3b \\ \tau &= -7b \end{aligned} \tag{3.32}$$

In fact λ can be shown [47] to be related to the kinematic viscosity ν by

$$\nu = -\frac{1}{4}\left(\frac{1}{\lambda} + \frac{1}{2}\right) \tag{3.33}$$

Note that the viscosity in equation (3.33) is specific to the D2Q7 lLB model, i.e. the viscosity is model dependent. To ensure a positive kinematic viscosity, λ is chosen to lie within the range

$$-2 \leq \lambda \leq 0$$

and to allow the f_i^{neqm} contribution to converge as quickly as possible (thus enhancing stability) σ and τ are usually chosen to be -1 [64].

Since the collision operator is now independent of the LGCA set of collision rules the model does not posses unconditional stability and as $\nu \to 0$ numerical instability can set in. In general the stability of LBE schemes is a neglected aspect of their behaviour, and seems to depend upon the "negativity" and local gradients of the link density distributions [65–67].

However the enhanced collision lLB model does recover Galilean invariant Navier-Stokes equations through a careful selection of the form of the equilibrium distribution function, without the need for rescaling of quantities.

3.4.3 The single relaxation LBGK model

The enhanced collision operator defined in equation (3.29) can be simplified even further by assuming all particle collisions relax towards equilibrium at a constant rate [66], i.e.

$$\Omega_{ij} = -\frac{1}{\tau} \tag{3.34}$$

where τ is the single relaxation parameter that ultimately controls the viscosity of the isotropic fluid and is valid within the range $-2 < \tau < 0$. Again instability can set in as $\tau \to 0$ since $\nu \to \infty$ and we stress that the stability and order of accuracy of LBE solution, especially with increasing Reynolds number and lattice resolution, is an on-going issue.

The evolution equation of an LBGK scheme therefore becomes

$$f_i\left(\mathbf{r} + \mathbf{e}_i\delta, t + \delta\right) = f_i\left(\mathbf{r}, t\right) - \frac{1}{\tau}\left(f_i - f_i^{eqm}\right) \tag{3.35}$$

This form of the collision operator produces what is called an LBGK evolution equation, because of its similarity to the Bhatnagar Gross Krook (BGK) Boltzmann operator [68] used to solve the full, classical Boltzmann equation.

In the original LG evolution equation a Fermi-Dirac distribution is used to find the local equilibrium. The origins of the Fermi-Dirac distribution form of the equilibrium distribution derived from the LG exclusion principle, allowing only one boolean particle to reside on a lattice link at any one time. This resulted in the overall state of a node being described by a boolean variable and limited the number of collisions which could take place on a node at each time step. However there is no physical basis for this exclusion principle, which was introduced to simplify the computations. The equilibrium distribution in the LBGK model is derived from an expanded, uniformly translating Maxwell-Boltzmann distribution [69], and it is mainly for this reason (essentially no definite underlying set of collisions) that LB models today are viewed as separate models to the LG models.

Having selected a single relaxation collision function, the mapping of the LBGK model onto hydrodynamics is performed in the same vein as the enhanced collision function mapping (see next section). The important step is to choose a suitable form for the equilibrium distribution function, that maps correctly onto the required macroscale hydrodynamical equations. However in the lLB enhanced collision mapping, it is the form of collision function Ω_{ij} that needs to satisfy the mass and momentum conservation constraints. In the LBGK model it is the form of the equilibrium distribution that has to satisfy the conservation constraints.

The momentum density distribution scheme is implemented in this work using an enhanced collision operator D2Q13 lLB model. The associated (second) angle distribution scheme is implemented using the single relaxation LBGK model.

3.4.4 D2Q13 lLB Isotropic Incompressible hydrodynamics

We define a two dimensional lattice with a thirteen link velocity basis (D2Q13) [63], which is a three-speed hexagonal lattice with velocity vectors $\mathbf{e}_\sigma$ given by

$$\begin{aligned} \mathbf{e}_0 &= \{0,0\} \\ \mathbf{e}_1 &= e\{\pm 1,0\}\ ,\ e\left\{\pm 1/2, \pm\sqrt{3}/2\right\} \\ \mathbf{e}_2 &= e\left\{0, \pm\sqrt{3}\right\}\ ,\ e\left\{\pm 3/2, \pm\sqrt{3}/2\right\} \end{aligned} \tag{3.36}$$

where the subscripts ($\sigma = 0, 1$ and 2) are associated with the particles with velocity 0, c and $\sqrt{3}c$ respectively. This D2Q13 lLB model is an extension of the D2Q7 lLB model [53] which takes into account not only nearest neighbours but next-nearest neighbours, see figure (3.6).

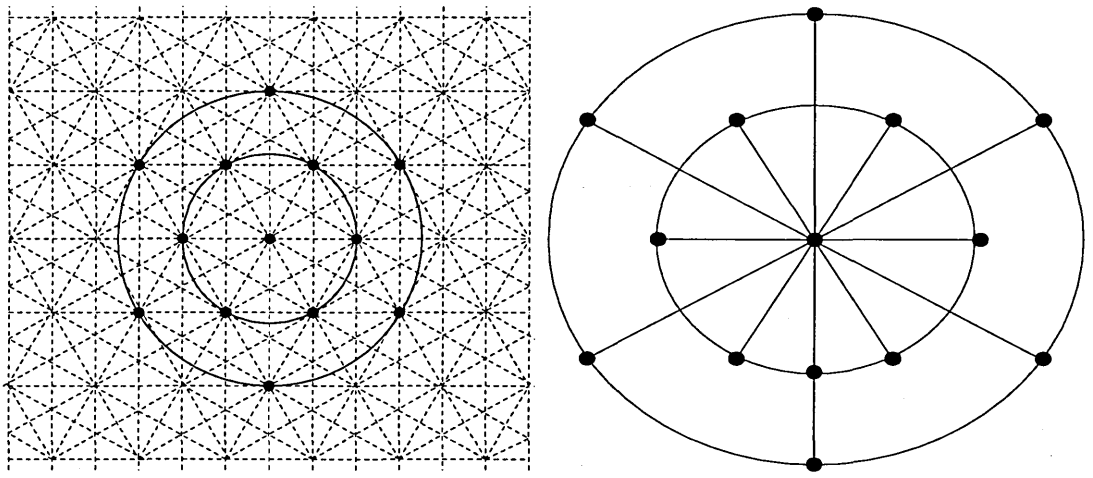

(a) (b)

Figure 3.6: The D2Q13 lattice model, (a) depicts the repeated lattice units showing the links between nearest and next-nearest neighbours. (b) shows a singular lattice unit for clarity, where the rings indicate the nearest neighbour $\mathbf{e}_1$ and the next-nearest neighbour $\mathbf{e}_2$ speeds respectively. The rest $\mathbf{e}_o$ speed is represented by the central dot.

The D2Q13 hexagonal lattice shown in figure (3.6) has velocity moment "tensors" of the form

$$\mathrm{T}_{\alpha_1 \ldots \alpha_n} = \sum_i t_\sigma \left(e_{i\alpha_1} \ldots e_{i\alpha_n} \right) \tag{3.37}$$

where, with respect to the link speed σ, $t_0 = 11/25$, $t_1 = 9/100$ and $t_2 = 1/300$.

The odd order tensors are zero and the even order tensors are isotropic up to 6^{th} order, given by [70]

$$\begin{aligned} \mathrm{T}^{(2)}_{\alpha\beta} &= \mathrm{T}[2]\,\delta_{\alpha\beta} \\ \mathrm{T}^{(4)}_{\alpha\beta\gamma\epsilon} &= \mathrm{T}[4]\left(\delta_{\alpha\beta}\delta_{\gamma\epsilon} + \delta_{\alpha\gamma}\delta_{\beta\epsilon} + \delta_{\alpha\epsilon}\delta_{\beta\gamma}\right) \\ \mathrm{T}^{(6)}_{\alpha\beta\gamma\epsilon\phi\delta} &= \mathrm{T}[6]\,\Delta_{\alpha\beta\gamma\epsilon\phi\delta} \end{aligned} \tag{3.38}$$

where the $\Delta_{\alpha\beta\gamma\epsilon\phi\delta}$ term is a sum of products containing 15 terms each of the form $\delta_{\alpha\beta}\delta_{\gamma\epsilon}\delta_{\phi\delta}$ [70]. The constants $\mathrm{T}[n]$ are found to be $\mathrm{T}[0] = 1$, $\mathrm{T}[2] = c_s^2$, $\mathrm{T}[4] = c_s^4$ and $\mathrm{T}[6] = c_s^4/4$.

We create an isotropic collision matrix $\Omega_{ij}^{(\mathrm{iso})}$ from block circulant matrices (required by symmetry [64]) that couples the three velocity sets. The collision matrix is written-down after the D2Q7 collision matrix [53], see equation (3.29)

$$\Omega_{ij}^{(\mathrm{iso})} = \begin{bmatrix} c & \mathbf{b} & \mathbf{d} \\ \mathbf{b}^T & \mathbf{A} & \mathbf{G} \\ \mathbf{d}^T & \mathbf{G}^T & \mathbf{E} \end{bmatrix} \tag{3.39}$$

where $\mathbf{b} = \mathbf{b}^T = \{b, b, b, b, b, b\}$ and $\mathbf{d} = \mathbf{d}^T = \{d, d, d, d, d, d\}$. Also $\mathbf{A}$,$\mathbf{E}$ and $\mathbf{G} = \mathbf{G}^T$ are 6×6 circulant matrices with first rows, $\{a_0, a_{60}, a_{120}, a_{180}, a_{120}, a_{60}\}$, $\{e_0, e_{60}, e_{120}, e_{180}, e_{120}, e_{60}\}$ and $\{g_{30}, g_{30}, g_{90}, g_{150}, g_{150}, g_{90}\}$ respectively.

The collision matrix must satisfy the requirements of conservation of mass and momenta laid out in equations (3.30). Whilst it must be stressed that there is a wide choice of matrix elements that would satisfy the requirements, we make the following choice of matrix elements.

$$\begin{aligned} b &= \tau/13 \quad , \quad c = 12\tau/13 \quad , \quad d = \tau/13 \\ g_{30} &= \tau/13 \quad , \quad g_{90} = \tau/13 \quad , \quad g_{150} = \tau/13 \\ a_0 &= -(10\tau + 13\phi)/39 \quad , \quad a_{60} = (6\tau + 13\phi) \\ a_{120} &= (-20\tau + 13\phi)/78 \quad , \quad a_{180} = (3\tau - 13\phi)/39 \end{aligned} \tag{3.40}$$

where τ and ϕ are eigenvalues of the collision matrix.

There are four eigenvectors with an eigenvalue τ, four with an eigenvalue ϕ and five with an eigenvalue of zero. For simplicity we explicitly set $\tau = -1$ and note that the eigenvalue ϕ is equivalent to $-\lambda$, the eigenvalue of the D2Q7 lLB model discussed earlier.

Recalling the lLB evolution equation (3.28), but for our D2Q13 collision matrix

$$f_i(\mathbf{r}+\mathbf{e}_i\delta, t+\delta) = f_i(\mathbf{r},t) + \sum_j \Omega_{ij}^{(\mathrm{iso})} f_j^{neqm} \tag{3.41}$$

we note that the macroscopic variables are velocity moments of the link density distributions, i.e. equations (3.18) and (3.19)

$$\rho(\mathbf{r},t) = \sum_i f_i(\mathbf{r},t) \qquad \rho(\mathbf{r},t)\,\mathbf{u} = \sum_i f_i(\mathbf{r},t)\,\mathbf{e}_i.$$

Taylor expanding the l.h.s of equation (3.41) using the spatial parameter δ and retaining terms to second order gives,

$$\delta\left[\partial_t + e_{i\alpha}\partial_\alpha\right] f_i + \frac{\delta^2}{2}\left[\partial_t + e_{i\alpha}\partial_\alpha\right]^2 f_i = \sum_j \Omega_{ij}^{(\mathrm{iso})} f_j^{neq} + \mathrm{O}\left(\delta^3\right). \tag{3.42}$$

where the space and time indexing has being omitted for the sake of clarity.

Expanding, as usual, the link density distribution function f_i and the time derivative ∂_t up to second order about the same small expansion parameter δ,

$$\begin{aligned} f_i &= f_i^{(0)} + \delta f_i^{(1)} + \delta^2 f_i^{(2)} + \mathrm{O}\left(\delta^3\right) \\ \partial_t &= \partial_{t_0} + \delta\partial_{t_1} + \delta^2\partial_{t_2} + \mathrm{O}\left(\delta^3\right). \end{aligned} \tag{3.43}$$

Where the equilibrium distribution $f_i^{(0)} \equiv f_i^{(\mathrm{eqm})}$ actually determines the macroscopic observables through the requirements,

$$\rho = \sum_i f_i^{(0)} \quad , \quad \rho\mathbf{u} = \sum_i f_i^{(0)}\mathbf{e}_i \tag{3.44}$$

thus ensuring that the moments of higher-order components of the link density distribution are neutral:

$$\sum_i f_i^{(n)} = 0 \quad , \quad \sum_i f_i^{(n)}\mathbf{e}_i = 0 \quad (n \geq 1). \tag{3.45}$$

Substituting the expanded terms in equation (3.43) into the evolution equation (3.42) results in

$$\delta\left[\partial_{t_0}+e_{i\alpha}\partial_\alpha\right]f_i^{(0)}+\delta^2\left[\partial_{t_1}f_i^{(0)}+\left(\partial_{t_0}+e_{i\alpha}\partial_\alpha\right)f_i^{(1)}+\tfrac{1}{2}\left(\partial_{t_0}+e_{i\alpha}\partial_\alpha\right)^2 f_i^{(0)}\right] = \textstyle\sum_j \Omega_{ij}^{(\mathrm{iso})}\left[\delta f_j^{(1)}+\delta^2 f_j^{(2)}\right]+\mathrm{O}\left(\delta^3\right), \tag{3.46}$$

taking the terms of first order in δ gives

$$\partial_{t_0}f_i^{(0)}+e_{i\alpha}\partial_\alpha f_i^{(0)}=\sum_j \Omega_{ij}^{(\mathrm{iso})}f_j^{(1)}. \tag{3.47}$$

Taking zero and first order velocity moments respectively

$$\partial_{t_0}\sum_i f_i^{(0)}+\partial_\alpha\sum_i f_i^{(0)}e_{i\alpha}=\sum_{ij}\Omega_{ij}^{(\mathrm{iso})}f_j^{(1)} \tag{3.48}$$

$$\partial_{t_0}\sum_i f_i^{(0)}e_{i\beta}+\partial_\alpha\sum_i f_i^{(0)}e_{i\alpha}e_{i\beta}=\sum_{ij}\Omega_{ij}^{(\mathrm{iso})}f_j^{(1)}e_{i\beta} \tag{3.49}$$

which, upon application of the macroscopic variable definitions in equation (3.44) and the summation constraints on the collision matrix in equation (3.30), produces the first order contributions to the continuity and Navier-Stokes equations respectively

$$\partial_{t_0}\left(\rho\right)+\partial_\alpha\left(\rho u_\alpha\right)=0 \tag{3.50}$$

$$\partial_{t_0}\left(\rho u_\beta\right)+\partial_\alpha\Pi_{\alpha\beta}^{(0)}=0 \tag{3.51}$$

where $\Pi_{\alpha\beta}^{(0)}$ is the zeroth order contribution to the momentum flux tensor,

$$\Pi_{\alpha\beta}^{(0)}=\sum_i f_i^{(0)}e_{i\alpha}e_{i\beta}. \tag{3.52}$$

Next we extract the second order expansion of the evolution equation,

$$\partial_{t_1} f_i^{(0)} + \left(\partial_{t_0} + e_{i\alpha}\partial_\alpha\right) f_i^{(1)} + \frac{1}{2}\left(\partial_{t_0} + e_{i\alpha}\partial_\alpha\right)^2 f_i^{(0)} = \sum_j \Omega_{ij}^{(\mathrm{iso})} f_j^{(2)} \tag{3.53}$$

which upon using the first order expansion (3.47) yields

$$\partial_{t_1} f_i^{(0)} + \left(\partial_{t_0} + e_{i\alpha}\partial_\alpha\right) f_i^{(1)} + \frac{1}{2}\left(\partial_{t_0} + e_{i\alpha}\partial_\alpha\right) \sum_j \Omega_{ij}^{(\mathrm{iso})} f_j^{(1)} = \sum_j \Omega_{ij}^{(\mathrm{iso})} f_j^{(2)}. \tag{3.54}$$

Taking zero and first order velocity moments on equation (3.54) produces the second order contributions to the continuity and the Navier-Stokes equations respectively

$$\partial_{t_1}\left(\rho\right) = 0 \tag{3.55}$$

$$\partial_{t_1}\left(\rho u_\beta\right) + \partial_\alpha \Pi_{\alpha\beta}^{(1)} + \frac{1}{2}\partial_\alpha \Omega_{\alpha\beta}^{(1)} = 0 \tag{3.56}$$

where we have defined the second order contribution to the momentum flux tensor as

$$\Pi_{\alpha\beta}^{(1)} = \sum_i f_i^{(1)} e_{i\alpha} e_{i\beta} \tag{3.57}$$

and $\Omega_{\alpha\beta}^{(1)}$ is defined as

$$\Omega_{\alpha\beta}^{(1)} = \sum_{ij} \Omega_{ij}^{(\mathrm{iso})} f_j^{(1)} e_{i\alpha} e_{i\beta} \tag{3.58}$$

Combining the first and second order extractions gives the macroscopic equations to second order as

$$\partial_t\left(\rho\right) + \partial_\alpha\left(\rho u_\alpha\right) = 0 \tag{3.59}$$

$$\partial_t\left(\rho u_\beta\right) + \partial_\alpha\left(\Pi_{\alpha\beta}^{(0)} + \Pi_{\alpha\beta}^{(1)}\right) + \frac{1}{2}\partial_\alpha \Omega_{\alpha\beta}^{(1)} = 0. \tag{3.60}$$

We now need to select a suitable form for the equilibrium distribution function that maps equations (3.59) and (3.60) onto the target macroscopic equations, continuity and momentum (Navier-Stokes) respectively.

The most general form of the equilibrium distribution function up to $O(u^2)$ that satisfies these conditions was determined for our D2Q13 lLB model [70] and found to be equivalent to the the D2Q7 lLB form given by Higuera *et al* [53]

$$f_i^{(0)} = \rho\, t_\sigma \left(1 + \frac{1}{c_s^2} e_{i\alpha} u_\alpha - \frac{1}{2c_s^2} u_\alpha u_\alpha + \frac{1}{2c_s^4} e_{i\alpha} e_{i\beta} u_\alpha u_\beta\right) \tag{3.61}$$

except that, for our D2Q13 lLB model, the velocity of sound is $c_s = \sqrt{3/10}$ [70].

The first order contribution to the momentum flux tensor $\Pi_{\alpha\beta}^{(0)}$ therefore becomes

$$\Pi_{\alpha\beta}^{(0)} = c_s^2 \rho \delta_{\alpha\beta} + \rho u_\alpha u_\beta \tag{3.62}$$

and in appendix (B) we demonstrate that to first order in $\mathbf{u}$ we can approximate the right hand side of equation (3.47) as

$$\sum_j \Omega_{ij}^{(i)} f_j^{(1)} \approx \frac{1}{c_s^2} \partial_\gamma \left(\rho u_\epsilon\right) Q_{i\gamma\epsilon} \tag{3.63}$$

where $Q_{i\gamma\epsilon}$ is defined as

$$Q_{i\gamma\epsilon} = t_\sigma \left(e_{i\gamma} e_{i\epsilon} - c_s^2 \delta_{\gamma\epsilon}\right)$$

and so, using result in equation (3.63), we can re-write equation (3.58) as

$$\Omega_{\alpha\beta}^{(1)} = \frac{1}{c_s^2} \partial_\gamma \left(\rho u_\epsilon\right) \sum_i Q_{i\gamma\epsilon} e_{i\alpha} e_{i\beta}. \tag{3.64}$$

Turning now to the momentum flux tensor, the first order link density distribution $f_i^{(1)}$ can be expanded in terms of the eigenvectors ξ_i^ν of the isotropic lLB schemes matrix, given in equation (3.39), thus

$$f_i^{(1)} = \sum_\nu a_\nu \xi_i^\nu \tag{3.65}$$

where the a_ν are the coefficients of the expansion. Equation (3.63) now takes the form,

$$\sum_j \Omega_{ij}^{(i)} \sum_\nu a_\nu \xi_j^\nu \approx \frac{1}{c_s^2} \partial_\gamma \left(\rho u_\epsilon\right) \mathrm{Q}_{i\gamma\epsilon}. \tag{3.66}$$

Making an index change $\sum_j \Omega_{ij}^{(i)} \xi_j^\nu = \lambda_\nu \xi_i^\nu$, where, λ_ν is the eigenvalue associated with the eigenvector ξ_i^ν yields

$$\sum_\nu a_\nu \lambda_\nu \xi_i^\nu \approx \frac{1}{c_s^2} \partial_\gamma \left(\rho u_\epsilon\right) \mathrm{Q}_{i\gamma\epsilon}. \tag{3.67}$$

Taking the inner product of equation (3.67) with an arbitrary eigenvector with non-zero eigenvalue gives

$$\sum_\nu a_\nu \lambda_\nu \sum_i \xi_i^\mu \xi_i^\nu \approx \frac{1}{c_s^2} \partial_\gamma \left(\rho u_\epsilon\right) \sum_i \xi_i^\mu \mathrm{Q}_{i\gamma\epsilon}, \tag{3.68}$$

relabelling $\sum_i \xi_i^\mu \mathrm{Q}_{i\gamma\epsilon} \rightarrow q_{\gamma\epsilon}^\mu$, where, $\mathrm{Q}_{i\gamma\epsilon} = \sum_\mu q_{\gamma\epsilon}^\mu \xi_i^\mu$ and noting $\sum_i \xi_i^\mu \xi_i^\nu = \delta_{\mu\nu}$ we easily obtain an expression for the co-efficients in of the expansion in equation (3.65)

$$a_\nu \approx \frac{1}{c_s^2 \lambda_\mu} \partial_\gamma \left(\rho u_\epsilon\right) q_{\gamma\epsilon}^\mu \tag{3.69}$$

This procedure is, however, valid only for eigenvectors with a non-zero eigenvalue, so for completeness, we can write equation (3.65) as the combination of the contributions from equation (3.69) and the zero eigenvalue contributions.

$$f_i^{(1)} \approx \sum_\mu \frac{1}{c_s^2 \lambda_\mu} \partial_\gamma \left(\rho u_\epsilon\right) q_{\gamma\epsilon}^\mu + \sum_{\nu_2} a_{\nu_2} \xi_i^{\nu_2} \tag{3.70}$$

It can be shown that, for the case of an isotropic fluid, the second term on the r.h.s of equation (3.70) vanishes and that the remaining terms can be used to write the first order distribution function as, [70]

$$f_i^{(1)} \approx \frac{1}{c_s^2} \partial_\gamma \left(\rho u_\epsilon\right) \left\{ -\frac{1}{\phi} \mathrm{Q}_{i\gamma\epsilon} + \left(g_2 \xi_i^2 + g_3 \xi_i^3\right) \delta_{\gamma\epsilon} + g_1 \xi_i^1 \right\} \tag{3.71}$$

which we can use to write the second order contribution to the momentum flux tensor as †

$$\Pi_{\alpha\beta}^{(1)} = \frac{1}{c_s^2}\partial_\gamma\left(\rho u_\epsilon\right)\sum_i\left\{-\frac{1}{\phi}\mathrm{Q}_{i\gamma\epsilon} + \left(g_2\xi_i^2 + g_3\xi_i^3\right)\delta_{\gamma\epsilon} + g_1\xi_i^1\right\}e_{i\alpha}e_{i\beta}. \tag{3.72}$$

The last two terms inside the braces on the r.h.s of equation (3.72) correspond to eigenvectors of the isotropic collision matrix. In the incompressible limit the terms associated with the post-multiplying Kronecker delta $\delta_{\gamma\epsilon}$ vanish and the g_1 term can be shown to contribute only to the hydrostatic pressure and as such can be omitted [70].

Replacing the terms in equation (3.60) with equations (3.62),(3.64) and (3.72) we can write (in the incompressible limit) the emergent Navier-Stokes equation of the lattice fluid [70] :

$$\partial_t\left(u_\alpha\right) + u_\beta\partial_\beta\left(u_\alpha\right) = -\frac{1}{\rho}\partial_\alpha \mathrm{P} + \nu\partial_\beta\partial_\beta\left(u_\alpha\right) \tag{3.73}$$

where P is the scalar pressure term, which, for our model, is equivalent to $c_s^2\rho$ and ν is the kinematic viscosity of the isotropic fluid, controlled through eigenvalue ϕ according to :

$$\nu = \frac{c_s^2}{2}\left(\frac{2}{\phi} - 1\right). \tag{3.74}$$

† in the limit of small departures from equilibrium we can replace the approximation with an equality.

3.4.5 Dimensionality of LBE models

We need to briefly discuss the dimensional units of a LG or LB model. A lattice with dimensions $L \times W$, is specified in terms of lattice units (lu). To convert these to actual units (au), the relevant dimension is multiplied by the lattice link distance. For the case of the hexagonal lattice, the length unit is traditionally taken to be unity, therefore a length of L lu's corresponds to a length L in au's. However the width unit is $\sqrt{3}/2$ and so a width of W lu's corresponds to a width of $W\sqrt{3}/2$ au's.

The basic time step is unity and therefore all other quantities such as velocity (lattice units per time step) are derived from these basic units.

3.5 Review of Principle Applications of LB

Here we briefly review some of the principle applications in fluid dynamics of the LB scheme. Starting with standard flow applications we shall then move onto the thermodynamics and lastly immiscible fluids. The latter two fields have seen some of the most intensive but problematic applications. Finally we shall cover a few other applications of the technique.

Succi *et al* [71] introduced LB models for isotropic 2D and 3D fluid dynamics and since then a number of flow geometries and regimes have been investigated [63]. Koelman [72] presents a simple LB scheme for Navier-Stokes fluid flow and Hou *et al* [73] provide a detailed analysis of cavity flow using the LB method. Creeping flow is investigated by Flekkøy *et al* [74], Sun [75] investigated high speed flows and

Amati *et al* [76] performed simulations of high resolution turbulent channel flow.

Alexander *et al* [77] introduced an LBGK scheme that modelled thermodynamic flow of monatomic gases and Chen *et al* [78] developed higher order schemes that removed the LB nonlinear deviations from the target equations of macroscopic thermodynamics. Since then LB models have been used to investigate many thermodynamical problems, including single and two-species thermal turbulence [79, 80], Rayleigh-Bernard convection [81, 82], as well as non-ideal gases and high-Mach number thermodynamics [83, 84]. A concise study of hydrodynamic and thermo-hydrodynamic internal pressure-driven flows is presented in [85] which also contains a good review of current LB thermodynamics.

Gunstensen *et al* [64, 86] introduced 2D and 3D LB models of immiscible fluids, discussing the observed surface-tension with experimental results. Investigations into the hydrodynamics of LB immiscible models have been performed in [87–89] with good reviews of the LBGK two component models covered in [90, 91]. Recently ternary LB models [92–94] have been presented which, when compared to existing binary LB models, have produced richer and more accessible phenomenology.

Lattice Boltzmann models have also been applied to other areas of fluid dynamics including non-ideal gases [95], complex fluids [96], bubble growth [97], contact line dynamics [98], granular flow [99], magneto-hydrodynamics [100, 101] and electro-viscous transport [102]. This list is not exhaustive and is intended only to imply the extent and range of the LB technique.

3.6 Boundary Conditions in Lattice Models

Bounding a computational flow domain can be a non-trivial problem even in mature applications of CFD. However, in LG and LB models the algorithmic process of imposing a wall can be relatively simple. On the discrete lattice nodes a bounding wall can be implemented by labelling specific nodes as 'wall' nodes and applying a different operation on the propagating particles other than the 'bulk' collision at every time step. Wolfram [40] showed that the simplest operation that ensured non-slip conditions at a bounding wall node was a *bounce-back* closure rule which, despite its widespread use, is only first order accurate.

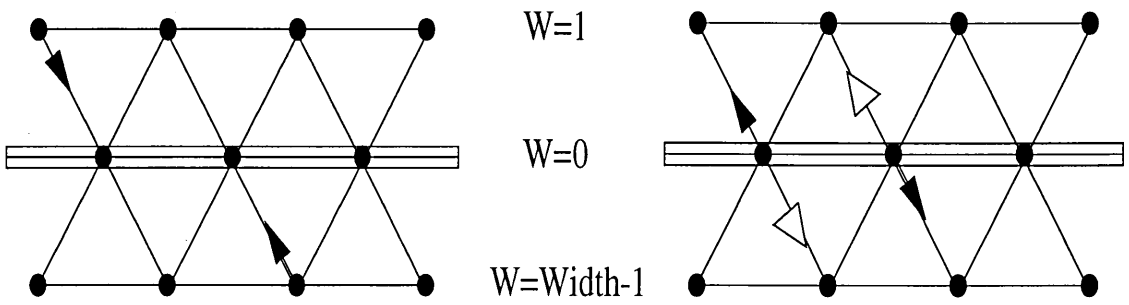

(a) Before propagation. (b) After propagation.

Figure 3.7: Schematic of the bounce back wall operation, (a) shows two link distributions before propagating onto the wall layer (W=0). The white arrows in (b) show the positions of the link distributions after propagation but before bounce-back is applied, the black arrows show the link distributions after the bounce-back operation.

Instead of experiencing a collision, the particles on a wall node are returned along the link on which it approached, see figure (3.7). This effectively introduces friction and produces a non-slip wall at the designed wall nodes. Cornubert *et al* [51] showed, however, that the bounce-back method is only first order accurate and so suppresses the Knudsen layer associated with a bounding wall. The ease in which a bounce-

back wall can be implemented allows for the simulation of complex geometries. However, the exact position of the imposed wall is unknown, in general the first order accuracy making the effective zero in macroscopic velocity occur slightly off-lattice. He *et al* [103] rigorously analyzed the near wall velocity for Poiseuille flow using a first-order bounce-back closure rule and confirmed an off-lattice wall position with zero velocity.

The errors introduced in the first order bounce-back boundary closure rules will affect the accuracy of the method, especially in the near wall lattice fluid. For this reason several attempts at producing a second order accurate boundary condition have being developed, resulting in smaller (higher order) errors. Skordos [104] introduced velocity gradients into a wall layer equilibrium distribution, Noble *et al* [105] applied a pressure constraint at the wall layers and Inamuro *et al* [106] used a combination of bounce-back and specular reflection. All the above boundary methods improved the accuracy of the wall layers and have being studied and compared by Zou *et al* [107], but the general problem of lattice closure remains. For the purposes of the work presented here we concern ourselves with bulk schemes only and neglect lattice closure as an issue.

3.7 Forcing in Lattice Models

Forcing a LG or LB scheme is usually achieved through one of two methods: body forcing or equilibrium forcing. In this section we shall briefly discuss both methods of forcing. However, throughout this work the body forcing method is used.

Body forcing is associated with the process of imposing a pressure gradient on the lattice fluid and entails adding/subtracting fixed amounts of link density distributions from specific/all bulk node links, to produce the required flow profile. When a forcing term of the form

$$F_i = \Delta\, t_\sigma e_{ix} \tag{3.75}$$

is added to all bulk node link densities at every time step within a translationally invariant channel geometry, at steady state a Poiseuille flow profile develops. The resultant pressure gradient, $G_{CE} = -\partial_x\, P$ is shown, through a suitably adjusted Chapman-Enskog expansion, to be of the form (see appendix A) [2]

$$G_{CE} = \Delta \sum_i t_\sigma e_{ix}^2. \tag{3.76}$$

Equilibrium forcing entails setting a known velocity profile along a specific line of sites, e.g. a channel inlet and outlet. Along the line of sites, the node densities are redistributed across the node links using a known equilibrium distribution function that produces a flow profile of the correct form. In terms of channel (duct) flow, equilibrium forcing imposes a pressure gradient down the channel that at steady state results in a Poiseuille flow profile.

3.8 Summary of the Lattice Models

In this section we have introduced and reviewed the history of the evolution of discrete lattice models. Since the formulation of cellular automata, a diverse range of LG and LB models have appeared that map onto macroscopic hydrodynamics.

A brief explanation of some of the more popular types of LG models used to model fluids and their differences are presented with a view to covering the general ideas and methodology of LGs. Next the process of performing a Chapman-Enskog analysis on an LG evolution equation to recover a set of macroscopic equations that (after a suitable rescaling of variables) map onto hydrodynamics is reviewed. A general discussion of some of the intricacies of such an analysis is followed by remarks on the technique. The section on LGs is finished with a brief literature review of some of the key applications showing the scope of the method.

Having discussed the LG models, the historical development of the LB models was introduced. The key developmental stages of the LB models are covered, culminating in the two main algorithms used within the LB community,i.e. the lLB and LBGK models. A classical D2Q7 lLB model is introduced along with the simpler single relaxation LBGK model. Since however we have used a D2Q13 lLB throughout this thesis, it is this model that we have mapped onto the macroscopic equations of hydrodynamics by performing a Chapman-Enskog analysis on the D2Q13 lLB mesoscopic evolution equation.

A short literature review of LB models is presented before the chapter concludes with a discussion on bounding and forcing issues within LG and LB models. The boundary and forcing mechanisms introduced in this chapter are consistent with the mechanisms used to produce the results presented in chapters 5, 6 and 7.

Chapter 4

Anisotropic Extensions to the LBE Model

4.1 Introduction

In chapters 2 and 3 we covered the continuum theory of both isotropic and anisotropic fluids and showed how the macroscopic dynamics of a discrete isotropic Lattice Boltzmann model recovers the continuum conservation equations of continuity and momenta.

Having specified the form of our target macroscopic dynamics (i.e. the ELP equations of nemato-dynamics) we introduce to the isotropic momentum scheme a second (link angle) distribution that undergoes its own LBGK collision step and advects (propagates) along with the momentum densities. By careful selection of a

suitable equilibrium distribution and forcing terms we recover on the macroscale, the coupled equations of motion for the director. Subsequently we introduce the necessary anisotropic extensions to the core momentum lLB scheme which introduces anisotropy into the macroscopic momentum equations through the use of an anisotropic collision matrix and specific forcing terms.

At each time step we calculate the macroscopic observables of mass, momentum and director angle which are subsequently used to produce the required terms used in the coupled equations in the evolution schemes of the momentum and angle distributions.

4.2 Director Equations of Motion

We associate with the lattice Boltzmann link momentum density distributions $f_i(\mathbf{r}, t)$ a second distribution, the (scalar) link angle $\theta_i(\mathbf{r}, t)$. We assume this link angle distribution advects (propagates) with the momentum density distributions and undergoes its own collision step to achieve evolution. Further, we assume that the lattice nematic's Reynolds number is small, that the fluid is incompressible and that spatial director gradients are small - an assumption already implicit in the formulation of the target dynamics we note. Accordingly, in the spirit of lattice Boltzmann simulation we propose an evolution equation for the link angle distributions, akin to the LBGK scheme,

$$\theta_i(\mathbf{r} + \mathbf{e}_i\delta, t + \delta) = \theta_i(\mathbf{r}, t) - \bar{\omega}\left\{\theta_i(\mathbf{r}, t) - \theta_i^{(\mathrm{eqm})}(\theta, \rho, \mathbf{u})\right\} + \mathrm{F}_i \qquad (4.1)$$

where $\bar{\omega}$ is the LBGK relaxation parameter, F_i represents position/time dependent forcing terms and $\theta_i^{(\mathrm{eqm})}(\theta, \rho, \mathbf{u})$ is the link angle equilibrium distribution function. For brevity we shall drop the spatial and time labels in the following analysis.

We define the macroscopic observable as a density weighted summation of link angle distributions, thus

$$\theta = \frac{1}{\rho} \sum_i f_i \theta_i. \tag{4.2}$$

The summation is considered more fully at the end of this chapter.

We can expand the link angle, time derivative and, crucially, forcing terms [2] using the same parameter δ as the scheme for momentum densities :

$$\begin{aligned} \theta_i &\rightarrow \theta_i^{(0)} + \delta\theta_i^{(1)} + \delta^2\theta_i^{(2)}, \\ \partial_t &\rightarrow \partial_{t_0} + \delta\partial_{t_1} + \delta^2\partial_{t_2}, \\ \mathrm{F}_i &\rightarrow \delta\mathrm{F}_i^{(1)} + \delta^2\mathrm{F}_i^{(2)}, \end{aligned} \tag{4.3}$$

where we note the forcing term contains no δ^0 contributions.

As usual, we implicitly link the zeroth order expansion of the link angle to the link angle equilibrium distribution function $\theta_i^{(0)} \equiv \theta_i^{(\mathrm{eqm})}$ acting on the shortest time scale ∂_{t_0}. The specific form of the link angle equilibrium distribution function $\theta_i^{(0)}$ is confined by the following requirements which we place upon the velocity moments

$$\begin{aligned} \textstyle\sum_i \theta_i^{(0)} &= \theta \quad \Leftrightarrow \quad \sum_i \theta_i^{(n)} = 0 \quad (n \geq 1) \\ \textstyle\sum_i \theta_i^{(0)} e_{i\alpha} &= \theta u_\alpha \\ \textstyle\sum_i \theta_i^{(0)} e_{i\alpha} e_{i\beta} &= c_s^2 \theta \delta_{\alpha\beta} + \theta u_\alpha u_\beta. \end{aligned} \tag{4.4}$$

Substituting the expanded quantities in equation (4.3) into the evolution equation

(4.1) results in

$$\begin{aligned}\delta\left[\left(\partial_{t_0}+e_{i\alpha}\partial_\alpha\right)\theta_i^{(0)}\right] &+ \delta^2\left[\partial_{t_1}\theta_i^{(0)}+\left(\partial_{t_0}+e_{i\alpha}\partial_\alpha\right)\theta_i^{(1)}+\frac{1}{2}\left(\partial_{t_0}+e_{i\alpha}\partial_\alpha\right)^2\theta_i^{(0)}\right] \\ &= -\bar{\omega}\left[\delta\theta_i^{(1)}+\delta^2\theta_i^{(2)}\right]+\delta \mathrm{F}_i^{(1)}+\delta^2\mathrm{F}_i^{(2)}.\end{aligned} \tag{4.5}$$

Extracting to first order in δ therefore gives

$$\partial_{t_0}\theta_i^{(0)}+\partial_\alpha\theta_i^{(0)}e_{i\alpha}=-\bar{\omega}\theta_i^{(1)}+\mathrm{F}_i^{(1)} \tag{4.6}$$

which, upon summation on i, gives the first order contributions to the scalar director acceleration equation :

$$\partial_{t_0}\theta+u_\alpha\partial_\alpha\theta=\mathrm{F}^{(1)}. \tag{4.7}$$

where $\sum_i F_i^{(1)}=F^{(1)}$ is the cumulative effect of forcing.

Extracting to second order in δ using the first order equation (4.6), gives

$$\partial_{t_1}\theta_i^{(0)}+\left(1-\frac{\bar{\omega}}{2}\right)\left(\partial_{t_0}+e_{i\alpha}\partial_\alpha\right)\theta_i^{(1)}=-\bar{\omega}\theta_i^{(2)}+\mathrm{F}_i^{(2)} \tag{4.8}$$

Upon summation on i, results in

$$\partial_{t_1}\theta+\left(1-\frac{\bar{\omega}}{2}\right)\partial_\alpha\sum_i\theta_i^{(1)}e_{i\alpha}=\mathrm{F}^{(2)} \tag{4.9}$$

where $F^{(2)}=\sum_i F_i^{(2)}$.

Using equation (4.6) to replace the first order link angle distribution $\theta_i^{(1)}$ gives

$$\begin{aligned}\partial_{t_1}\theta &= \frac{1}{2}\left(\frac{2}{\bar{\omega}}-1\right)\left[\partial_\alpha\partial_{t_0}\sum_i\theta_i^{(0)}e_{i\alpha}+\partial_\alpha\partial_\beta\sum_i\theta_i^{(0)}e_{i\alpha}e_{i\beta}\right]+ \\ &\quad \frac{1}{\bar{\omega}}\left(1-\frac{\bar{\omega}}{2}\right)\sum_i\left(\partial_{t_0}+e_{i\alpha}\partial_\alpha\right)F_i^{(1)}+\mathrm{F}^{(2)}\end{aligned} \tag{4.10}$$

and postponing further discussion of the F terms in the r.h.s of equation (4.10) until the end of this section, we write :

$$\partial_{t_1}\theta = \frac{c_s^2}{2}\left(\frac{2}{\bar{\omega}} - 1\right)\partial_\alpha\partial_\alpha\theta + \mathrm{F}^{(2)} + \frac{1}{\bar{\omega}}\left(1 - \frac{\bar{\omega}}{2}\right)\sum_i \left(\partial_{t_0} + e_{i\alpha}\partial_\alpha\right) F_i^{(1)} \tag{4.11}$$

Combining equations (4.7) and (4.11), we obtain the macroscopic director equation of motion derived from the Chapman-Enskog expansion of our scalar link angle evolution equation as

$$\partial_t\theta + u_\alpha\partial_\alpha\theta = \frac{K}{\gamma_1}\partial_\alpha\partial_\alpha\theta + \mathrm{F}^{(1)} + \mathrm{F}^{(2)} + \frac{1}{\bar{\omega}}\left(1 - \frac{\bar{\omega}}{2}\right)\sum_i \left(\partial_{t_0} + e_{i\alpha}\partial_\alpha\right) F_i^{(1)} \tag{4.12}$$

we immediately make the association,

$$\frac{K}{\gamma_1} = \frac{c_s^2}{2}\left(\frac{2}{\bar{\omega}} - 1\right) \tag{4.13}$$

where K is the single elastic constant and γ_1 a specific combination of the Leslie coefficients. Thus equation (4.13) tells us that for our particular scheme, the single elastic constant of our nematic is controlled by the LBGK scalar relaxation parameter $\bar{\omega}$.

The forcing terms in the r.h.s for our director equation of motion (4.12) are added to the link angle evolution equation in the form $F_i^{(n)} = t_\sigma \mathrm{F}^{(n)}$. The t_σ's are the rest distribution constants and F generates the forcing terms derived in equation (2.122). The forcing in the r.h.s of our lattice fluid director equation (4.12) can be solved independent of the f_i's [2]. On writing $F_i^{(n)} = t_\sigma F^{(n)}\left(\nabla^{(n)}\mathbf{u}, \theta, \mathbf{H}\right)$, there are Q $F_i^{(1)}$'s and Q $F_i^{(2)}$'s (where $Q = 13$ for our scheme) which can be chosen so as to recover from the last three terms in the r.h.s of equation (4.12), the appropriate (target) coupling of the lattice director to the velocity field.

The final (target) form of the derived macroscopic director equation of motion is thus

$$\partial_t\theta + u_\alpha\partial_\alpha\theta = \frac{K}{\gamma_1}\partial_\alpha\partial_\alpha\theta + \Omega|_z + \frac{\gamma_2}{\gamma_1}n_\alpha \mathrm{A}_{\alpha\beta} + \frac{1}{\gamma_1}\mathrm{M}. \tag{4.14}$$

So to map our link angle evolution equation onto the target macroscopics we need to define a suitable link angle equilibrium distribution function $\theta_i^{(0)}$ which satisfies the constraints laid out in equation (4.4). For simplicity, we assume a form of

$$\theta_i^{(0)} = \frac{f_i}{\rho}\theta \tag{4.15}$$

where f_i is the link momentum density distribution and ρ is the macroscopic density. It can be shown that our choice of the link angle equilibrium distribution function satisfies all the requirements in equation (4.4), subject to the arguments presented below. It should be noted however that this is not a unique solution and there other possible forms that would equally satisfy all the constraints.

4.2.1 Discussion

Within the methodology discussed above we incur two types of error terms, firstly any first order forcing contribution $F_i^{(1)}$ will produce an "error" term at second order. These terms can often be corrected by revised second order forcing contributions $F_i^{(2)}$ [2]. Second order forcing terms likewise incur third order error terms. Since, however, we are only recovering the target macroscopics up to second order we need only discuss error terms due to the first order forcing.

From the last section we see that the Chapman-Enskog procedure applied to our

angle evolution produces the following first order forcing "error" terms at second order

$$-\frac{1}{2}\partial_{t_o}\sum_i F_i^{(1)} \quad \text{and} \quad -\frac{1}{\bar{\omega}}\partial_\alpha \sum_i F_i^{(1)} e_{i\alpha}.$$

On general grounds [2] we can argue that one appropriate choice for the first order forcing term $F_i^{(1)}$ in our scheme is the uniform magnetic field contribution. The forcing is applied according to $F_i = t_\sigma F$, where F represents the forcing terms derived at the end of chapter 2 in equation (2.122), from which it can easily be shown that the spatial gradients in the forcing term are always zero. Moreover, the time derivative forcing error term will be zero except for the instances when the field is switched on or off at which point the term will be discontinuous. At present we assume for now the second order "error" terms due to the first order forcing contribution are negligible and thus ignore them. In fact, in more general situations the error terms could by removed by insertion of equal but opposite forcing terms at second order, resulting in all forcing "error" terms being reduced to third order [2].

A second class of "error" terms produced in the director dynamics are a consequence of the Chapman-Enskog procedure upon our selection of the link angle equilibrium distribution function. In equation (4.10) the second term inside the square braces is of the form

$$\partial_\alpha \partial_\beta \sum_i \theta_i^{(0)} e_{i\alpha} e_{i\beta}$$

where the second velocity moment summation should, according to the constraints in equation (4.4), equal

$$\sum_i \theta_i^{(0)} e_{i\alpha} e_{i\beta} = c_s^2 \theta \delta_{\alpha\beta} + \theta u_\alpha u_\beta.$$

The second term on the r.h.s of the last equation is a consequence of the constraints on the momentum equilibrium distribution function, $f_i^{(0)}$. However, in the director evolution scheme this is an error term that is of second order in $\mathbf{u}$ and therefore it is small in the target creeping flow. The form of the equilibrium distribution function in equation (4.15), produces one other error term of the form

$$\partial_\alpha \partial_\beta \Pi_{\alpha\beta}^{(1)}.$$

which involves second order spatial derivatives of the first order contributions to the momentum flux tensor. In the next section we show that in the anisotropic case the first order momentum flux tensor is a function of velocity and director gradients. We can therefore argue that this term is at most third order and as such can be ignored.

4.3 Anisotropic Viscous Stress Tensor

The anisotropy is introduced into the momentum evolution scheme through an anisotropic collision process. We write the anisotropic momentum evolution equation as

$$f_i\left(\mathbf{r}+\mathbf{e}_i\delta, t+\delta\right) = f_i\left(\mathbf{r},t\right) + \sum_j \left(\Omega_{ij}^{(a)} - \mathrm{S}_{ij}\right) f_j^{(\mathrm{neq})} + \mathrm{F}_i \tag{4.16}$$

where $\Omega_{ij}^{(a)}$ is the anisotropic collision matrix, S_{ij} is defined below, $f_j^{(\mathrm{neq})}$ is the non-equilibrium component of the momentum link density distribution and the 'forcing' term F_i is of the form

$$\mathrm{F}_i = \frac{1}{\gamma_1 c_s^2} t_\sigma e_{i\beta} \partial_\alpha \left(\alpha_2 n_\alpha h_\beta + \alpha_3 n_\beta h_\alpha\right). \tag{4.17}$$

The forcing term recovers the momentum evolution arising from the α_2 and α_3 terms of the anisotropic viscous stress tensor. In order to recover the remaining terms, the anisotropic matrix is taken to be of the form

$$\Omega_{ij}^{(a)} = \frac{\Omega_{ij}^{(\mathrm{iso})}}{1 + \lambda_j^{(0)} + \lambda_j^{(2)} + \lambda_j^{(4)}} \tag{4.18}$$

where $\Omega_{ij}^{(\mathrm{iso})}$ is the *isotropic* collision matrix defined in equation (3.39) and

$$\lambda_j^{(0)} = \delta^0 \left(e_{j\alpha} e_{j\alpha}\right) \qquad \lambda_j^{(2)} = \delta^2 \left(e_{j\alpha} n_\alpha\right)^2 \qquad \lambda_j^{(4)} = \delta^4 \left(e_{j\alpha} n_\alpha\right)^4 . \tag{4.19}$$

The $\lambda_j^{(0)}$ term contributes only to the isotropic viscosity, $\lambda_j^{(2)}$ yields the terms associated with the α_5 and α_6 coefficients whilst $\lambda_j^{(4)}$ gives the term associated with the α_1 coefficient. In order to recover the α_1 term from the $\lambda_j^{(4)}$ term in the correct form, it is necessary for the velocity summation tensor introduced in equation (3.37) to be isotropic up to 8^{th} order. For this reason we do not attempt to recover the term associated with the α_1 viscosity in this scheme and concern ourselves only with recovering the terms associated with $\lambda_j^{(2)}$, which require lattice isotropy up to 6^{th} order only.

The S_{ij} term in the momentum evolution equation (4.16) is defined as

$$\mathrm{S}_{ij} = \sum_{\nu=4}^{7} \xi_i^{(\nu)} \xi_j^{(\nu)} \tag{4.20}$$

where the summation is implied over the 4 eigenvectors $\xi^{(\nu)}$ of the collision matrix with zero eigenvalue. The effect of the S_{ij} matrix is to remove the contributions of these eigenvectors from f_i^n for all $n \geq 1$. It is necessary to accomplish this removal of terms in order to recover the required form for the macroscopic anisotropic viscous stress tensor. A recent development of this scheme with a more general scattering matrix removes the need for this matrix.

Following the isotropic Chapman-Enskog analysis performed in chapter 3, the anisotropy enters through the extension of the first order link density distribution function

$$f_i^{(1)} = \left(1 + \lambda_i^{(0)} + \lambda_i^{(2)}\right) g_i^{(1)} \tag{4.21}$$

where the $g_i^{(1)}$ are terms which can be determined from a similar analysis as in chapter 3 :

$$g_i^{(1)} = \frac{1}{c_s^2}\partial_\gamma\left(\rho u_\epsilon\right)\left(-\frac{1}{\phi}\mathrm{Q}_{i\gamma\epsilon} + \left(g_2\xi_i^{(2)} + g_3\xi_i^{(3)}\right)\delta_{\gamma\epsilon}\right) + g_1\xi_i^{(1)} + \sum_{\nu=4}^{7} g_\nu\xi_i^{(\nu)} \tag{4.22}$$

So the first order correction to the equilibrium distribution function is now

$$\begin{aligned} f_i^{(1)} = \left(1 + \lambda_i^{(0)} + \lambda_i^{(2)}\right) & \left[\frac{1}{c_s^2}\partial_\gamma\left(\rho u_\epsilon\right)\left(-\frac{1}{\phi}\mathrm{Q}_{i\gamma\epsilon} + \left(g_2\xi_i^{(2)} + g_3\xi_i^{(3)}\right)\delta_{\gamma\epsilon}\right) + \right. \\ & \left. g_1\xi_i^{(1)} + \sum_{\nu=4}^{7} g_\nu\xi_i^{(\nu)}\right] \end{aligned} \tag{4.23}$$

Now, unlike the isotropic scheme, the last term in equation (4.23) describing the contributions from the eigenvectors with zero eigenvalues is non-zero. These contributions are removed in this work by the matrix S_{ij}. However, a more general form of the scattering matrix removes the need for this tensor. In the incompressible limit, all terms in equation (4.23) multiplied by $\delta_{\gamma\epsilon}$ vanish and the eigenvector associated with the g_1 term can be shown [70] to contribute only to the hydrostatic pressure and so we can write equation (4.23) as

$$f_i^{(1)} = \left(1 + \lambda_i^{(0)} + \lambda_i^{(2)}\right)\left[\frac{1}{c_s^2}\partial_\gamma\left(\rho u_\epsilon\right)\left(-\frac{1}{\phi}\mathrm{Q}_{i\gamma\epsilon}\right)\right] \tag{4.24}$$

and inserting the correct form for the $\lambda_i^{(n)}$ terms from equation (4.19) results in

$$f_i^{(1)} = -\frac{1}{c_s^2\phi}\partial_\gamma\left(\rho u_\epsilon\right)\mathrm{Q}_{i\gamma\epsilon} - \frac{\delta^0}{c_s^2\phi}\partial_\gamma\left(\rho u_\epsilon\right)\mathrm{Q}_{i\gamma\epsilon}e_{i\phi}e_{i\delta}\delta_{\phi\delta} - \frac{\delta^2}{c_s^2\phi}\partial_\gamma\left(\rho u_\epsilon\right)n_\phi n_\delta\mathrm{Q}_{i\gamma\epsilon}e_{i\phi}e_{i\delta} \tag{4.25}$$

Provided the velocity set has the correct isotropy, the form of $f_i^{(1)}$ given by equation (4.25) leads to the following form for the anisotropic viscous stress tensor.

$$\begin{aligned}\sigma'_{\alpha\beta} &= c_s^2\rho\left(1-\tfrac{2}{\phi}-\tfrac{3\delta^0}{\phi}-\tfrac{\delta^2}{2\phi}\right)A_{\alpha\beta}+ \\ &\left(\tfrac{c_s^2\rho\delta^2}{\phi}-\alpha_2\lambda\right)n_\alpha n_\mu A_{\mu\beta}+\left(\tfrac{c_s^2\rho\delta^2}{\phi}-\alpha_3\lambda\right)n_\beta n_\mu A_{\mu\alpha}\end{aligned} \tag{4.26}$$

Recalling that we are not recovering the term associated with the α_1 coefficient and that the terms associated with the α_2 and α_3 coefficients are introduced as forcing terms, we can make the following identifications

$$\begin{aligned}\alpha_4 &= c_s^2\rho\left(1-\tfrac{2}{\phi}-\tfrac{3\delta^0}{\phi}-\tfrac{\delta^2}{2\phi}\right) \\ \alpha_5 &= \tfrac{c_s^2\rho\delta^2}{\phi}-\alpha_2\lambda \\ \alpha_6 &= \tfrac{c_s^2\rho\delta^2}{\phi}-\alpha_3\lambda\end{aligned} \tag{4.27}$$

We have therefore obtained a momentum evolution scheme which gives direct control over the Leslie viscosity coefficients in the anisotropic viscous stress tensor $\sigma'_{\alpha\beta}$ through the simulation parameters $\alpha_2, \alpha_3, \delta^0, \delta^2$ and ϕ.

In order for the algorithm to remain dynamically stable, the parameters associated with the anisotropic scattering matrix $(\delta^0, \delta^2, \phi, \tau)$ must be chosen to ensure that $-2 < \sum_{ij}\xi_i^\nu\Omega_{ij}\xi_j^\nu < 0$ for each eigenvector ξ^ν and $|\sum_{ij}\xi_i^\nu\Omega_{ij}\xi_j^\mu| < 1$ for $\nu \neq \mu$.

4.4 Anisotropic D2Q13 lLB Implementation

We shall now cover some of the key issues involved in incorporating the anisotropy into an isotropic D2Q13 lLB model. Implementation of the D2Q13 isotropic model was carried out after Higuera *et al* [47].

At each time step we calculate the nodal macroscopic observables of mass ρ, momentum $\rho\mathbf{u}$ and director angle θ. The first two are derived using the standard LB method of summation over i of the zero and first velocity moments of the link density distribution. However for the macroscopic scalar angle the required summation is a little more subtle.

The apolar nature of the director imposes a $\mathbf{n} \Leftrightarrow -\mathbf{n}$ condition on the nematic. In our algorithm we adhere to this condition * by finding the principle eigenvalue eigenvector from a density weighted order matrix of the thirteen link angles [3],

$$Q_{\alpha\beta} = \frac{1}{\rho}\sum_i \left(3n_{i\alpha}n_{i\beta} - \delta_{\alpha\beta}\right) f_i \tag{4.28}$$

obtaining the average angle from the components of the principle eigenvalue eigenvector.

However to conform to the Chapman-Enskog expansion our macroscopic variable needs to be a weighted sum of the link angle distributions, see equation (4.2). For this reason we subtract the principle eigenvector angle from each link angle before "ranging" the link angles to lie within $-\pi/2 < \theta_i < \pi/2$.

*It should be noted that this is not the only possible solution.

The density weighted summation in equation (4.2) was then performed on these suitably adjusted link angles to find, in effect, the average deviation from the principle eigenvector angle. Since the model assumes small gradients in the director field then the deviations from the principle eigenvector angle should be small and, in the situations considered, the apolar nature of $\mathbf{n}$ does not now affect the summation. The average angle θ is then simply the combination of the principle eigenvalue eigenvector angle plus the average deviation angle.

Having obtained the macroscopic observables we then use the method covered in appendix (C) to find the local gradients of the director and velocity fields, required to calculate the molecular field,

$$h_\mu = \gamma_1 \left(d_t n_\mu - \omega \times \mathbf{n}|_\mu \right) + \gamma_2 n_\alpha A_{\alpha\mu}$$

which are used along with the director components to form a 2×2 tensor field, $\mathrm{T}^h_{\alpha\beta}$ of the form

$$\mathrm{T}^h_{\alpha\beta} = \begin{bmatrix} (\alpha_2 + \alpha_3)\ n_x h_x & \alpha_2\ n_x h_y + \alpha_3\ n_y h_x \\ \alpha_2\ n_y h_x + \alpha_3\ n_x h_y & (\alpha_2 + \alpha_3)\ n_y h_y \end{bmatrix} \tag{4.29}$$

whose gradients (again calculated according to appendix (C)) are used in the anisotropic forcing term for the momentum evolution equation, i.e. equation (4.17)

$$\mathrm{F}_i = \frac{1}{\gamma_1 c_s^2} t_\sigma e_{i\beta}\ \partial_\alpha \mathrm{T}^h_{\alpha\beta} \tag{4.30}$$

The forcing terms to the director evolution equation are calculated at every time step using the velocity gradients calculated in the above process where appropriate.

4.5 Discussion and Conclusions

We have shown that the coupled set of the ELP equations of nemato-dynamics introduced in chapter 2 can be mapped onto by our enhanced D2Q13 lLB scheme.

Introduction of a separate link angle distribution evolution scheme that undergoes its own LBGK collision process and advects (propagates) along with the momentum density evolution scheme was shown (with the addition of suitable forcing terms) correctly to recover the scalar director equation of motion. Enhancing the isotropic D2Q13 lLB scheme introduced in chapter 3 by inclusion of an anisotropic collision matrix and suitable forcing terms was shown to recover the anisotropic form of the viscous stress tensor for the momentum equation of motion.

A general discussion on the forms and order of the incurred error terms for the link angle distribution evolution scheme was presented and some of the issues involved in the implementation of the algorithm were discussed. Importantly we have raised the issue of the apolar nature of the director unit vector, $\mathbf{n}$, and introduced a scheme that correctly recovers the nodal average angle from the link angle distributions consistent with the methodology of the Chapman-Enskog procedure.

The algorithmic implementation section concludes with a brief review of how the forcing contributions by the terms corresponding to the α_2 and α_3 Leslie viscosity coefficients are introduced into the momentum evolution scheme.

Chapter 5

Model Validation

5.1 Introduction

This chapter describes the validation of the isotropic scheme developed in chapter 3 and the anisotropic extensions developed in chapter 4.

We first demonstrate that the isotropic model correctly maps onto the hydrodynamical continuum equations of mass continuity and Navier-Stokes. We then show that the full anisotropic algorithm correctly recovers some known solutions of the ELP equations of nemato-dynamics.

5.2 Isotropic D2Q13 lLB scheme

It is prudent to validate the isotropic D2Q13 lLB scheme developed in chapter 3 before any anisotropic extensions are implemented. Naturally there are any number of flow regimes one could use to validate an isotropic lattice Boltzmann scheme [107]. For the purpose of validating our algorithm the process of matching a constant body forcing pressure gradient G in a uniform Poiseuille flow was selected as it has the advantage of a known analytical solution. Moreover, to obtain the correct relationship between pressure head and resultant flow rate is known to be a stringent test.

This method not only provides a good way of testing the algorithm but utilizes the same geometry, boundary conditions and forcing mechanisms used later in the anisotropic scheme.

5.2.1 Duct Flow

We begin by considering the flow geometry shown in figure (5.1). The system is bounded in the y-direction by a pair of non-slip walls but is periodic in the x-direction, hence it is translationally invariant. Although we work in two dimensions, we can consider that in the z-direction the system is infinitely deep and therefore the z co-ordinate does not enter into the hydrodynamics. This geometry is generally referred to as duct flow and imposing a constant body force throughout the fluid directed along the channel, results in a Poiseuille (parabolic) flow profile. The fluid

is at rest at the walls and the maximum velocity occurs at the centre of the channel width [9].

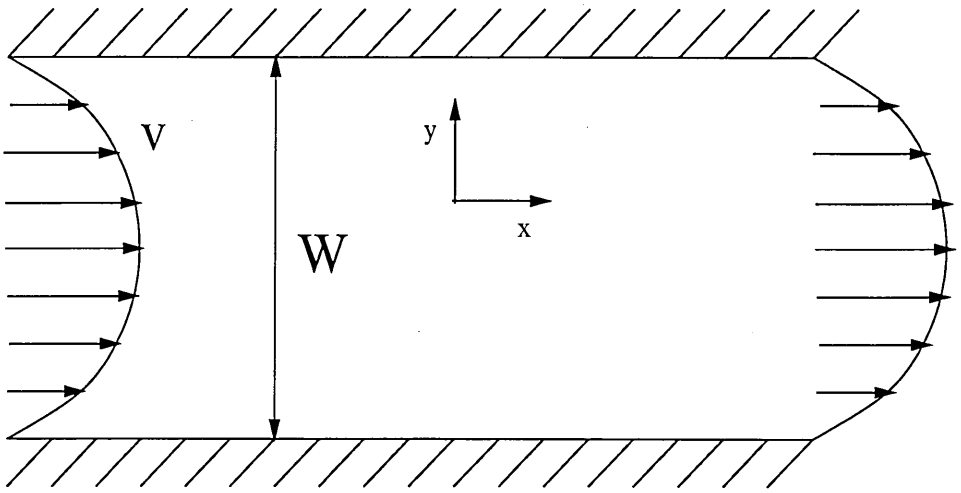

Figure 5.1: Geometrical setup for simple laminar Poiseuille (duct) flow. The system is periodic and translationally invariant in the x-direction and bounded by non-slip walls in the y-direction separated by a distance W. The z-direction can be considered to be infinitely deep and so therefore does not contribute to the hydrodynamics.

It is well known that for steady state incompressible uni-directional flow, such as that depicted in figure (5.1), the Navier-Stokes equations [9] reduce to,

$$\frac{1}{\rho}\nabla P = \nu \nabla^2 \mathbf{u} \tag{5.1}$$

where u_x is the only non-vanishing velocity component. This allows us to write equation (5.1) as

$$\frac{1}{\rho} G_E = \nu \partial_y^2 u_x \tag{5.2}$$

where $G_E \equiv \partial_x P$ and is defined as the pressure gradient.

For Poiseuille flow there is no u_y-component of velocity and on general grounds the u_x-component of velocity varies only as a function of y. The solution :

$$u_x(y) = \frac{4\, u_x^{max}}{W^2}\,(W - y)\, y \tag{5.3}$$

where W is the width of the system (in actual units, au) and u_x^{max} is the maximum x-component of velocity is easy to obtain.

Substitution of equation (5.3) into equation (5.2) gives

$$u_x^{max} = -\left(\frac{W^2 G_E}{8\,\rho}\right)\frac{1}{\nu} \tag{5.4}$$

Therefore a plot of u_x^{max} versus $1/\nu$ results in a straight line with zero y-intercept and a slope which allows us to find the emergent pressure gradient G_E from

$$G_E = -\frac{8\,\rho}{W^2} \times \text{Gradient} \tag{5.5}$$

A series of Poiseuille flow simulations in the geometry described above, varying the viscosity ν and measuring u_x^{max} therefore allows us to measure a value of the pressure gradient G_E.

The non-slip bounding walls were implemented in our test-bench D2Q13 lLB model by applying bounce-back boundary conditions along a pre-designated *wall* layer of sites on the simulation lattice (usually $W = 0$). A constant body force of $\Delta t_\sigma e_{ix}$ (where Δ is the free forcing parameter) is applied to all bulk (non *wall*) node link distributions at each time step.

At steady state a Poiseuille profile was obtained where the maximum x-component of the velocity u_x^{max} occurs in the centre of the channel with zero velocity at the bounding walls.

Using a Chapman-Enskog expansion of the momentum evolution equation, it can be demonstrated (see appendix A) that the pressure gradient, which is constant

throughout the system, is related to the free forcing parameter Δ by

$$G_{CE} = c_s^2 \Delta. \tag{5.6}$$

The comparison between the derived pressure gradient G_{CE} in equation (5.6) and the emergent (measured) pressure gradient G_E obtained from equation (5.5) over a range of forcing values Δ should therefore be in agreement if the algorithm correctly recovers isotropic hydrodynamics.

Figure (5.2), shows a typical steady state $\langle u_x \rangle$ profile across the width of the system compared to a parabolic profile with the same $\langle u_x \rangle^{\max}$. Due to the system being translationally invariant, the x-component of velocity can be averaged down the channel to produce $\langle u_x \rangle$. The actual value of $\langle u_x \rangle^{\max}$ is dependent on the degree of forcing applied Δ and the viscosity ν of the fluid set through the simulation parameter ϕ.

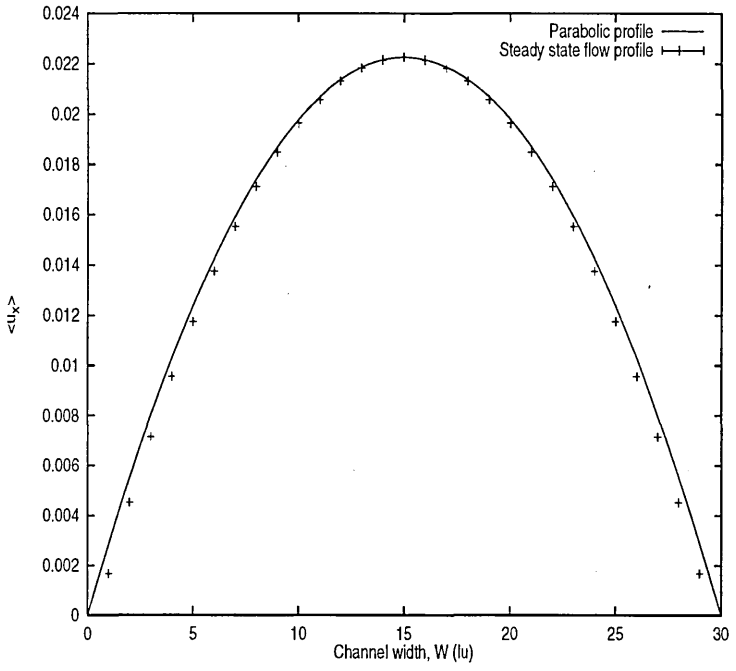

Figure 5.2: Steady state Poiseuille flow profile obtained from simulation compared to a theoretical parabolic profile with the same $\langle u_x \rangle^{\max}$.

Note that the fully developed flow profile deviates from the theoretical curve as we approach the walls of the system. This effect is due to the first order accuracy of the imposed bounce-back boundary conditions*.

*See end of chapter 3 for a general discussion on bounce-back boundary conditions.

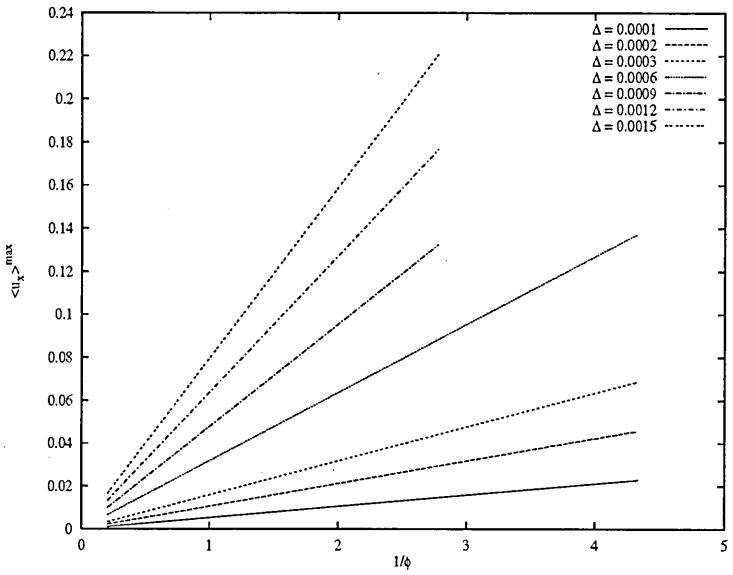

Figure 5.3: Variation of $\langle u_x \rangle^{\max}$ with simulation parameter ϕ for several values of the forcing parameter Δ. The increasing slope of the straight lines is indicative of the increase in pressure head.

Figure (5.3), show the variation of $\langle u_x \rangle^{\max}$ with $1/\phi$ for several values of forcing Δ. As predicted the variations map onto straight lines with specific gradients and a y-intercept of zero. The emergent pressure gradient G_E is extracted from the gradients of these curves using equation (5.5).

Figure (5.4), shows the final comparison between the Chapman-Enskog derived pressure gradient and the emergent pressure gradient from the simulations. As can be seen the results are in very good agreement with the expected values. This comparison not only validates the isotropic algorithm but also the forcing mechanism employed and the applied boundary conditions (which, despite their limited accuracy, seem to perform acceptably), all of which will be used in the anisotropic model.

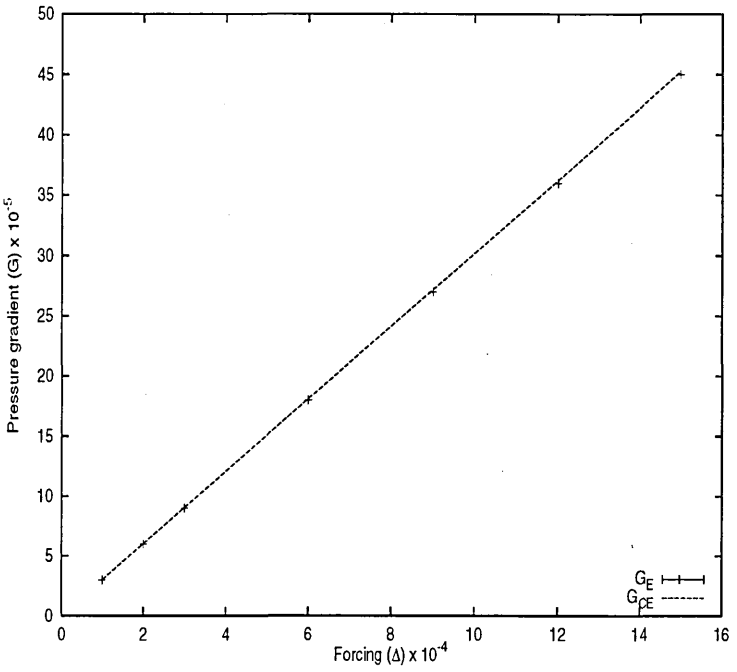

Figure 5.4: Comparison between the emergent pressure gradient G_E and the theoretical pressure gradient G_{CE} derived through the Chapman-Enskog expansion of the isotropic D2Q13 lLB evolution equation.

Note that although the results deviate from the parabolic profile as we approach a wall, the results are still in good agreement with theory because $\langle u_x \rangle^{\max}$ is used to find the pressure gradient. The maximum velocity occurs in the centre of the channel where we get a good correlation with the parabolic profile of Poiseuille flow.

Model stability can be monitored by checking the mass does not fluctuate during the simulation (i.e. there are no mass sinks or source in the simulations). The total mass of the system at each time step is calculated as

$$\mathrm{M_c}\,(t) = \sum_{\forall x,y,i} f_i \tag{5.7}$$

Throughout a typical run the variation in the system mass was of the order of 10^{-7}, indicating not only a stable simulation but that the imposed boundary and flow conditions are not adding or removing mass from the system.

We can also test the convergence of the simulation onto a steady state by calculating the residual of the velocity field. The residual is a common test of convergence in traditional CFD simulations and essentially calculates the difference in the entire velocity field between successive time steps. As the simulation reaches a stable state the residual, which is calculated from the following equation,

$$\mathcal{R}(t) = \sum_{\forall x,y} (|\mathbf{u}|_{x,y,t} - |\mathbf{u}|_{x,y,t-1}) \tag{5.8}$$

will tend to zero. Here $|\mathbf{u}|$ is the position and time dependent nodal velocity magnitude.

Figures (5.5 a) and (5.5 b) show time correlation plots of the calculated residual $\mathcal{R}(t)$ for the isotropic simulations carried out with the maximum and minimum forcing values.

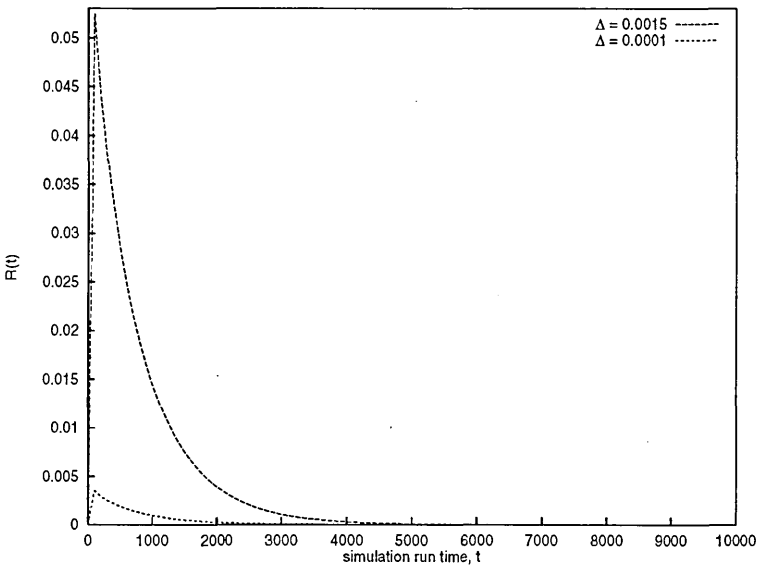

(a) Residual decays for the maximum and minimum forcing values.

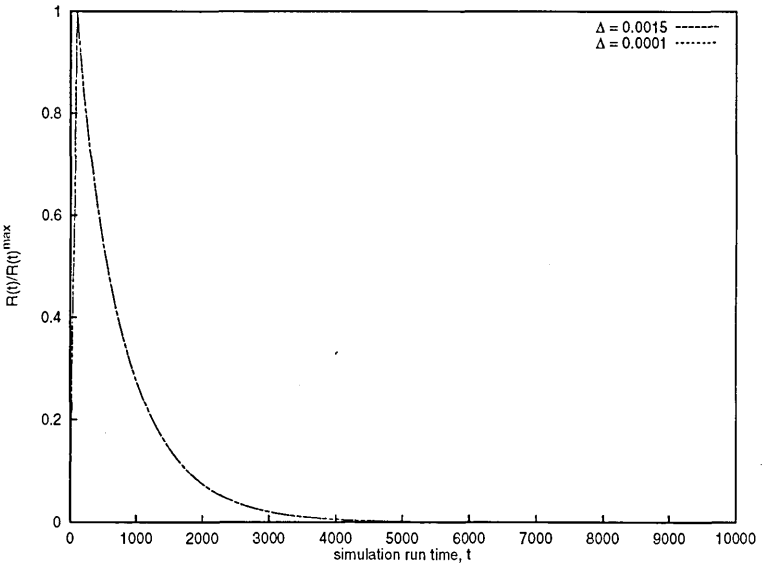

(b) Normalized residuals showing an equal decay time.

Figure 5.5: Residual decays for the maximum ($\Delta = 0.0015$) and minimum ($\Delta = 0.0001$) forcing values used in the isotropic Poiseuille (duct) flow simulations. System size was 10×30 lu's and $\phi = 1.2$.

Note the residual rapidly approaches zero and remains at zero for the remaining simulation run time, which is taken to indicate that the system has reached steady state and therefore the $\langle u_x \rangle$-component of velocity at mid-channel has attained its maximum value $\langle u_x \rangle^{\max}$.

The mass check and residual are calculated at every time step during the simulation run time and are displayed during the run. All results presented in this isotropic validation section are for simulations that remained stable during the run time. At larger values of the forcing parameter Δ the simulation becomes unstable which set an upper limit to the available forcing range and accessible Reynolds number.

5.3 Anisotropic D2Q13 lLB Scheme

In chapter 4 the extensions to an isotropic D2Q13 lLB model were introduced and discussed. To validate these extensions we examine two cases: firstly we consider the coupling between flow and director orientation by examining the response of the bulk director due to a simple laminar flow in the absence of any external fields [3]. Secondly we consider how the director orientation affects the flow properties by matching onto the Miesowicz viscosities of a nematic [3, 4, 108].

At this stage we need to specify the Leslie viscosity coefficients of the nematic we are simulating. Although there are five† Leslie viscosity coefficients $\alpha_1 ... \alpha_5$ to recover we shall currently consider only four of these. The term associated with the α_1 Leslie coefficient would require 8^{th} order isotropy of our underlying lattice and so we have chosen not to include this term in our model. Omitting this term should not seriously alter the resulting nemato-dynamics and it could, in future, be included by a suitable enhancement to the lattice structure.

From [109] we can write down the relevant Leslie viscosity coefficients for the liquid crystal N-(p-methoxybenzylidene)-p-n-butyl-aniline (usually abbreviated to MBBA) at 25°C, well within its nematic phase.

Leslie viscosity coefficients 10^{-3} poise					ELP parameters 10^{-3} poise		
α_2	α_3	α_4	α_5	α_6	γ_1	γ_2	λ
-77.5	-01.2	+83.2	+46.3	-34.4	+76.3	-78.7	+1.03146

Table 5.1: The 5 relevant Leslie viscosity coefficients for MBBA at 25°C, well within its nematic phase. Also resulting ELP parameters γ_1, γ_2 and λ.

†Actually there are six but the Parodi relationship reduces the number to five.

5.3.1 Director Alignment in Simple Laminar Flow

In validating the director evolution equation, we shall consider the case of director alignment in simple laminar flow in the absence of any external fields. As in the isotropic validation method we employ periodic boundaries in the x-direction and bounded non-slip wall conditions in the y-direction.

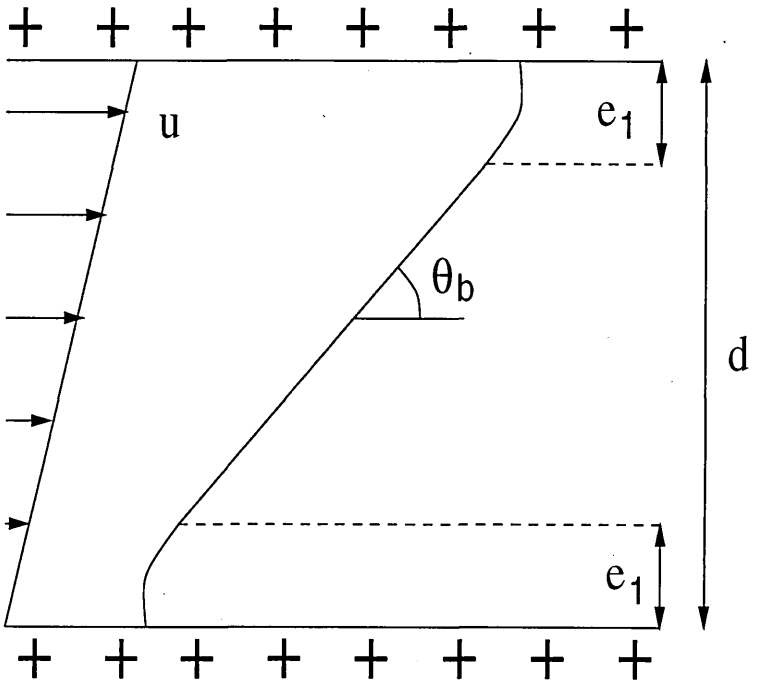

Figure 5.6: Schematic of the bulk director orientations θ_b varying across the system width d showing the boundary transition regions e_1 for a simple Couette (shear) flow of magnitude $|\mathbf{u}|$ in the absence of any applied field.

In [3], de Gennes introduces three parameters γ_1, γ_2 and λ that characterize the nematic in terms of the Leslie viscosity coefficients, thus:

$$\gamma_1 = \alpha_3 - \alpha_2 \quad , \qquad \gamma_2 = \alpha_3 + \alpha_2 \quad , \qquad \lambda = -\frac{\gamma_2}{\gamma_1} \tag{5.9}$$

For $|\lambda| > 1$ there is a certain critical angle θ_b between the bulk director orientations and the direction of the flow field for which the hydrodynamic torque vanishes. Far from the walls, the molecules will tend to lie precisely at the angle θ_b while nearer to the wall the molecules will experience a transition region e_1 between the bulk alignment and the wall alignment.

For $|\lambda| < 1$ the hydrodynamic torque is non-zero throughout the nematic and more complex (unsteady) regimes such as tumbling can be observed [110–113]. For these validation results and all subsequent anisotropic results discussed in this work we shall not enter the $|\lambda| < 1$ regimes, since for most physical nematics $|\lambda|$ is slightly larger than unity [3]. The algorithm however does have the ability to enter these regimes and this could be an interesting future area of study.

In the presence of a steady state simple laminar flow, having fixed λ, the bulk directors should align to the theoretical angle θ_b, given by

$$\theta_b = \frac{1}{2}\cos^{-1}\left(\frac{1}{\lambda}\right) \tag{5.10}$$

For $\lambda \approx 0$ the angle between the bulk director alignment and the direction of the flow field should be small $\theta_b \approx 0$. At larger λ the bulk director orientations θ_b will tend towards a maximum deviation away from the direction of flow field. [‡].

[‡] $\theta_b \to \pi/4$ due to the apolar nature of the nematic director

To implement the arrangement in figure (5.6) we employ bounce-back boundary conditions along the $W = 0$ line of sites, designating them *wall* nodes. At these *wall* nodes we overwrite at every time step the current link angle distributions $\theta_i(\mathbf{r}, t)$ with the required wall angle θ_w distributing the *wall* angle onto the links by setting $\theta_i(\mathbf{r}, t) = t_\sigma \theta_w(\mathbf{r}, t)$, mimicking strong anchoring.

In order to generate a shear flow we apply a constant body force $\Delta t_\sigma e_{ix}$ (as introduced in the last section to recover isotropic Poiseuille flow). However for shear flow we only apply the forcing along one line of sites (usually $W = \text{Width}/2$). The resulting steady state solution corresponds to two "back-to-back" translationally invariant (Couette) shear flows. The maximum x-component of velocity $\langle u_x \rangle^{max}$ appears at mid-channel whilst at the walls the fluid is at rest. The u_y-component of velocity is zero and the only non-zero velocity gradient is $\partial_y u_x$.

Selecting the physical nematic viscosity coefficients $\alpha_2 ... \alpha_5$ of MBBA shown in table (5.1) fixes γ_1 and γ_2 and therefore λ. Higher values of λ were achieved by changing α_3 whilst keeping α_2 fixed. Table (5.2) shows the change in Leslie coefficients upon altering the α_3 viscosity coefficient and keeping all other simulation parameters constant.

Leslie viscosity coefficients 10^{-3} poise					ELP parameters 10^{-3} poise			
α_2	α_3	α_4	α_5	α_6	γ_1	γ_2	λ	θ_b degs
-077.5	-001.20	083.20	+044.70	-033.99	76.30	-078.70	1.031455	06.949
-077.5	-003.37	083.20	+049.31	-031.56	74.13	-080.87	1.090909	11.778
-077.5	-004.31	083.20	+051.38	-030.43	73.19	-081.81	1.117647	13.263
-077.5	-007.05	083.20	+057.76	-026.78	70.46	-084.55	1.200000	16.779
-077.5	-010.11	083.20	+065.51	-022.10	67.39	-087.61	1.300000	19.858
-077.5	-017.88	083.20	+088.76	-006.62	59.62	-095.39	1.600000	25.659
-077.5	-025.83	083.20	+119.76	+016.45	51.67	-103.33	2.000000	30.000
-077.5	-038.75	083.20	+197.26	+081.01	38.75	-116.25	3.000000	35.264
-077.5	-046.50	083.20	+274.76	+150.76	31.00	-124.00	4.000000	37.761
-077.5	-051.67	083.20	+352.26	+223.10	25.83	-129.17	5.000000	39.232
-077.5	-058.13	083.20	+507.26	+371.64	19.36	-135.63	7.000000	40.894

Table 5.2: Leslie viscosity coefficients, fixing γ_1, γ_2, λ and θ_b for director alignment in steady state simple (Couette) shear flow in the absence of any applied field.

Figures (5.7) and (5.8) show typical steady state director and velocity profiles across the width of the system respectively. Each figure shows the steady state results for the cases when the flow field is either coupled or uncoupled from the director field. Note the velocity graph shows the two back-to-back Couette flow profiles with zero velocity at the walls and equal but opposite shear gradients. The full coupling between the director field and the flow field produces a distorted (bulged) shear profile and a slightly different bulk director field. The discontinuities in the flow field profile at the wall and centre positions are a consequence of the imposed flow and boundary conditions. However the bulk of the flow profile in figure (5.8) is that of simple shear flow.

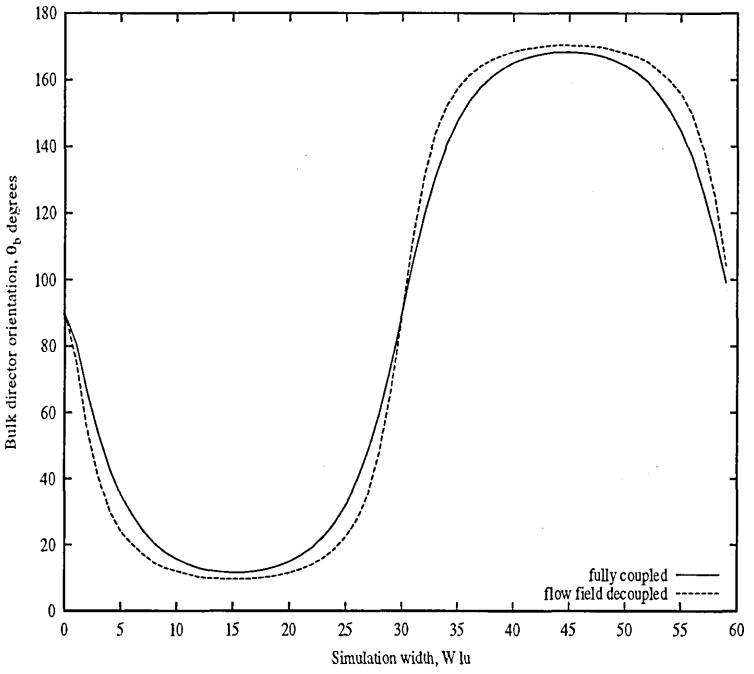

Figure 5.7: Comparison between the steady state director field for the fully coupled system and the flow field decoupled system. The director field coupling to the flow field affects the resultant flow profile which consequently re-affects the director field.

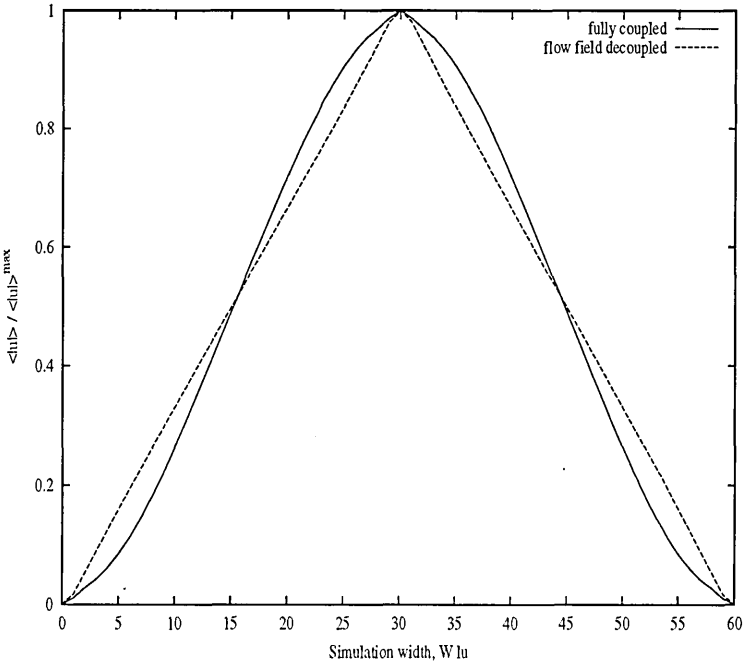

Figure 5.8: Comparison between the steady state flow field (back-to-back Couette flow) for the fully coupled system and the flow field decoupled system. The effect of the director field on the resulting flow field is to 'bulge' the flow from a straight shear profile to a curved profile.

Figure (5.9) shows a comparison plot of the theoretical curve of θ_b versus λ over the range of parameters listed in table (5.2). The free forcing parameter Δ was chosen to produce a steady state laminar shear flow below the critical shear rate for flow instability [114].

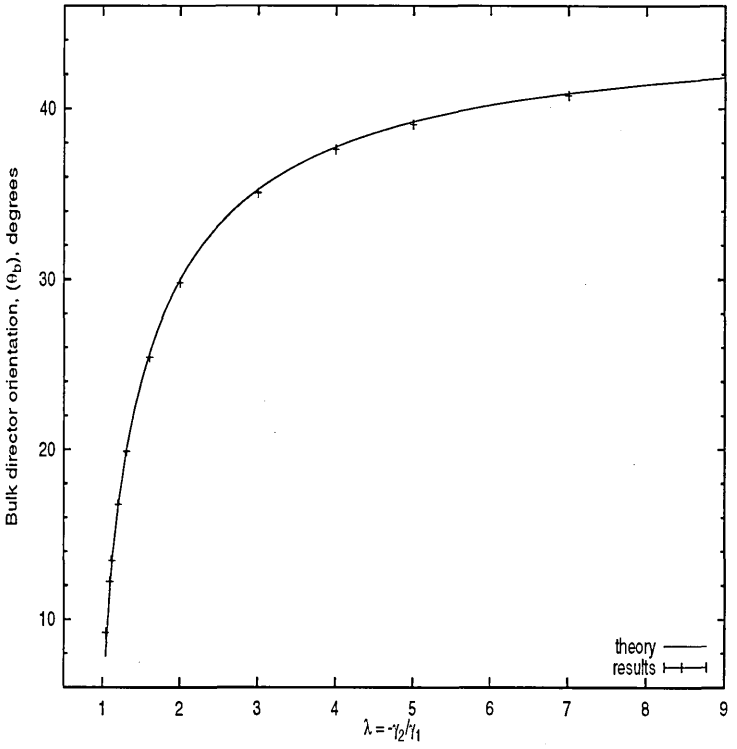

Figure 5.9: Steady state director bulk orientations θ_b versus nematic parameter λ for a strongly orientating laminar flow in the absence of any applied field. The solid line represents the theoretical curve obtained from equation (5.10). The points are the steady state results obtained from simulation.

The results presented in figure (5.9) indicate that, in the absence of an applied magnetic field, the coupling behavior between flow and director alignment is successfully recovered and that the ELP director equations of motion are correctly recovered by our model. A discussion on the absence of the transition regions e_1 in our results is presented at the end of this chapter.

5.3.2 Measuring the Miesowicz Viscosities

Finally in this section we need to validate the anisotropic extensions to the momentum evolution equation which is aimed at recovering the anisotropic Navier-Stokes equations. These extensions dictate how the changes in director orientation affect the flow properties of the nematic.

The Leslie coefficients are often determined experimentally by measuring the Miesowicz viscosities from the measurements of laminar shear flow in the presence of a strongly orientating magnetic field [3, 4, 13].

In these experiments the bulk director orientations are firmly aligned in one direction by a constant homogeneous magnetic field H. To achieve such strong alignment we need to satisfy the following conditions

1. The walls bounding the flow may impose some preferred state of alignment other than the direction of H. To avoid this we need to ensure the diameter of our simulation is much larger than the magnetic coherence length of the walls, i.e. $\xi(H) \ll d$ where

$$\xi(\mathrm{H}) = \left(\frac{K}{\chi_a}\right)^{\frac{1}{2}} \frac{1}{H} \tag{5.11}$$

   K is the nematic elastic constant (in the one constant approximation) and χ_a is the magnetic susceptibility of the nematic.

2. We saw in the previous experiment, the flow itself will tend to orientate the bulk directors. In a velocity gradient A the hydrodynamic torque γA [§] needs to be balanced by the restoring torque of the magnetic field which is $\chi_a H^2 \sin(\theta_{\text{def}})$. Therefore,

$$\theta_{\text{def}} \sim \sin^{-1}\left(\frac{\gamma A}{\chi_a H^2}\right) \tag{5.12}$$

and so ensuring that $\theta_{\text{def}} \ll 1^o$ will result in an essentially unperturbed alignment.

With the above two conditions satisfied, figure(5.10) shows three types of alignment experiments for simple laminar Couette (shear) flow. However since we are only dealing with a two dimensional system, case (a) in figure (5.10) is not possible, which leaves us with cases (b) and (c).

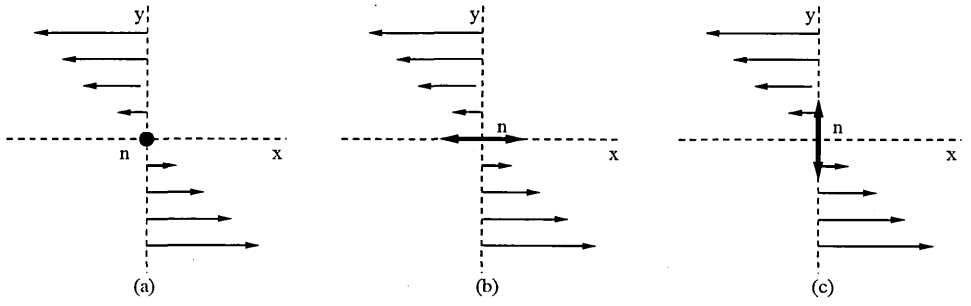

Figure 5.10: Schematic of the three fundamental geometries for viscosity measurements in a well aligned nematic. **n** is the bulk director orientation which is firmly aligned by a magnetic field. The arrows indicate the direction of the imposed shear flow profile.

[§] A is of order γA, where γ is some average of γ_1 and $\gamma 2$.

For each case an effective viscosity η_{eff} can be defined as

$$\eta_{\text{eff}} = \frac{\sigma'_{\alpha\beta}}{2A_{\alpha\beta}} \tag{5.13}$$

where $\sigma'_{\alpha\beta}$ is the viscous stress tensor given by equation (2.112) and $A_{\alpha\beta}$ is the symmetric component of the velocity gradient tensor given by equation (2.100). When applied to the three cases shown in figure (5.10), equation (5.13) yields three different effective (Miesowicz) viscosities.

$$\begin{aligned} \eta_{\text{a}} &= \eta_{\otimes} &&= \tfrac{1}{2}\alpha_4 \\ \eta_{\text{b}} &= \eta_{\parallel} &&= \tfrac{1}{2}\left(\alpha_4 + \alpha_6 + \alpha_3\right) \\ \eta_{\text{c}} &= \eta_{\perp} &&= \tfrac{1}{2}\left(\alpha_4 + \alpha_5 - \alpha_2\right) \end{aligned} \tag{5.14}$$

The Miesowicz viscosities shown in equations in (5.14) can be recast in terms of the parameters used in our anisotropic lLB model, i.e. equations (5.15)

$$\begin{aligned} \eta_{\parallel} &= \tfrac{1}{2}\left(\alpha_4 + \alpha_6 + \alpha_3\right) &&= c_s^2\rho\left(1 + \tfrac{3}{4}\left(2\delta^0 + \delta^2\right)\right)\tfrac{1}{\phi} + \left(\tfrac{\alpha_3^2}{\alpha_3 - \alpha_2} - \tfrac{1}{2}c_s^2\rho\right) \\ \eta_{\perp} &= \tfrac{1}{2}\left(\alpha_4 + \alpha_5 - \alpha_2\right) &&= c_s^2\rho\left(1 + \tfrac{3}{4}\left(2\delta^0 + \delta^2\right)\right)\tfrac{1}{\phi} + \left(\tfrac{\alpha_2^2}{\alpha_3 - \alpha_2} - \tfrac{1}{2}c_s^2\rho\right) \end{aligned} \tag{5.15}$$

where ϕ is the eigenvalue of the isotropic lLB collision matrix controlling the viscosity of the isotropic fluid and δ^0 and δ^2 are the simulation parameters used to specify the anisotropy.

From simulation, we calculate velocity gradients and hence we can find $A_{\alpha\beta}$. The viscous stress tensor $\sigma'_{\alpha\beta}$ is assumed to be linearly related to the free forcing parameter Δ and as such we can use equation (5.13) to calculate an emergent Miesowicz viscosity. On comparison, the emergent Miesowicz viscosities and the predicted Miesowicz viscosities should be in close agreement if the coupling of the director field to the hydrodynamic equations of motion is correctly recovered by our model.

The mapping will be done in two parts, firstly we shall consider the Miesowicz viscosities without any contribution from the α_2 and α_3 Leslie coefficients. In this case the two Miesowicz viscosities $\eta_{||}$ and $\eta_{\perp}$ in equation (5.14) reduce to a single anisotropic viscosity [¶] different to the isotropic viscosity but independent of the director orientation [3] (i.e. viscosity is constant under director rotation).

The second part is when we insert the α_2 and α_3 contributions: in this case we should see a difference between the $\eta_{||}$ and $\eta_{\perp}$ viscosities (i.e viscosity changes due to director rotation).

The geometrical setup is the same as for director alignment in simple laminar flow. We employ bounce-back boundary conditions at the walls for the momentum densities and align the wall director orientations to the required angle. The fluid is forced at the half width line of sites, using the body forcing already introduced in the last section, resulting in a pair of equal but opposite back-to-back Couette shear flows. We apply a homogeneous magnetic field strong enough to overcome the deformations in the director field caused by the presence of the wall alignment and the shear flow.

[¶]assuming the Parodi relationship ($\alpha_6 - \alpha_5 = \alpha_2 + \alpha_3$)

The magnetic field is applied thus :

1. The magnetic susceptibility χ_a (set to unity for simplicity).

2. The magnitude of the magnetic field, H.

3. The angle of application for the homogeneous magnetic field θ_m. [‖]

The components of the magnetic field in two dimensions are thus

$$H_x = \chi_a \mathrm{H} \cos(\theta_m) \quad , \quad H_y = \chi_a \mathrm{H} \sin(\theta_m) \tag{5.16}$$

The Miesowicz viscosities defined in equation (5.15) are inversely related to ϕ with identical gradients and non-zero y-intercepts, varying according to the α_2 and α_3 viscosity coefficients.

Without the terms in the anisotropic viscous stress tensor controlled through the α_2 and α_3 viscosity coefficients, the nematic viscosity is independent of the bulk director orientations.

We now consider the two conditions required to ensure we have an unperturbed system in which we can measure the Miesowicz viscosities.

The first condition required is that the wall orientations do not impinge upon the magnetically aligned bulk orientations. We have to make sure that the diameter of our system is much larger than the magnetic coherence length given by equation (5.11).

[‖]where 0^o is parallel to the x-plane.

It is not intended to measure the magnetic coherence length in this chapter, rather, we simply wish to ensure that the bulk director orientations which we shall use to find the Miesowicz viscosities are not adversely affected by the magnetic coherence lengths.

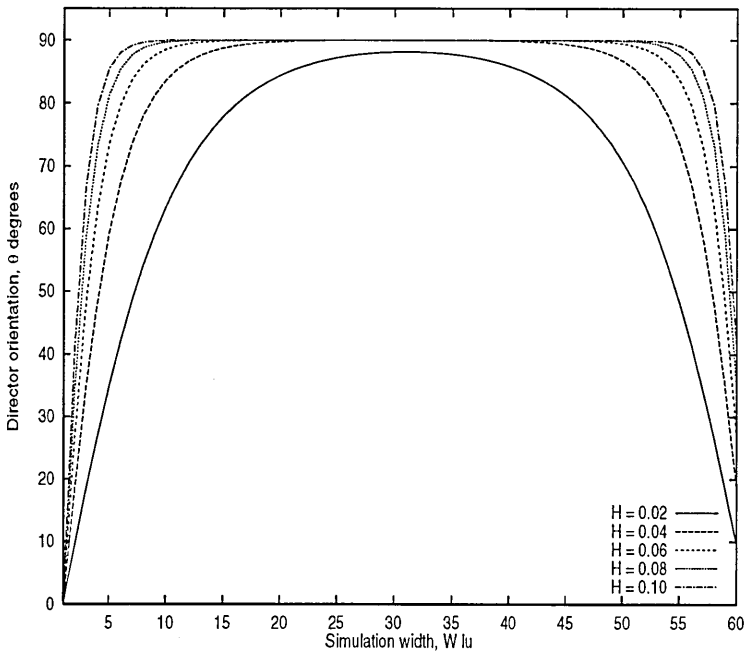

Figure 5.11: Bulk director orientations for increasing magnetic field strength for simulation of size 10×60 lu's. The wall orientations are strongly anchored parallel to the plane of the wall whilst the magnetic field application angle is normal to the plane of the wall. The bulk orientations experience a magnetic coherence layer $\xi(H)$ as they approach a wall. The relative size of the coherence length decreases with increasing magnetic field strength H.

Figure (5.11) shows the bulk director orientations for a system diameter of 10×60 lattice units for increasing values of magnetic field. We observe a magnetic coherence length whose relative size diminishes with increasing field. At higher magnetic field values we can state that the majority of the bulk director orientations are aligned to the magnetic field direction and that the coherence length is sufficiently small $\xi(H) \ll d$ so as not to affect the obtained Miesowicz viscosity. Performing the

Miesowicz viscosity simulations at these higher field values therefore satisfies the first condition.

We can however show that the coherence lengths obtained from our simulations do indeed diminish according to reciprocal field strength. If we take $\xi(H)$ as the lattice diameter position just before the bulk director orientation aligns to the imposed magnetic field direction we can compare the relationship between $\xi(H)$ and H from our simulations to the expected theory, given by equation (5.15), see figure (5.12).

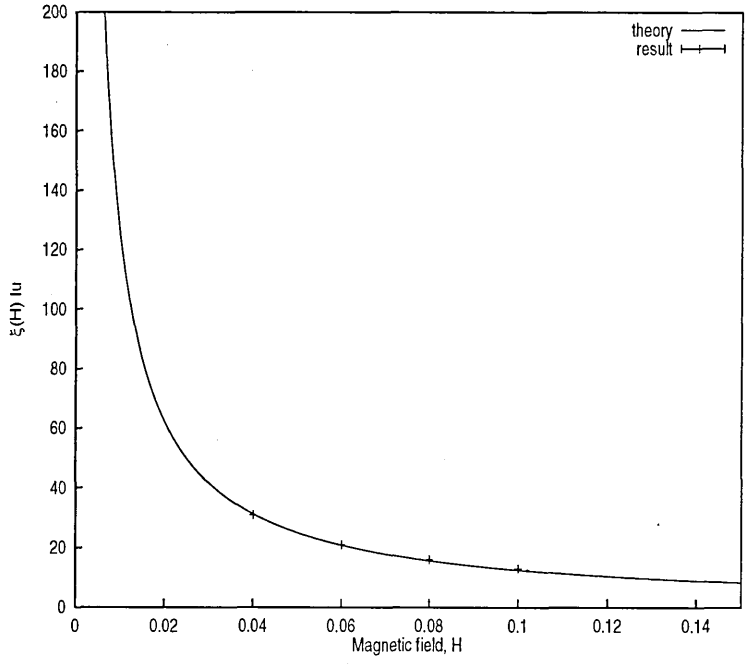

Figure 5.12: Comparison between theory and simulation results for the decrease in the magnetic coherence length $\xi(H)$ versus increasing magnetic field strength H.

We now turn to the second condition, namely, the re-orientating affects of an imposed simple laminar flow field. The results presented in figures (5.11) and (5.12) are in the absence of such a flow field. However we know from the previous section that any

imposed flow will tend to align the bulk directors to the direction of the flow field. Taking the above results as guidance we can essentially determine an upper limit to the strength of the imposed flow field. For the larger magnetic field strengths used to ensure no coherence length problems we need to select the strength of the flow field such that the bulk orientations are deformed by less than 1^o.

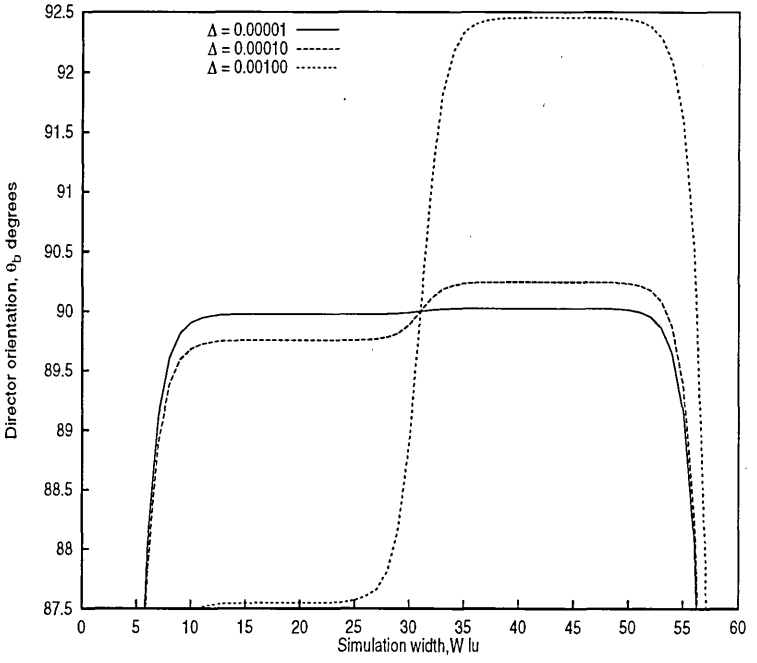

Figure 5.13: Bulk director orientation deformations due to increasing imposed flow fields for a magnetic field strength $H = 0.1$ corresponding to the small magnetic coherence length $\xi\,(0.1)$. The deformation due to the flow should be less than 1^o to satisfy the conditions required to measure the Miesowicz viscosities.

Figure (5.13) shows the deformation of the bulk director orientation due to an increasing flow field strength, for a magnetic field strength of $H = 0.1$ corresponding to the small coherence length $\xi\,(0.1)$.

The next step is to measure the effective viscosity, $\langle \eta_{\text{eff}} \rangle$ **, of the fluid. We should observe a different effective viscosity for the anisotropic fluid ($\delta^2 \neq 0$) than for the isotropic fluid. However without the α_2 and α_3 contributions the anisotropic viscosity will be invariant with respect to bulk director orientation.

Figure (5.14) depicts the change in the effective viscosity $\langle \eta_{\text{eff}} \rangle$ across the simulation channel width for the isotropic and anisotropic simulations.

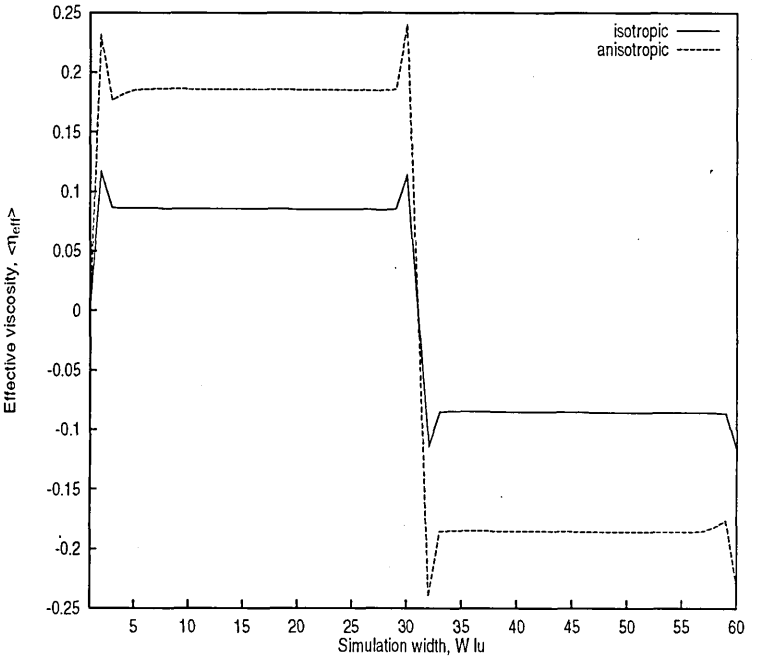

Figure 5.14: Difference in the resultant steady state effective viscosity $\langle \eta_{\text{eff}} \rangle$ between the anisotropic director orientation independent simulation and the isotropic simulation. The anisotropic simulation has a higher resultant effective viscosity than the isotropic simulation.

**Again we can take the average down the system length due to the translational invariance of the geometrical setup.

Figure (5.15) shows the resulting change in the steady state $\langle u_x \rangle$-component velocity profile for the isotropic and anisotropic simulations, due to the change in the effective viscosity.

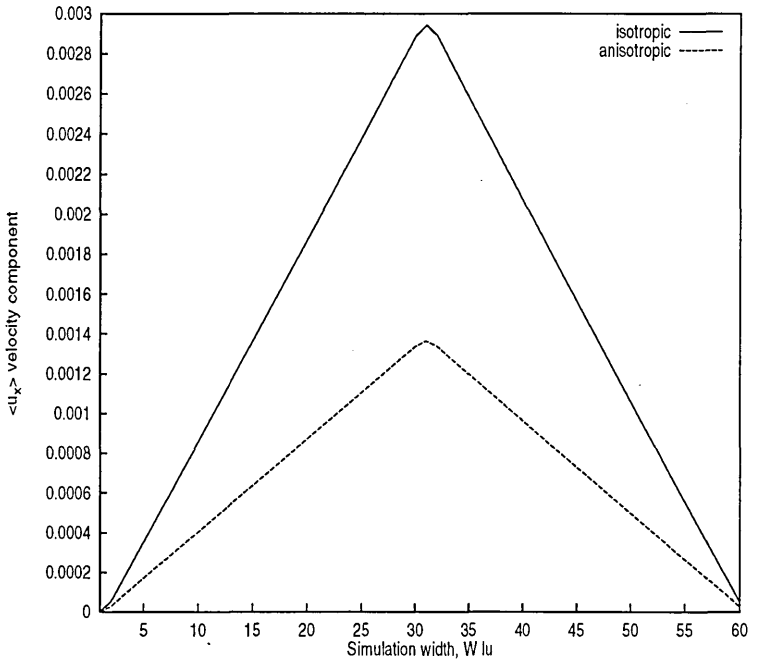

Figure 5.15: Corresponding change in the fluid flow profile between the anisotropic and isotropic simulations. Since the forcing in both simulations remained constant then the higher resultant effective viscosity of the anisotropic fluid results in a smaller steady state flow profile.

From figure (5.14) we can see that the viscosity of the anisotropic fluid is markedly greater than the isotropic fluid. This increase in the effective viscosity causes a smaller steady state flow profile, for the same forcing value as the isotropic fluid. This smaller flow profile is shown in figure (5.15).

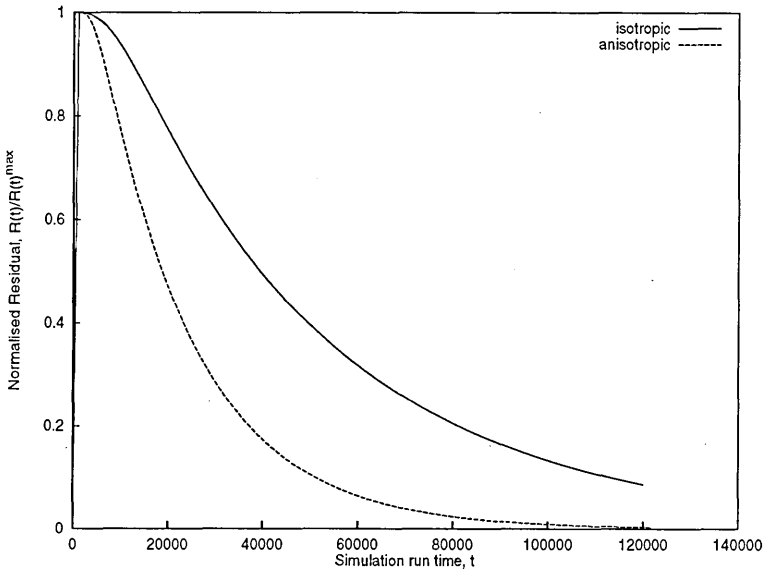

(a) Time correlation function of the normalized residual, $\mathcal{R}(t)/\mathcal{R}(t)^{\max}$ for the isotropic and anisotropic simulations. Each residual plot is normalized to their respective maximum initial residual value.

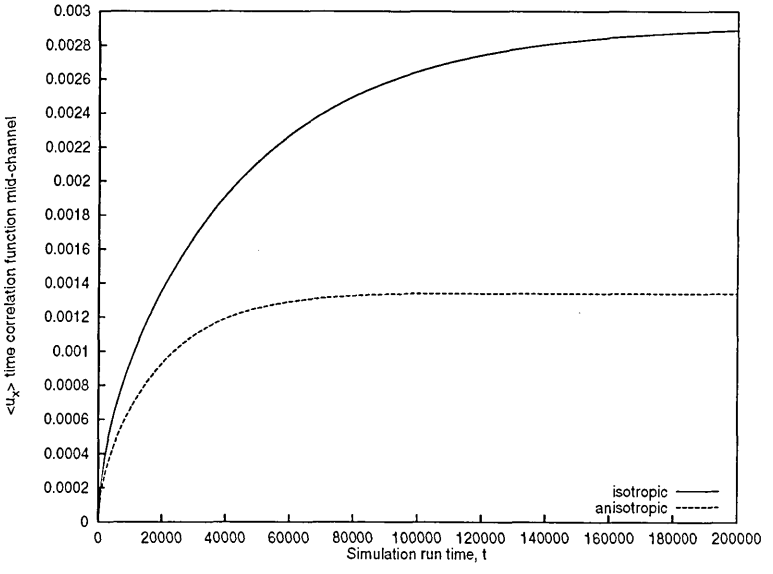

(b) Time correlation function of the mid-channel $\langle u_x \rangle$-component of velocity showing the steady state convergence of the flow profile for the isotropic and anisotropic simulations.

Figure 5.16: Isotropic and anisotropic simulation time correlation functions of the residual and mid-channel $\langle u_x \rangle$-component of velocity.

Figures (5.16 a) and (5.16 b) show the residual $\mathcal{R}(t)$ and $\langle u_x \rangle$ time correlation functions for both the isotropic and anisotropic simulations respectively. Note that in both cases the total mass of the simulation remained constant throughout, varying on the order of 10^{-7}, indicating a stable simulation. The difference in the residual profiles is due to the fact that since the anisotropic fluid is more viscous than the isotropic fluid, a smaller velocity profile is obtained which is also shown in the different velocity time correlation curves. Both the residual and time correlation function graphs indicate that the steady state solution has being reached.

Referring back to figure (5.14), we can see that the effective viscosity is constant across the width of each back-to-back flow profile. The only gradients in the effective viscosity occur near the wall and in the centre of the channel, where the back-to-back Couette flows are forced. We can therefore take the value of the effective viscosity from around the Width/4 lattice position for steady state simulations with pinned director orientation between 0^o and 180^o.

Figure (5.17) shows that without the terms associated with the α_2 and α_3, viscosities, the anisotropic effective viscosity is, as expected, independent of the director angle with a total variation of only $\approx 0.05\%$.

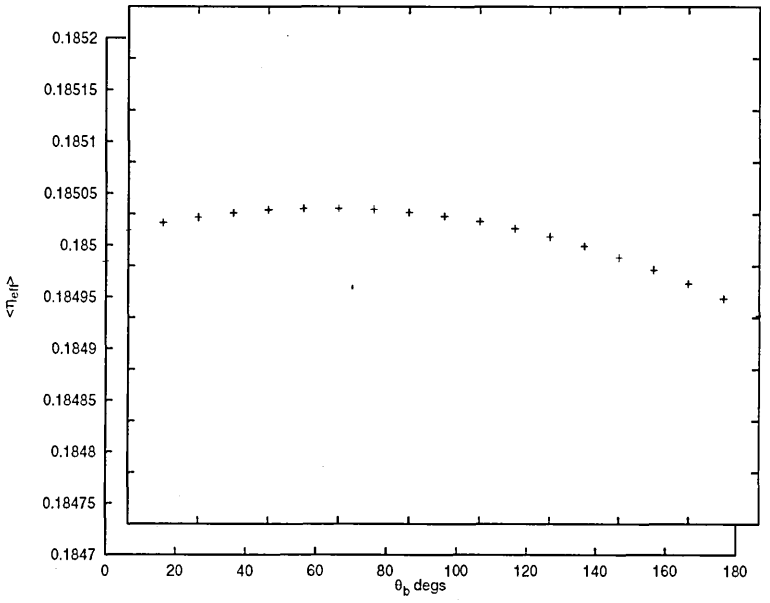

Figure 5.17: Steady state variation in the effective viscosity $\langle \eta_{\text{eff}} \rangle$ with respect to bulk director orientations θ_b for the case when the terms associated with the α_2 and α_3 Leslie coefficients are not included. The effective viscosity in this case is independent of the bulk director orientation.

Therefore the results from our simulations are in agreement with expected theory. A similar result is found for the effect of director orientation on the induced shear flow field.

Figure (5.18) shows the change in the anisotropic effective viscosity $\langle \eta_{eff} \rangle$ with the α_2 and α_3 viscosity terms included. For each simulation the bulk director orientation was pinned to a specific angle and allowed to reach steady state. The resulting effective viscosities are now angle dependent being at a maximum and symmetric about $\pi/2$.

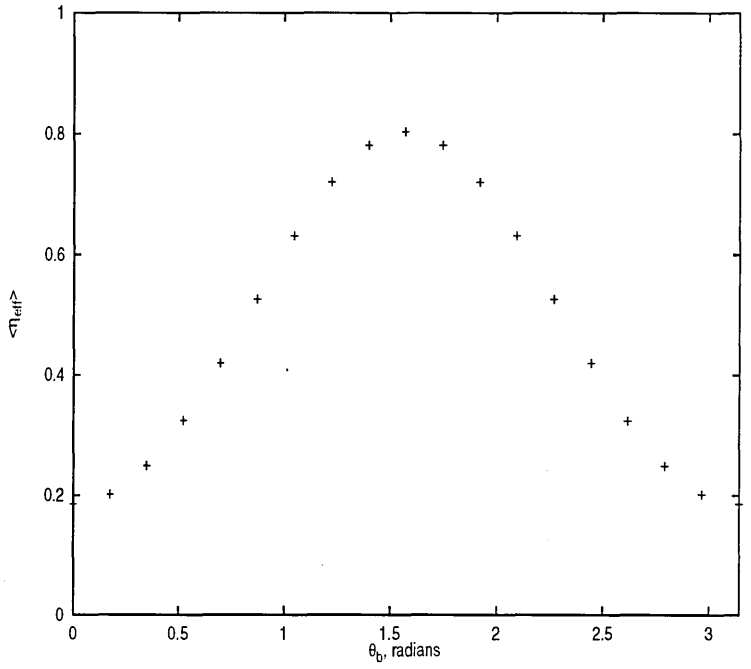

Figure 5.18: Steady state variation in the effective viscosity $\langle \eta_{\text{eff}} \rangle$ with respect to bulk director orientations θ_b for the case when the terms associated with the α_2 and α_3 Leslie coefficients are included. The effective viscosity now varies with bulk director orientation, being at a maximum and symmetric about $\pi/2$.

It is worth noting that when the pinned angle is parallel to the flow direction the resultant effective viscosity is approximately the same as the effective viscosities obtained in the angle independent case. This is due to the fact that the parallel alignment case produces the least anisotropic effect on the flow (since the torque acting on the flow due to the director orientation is at a minimum).

Figure (5.19) depicts the corresponding changes in the steady state $\langle u_x \rangle$-component of velocity.

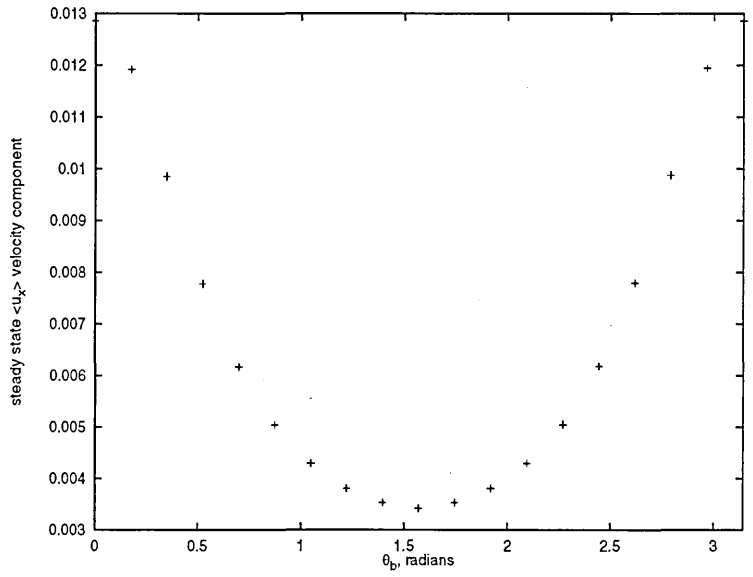

Figure 5.19: Steady state variation in the mid-channel $\langle u_x \rangle$-component of velocity, with respect to bulk director orientations θ_b for the case when the terms associated with the α_2 and α_3 Leslie coefficients are included. The velocity profile now varies according to the change in the effective viscosity of the fluid which varies with director orientation.

The fall in the resulting velocity as the angle changes from being parallel to perpendicular to the flow direction is due to the fact that, as the fluid effectively becomes more viscous and since we have constant forcing, the resultant flow profile is smaller.

Finally we shall examine the cases for the Miesowicz viscosities, namely the parallel and perpendicular bulk director alignments. Figure (5.20) shows the linear relationship between effective viscosity $\langle \eta_{\text{eff}} \rangle$ and $1/\phi$ for the two Miesowicz viscosity cases.

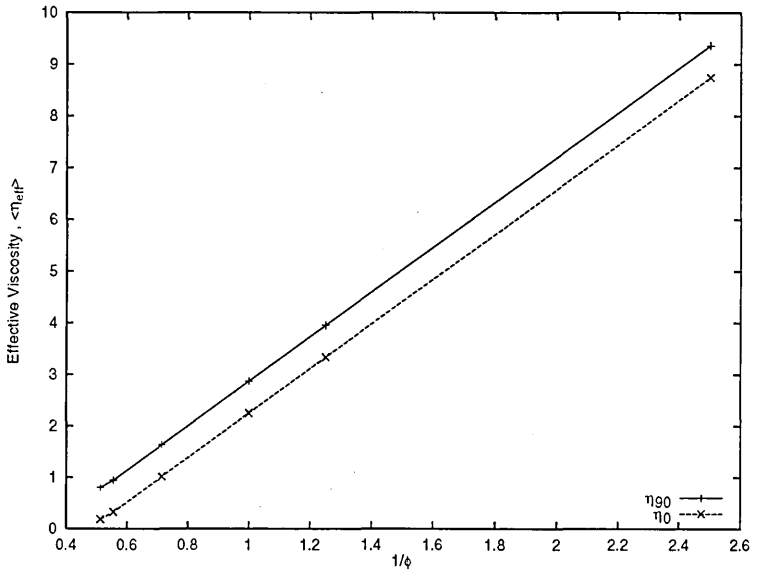

Figure 5.20: The variation in the Miesowicz viscosities with reciprocal simulation parameter ϕ. The $\eta_{||}$ and $\eta_{\perp}$ viscosities map onto straight lines showing the expected theoretical behaviour of equal gradients with different y-intercepts.

As predicted, the variations produce a pair of straight lines with equal gradients but different y-intercepts. The ratio of the gradients to the y-intercepts will be independent of any pre-multiplying constants relating the theoretical Miesowicz viscosities to the Miesowicz viscosities obtained from simulation.

Slope to y-intercept ratio	$\eta_{\|\|}$	$\eta_{\perp}$
Theory	-1.8425	-2.6005
Simulation	-1.8438	-2.6000

Table 5.3: Comparison of the predicted slope to intercept ratios and the ratios from the simulation results of the Miesowicz viscosities $\eta_{||}$ and $\eta_{\perp}$.

Moreover, the ratio of the gradients to y-intercepts for the two Miesowicz viscosities obtained from simulation compared to the predicted ratios from the Leslie viscosity coefficients for MBBA are shown in table (5.3). The agreement shows a very good

correlation (less that 0.1% error) between the predicted theory and our results.

We are thus confident that recovering the Miesowicz viscosities to such a high degree of accuracy validates the second part of our anisotropic extensions to the isotropic D2Q13 lLB model.

5.4 Discussion and Conclusions

We have developed an isotropic D2Q13 lLB model and performed a suitable validation exercise (duct flow) upon the model to ensure that the correct macroscopic fluid dynamics were recovered. During the validation the criteria for model stability and steady state convergence were introduced and shown to be satisfied by our isotropic model. From this basis we then proceeded to validate the anisotropic extensions to our model in two separate stages.

To test the director field's response to the flow field we used the fact that the bulk director orientations θ_b in a simple laminar flow in the absence of any external fields is dependent only upon a specific combination of nematic viscosities λ. Results from these simulations showed good agreement with theory over a wide range of λ's. However the theory also predicted transition regions e_1 between the bulk alignment θ_b and the strongly anchored wall alignment θ_w. In our simulations we noticed an absence of such transition regions and so a brief discussion of this fact is necessary.

The transition regions occur in the vicinity of the walls as the bulk director orientations change rapidly to orientate themselves tangential to the strongly anchored

wall orientations. In chapter 3 a general discussion on bounding lattice models is presented including the properties of the type of boundary conditions used in these simulations, i.e. first order bounce-back. Cornubert *et al* [51] showed that the "Knudsen layer" in a bounded forced fluid (the region where the flow profile changes rapidly to become zero at a non-slip wall) is not recovered accurately by the bounce-back technique. The first order constraint on the bounce-back boundary condition suppresses the Knudsen layers associated with the flow field, and since the director field transition regions e_1 can be likened to a Knudsen layer we can argue that they are also suppressed by the imposed first order boundary conditions. As support for this argument we look to Clark and Leslie [5] who discuss the presence of the *thin* boundary layers in strong anchoring and state that the director orientation changes rapidly whilst aligning to the wall orientation and so neglect transition regions in their subsequent calculations.

The second part of the anisotropic extensions was to modify the momentum density evolution equation, to recover the specific form of the anisotropic viscous stress tensor $\sigma'_{\alpha\beta}$ given by equation (2.112). The flow properties of our nematic should now be coupled to the director field and so any change in the bulk director orientations should affect the resultant flow profiles. The method employed here to validate this coupling (recovering the expected Miesowicz viscosities) showed good agreement (less than 0.1%) with the theoretical predictions.

We now confirm a model in which changes in the flow profile cause reorientation of the director field, and reorientation of the director field can induce flow. The validations prove the ability of the algorithm to map onto the steady state ELP theory to a satisfactory degree. In subsequent chapters we use the fully coupled model to examine some of the more interesting properties of nemato-dynamics.

Chapter 6

Simple Geometry Simulations

6.1 Introduction

Having, in the previous chapter, validated the algorithm with some known theoretical results we can now proceed to consider other theoretical experiments that can be performed in the simple geometrical configurations already introduced.

The main topic of the previous chapter was the anisotropic effects in steady state laminar flow. However some of the more interesting physical properties of nematics occur in transient flows where rapid director orientation can produce a velocity field which affects the director dynamics. Accordingly in the following experiments there will be no imposed flow profile and all velocity fields produced are driven by director reorientation, are transient and decay away to zero at steady state.

The first part of this chapter explores the coupling between director orientation and an imposed bulk magnetic field by considering the well known Fréedericksz transition [3,4]. Afterwards we shall use the results from our Fréedericksz transition numerical experiments to investigate the nematic effect of velocity 'back-flow' with director 'kick-back'. We shall consider the origins of back-flow and kick-back, commenting on some previous theoretical work [5, 7].

6.2 The Fréedericksz Transition

In two dimensions with the director confined to the plane we consider the experimental situation of a nematic liquid crystal, bounded in the y-direction by non-slip walls and periodic in the x-direction. Assuming strong uniform anchoring at the bounding walls, then at steady state the bulk director orientations will be aligned tangential to the wall director orientations, in the absence of any induced flow or applied field.

Figures (6.1 a) and (6.1 b) show schematic diagrams of steady state aligned bulk director orientations for the cases of parallel and perpendicular wall alignments respectively.

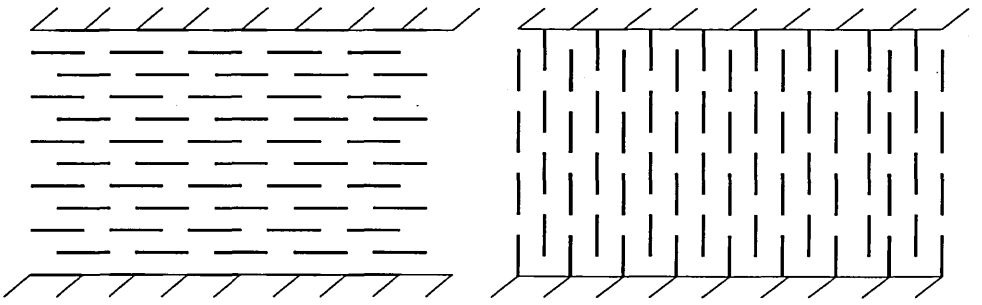

(a) Parallel wall alignment. (b) Perpendicular wall alignment.

Figure 6.1: Schematic of a wall aligned bulk nematic at steady state in the absence of any external fields.

If a magnetic field H is applied normal to the wall alignments in figures (6.1 a) and (6.1 b), an induced magnetic torque is experienced by the bulk directors of the form

$$\Gamma_M = \chi_a \left(\mathbf{n} \cdot \mathbf{H}\right) \mathbf{n} \times \mathbf{H} \tag{6.1}$$

which vanishes in an unperturbed configuration ($\mathbf{n} \cdot \mathbf{H} = 0$).

At large H values the bulk orientations will be aligned in the direction of the magnetic field except for two thin transition regions, ξ (H), near the walls [3]. In chapter 5 we discussed the appearance of these magnetic coherence lengths for an imposed magnetic field as a bounding wall is approached. At low field strengths the coherence length will extend further into the bulk and in the extreme case of the coherence lengths covering the width of the system then the bulk will all be aligned to the wall orientation.

We can therefore define a critical field strength H_c for which the centre of the bulk first begins to align to the direction of the applied field, away from the imposed wall orientation. Around this critical field value there will be a phase transition between the unperturbed configurations shown in figures (6.1 a) and (6.1 b) to the distorted configurations shown in figures (6.2 a) and(6.2 b).

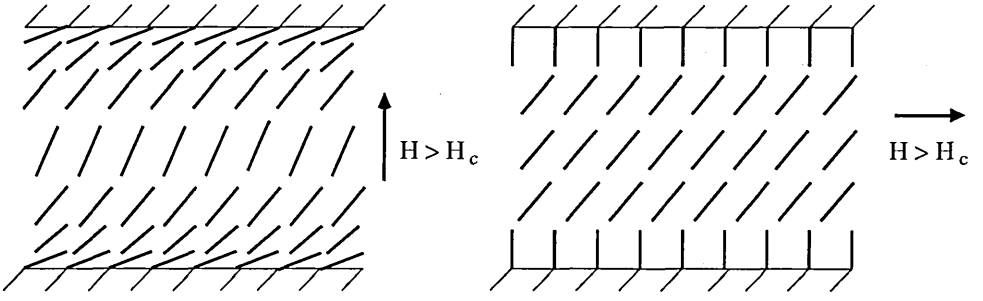

(a) Perpendicular applied magnetic field. (b) Parallel applied magnetic field.

Figure 6.2: Schematic of the steady state bulk aligned nematic in the presence of a strongly orientating magnetic field $H \gg H_c$ applied normal to the easy axis of the wall.

The critical magnetic field strength H_c in the one constant approximation is [3, 4],

$$H_c = \frac{\pi}{d}\left(\frac{K}{\chi_a}\right)^{\frac{1}{2}} \tag{6.2}$$

and so the product of H_c and d is a constant dependent on the elasticity K and the magnetic susceptibility χ_a of the nematic.

This phase transition is named after V.Fréedericksz who first observed it optically in 1927 [115]. The transition is *second* order (i.e. distortions around the threshold are small) and can be calculated using an elliptic integral [116, 117].

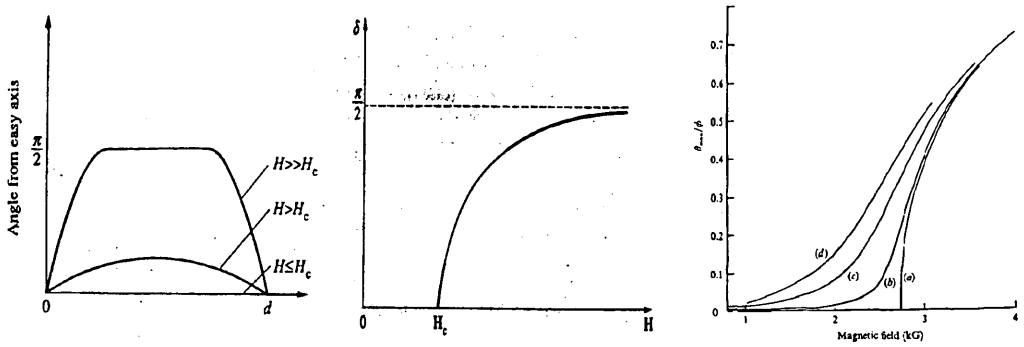

(a) Bulk director orientational changes through the Fréedericksz transition.

(b) Qualitative second order Fréedericksz transition curve showing the rotation away from the imposed wall angle for magnetic fields exceeding the critical field H_c.

(c) Relaxation away from the theoretical curve for applied fields angles of (a) 90° (b) 89° (c) 85° and (d) 80°.

Figure 6.3: Schematic representations of the properties of the nematic Fréedericksz transition. (a) and (c) are from [4] and (b) is from [3].

Figure (6.3 a) shows a schematic diagram of the changes in the director orientation across the width of the system at critical and sub-critical magnetic field values. Figure (6.3 b) is the theoretical plot of a second order Fréedericksz transition : where the y-axis corresponds to the director orientation in the centre line of the system relative to the wall director orientation. The x-axis represents increasing magnetic field intensity and the point where the curve cuts the x-axis is defined as the critical magnetic field H_c. Finally figure (6.3 c) from [4] shows qualitatively the relaxation of the Fréedericksz transition as the applied magnetic field is tilted away from the normal towards the wall alignment angle.

6.2.1 LBE simulation of the Fréedericksz transition

To simulate the Fréedericksz transition using our anisotropic lLB scheme we model the simple geometrical setup shown in figure (6.1 a). We bound the nematic in the y-direction with bounce-back wall conditions on the link density distributions [85] and apply periodic boundaries in the x-direction to produce an infinite length. We fix the director orientations at the walls to a parallel alignment* by distributing (overwriting) the wall angle θ_w over the wall link directions using $\theta_i = t_\sigma \theta_w$ at every time step thus mimicking strong anchoring at the horizontal wall.

The following simulation results were obtained for a lattice 5 lu's in length and a width ranging from 5 to 60 lu's. The Leslie coefficients used were those in table (5.1) relating to MBBA and the magnetic susceptibility of the nematic χ_a was set to unity for simplicity. The value of the single elastic constant K was set according to a relaxation parameter of $\bar{\omega} = 1.8$.

We impose no flow profile and align all the bulk directors to a specified initial orientation. Care has to be taken when selecting the applied magnetic, wall, and bulk angles to ensure that a bias is given to the Fréedericksz transition. The reason for biasing the initial director configuration is to ensure that no nematic domains separated by disclination walls terminating in $\pm 1/2$ defects [118] are formed during the simulation. Such defect induced domains and disclination walls are discussed elsewhere (chapter 7) since, here we want to concentrate solely on the Fréedericksz transition and do not wish to enter into these issues.

*The actual wall alignment is slightly biased to ensure a clean transition.

To prevent the formation of domains we slightly bias the alignment of the wall and magnetic field so that a single domain is preferred in the bulk. Note, however, that we have observed in our simulations, when no such biasing was employed, domain formation which would clearly provide interesting material for future work.

Having selected an initial configuration we gradually increase the strength of the applied magnetic field from well below the critical value, through the transition and up to a value well above the transition value. Between each field strength increment we allow sufficient relaxation time for the bulk orientations to reach the steady state configuration. In this kind of experiment, with small applied field strength increments and long intermediate relaxation times, one expects induced velocity fields to be extremely small and to decay away quickly to zero.

Figure (6.4 a) shows the length averaged bulk director orientations $\sin^2\langle\theta_b\rangle$ across the channel width for a simulation with a relatively large diameter. Notice the emergence of a *plateau* of director orientations at magnetic field values well above the critical magnetic field value $H \gg H_c$ corresponding to the direction of the applied field and the emergence of the coherence lengths ξ (H) as the director orientation changes in the approach to a wall. Figure (6.4 b) shows the coherence lengths ξ (H) diminishing with increasing magnetic field strength. Ultimately at very large magnetic field values $H \to \infty$ the magnetic coherence length will tend to zero. Figure (6.4 c) shows the length averaged bulk director orientations $\sin^2\langle\theta_b\rangle$ across the channel width for a system with a small diameter (5 lu's): even at large field strengths the size of the *plateau* is relatively small.

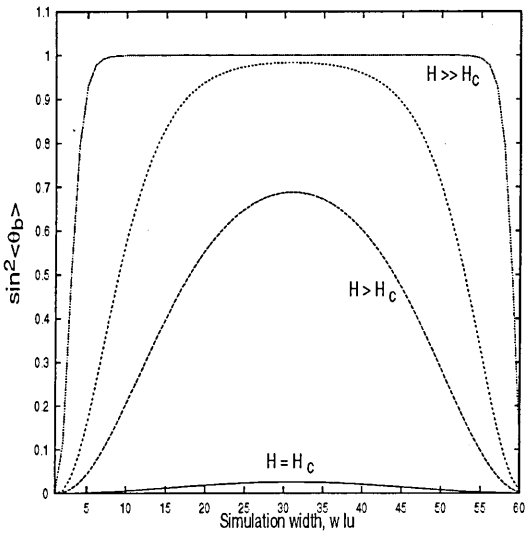

(a) Length averaged bulk director orientations $\sin^2\langle\theta_b\rangle$ across the system width for magnetic field strengths increasing from $H = H_c$ through to $H \gg H_c$.

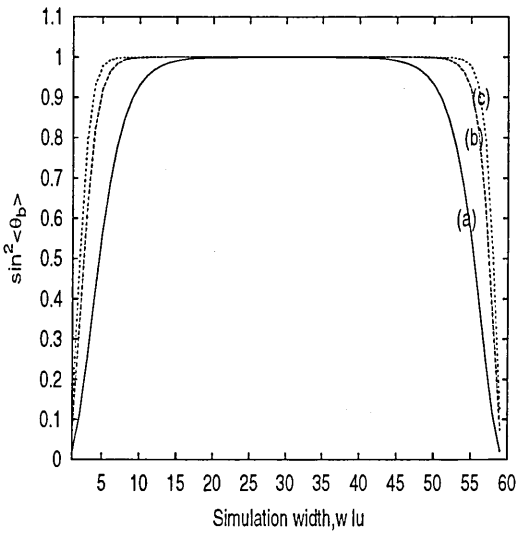

(b) Final steady state length averaged bulk director orientations $\sin^2\langle\theta_b\rangle$ across the system width for magnetic field strengths (a) $2.5H_c$ (b) $4.5H_c$ and (c) $6H_c$, showing the reduction of the magnetic coherence length $\xi(H)$.

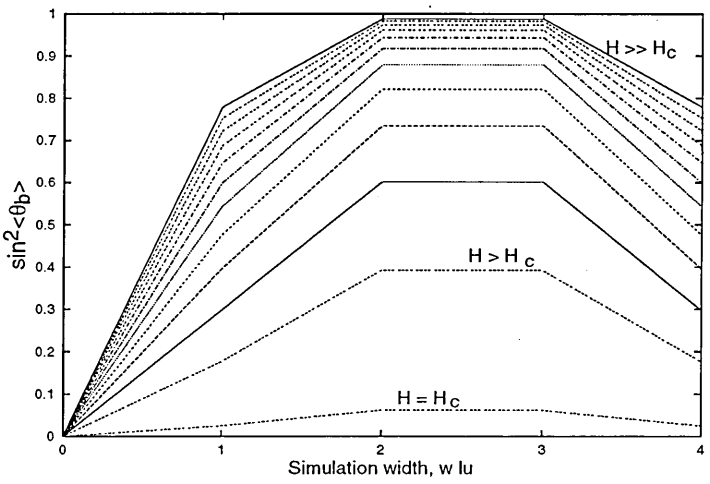

(c) Final steady state bulk director orientations $\sin^2\langle\theta_b\rangle$ across a small system width (5 lu's) showing coherence layer $\xi(H)$ effects on the field induced *plateau*, the magnetic field strength is shown increasing from $H = H_c$ through to $H \gg H_c$.

Figure 6.4: Simulation results for the length averaged bulk director angle response to an increasing magnetic field strength. Results were obtained for a lattice 5 lu's in length and a width of 60 lu's in (a) and (b) and 5 lu's in (c). Leslie coefficients are for MBBA in table (5.1) χ_a, was set to unity and K was set according to a relaxation parameter $\bar{\omega} = 1.8$.

Using equation (6.2) allows us to calculate the values of the critical field strength H_c in our simulations at various system diameters d. Table (6.1) shows the expected critical magnetic field strength for several system diameters ranging from 5 to 60 lattice units. The value of the diameter d used in the calculation is for actual units (au) and so the lattice diameters need to be converted [†].

System diameter		Critical Field
d (lu)	d (au)	H_c
5	4.33012	0.07843
10	8.66025	0.03921
15	12.99038	0.02614
20	17.32051	0.01961
30	25.98076	0.01307
40	34.64102	0.00980
50	43.30127	0.00784
60	51.96152	0.00654

Table 6.1: Critical magnetic field H_c values for increasing system diameters of a nematic with unity magnetic susceptibility χ_a and the single elastic constant K set through the simulation parameter $\tilde{\omega} = 1.8$.

We can now plot the theoretical second order Fréedericksz transitions, as shown in figure (6.3 b), for the various system diameters and compare them to the simulation transitions obtained at the central line of the system $\sin^2 \langle \theta_m \rangle$

[†]See chapter 3 for a discussion on the difference between lu and au system dimensions.

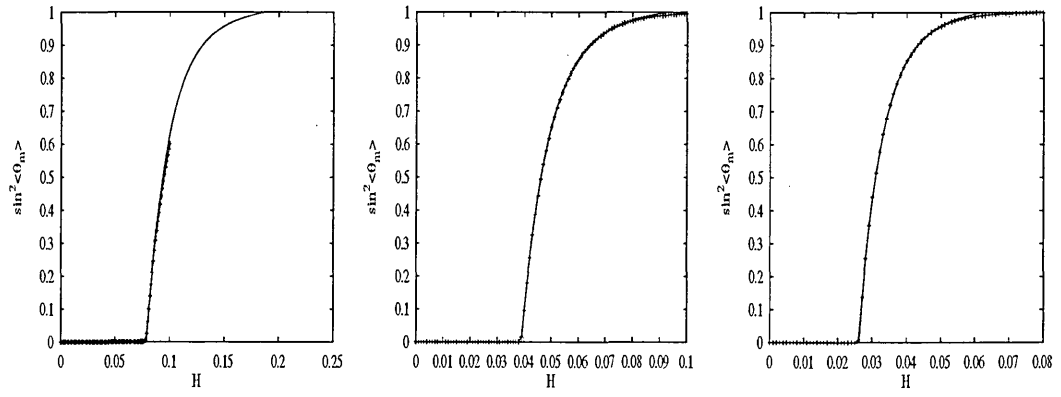

(a) Simulation width, 5 lu. (b) Simulation width, 10 lu. (c) Simulation width, 15 lu.

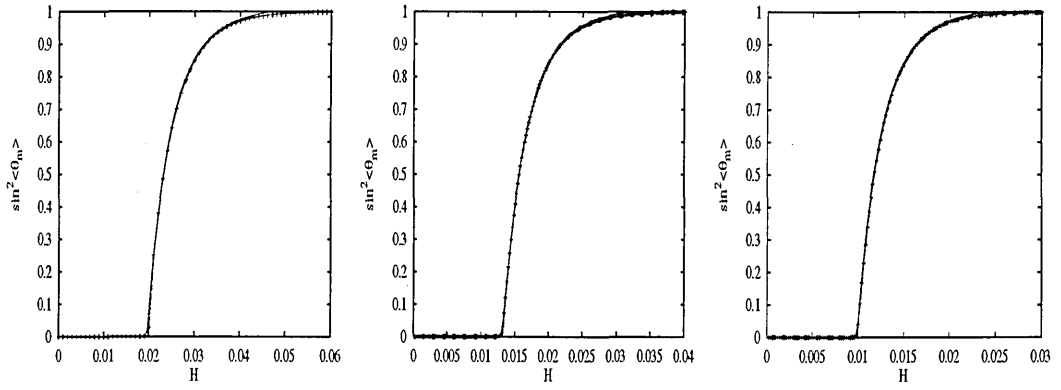

(d) Simulation width, 20 lu. (e) Simulation width, 30 lu. (f) Simulation width, 40 lu.

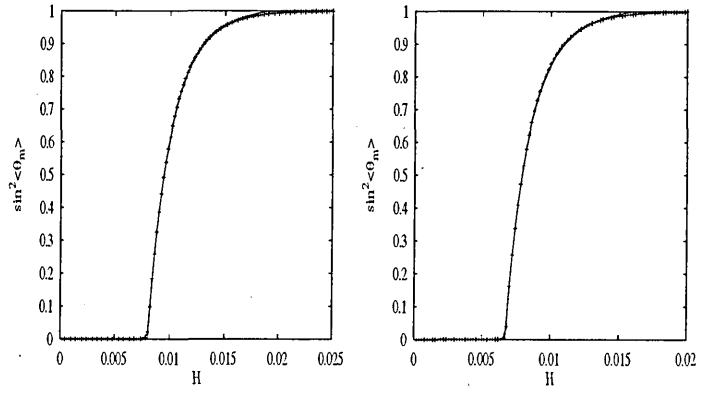

(g) Simulation width, 50 lu. (h) Simulation width, 60 lu.

Figure 6.5: Simulation Fréedericksz transition results (crosses) mapped onto the expected theoretical transition curves (solid lines) using the critical field values obtained in table (6.1), for system diameters between 5 and 60 lattice units. Results obtained are from the central line of the system $\sin^2 \langle \theta_m \rangle$.

Figures (6.5 a - h) show the comparisons between the Fréedericksz transitions obtained from simulation and the theoretical curves, for several simulation diameters. We can see that we get very good agreement between simulation and theory. Accordingly we are re-assured that the transitions observed in our lLB simulations scale with system diameter according to equation (6.2).

For small system diameters our results begin to depart from the theoretical curve. This departure is due to the fact that at these small diameters the centre of the channel is very close to the wall and so is affected by the magnetic coherence lengths. This means that, although at large magnetic fields $H \gg H_c$, the central angle $\sin^2 \langle \theta_m \rangle$ will align to the applied field direction but the *strongly anchored* wall will exert a competing influence and affect the phase transition.

Clearly, to examine the Fréedericksz transition in this "wall-influenced" regime would necessarily involve some modification of the wall alignment to allow for competition between the influence of the wall and the applied field. Indeed the Fréedericksz transition could be utilized to calibrate some lattice closure rule which is "softened" by an applied field.

Having obtained what appears to be a second order Fréedericksz transition for *increasing* magnetic field strength, we check that our system exhibits no hysteresis, the presence of which would undermine the conclusion that our observed Fréedericksz transition is second order.

However we must be careful in applying such classifications of thermodynamics, and emphasize that the underlying lLB simulation is isothermal. Perhaps more important, the lLB method in general has no proven H-theorem. So we use the term "second order" in the widest sense for the remainder of this section. However the nematic's elasticity is incorporated, so it is reasonable to consider the extent to which our lLB model captures the energetically stable state

Once we had obtained fully equilibrated director fields for $H \gg H_c$ shown in figures (6.5 a - h), we commenced decreasing the magnetic field by small amounts, again ensuring a fully equilibrated state between successive decrements. If no hysteresis is present, then the reverse phase transition should follow the same curve as the forward Fréedericksz phase transition observed above. Figures (6.6 a - h) show the decremented magnetic field simulation results against theoretical curves, for the same system diameters as before. The results appear to be free of hysteresis.

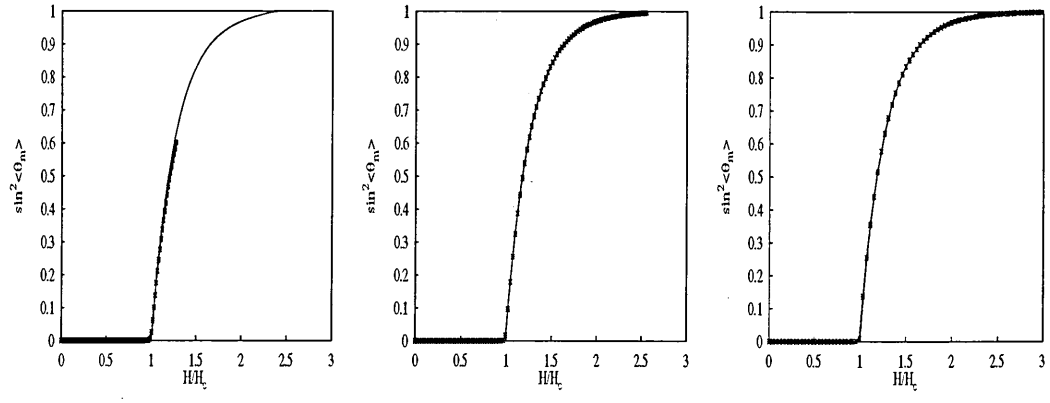

(a) Simulation width, 5 lu. (b) Simulation width, 10 lu. (c) Simulation width, 15 lu.

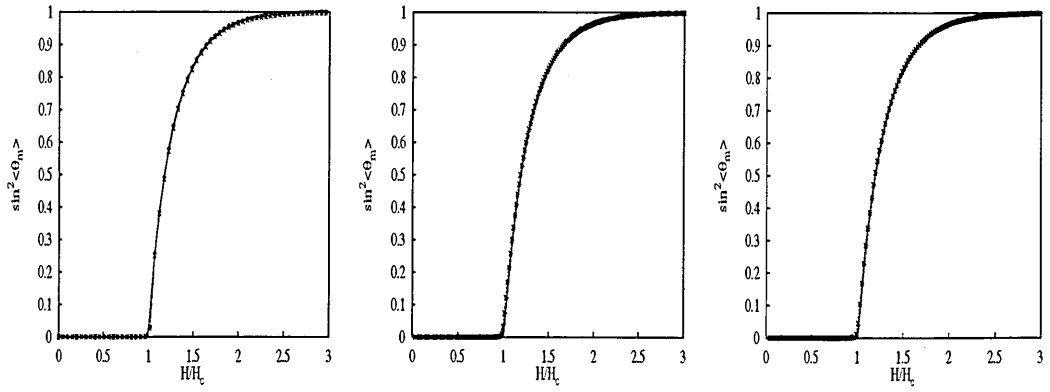

(d) Simulation width, 20 lu. (e) Simulation width, 30 lu. (f) Simulation width, 40 lu.

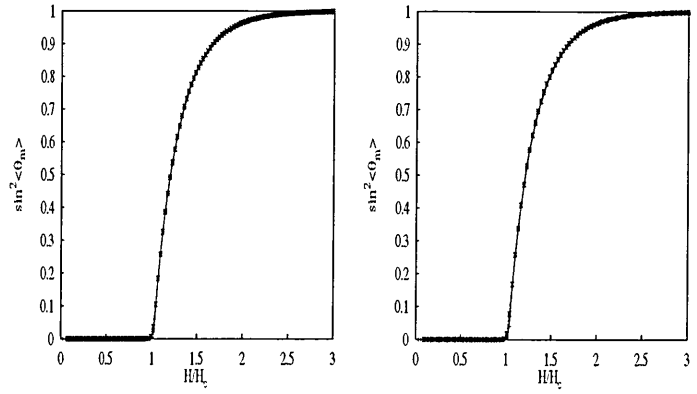

(g) Simulation width, 50 lu. (h) Simulation width, 60 lu.

Figure 6.6: Simulation results of forward and reverse phase transitions to check for hysteresis. Results (crosses) are for system diameters between 5 and 60 lattice units where again the transitions were taken from the central line of the system $\sin^2 \langle \theta_m \rangle$.

6.2.2 Discussion

From the simulations reported here we note that the observed transition was very sensitive to certain simulation parameters. Careful simulation is essential if one is to observe a hysteresis free second order Fréedericksz transition, or to obtain agreement with the theoretical critical magnetic field value.

Key considerations were found to be:

1. The exact position of the wall in lLB models employing bounce-back lattice closure is unknown, being off-lattice, (this velocity boundary method is only first-order accurate [85]). Since H_c depends on the diameter d and we have a small uncertainty in our wall placement, then the actual value of H_c cannot be determined exactly by our model. Nevertheless fitting the theoretical curve to the simulation transition gives the accepted value of H_c. This method of determining the critical field from curve fitting to a theoretical Fréedericksz transition has been used before in MC simulations [117].

2. The transition observed from our simulation is dependent on two effects (applied field and wall alignment) which operate on different time scales. The magnetic field is applied homogeneously and instantaneously throughout the system and so induces a fast response in the director field. The orientating effects of the wall alignment must propagate through the system - and so take longer to affect the bulk (depending on the system diameter). A sufficient time interval (equilibration time) between field strength increments was found to

be a crucial factor in controlling the observed hysteresis.

3. Similarly, if the size of the field strength increment was too large one might fail to obtain a second order transition. As the system diameter increased, and the resulting critical field value decreased, we needed to ensure that the step increase was small enough to capture the true nature of the transition.

4. Finally system diameter size is important. At very small diameters the coherence lengths adversely affected the transition.

Having by inspection resolved the above four issues, we can be confident that the transitions we obtain from our simulations, shown in figures (6.5 a - h), are a good representation of a second order Fréedericksz transition.

Finally in this section we consider the relaxation of our second order Fréedericksz transitions as the angle of the applied magnetic field is tilted away from the normal towards the easy angle of the bounding walls. The plots shown in figures (6.7 a - h) are normalized to their respective critical field value H_c calculated in table (6.1). Comparison of the simulation results to the plot shown in figure (6.3 c) indicates good qualitative agreement.

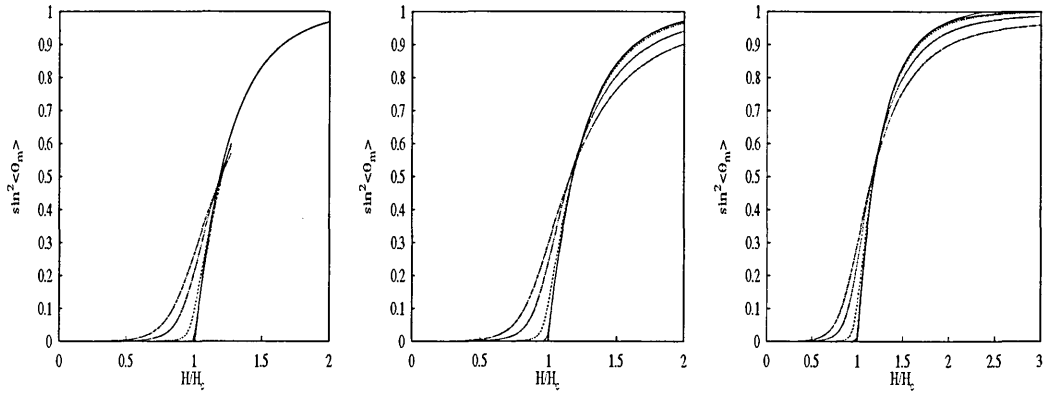

(a) Simulation width, 5 lu. (b) Simulation width, 10 lu. (c) Simulation width, 15 lu.

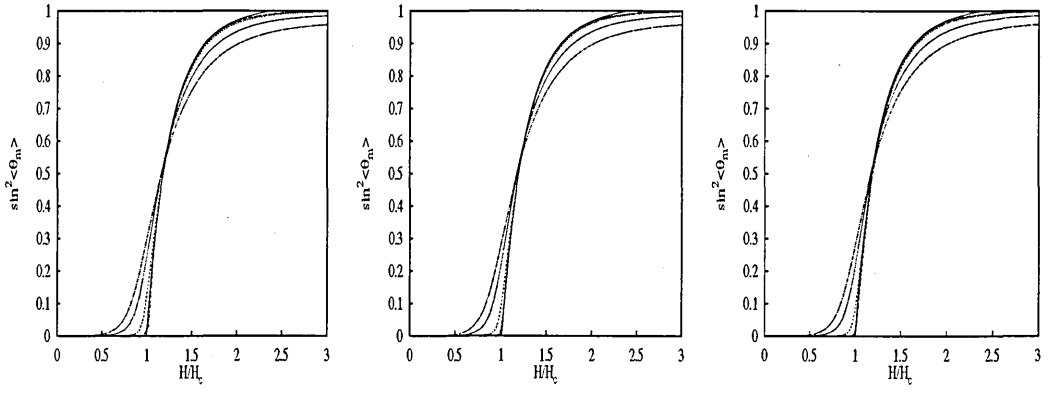

(d) Simulation width, 20 lu. (e) Simulation width, 30 lu. (f) Simulation width, 40 lu.

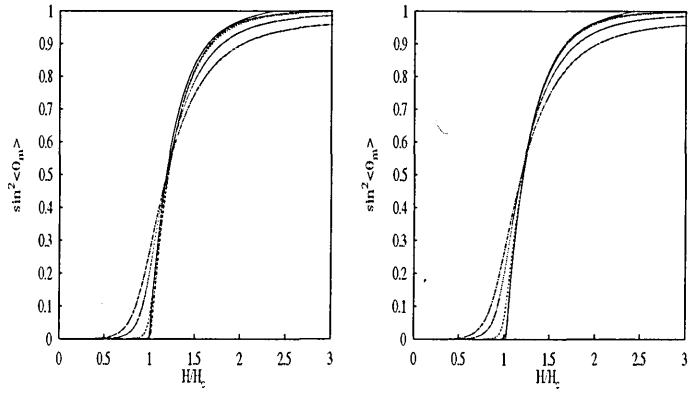

(g) Simulation width, 50 lu. (h) Simulation width, 60 lu.

Figure 6.7: Simulation results of the relaxation away from the theoretical Fréedericksz transition for applied field angles of 90°, 89°, 85° and 80°. For each result the plots have being normalized to their respective critical field strength H_c. The bulk angle was averaged down the central line of the system $\sin^2 \langle \theta_m \rangle$.

6.3 Velocity Back-flow with Director Kick-Back

In the last section we established that our lattice nematic reproduces a second order Fréedericksz phase transition above a specific critical applied magnetic field H_c. We shall now consider what happens when an aligned nematic is released from a strongly orientating magnetic field.

In the limit of infinite applied magnetic field strength $H \rightarrow \infty$ we obtain an idealized aligned nematic with a magnetic coherence length ξ(H) of zero. For the case of parallel wall alignment and perpendicular applied field angle we get the *pinned* system shown in figure(6.8).

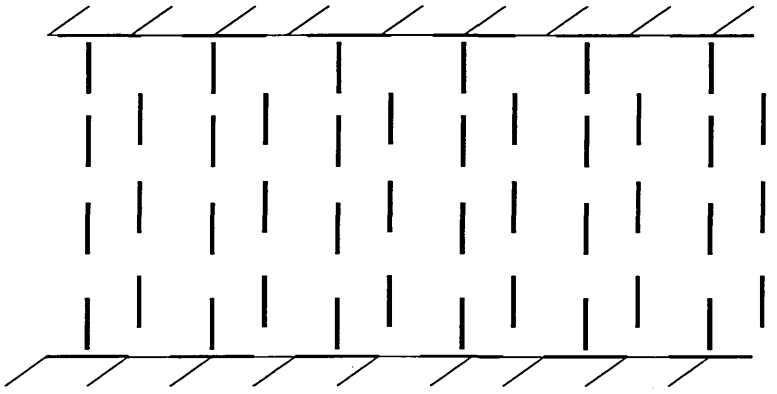

Figure 6.8: Schematic of the geometrical setup of the *ideal* starting configuration used to simulate velocity back-flow with director kick-back.

Upon release of such a system from the imposing field, the nematic fluid orientations near the walls are going to change rapidly inducing a so called back-flow in the velocity field which propagates into the bulk. This back-flow subsequently couples into the bulk director orientations in the bulk, causing kick-back. The initial back-

flow rapidly dies away and as the bounding walls re-impose their orientation on the bulk directors a smaller forward-flow velocity field is induced decaying away on a much longer time scale than the back-flow.

Clark and Leslie [5], performed an approximate analysis of the ELP continuum equations for nemato-dynamics and solutions are presented in the form of an infinite series [5]. Results of the observed kick-back and back-flow are reproduced here in figures (6.9 a) and (6.9 b) respectively and compared well to existing numerical integration results by Van-Doorn [7].

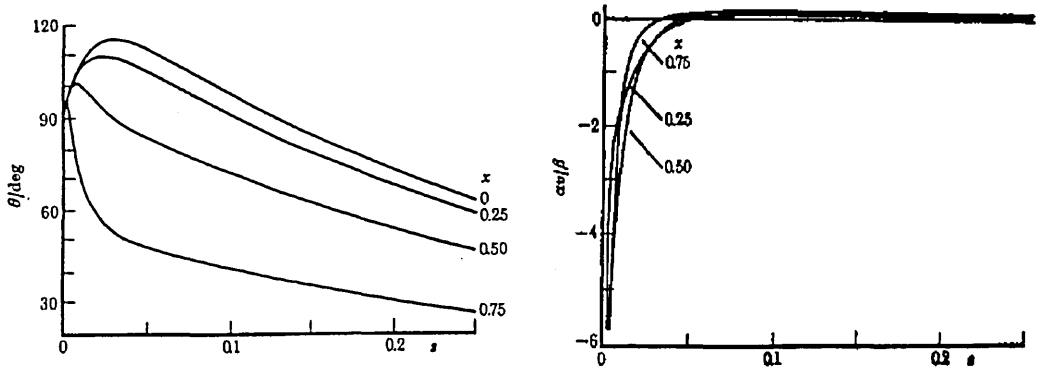

(a) Director tilt angle as a function of reduced time at four positions across the half width, (0) is the centre (1) is the wall.

(b) Reduced velocity as a function of reduced time at four positions across the half width, (0) is the centre (1) is the wall.

Figure 6.9: Director and flow reduced time correlation functions at various position across half the system diameter, from Clark *et al* [5].

However in the cases considered by Clark and Leslie, the initial director configuration contained zero magnetic coherence lengths, corresponding to an infinite applied field strength.

6.3.1 Implementation of Back-Flow/Kick-Back Simulations

We can initialize our simulation with the ideal starting director orientation configuration assumed by Clark and Leslie [5] and observe the resulting back-flow and kick-back upon release of the aligning field. Boundaries are implemented after the manner discussed in the previous sections. The system size was 10×60 lu's and the nematic parameters are those of MBBA from table (5.1), the elasticity of the nematic was set using $\bar{\omega} = 1.8$ with the susceptibility again set to unity.

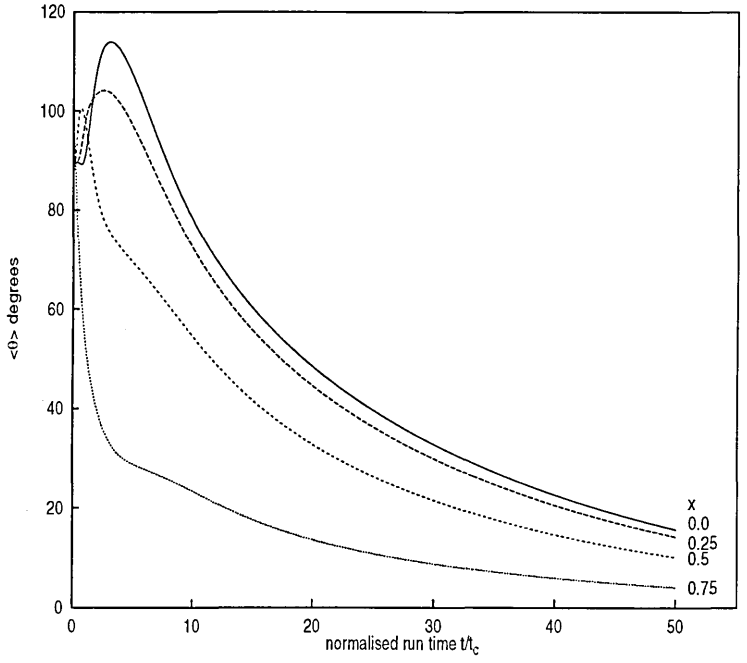

Figure 6.10: Simulation result for a system diameter of 60 lu's, showing the length averaged angle $\langle\theta\rangle$ as a function of the normalized time for several positions across half the system diameter, (0) centre (1) wall.

Figure (6.10) shows a normalized time correlation function of the director orientation across half our lattice system (the other half being an inverted image of the first due to the symmetry of the imposed geometry).

Note that at the mid-channel position, the degree and period of director kick-back are at a maximum. As we approach either of the bounding walls, the degree and period of director kick-back decreases and it eventually disappears. Each curve in figure (6.10) has been normalized to the time when the angle at that position first exceeded 90^o.

Clearly, we observe good qualitative agreement with the Clark and Leslie result (figure (6.9 a)) and, moreover, a similar degree of maximum kick-back angle. However, as we approach the wall in figure (6.10), we observe some deviation in our director time correlations from the results presented in figure (6.9a), which has being accentuated by the time normalization. This deviation could be due to our imposed boundary conditions and would suggest further investigation.

We turn now to the induced flow field, figure (6.11) shows a time correlation function of the $\langle u_x \rangle$-component of velocity across the same half of the width as figure (6.10).

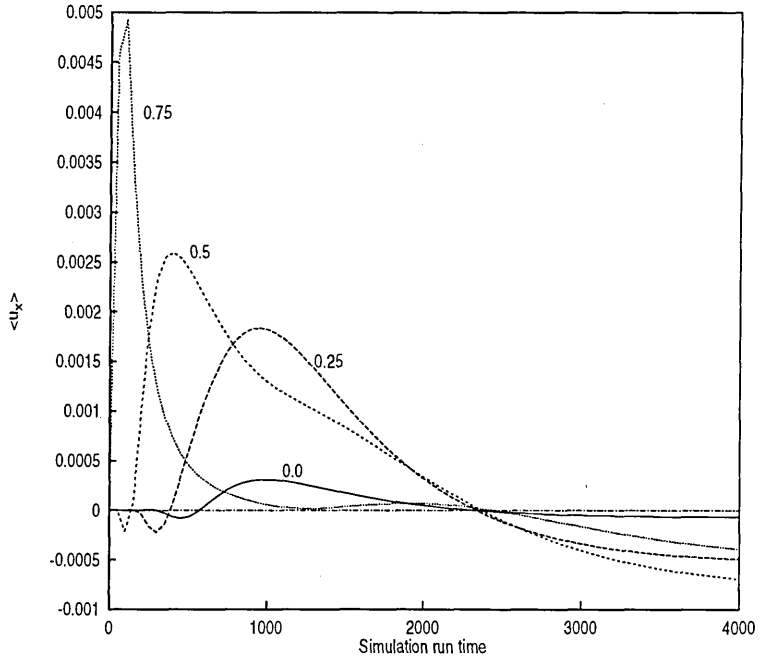

Figure 6.11: Simulation results for a system diameter of 60 lu's, showing the $\langle u_x \rangle$-component of velocity time correlation function at various positions across half the system width, (0) centre (1) wall.

Again the top half of the flow is just the reverse of the bottom half with the mid-channel velocity equal to zero. As can be seen, back-flow is produced at the wall layer, which then propagates rapidly into the centre of the bulk, decaying away quickly. After a time the flow reverses into a relatively small forward-flow which decays away more slowly, as the bulk alignment gradually reorientates towards the strongly anchored wall angle.

The flow profile time correlations from our simulations shown in figure (6.11) indicate that we correctly recover the two flow modes involved, namely the initial large back-flow and the longer, more persistent, smaller forward flow. The flow profile from Clark and Leslie reproduced here in figure (6.9 b) shows the symmetric but opposite flow field to our results. The normalization involved in figure (6.9 b) qualitatively changes the appearance of the induced flow field from our results but we can still observe the large initial flow and the smaller more persistent secondary flow.

We can visually represent the director field and the induced flow profiles of this *ideal* aligned nematic to get a better qualitative view of the kick-back and back-flow. Each snapshot of following time sequence of pictures, figures (6.12) to (6.16), displays the averaged director profile $\langle\theta\rangle$ across the system width on the left and the averaged velocity $\langle\mathbf{u}\rangle$ across the width on the right. The velocity field is normalized to the overall induced maximum velocity magnitude. The size and colour of the velocity vector represents this normalization.

Figure 6.12; **Time evolution of the director and normalized flow fields for the *ideal* aligned nematic back-flow and kick-back simulation, time t — 0 to time t = 450. To show the initial induced back-flow a time step of 50 is used here.**

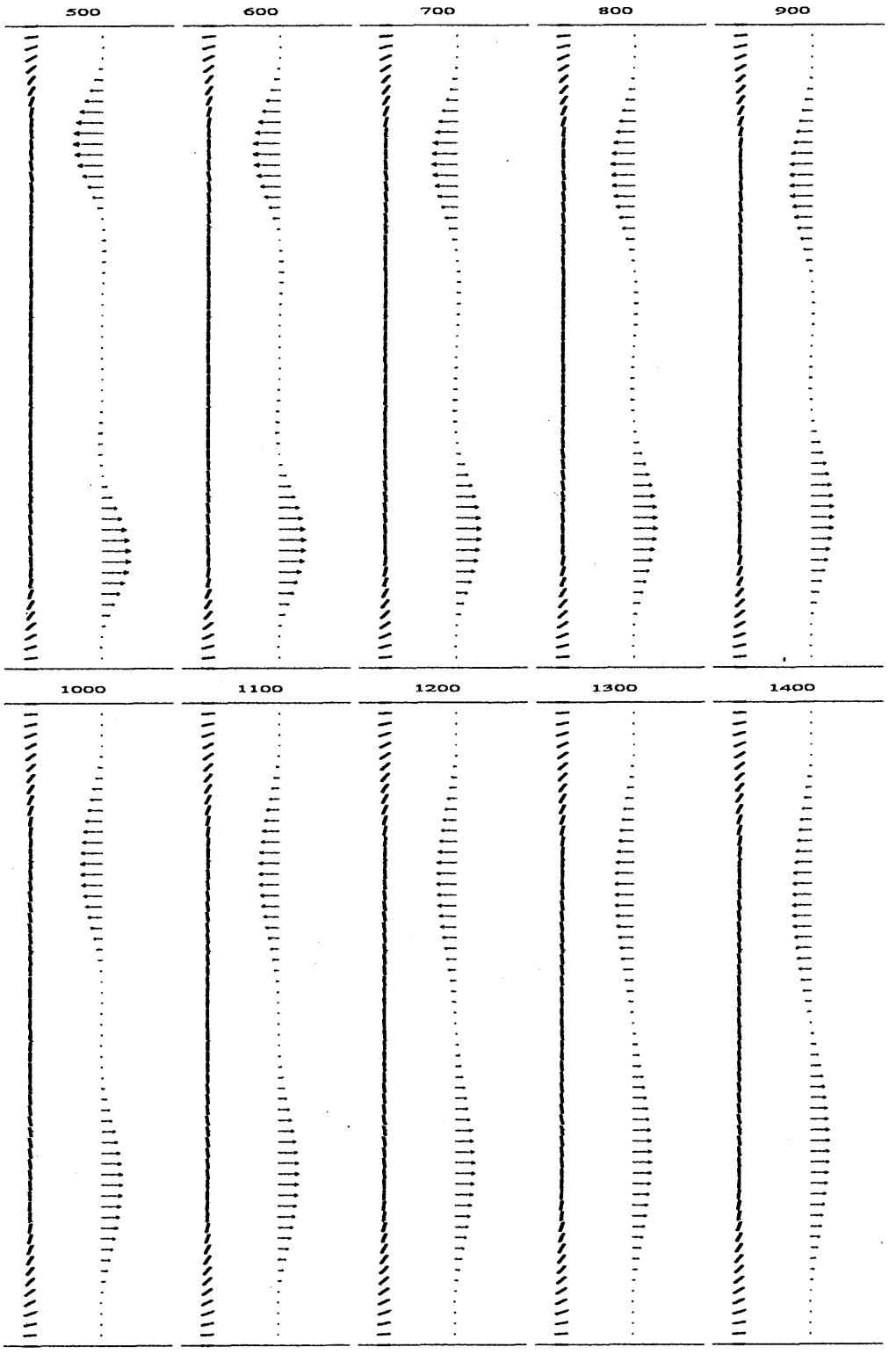

Figure 6.13: Time evolution of the director and normalized flow fields for the *ideal* aligned nematic back-flow and kick-back simulation, time $t = 500$ to time $t = 1400$. To capture the intermediate system dynamics a time step of 100 is used here.

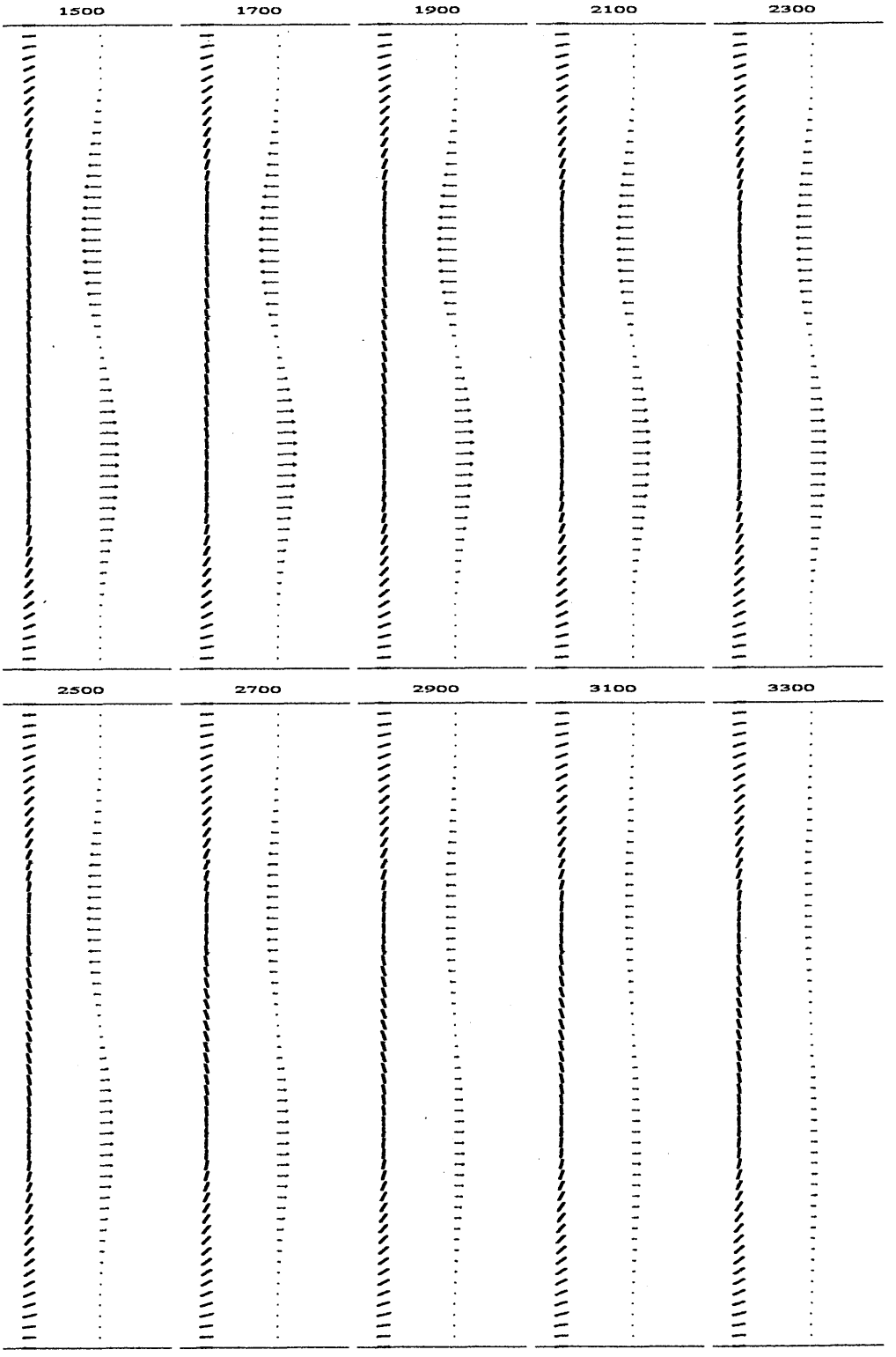

Figure 6.14: Time evolution of the director and normalized flow fields for the *ideal* aligned nematic back-flow and kick-back simulation, time $t = 1500$ to time $t = 3300$. To capture the kick-back development, a time step of 200 is used here.

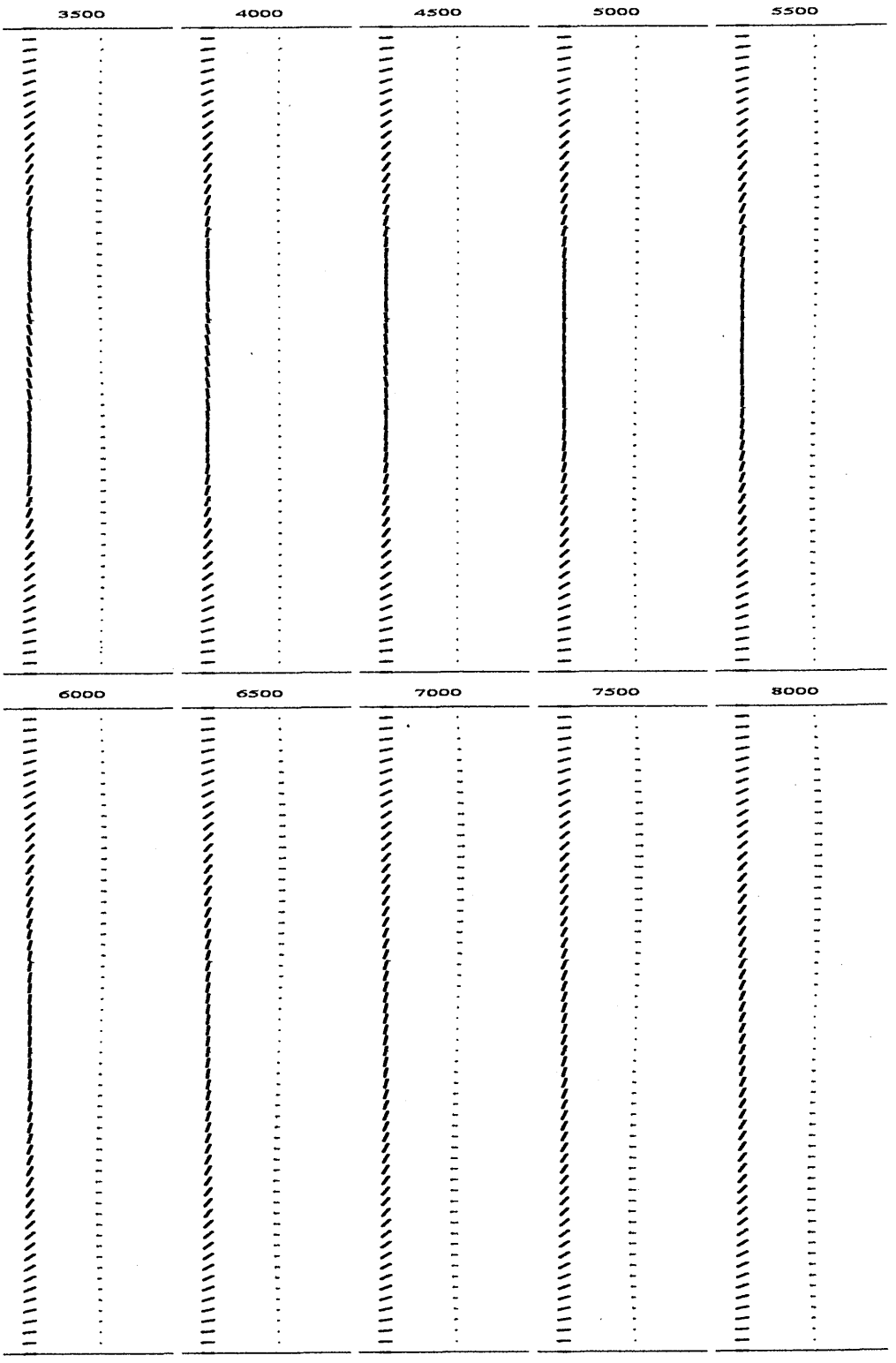

Figure 6.15: Time evolution of the director and normalized flow fields for the *ideal* aligned nematic back-flow and kick-back simulation, time $t = 3500$ to time $t = 8000$. To capture the long term relaxation of the system, a time step of 500 is used here.

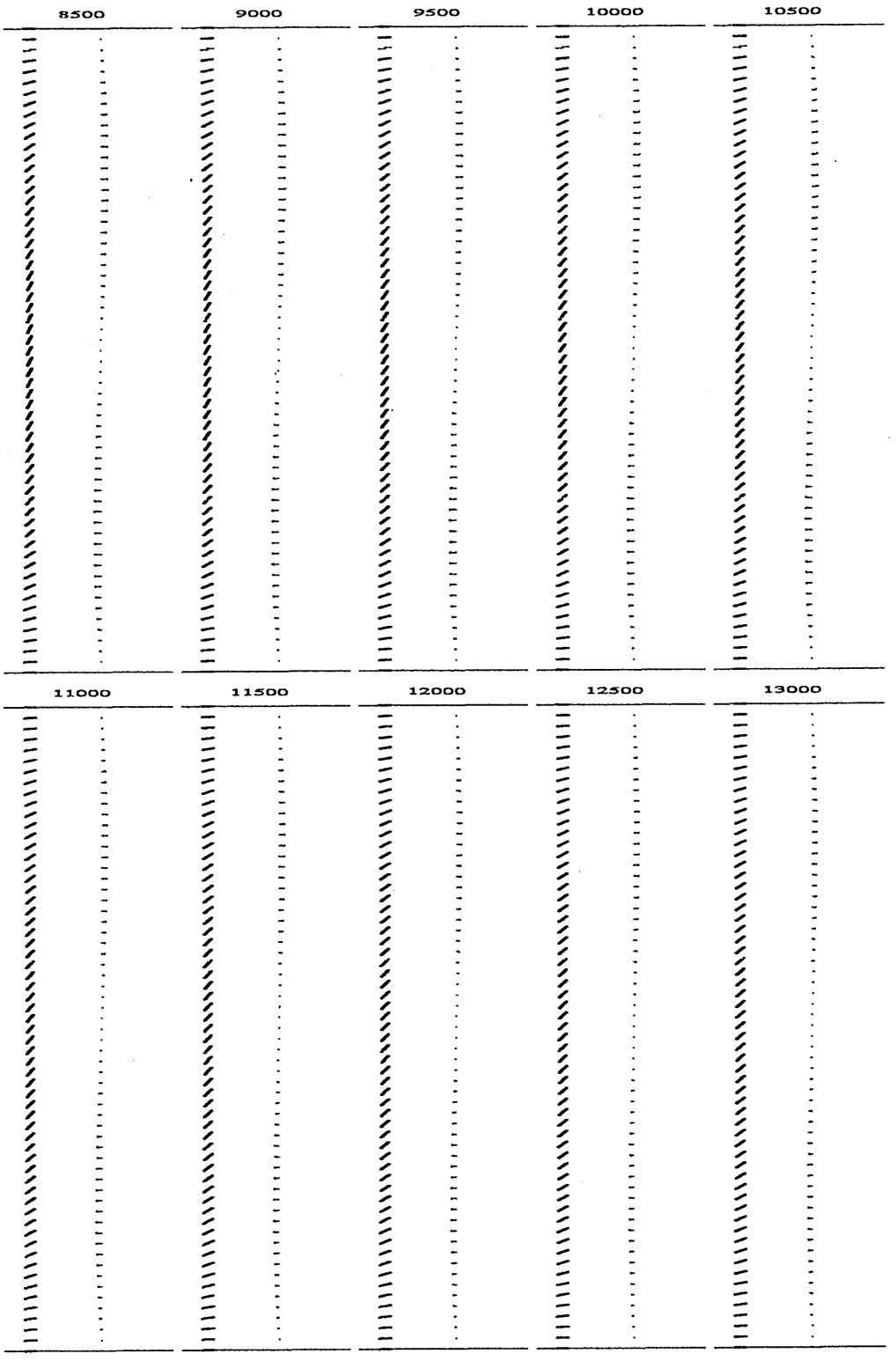

Figure 6.16: Time evolution of the director and normalized flow fields for the *ideal* aligned nematic back-flow and kick-back simulation, time $t = 8500$ to time $t = 13000$. To capture the long term relaxation of the system, a time step of 500 is used here.

The time sequences represented in figures (6.12) to (6.16) show visually the induced back-flow and resulting kick-back for the simulations, discussed in figures (6.10) and (6.11). The initial back-flow "wave" is observed propagating into the centre of the bulk and causing a director kick-back. The back-flow quickly decays away and reverses into a more persistent forward-flow field, while the director slowly rotates from the kick-back angle towards the aligned direction at the wall.

Having observed back-flow and kick-back for the *ideal* aligned system we shall now examine the dependence of the kick-back angle and the induced back-flow on our system parameters. Obviously for fixed nematic viscosities, the only free parameter apart from the nematic elasticity is the dimensionality of the system. For the geometry considered here, the system is translationally invariant and therefore the effect is not dependent on the system length. We can investigate, however, the result of varying the system diameter with all other nematic parameters remaining fixed.

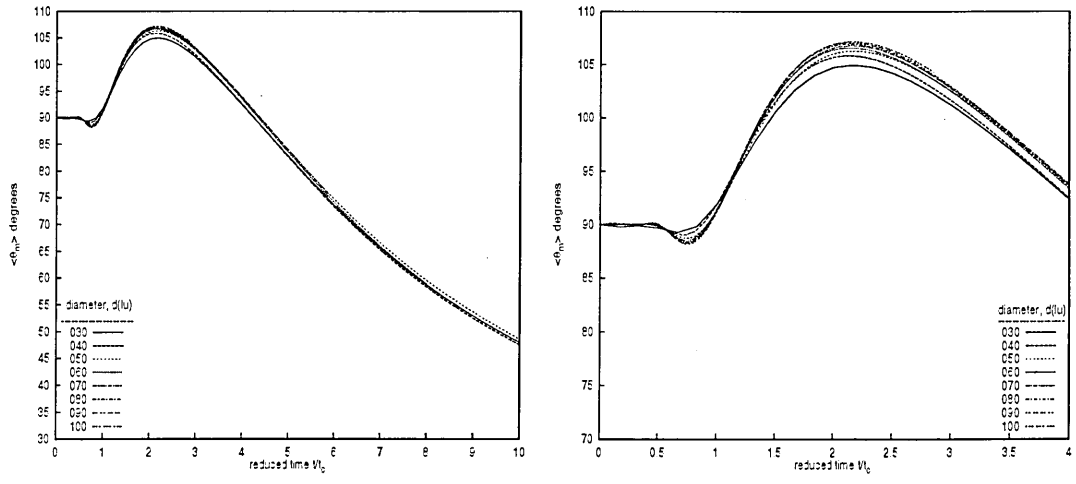

(a) Reduced time correlation functions of the mid-channel averaged director orientation for increasing system diameters.

(b) Enlargement of the kick-back region for the reduced time correlation functions shown in figure (6.17 a).

Figure 6.17: Reduced time correlation functions of the mid-channel averaged director orientation for increasing system diameters.

Figure (6.17 a) shows the change in the director kick-back at the centre of the channel for varying system diameters. Figure (6.17 b) shows the same data, focusing in on the kick-back section of the graph. The time axis is again normalized to the time, for each diameter, when the angle in the centre of the system diameter first exceeds 90^o. There are two points to note about these results. First, as the channel width increases, we appear to converge onto a maximum kick-back angle (for fixed nematic parameters). Figure (6.18) shows the maximum kick-back angle obtained in the centre as a function of the system diameter. The degree of kick-back appears to be converging onto a final angle of around 107^o.

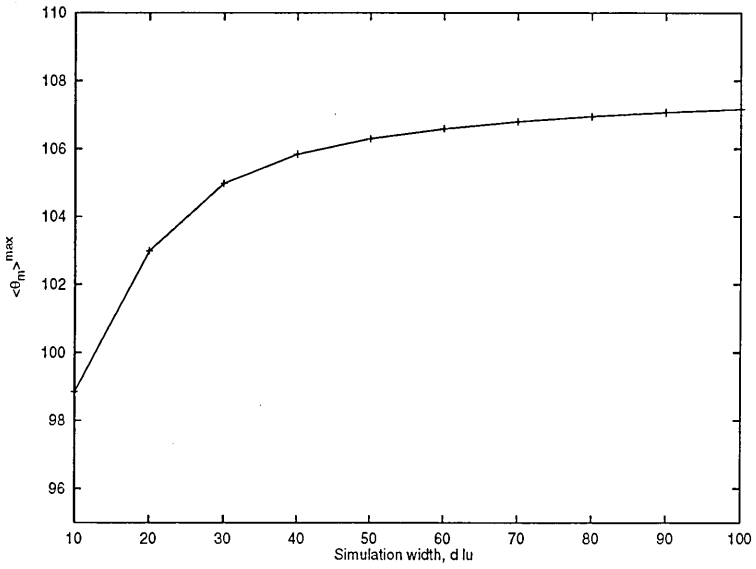

Figure 6.18: Convergence onto a maximum mid-channel length averaged kick-back angle for increasing system diameters.

Secondly, before the onset of kick-back we observe a kick-*forward*, i.e. the director orientation at the centre of the system diameter rotates a few degrees below 90^o before increasing to the kick-back angle. We shall return to these observations in the discussion section at the end of this section.

Consider now the equivalent induced flow profiles near the centre of the system for the various system diameters.

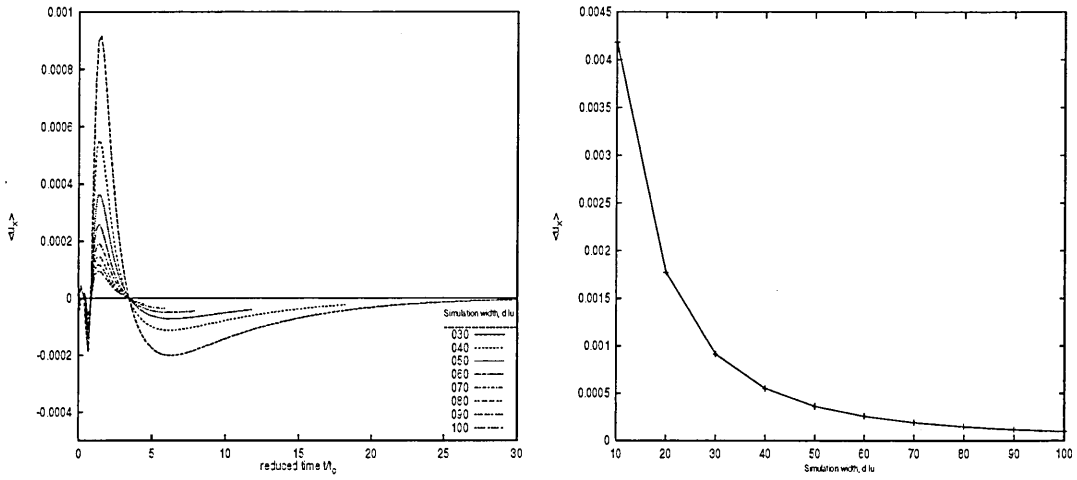

(a) $\langle u_x \rangle$ near mid-channel velocity time correlation functions for increasing system diameters.

(b) Decay of the $\langle u_x \rangle$ near mid-channel velocity for increasing system diameters.

Figure 6.19: Simulation results of the $\langle u_x \rangle$ velocity time correlation function near mid-channel velocity for increasing system diameters.

Figure (6.19 a) shows the $\langle u_x \rangle$-component of velocity at one lattice unit away from the centre of the channel for various system diameters. We observe that as the system diameter increases the strength of the flow field at the centre decreases. This is expected since the flow field is induced by the rapid director changes at the wall and then propagates into the bulk: the wider the system, the more the flow field can dissipate before the centre is reached. This decay with increasing system diameter is shown in figure (6.19b). Again we observe an initial *forward*-flow profile just before the back-flow reaches the centre of the system and we tentatively associate the kick-forward observed in figure (6.17 b) with this forward-flow.

We shall now consider simulations for director configurations aligned with a finite applied magnetic field. From the previous section we can take the final configurations of the Fréedericksz aligned systems and observe the resulting director and flow fields when the field is switched off. These aligned systems posses a magnetic coherence layer ξ (H) of a specific thickness, dependent on the strength of the applied field H see figure (6.20).

In the following, the field strength is specified as a multiple of the critical field H_c for a simulation of dimensions 10x60 lu's, other simulation parameters used are the MBBA nematic viscosities from table (5.1), a magnetic susceptibility $\chi_a = 1$ and an elasticity K set according to $\bar{\omega} = 1.8$.

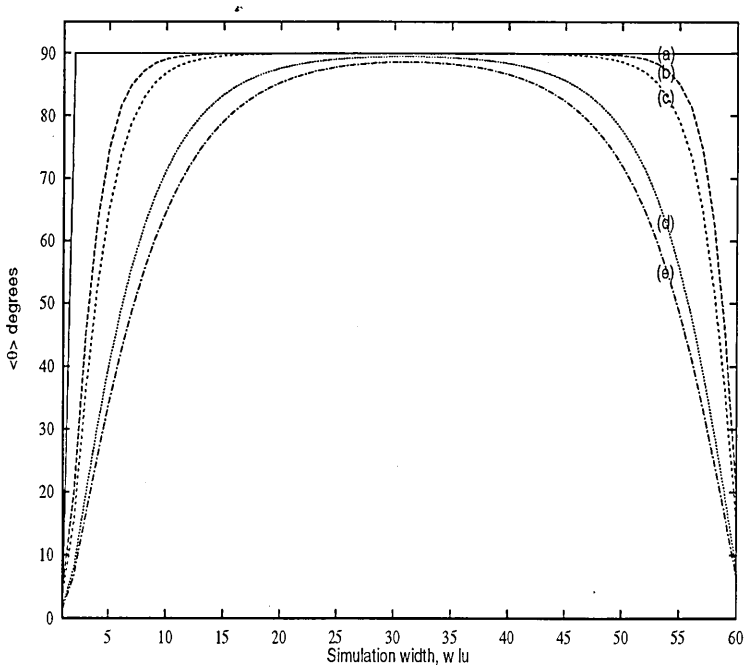

Figure 6.20: Aligned director profiles across the channel width for normalized applied field strengths H/H_c of (a) *ideal* (b) 6.0 (c) 4.5 (d) 2.5 and (e) 2.0.

Figures (6.21 a) shows the normalized time correlation function of the mid-channel averaged director orientations upon release, for increasing magnetic field strengths (see figure caption).

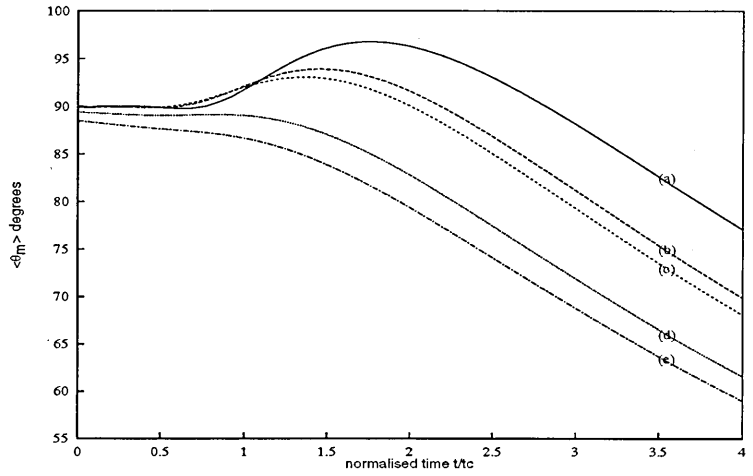

(a) Normalized time correlation function of the averaged mid-channel director orientation for simulations with normalized applied field strengths H/H_c of (a) *ideal* (b) 6.0 (c) 4.5 (d) 2.5 and (e) 2.0.

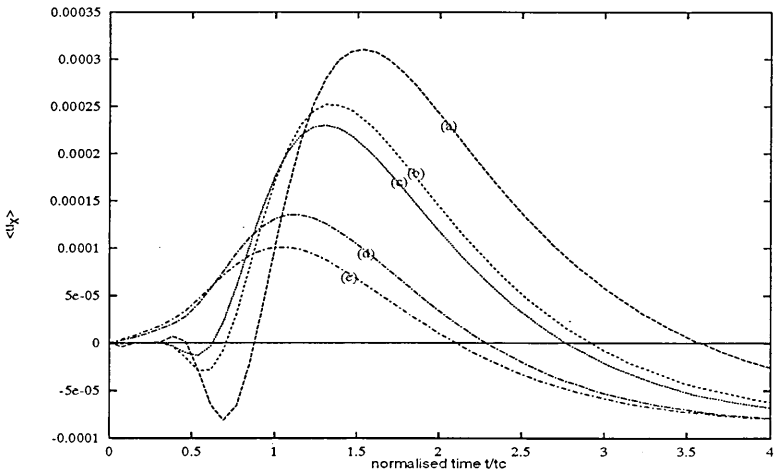

(b) Normalized time correlation function of the length averaged near mid-channel $\langle u_x \rangle$ component of velocity for simulations with normalized applied field strengths H/H_c of (a) *ideal* (b) 6.0 (c) 4.5 (d) 2.5 and (e) 2.0.

Figure 6.21: Normalized director and velocity time correlation functions of back-flow and kick-back simulations for normalized applied field strengths H/H_c of (a) *ideal* (b) 6.0 (c) 4.5 (d) 2.5 and (e) 2.0.

Figure (6.21 b) shows the equivalent normalized time correlation function of the near mid-channel averaged x-component of the induced velocity field upon release from the various magnetic field ratios.

For *ideal* and large H/H_c values, the kick-back can clearly be observed but as the relative strength of the initially aligning magnetic field decreases, the degree of kick-back also decreases. As the initial applied field strength drops to around the critical field strength, the mid-channel director appears to experience no kick-back and simply relaxes monotonically towards the wall alignment. The induced velocity fields near the mid-channel position also decrease for smaller initial applied field values.

The initial kick-forward observed in the *ideal* simulation is not apparent in the simulations with a magnetic coherence length and would suggest that the kick-forward was an artifact of the imposed first-order boundary conditions. However, the observed initial forward-flow is still apparent in the simulations with a small coherence length, only vanishing for larger coherence lengths. We shall reserve further comments on these observations until future publications.

We can tentatively shed some light on the dependence of the back-flow/kick-back effect on the initial configuration of the bulk orientations. To observe back-flow and kick-back a *plateau* of aligned bulk orientations is required, the larger the *plateau* (corresponding to a smaller (or zero) magnetic coherence length), the greater the induced back-flow . Within the magnetic coherence length the directors rapidly change from the imposed wall orientations to the direction of the imposed field. Back-flow

is induced at the point in the coherence length where there is a large difference in orientations between neighbouring directors. The more acute this difference the stronger the induced back-flow, for set nematic viscosities and elastic constant. The observed kick-back is induced by the back-flow but the degree of kick-back appears to be mainly dependent on the nematic viscosities and elasticity. The issues raised in this section are intended only as qualitative observations on the simulation results.

6.4 Discussion and Conclusions

We have performed simulations that show a second order phase transition between the imposed wall orientations and an applied magnetic field angle at some critical field strength H_c. The observed phase transitions agreed very well with the equivalent predicted Fréedericksz transition calculated using an elliptic integral [116]. The implied simulation critical field strengths agreed with the theoretical value derived through equation (6.2) [3] over the range of system diameters considered, inferring that our LBE simulation transitions scale with system diameter correctly.

Reverse transitions were observed to follow the same curve as the forward transitions and necessary simulation detail considerations required to produce a hysteresis free transition were discussed. Finally, results of the relaxation of our simulation Fréedericksz transitions as the applied field angle is rotated towards to the imposed wall orientations were presented, which compared very well with the theoretical predictions [4].

Next we introduced the nemato-dynamic effect of velocity back-flow with director kick-back. Results from a simulation with an *ideal* aligned initial bulk director configuration corresponding to a zero magnetic coherence length were presented. The degree and nature of the observed kick-back correlated well with existing simulation results [5] whilst the induced back-flow qualitatively appeared to be consistent with predictions. Time correlation function plots of the back-flow and kick-back were complemented with a visual time sequence of the system showing the evolution of the back-flow "wave" propagating from the wall into the bulk causing the director kick-back effect. Observations suggest that the back-flow rapidly decays away, ultimately reversing into a more persistent forward-flow as the bulk directors reorientate towards the imposed wall orientations.

Finally the effect of an increasing magnetic coherence length on the observed kick-back and back-flow is investigated and the results are again compared to the *ideal* simulation results.

Chapter 7

Complex Geometry Simulations

7.1 Introduction

Berreman [119] and de Genne [3] first recognized that bulk director orientation can be controlled by the geometry of the bounding walls in the nematic cell. In chapters 5 and 6 a simple planar geometry was imposed resulting in a mono-stable nematic cell which, in the absence of any induced flow or external fields, would align the bulk orientations tangential to the surface wall orientation.

A relatively new idea in the liquid crystal community is to control bulk alignment using a *bi-stable* grating wall profile. Barbero [120] [121] first reported on the possibility of a bi-stable nematic cell by using a saw-tooth grating. The sharp features of the saw-tooth profile pinned disclinations at the peaks and troughs of the grating.

Recently Brown *et al* [6] have reported on the properties of a Zenithly Bi-Stable Display (ZBD) device. In a ZBD device, an asymmetric grating profile (in which the "saw-teeth" have unequal sides) is used. In this geometry the director field configuration has two (local) minima in its energy-configuration landscape, thus allowing for configurational bistability. Once the bulk nematic orientations in such a device have been aligned to a certain angle by an external field (magnetic or electric), then upon removal of the field the cell will relax to one of *two* stable states. Which stable state the cell enters is dependent on the orientation of the bulk nematic upon "release" and the characteristic properties of the asymmetric grating (cell wall).

This bi-stability property has many obvious advantages over the mono-stable devices used in current liquid crystal displays that require constant *refreshing* to remain aligned *. As an obvious application, the ZBD device could be implemented to produce a range of very low power consumption liquid crystal displays that once set, are likely to remain stationary.

7.2 Zenithly Bi-Stable Display (ZBD) Device

The ZBD profile is an asymmetric 1D surface grating as shown in figure (7.1) where the asymmetry of the repeating structure is characterized by the dimensionless ratio h/w relating the peak height h to the peak width w.

*For a fuller review of the ZBD device and the potential applications, the interested reader is directed to [6] and the references given therein.

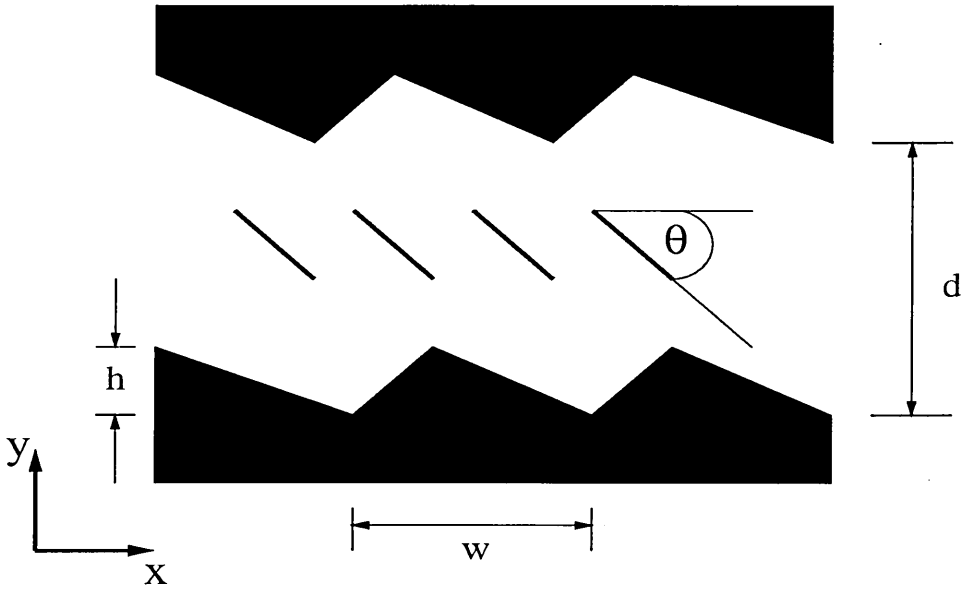

Figure 7.1: Schematic of the ZBD model geometry. The nematic is confined between a pair of identical but anti-parallel gratings. The geometry is fully specified by three quantities (i) a blaze factor A controlling the asymmetry of the grating (ii) the grating height to width ratio h/w and (iii) the cell diameter to grating width ratio d/w.

7.2.1 Implementing an LBE simulation of the ZBD device

This asymmetric periodic 1D surface grating profile can be conveniently modeled (approximated) using equation (7.1) [6],

$$f(x) = \frac{h}{2}\sin\left\{\frac{2\pi x}{w} + A\sin\left(\frac{2\pi x}{w}\right)\right\} \tag{7.1}$$

where the grating curve is characterized by the peak to trough amplitude h the peak period w and an asymmetry (*blaze*) factor A. The blaze factor controls the degree of change from a pure sinusoidal surface profile ($A = 0$) to a blazed profile ($A > 0$). The ZBD grating surface profile can be reasonably approximated by equation (7.1) for a blaze factor of $A < 0.5$ above which a point of inflection occurs making the profile unsuitable for modelling.

Equation (7.1) gives a continuous profile for the grating which we subsequently discretise to map onto our lattice. Figure (7.2) shows a typical discretised profile (crosses) in the xy plane, compared to the continuous profile (line).

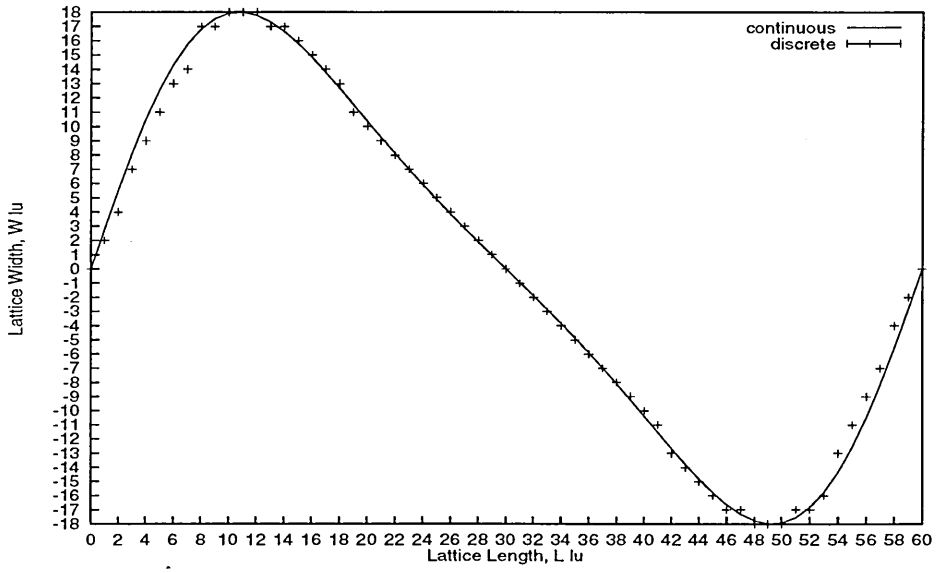

Figure 7.2: Discretised ZBD surface grating profile resolved onto the continuous ZBD surface grating profile, for a simulation lattice of 60 × 60 lu.

Obviously the approximation of the discretised profile to the actual continuous profile will affect the accuracy of the results and the larger the lattice dimensions, the better the discretised profile will resolve the continuous profile. By inspection we found that a lattice with a length of 30 lu's or greater produces a good approximation to the continuous profile.

Having obtained the discretised grating profile we can superimpose the profile onto our lattice and label each node that the grating covers as a wall node. If the grating is placed in the centre of our simulation lattice and we repeat the process (of wall

node labelling) to make the wall several layers thick we obtain solid wall boundary locators as shown in figure (7.3a). At the black sites, the LBE momentum densities are set to a value that corresponds to a rest equilibrium distribution, effectively "forcing" the fluid that occupies this region to zero velocity.

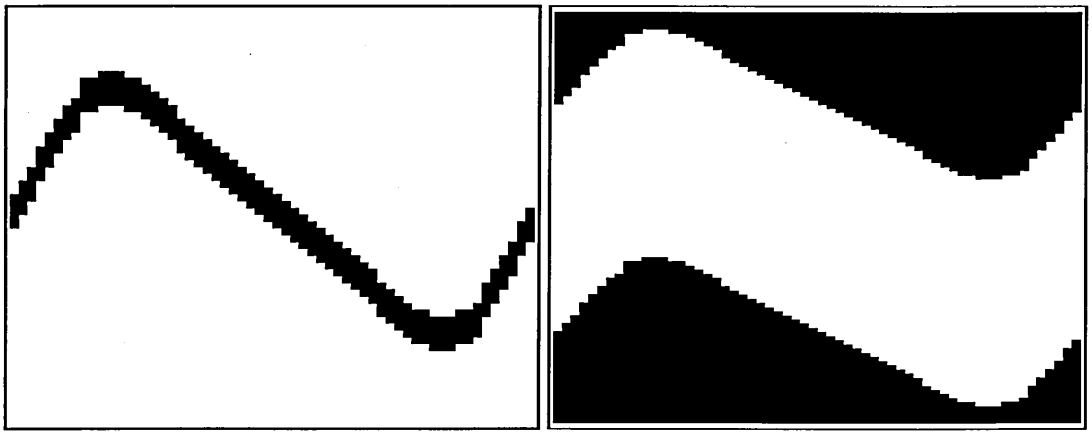

(a) Actual ZBD boundary configuration (b) Shifted ZBD boundary configuration

Figure 7.3: Lattice Boundary configuration for the discretised ZBD surface grating profile.

Note that the system is periodic in the horizontal direction, so it is clearly no longer translationally invariant, but repeats with period w. The system is periodic in the vertical direction at the lattice boundaries but is split horizontally by the wall layers in the centre of the cell. If we now associate the bottom and top of the black-shaded region in figure (7.1) with the imposed wall conditions at the top and bottom (respectively) of our ZBD cell then we can effectively consider the rest wall layers of our simulation in figure (7.3 a) to appear as in figure (7.3 b). †

†Note the actual simulation remains unaffected, the visual shift is purely a graphical means to make the resulting images visually resemble the ZBD wall in figure (7.1).

Next we have to fix the angles at the wall surfaces. We again set strong anchored wall angles by overwriting the wall node link angles by the distributed required wall angle, as in chapters 5 and 6. We can select any surface director orientation suggested by the microscopic physics and indeed later on in this section we shall examine the behaviour resulting from two different wall alignments.

Also note that because we have a complicated wall layer structure, it is difficult to apply the bounce-back method [122] to produce a non-slip zero velocity wall. The equilibrium forcing boundary condition used here produces a first-order approximation to the required non-slip wall condition [‡].

Finally we shall again impose no flow profile during the simulation (zero forcing) so any observed flow-fields are transient and have been induced by director re-orientations. Accordingly they will tend to zero at steady state (long times).

[‡]See the discussion on boundaries at the end of chapter 3.

Results presented in [6], reproduced in figures (7.4a) and (7.4b) show the low tilt singularity free and the high pre-tilt defect steady state solutions of the director field respectively. The characteristics of the grating used in the above results from [6] are $h/w = 0.6$, $d/w = 4$ and $A = 0.5$. Only the bottom half of the cell is shown for each simulation, the rest of the director field may be inferred from symmetry.

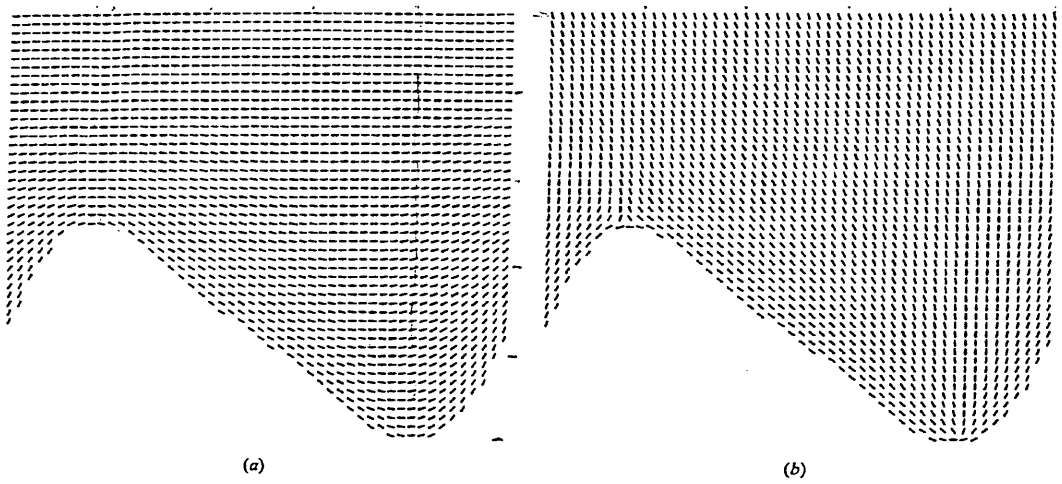

(a) Bulk director orientations for the smooth steady state profile.

(b) Bulk director orientations for the $\pm 1/2$ defect steady state profile.

Figure 7.4: Results from [6] of a ZBD cell simulation showing the bi-stable states. Calculation (in $2 \oplus 2$) of steady state using conformal mapping techniques to find solutions of Laplace equations.

The defect solution displays what appears to be a $-1/2$ nematic defect at the peak of the profile and a $+1/2$ nematic defect in the trough. The bulk directors for the low-tilt singularity free solution are aligned in the parallel stable state whereas for the defect solution the bulk is aligned to the perpendicular stable state.

We now need to review an important feature of the ELP equations of nemato-dynamics. At the point in a nematic where a disclination forms, the continuum ELP equations involve singularities and therefore cannot describe the nematic state [3]. However it appears in our model, where we map a discrete lattice onto the continuum ELP equations, that we can observe what appear to be $\pm 1/2$ defect disclinations, see figure (7.5). These specific disclinations are apparently also recovered by Brown *et al* [6] as shown in figure (7.4b).

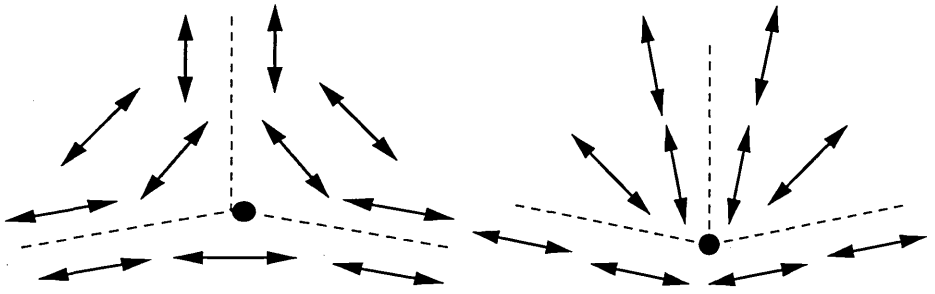

(a) -1/2 defect. (b) +1/2 defect.

Figure 7.5: The $\pm 1/2$ disclinations that can appear in a 2D nematic.

We attempt to resolve this apparent ambiguity by the following argument. In all probability, in our lLB simulation, the $\pm 1/2$ defect disclination singularity *point* occurs off-lattice (in-between the lattice nodes). The surrounding on-lattice node director orientations can then be considered to be governed by the nemato-dynamic continuum equations yet be influenced by the $\pm 1/2$ defect disclinations. The actual director *singularity* therefore is not recovered but the nearby director orientations are inferring a 2D disclination in the director field.

During simulations described in this thesis we have observed $\pm 1/2$ defect disclinations. In chapter 6 we had to bias the Fréedericksz transition simulations to avoid formation of $\pm 1/2$ defects in the bulk creating nematic domains which affect the nature of the transition. Here, we observe the predicted defects in the ZBD experiments forming on the surface grating profile.

It is appropriate to remark here that test runs were carried out for a simple channel geometry in which the bulk and wall director initial orientations were set randomly and the system allowed to reach steady state. Formation of nematic domains separated by disclination walls with a $\pm 1/2$ defects at the wall ends was observed. These domain structures were similar to those seen in the unbiased Fréedericksz transition simulations. Once the steady state was achieved a Poiseuille flow was imposed and as the flow developed the bulk disclinations were observed to move down the simulation channel. During this bulk disclination movement, annihilation and creation of $\pm 1/2$ defects was observed as several disclinations met and interacted.

These peripheral observations are not emphasized in this thesis since we are attempting a process of 'proof of concept' and in most instances require defect free simulations to test the algorithm. However the appearance of such defects is encouraging and would obviously be a very interesting area of further study. For now we shall assume that the observed defects are 2D nematic disclinations and investigate the ZBD cell without any further diversion. Further comments are postponed until future work is discussed.

7.2.2 Results of ZBD simulations

As stated earlier the bi-stability of the device cell means that if we align the bulk initially to below a critical orientation near the horizontal then the final steady state profile will be the smooth defect free profile. Initially setting the bulk angles above this, critical orientation and the steady state becomes the defect profile. If we set the initial orientation greater than 90° then we should still initially relax to the defect profile. As the initial angle is increased further towards 180° a second critical orientation should be observed as the final steady state switches back to the smooth profile.

The images in figure (7.6) show the long time steady state of the director field in our simulated ZBD cell having been released from a specific initial bulk angle.

The system set-up is a 30 x 60 lu cell with periodic images in the x-direction and bounded by rest walls (see above) in the y-direction. For clarity only the bottom half of the cell is represented since we are looking at the behavior of the directors at the grating wall. The nematic viscosity ratios are again set to the values characteristic of MBBA shown previously in table (5.1), and the nematic elasticity is set using an $\bar{\omega}$ relaxation value of 1.5. In terms of the ZBD cell, the peak width $w = 30$ lu (≈ 26 au) with characterizing ratio's of $h/w = 0.6$ and $d/w = 1.83$ with a blaze factor $A = 0.5$ [§].

[§]The discretisation of the ZBD curve can potentially alter the ZBD ratios and blaze factor. However at present we shall assume that the discretisation is a good approximation to the curve and therefore sufficiently recovers the ZBD configuration.

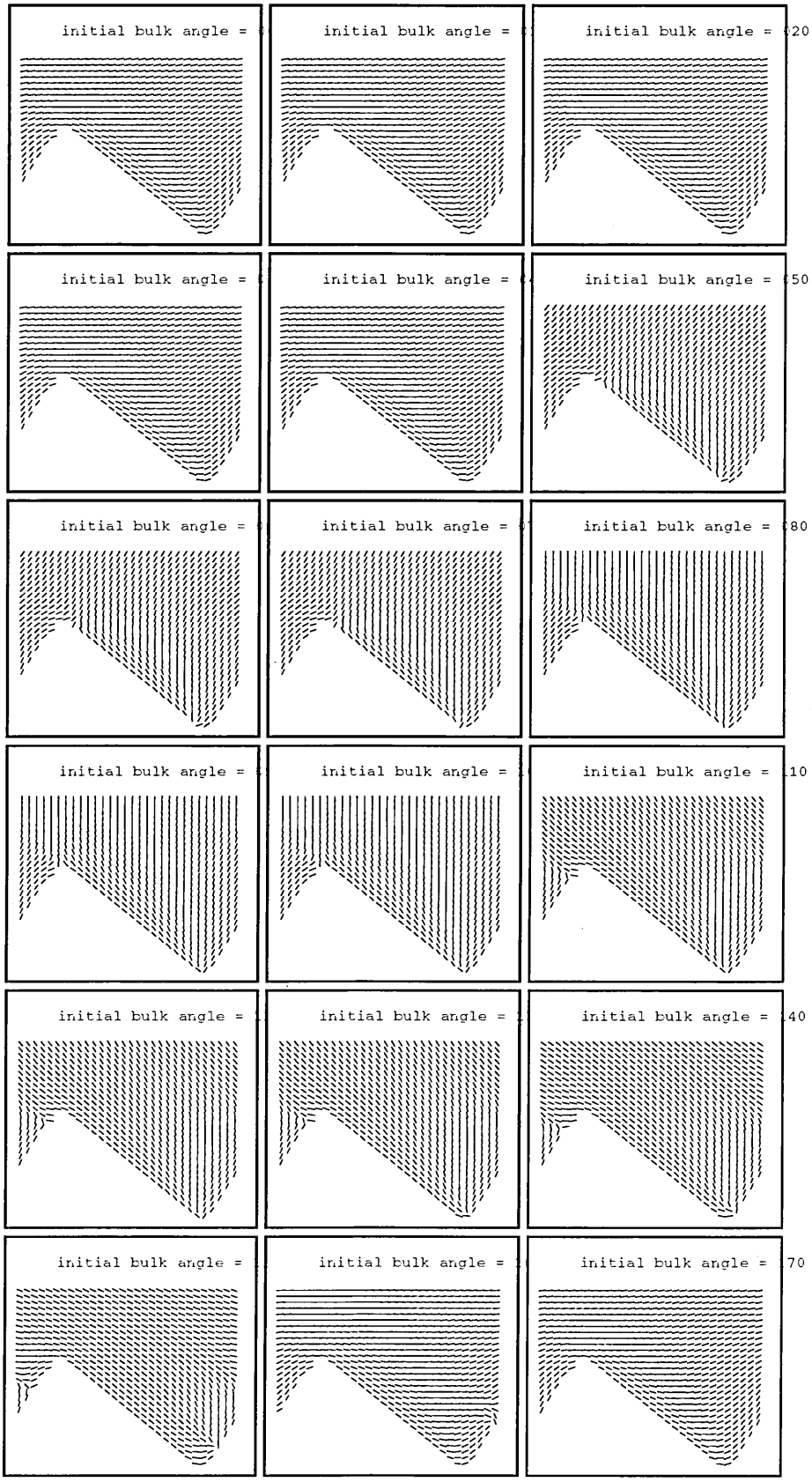

Figure 7.6: Tangential wall alignment steady state director orientations across 1/2 the width for different initial bulk orientations.

From figure (7.6), the switching in the bulk between the two stable states is apparent and shows that our simulations correctly captures the bi-stability of the surface grating. Remember the only difference between these simulations and the back-flow/kick-back simulations in chapter 6 is the asymmetric wall profile.

The 0^0 initial angle simulation results in a clean (defect free) director profile at the wall. For the 90^0 initial angle simulation the resultant director wall profile at steady state shows the $\pm 1/2$ defects exactly at the peaks and troughs of the grating. These two results qualitatively correspond very well with those presented in figures (7.4 a) and (7.4 b) [6]. From figure (7.6) we can also observe the steady state results from initial bulk alignments other than the two extremes discussed above.

Examining more closely the steady state results for all the initial bulk angles, we can observe the preferential formation of the defect state from the smooth state and vice-versa. At about a 50^0 initial bulk angle orientation, $\pm 1/2$ defects form on the long slope and as the initial bulk angle orientation increases towards 90^0 the position of the defect formations moves to the peaks and troughs of the grating respectively. Exceeding the 90^0 initial angle orientation, the defect formation position begins to converge along the sharp slope until around the 170^0 initial angle orientation, where the smooth steady state profile occurs.

The exact position of the $\pm 1/2$ defects on the grating surface, for a specific initial bulk angle orientation, is dependent on the topology of the grating [6], whilst the nemato-dynamics of the stable state transitions is dependent upon the nematic viscosities and elasticity.

We proceed now to consider what happens to the ZBD cell if we change the orientation of the anchored wall directors from the tangential anchoring used in the above simulations, figure (7.7 a), to a normal wall anchoring angle, figure (7.7 b).

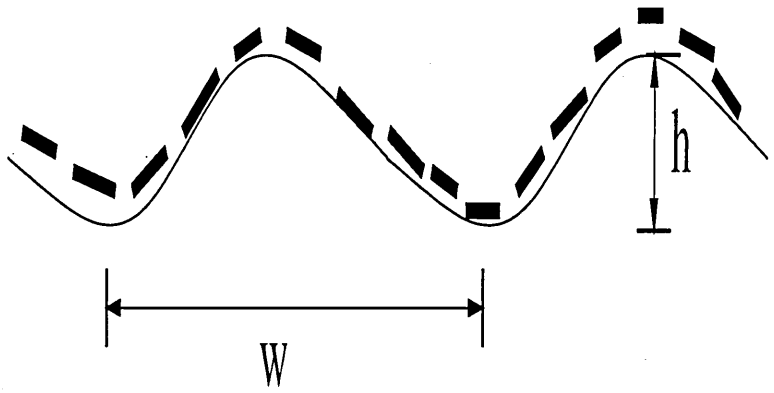

(a) Tangential wall alignment

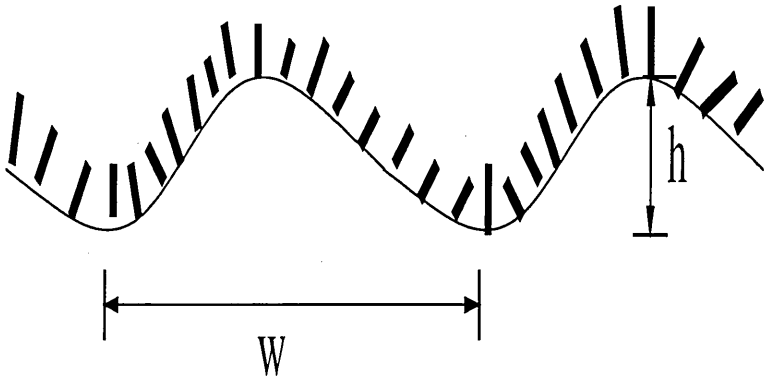

(b) Normal wall alignment

Figure 7.7: Tangential and Normal (strongly anchored) wall director orientations for the ZBD grating surface profile.

From experiments made upon a physical ZBD device, it has been found that the tangential anchoring configuration , figure (7.7 a), can slip over time causing the stable state to change [123]. This has been attributed to the relatively low wall anchoring strength of the tangential configuration. If the nematic wall angles are

aligned normal to the grating surface profile (figure (7.7 b)) then the anchoring strength is two or so orders of magnitude higher and hence the slipping does not occur. Although at present we cannot distinguish anchoring strengths between the two aligning orientations (only that they are strongly anchored) the problem of slipping is a relatively long time scale effect. Since we will be simulating the initial steady state convergence we shall only be interested in the effects of the different wall orientations on the bulk orientations and the defect formations at the wall, not slipping. The images in figure (7.8) show the same steady state simulations as before but this time with the wall angle set normal to the grating surface profile. All the simulation parameters remain the same as in the tangentially aligned simulations, the only difference is the (strongly anchored) director orientations at the profile wall.

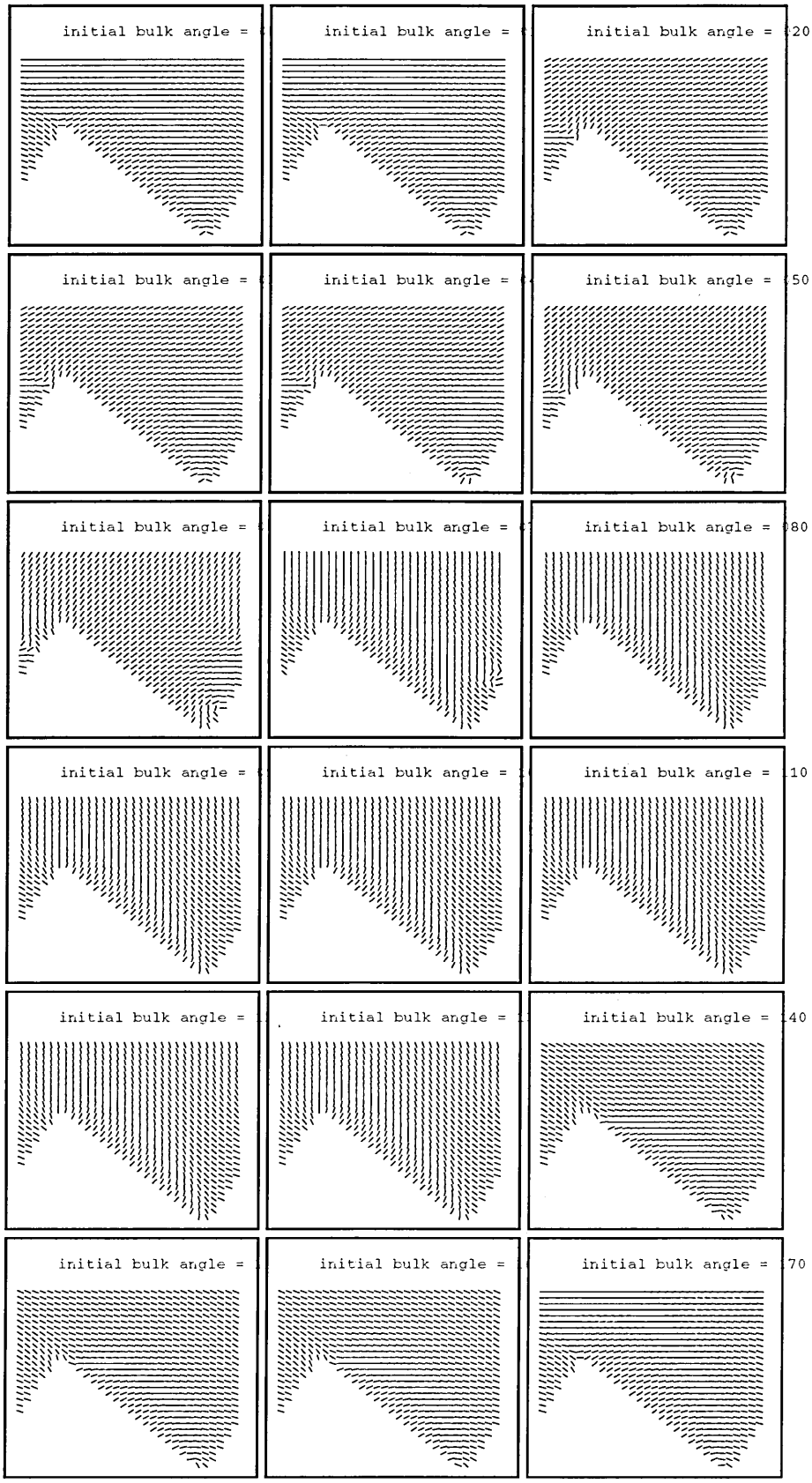

Figure 7.8: Normal wall alignment steady state director orientations across 1/2 the width for different initial bulk orientations.

In the case of normal director alignment at the surface grating profile we again observe relaxation into two different stable states (bi-stability). However the situation is the opposite of the tangentially aligned cases. For 0^o to around 80^o we notice defects at the wall but horizontal (parallel) bulk alignment. Above 80^o the director field relaxes to the vertical (perpendicular) steady state bulk alignment and the surface profile is defect free (smooth). At around 130^o we revert to the parallel bulk alignment and the defect surface profile.

An important issue to raise at this point is that when we observe the formation of a defect at the surface of the grating (in either the tangential or normal orientations) the defect remains stationary (stuck) at its position on the grating. Hui *et al* [124] have reported defect formations on surface profiles that are free to move around on the profile. However Hui's work had a different goal in mind and under the assumption of strong anchoring we can reasonably expect our defects to remain static where they form on the surface grating.

We now present an informal argument that explains the switching of the ZBD cell between the two possible stable states, which also explains the dependence on the initial bulk orientation of the defect position at the ZBD wall profile during the defect steady state.

We first consider a simple channel geometry simulation bounded with a flat non-slip horizontal wall with tangentially aligned wall orientations. If we align the bulk orientations exactly normal to the wall orientations, upon release, the bulk orientations are equally as likely to relax to the wall orientations by a clockwise rotation as by

an anti-clockwise rotation. This produces nematic domains in the bulk separated by disclination walls terminating in either of the $\pm 1/2$ defects, under the condition of strong anchoring and the fact that, once a defect has formed at the surface, then it remains stationary at that point unless it is destroyed.

For a ZBD surface profile, however, the surface tangent and normal change as one moves along the length of the device. Figure (7.9) shows this variation, for the tangential aligned surface, the bottom curve (+) is the surface tangent and the top curve (×) is the surface normal.

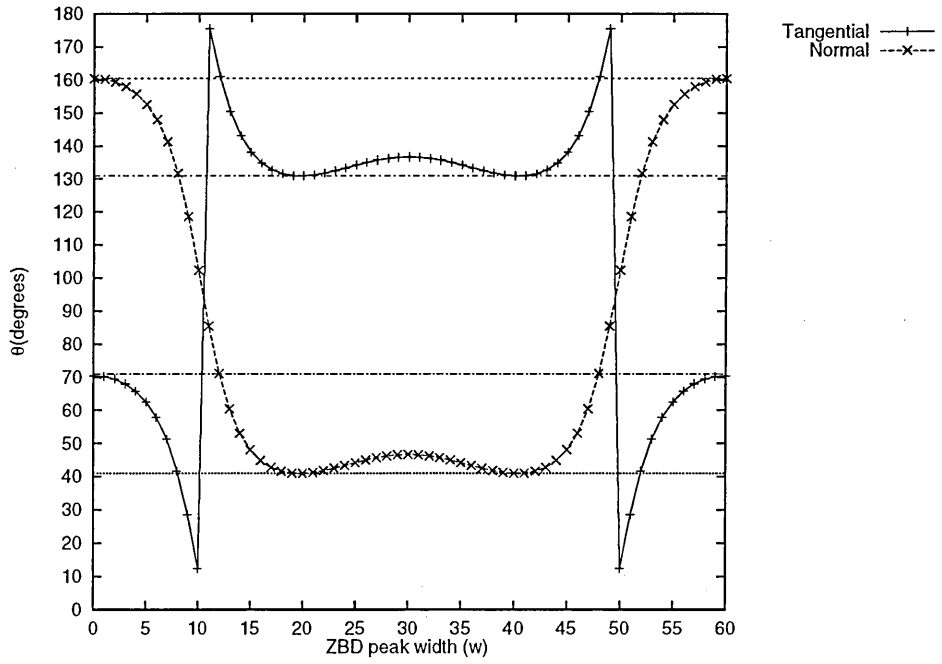

Figure 7.9: Variation of the normal (×) and tangential (+) wall orientations across the ZBD grating width, w. Dashed lines represent the banding of the angles to bulk orientations that correspond to a normal to the surface alignment and to bulk orientations that do not.

Therefore we can bound the surface normal curve (top and bottom continuous lines in figure (7.9)) indicating the maximum and minimum surface normal angles for the

tangentially aligned surface profile. If we align the bulk orientations initially to any of the angles within this bounded region, the bulk orientations will correspond to a surface normal somewhere along the length of the device. Upon release of the bulk orientations a defect will occur on the surface at the point of the surface normal and the ZBD cell will relax to the defect steady state configuration.

However, if we initially align the bulk orientations to some angle outside this banded range then there is no point across the surface for which the bulk orientations correspond to a surface normal. Upon release of these bulk orientations no defects will be formed on the surface profile and the ZBD cell will relax to the smooth (defect free) steady state configuration.

In terms of the normal anchoring of the director orientations on the surface profile, the situation is reversed. The top curve ($\times$) are the surface anchored angles and the bottom curve (+) represents the tangential angles. Bounding these tangential angles (inner continuous lines in figure (7.9)) shows the maximum and minimum angles for which a smooth (defect free) steady state is preferred. Initial bulk orientations aligned outside this banded range will, upon release, relax to the defect steady state configuration.

This geometrical argument not only predicts the bi-stability of the ZBD surface profile but the positional dependence of the surface defects on the initial bulk orientations. The results for the tangential surface profile simulations presented in figure (7.6) and the normal surface profile simulations presented in figure (7.8) support this argument. We observe the transitions between the steady states exactly at the

angles predicted by the geometrical argument as well as the defect position on the surface profile.

However we can go further than just modeling the director field. With the fully coupled model we can observe the complex interaction between the induced flow-field and the bulk director orientations.

We shall look initially at the maximum induced velocity magnitudes $|u|^{\max}$ obtained in the above simulations. That is, for each initial director orientation simulation we note the maximum induced velocity as the system converges onto the long-term steady state. Figure (7.10) displays $|u|^{\max}$ for both the tangential and normal wall orientations, as a function of initial bulk director orientation.

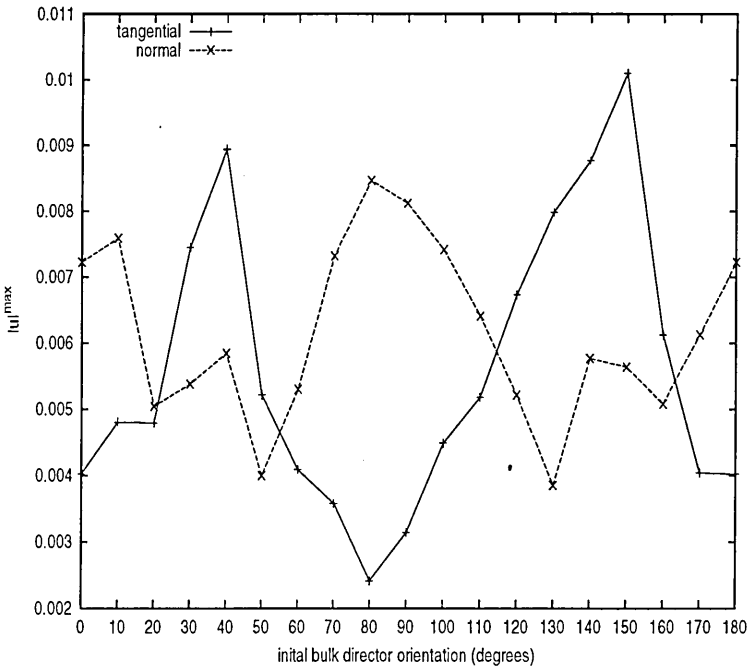

Figure 7.10: Maximum induced velocity magnitude's (crosses) for a series of steady state simulations with different initial bulk orientations in the absence of any applied field. Both the tangential and normal (strong anchored) wall director orientations are presented where the lines are drawn to guide the eye.

Figure (7.10) suggests that for the tangentially aligned wall nematic orientations, the induced flow-field intensity peaks for initial bulk orientation of around 40° and 150°. These peaks occur just prior to the formation and destruction of the $\pm 1/2$ defects respectively in the tangential aligned simulations. The minima in the induced velocity intensity occur just prior to the extreme angles of 0^0 and 90°. Recall that for the tangential alignment the wall profile is defect free at 0° and has $\pm 1/2$ defects exactly at the peaks and minima of the ZBD grating at 90°. Turning now to the normal aligned wall orientations we observe a different scenario. The maxima in the induced flow-field occur near the extreme angles around 10° and 80° and the minima in the induced flow-field occur around 50° and 130°.

Finally we examine, with a series of snapshots, the time evolution of the ZBD director and velocity fields from steady state when a strongly orientating magnetic field is either switched on or off. Since the ZBD cell possesses a complicated geometry then we characterize the time evolution of director and velocity fields only by a qualitative graphical representation in this work. To restrict the size of this thesis only the tangential wall profile is shown here. However, the normal wall profile or any other configuration could be applied to the ZBD cell just as easily.

The ZBD cell characteristics for the following simulations are $w = 60$ lu (≈ 52 au), $h/w = 0.6$, $d/w = 0.92$ and $A = 0.5$, The actual nematic viscosities used are again those characteristic of MBBA shown in table (5.1) and the elasticity K of the nematic was set using a $\bar{\omega}$ value of 1.5, In the simulations the strength of the applied magnetic field H was set to 0.2 (ensuring a strong response in the nematic) and $\chi_a = 1$ for simplicity.

Since we are only considering the qualitative form of the flow fields we do not calculate here the appropriate Reynolds/Ericksen numbers. However, approximate values of the Reynolds numbers for the "relaxation" and "field-on" simulations are 6.0 and 50 respectively. These indicate that we are working in a low Reynolds number regime. The Mach number (maximum velocity magnitude to sound speed ratio) for the larger induced flow "field-on" simulations is approximately 0.06, also indicating that we are working within the hydrodynamic limit. We shall discuss the upcoming results without further reference to flow regimes.

For each snapshot the velocity fields were normalized to 1/3 of the maximum obtained velocity magnitude. This is represented by the colour and size of the velocity vectors which were found to produce a good visual representation of the induced flow field. The arrowheads on the velocity vectors are indicative of the direction of the flow.

The first time evolution sequence represents a ZBD cell initially aligned by the strongly orientating magnetic field to 90^o (where we imply that 0^o is along the ZBD cell length). At time, $t = 0$, the field is removed and the initial 200 time steps of the relaxation of the ZBD cell to the steady state defect configuration are shown in intervals of 20 steps. The instantaneous snapshots show the director field at the top of the page with the corresponding flow-field time snapshot underneath.

We recall from figure (7.6) that this initial configuration should result in a steady state defect profile with the defects occurring at the peaks and troughs of the ZBD profile.

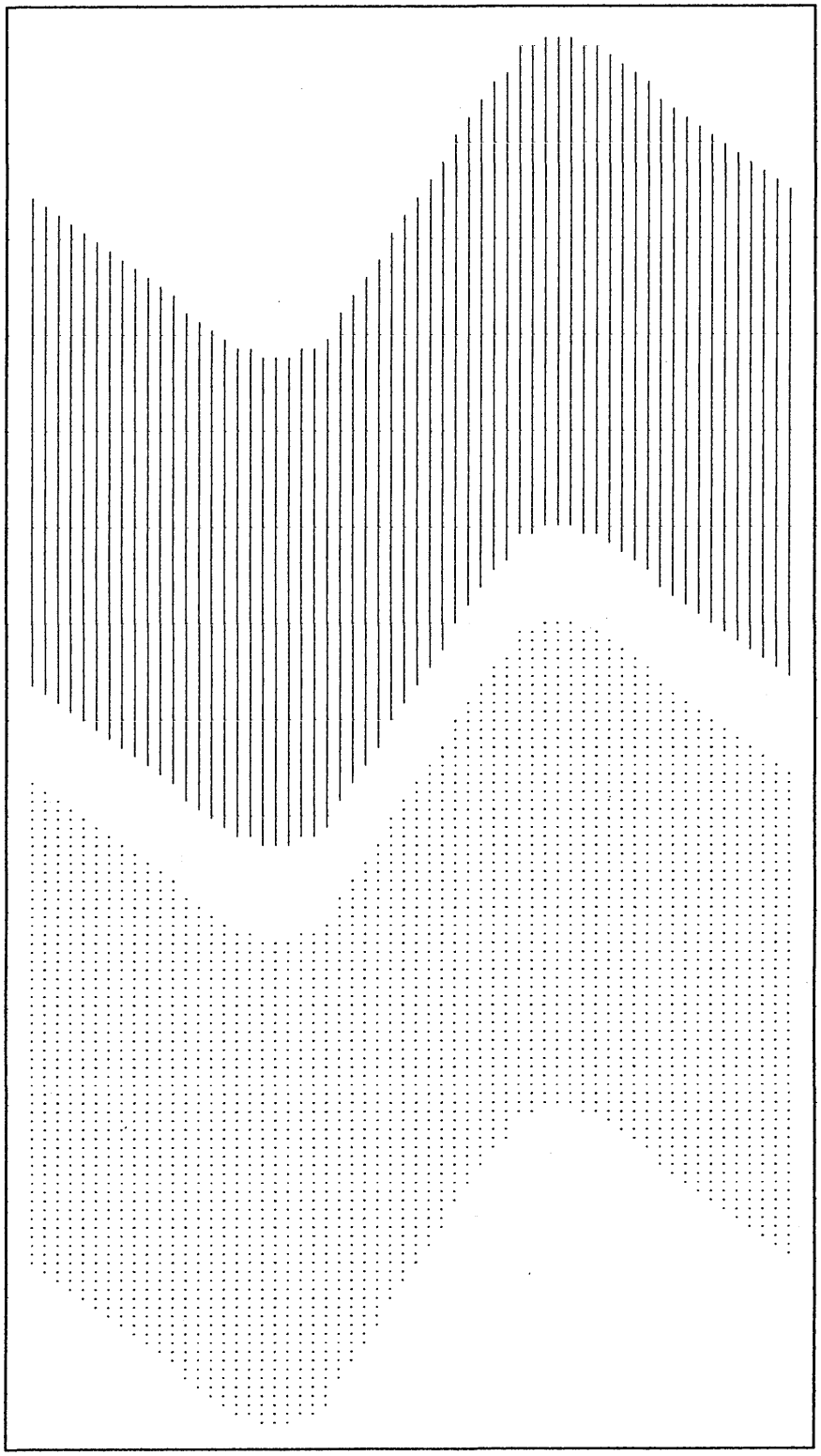

Figure 7.11: Director (top) and flow (bottom) fields for a ZBD cell of length 60 lu ($\approx$ 52 au) with nematic viscosities characteristic of MBBA shown in table (5.1) and an elasticity K set using $\bar{\omega} = 1.5$. ZBD characteristics are $h/w = 0.6$, $d/w = 0.92$ and $A = 0.5$. The bulk directors are aligned initially to 90° and the field is switched off at time $t = 0$.

Figure 7.12: Director (top) and flow (bottom) fields for a ZBD cell of length 60 lu (« 52 au) with nematic viscosities characteristic of MBBA shown in table (5.1) and an elasticity K set using **d) = 1.5. ZBD characteristics are h/w = 0.6, d/w = 0.92 and A = 0.5. The bulk directors are aligned initially to 90° and the field was switched off at time t —0, snapshot is at time t = 20.**

Figure 7.13; Director (top) and flow (bottom) fields for a ZBD cell of length 60 lu (« 52 au) with nematic viscosities characteristic of MBBA shown in table (5.1) and an elasticity K set using **Q = 1.5. ZBD characteristics are h/w — 0.6, d/w = 0.92 and A = 0.5. The bulk directors are aligned initially to 90° and the field was switched off at time t —0, snapshot is at time t = 40.**

Figlire 7.14: Director (top) and flow (bottom) fields for a ZBD cell of length 60 lu (?» 52 au) with nematic viscosities characteristic of MBBA shown in table (5.1) and an elasticity K set using Q = 1.5. ZBD characteristics are h/w = 0.6, d/w = 0.92 and A = 0.5. The bulk directors are aligned initially to 90° and the field was switched off at time t —0, snapshot is at time t = 60.

FigUfG 7.15: Director (top) and flow (bottom) fields for a ZBD cell of length 60 lu (« 52 au) with nematic viscosities characteristic of MBBA shown in table (5.1) and an elasticity K set using Q = 1.5. ZBD characteristics are h/w = 0.6, d/w = 0.92 and A = 0.5. The bulk directors are aligned initially to 90° and the field was switched off at time t = 0, snapshot is at time t = 80.

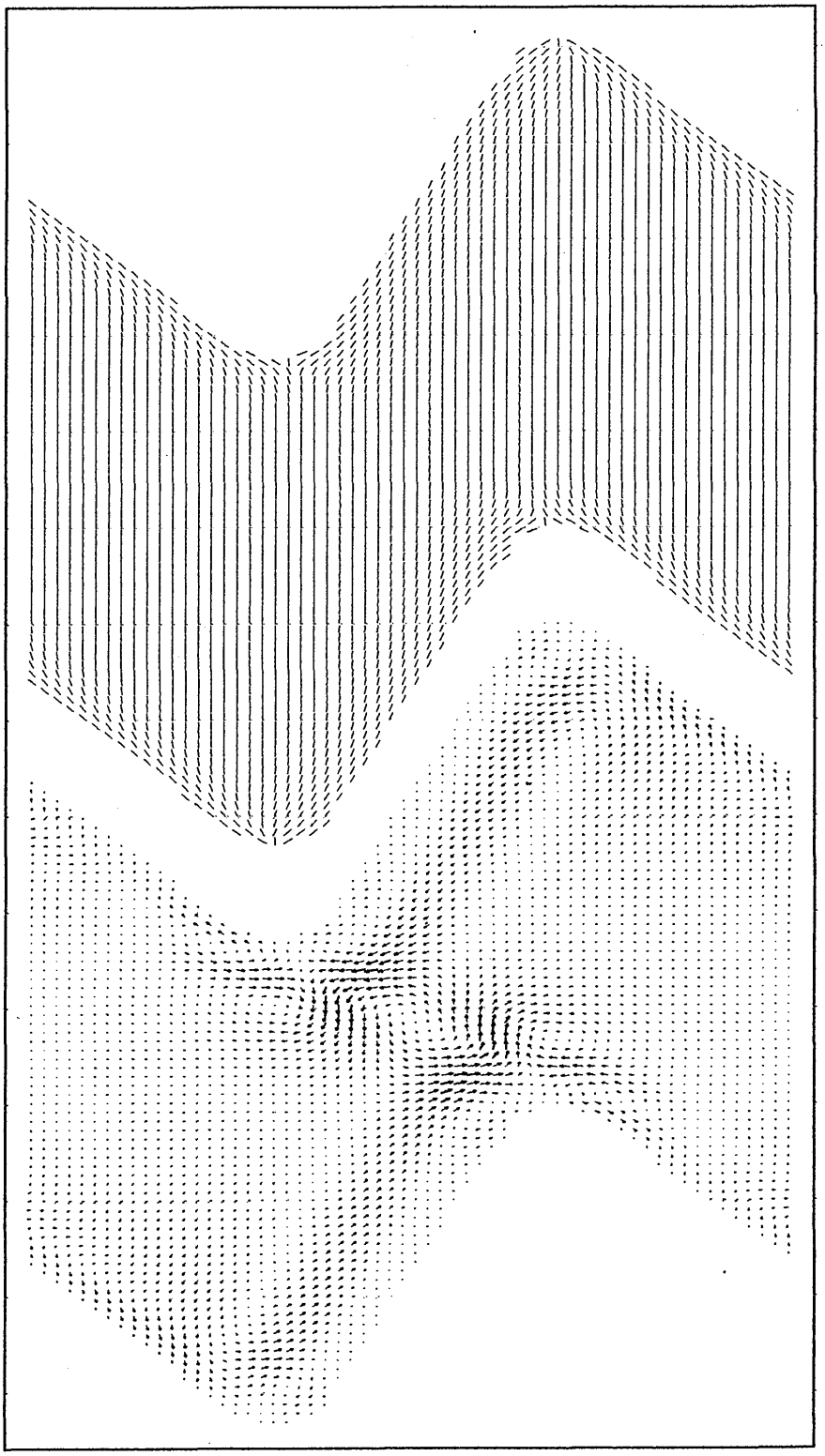

Figure 7.16: Director (top) and flow (bottom) fields for a ZBD cell of length 60 lu ($\approx$ 52 au) with nematic viscosities characteristic of MBBA shown in table (5.1) and an elasticity K set using $\bar{\omega} = 1.5$. ZBD characteristics are $h/w = 0.6$, $d/w = 0.92$ and $A = 0.5$. The bulk directors are aligned initially to 90° and the field was switched off at time $t = 0$, snapshot is at time $t = 100$.

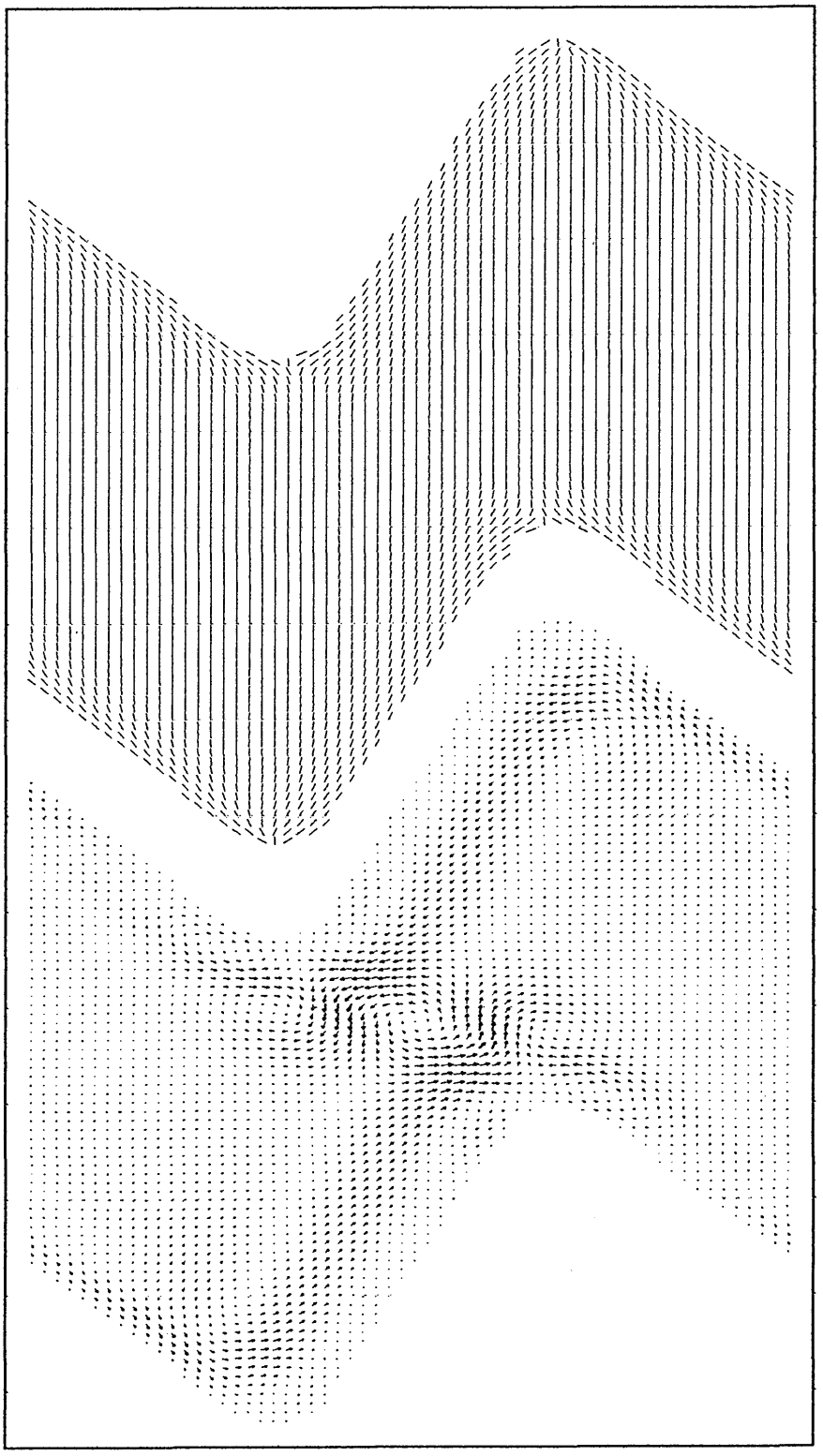

Figure 7.17: Director (top) and flow (bottom) fields for a ZBD cell of length 60 lu ($\approx$ 52 au) with nematic viscosities characteristic of MBBA shown in table (5.1) and an elasticity K set using $\bar{\omega} = 1.5$. ZBD characteristics are $h/w = 0.6$, $d/w = 0.92$ and $A = 0.5$. The bulk directors are aligned initially to 90° and the field was switched off at time $t = 0$, snapshot is at time $t = 120$.

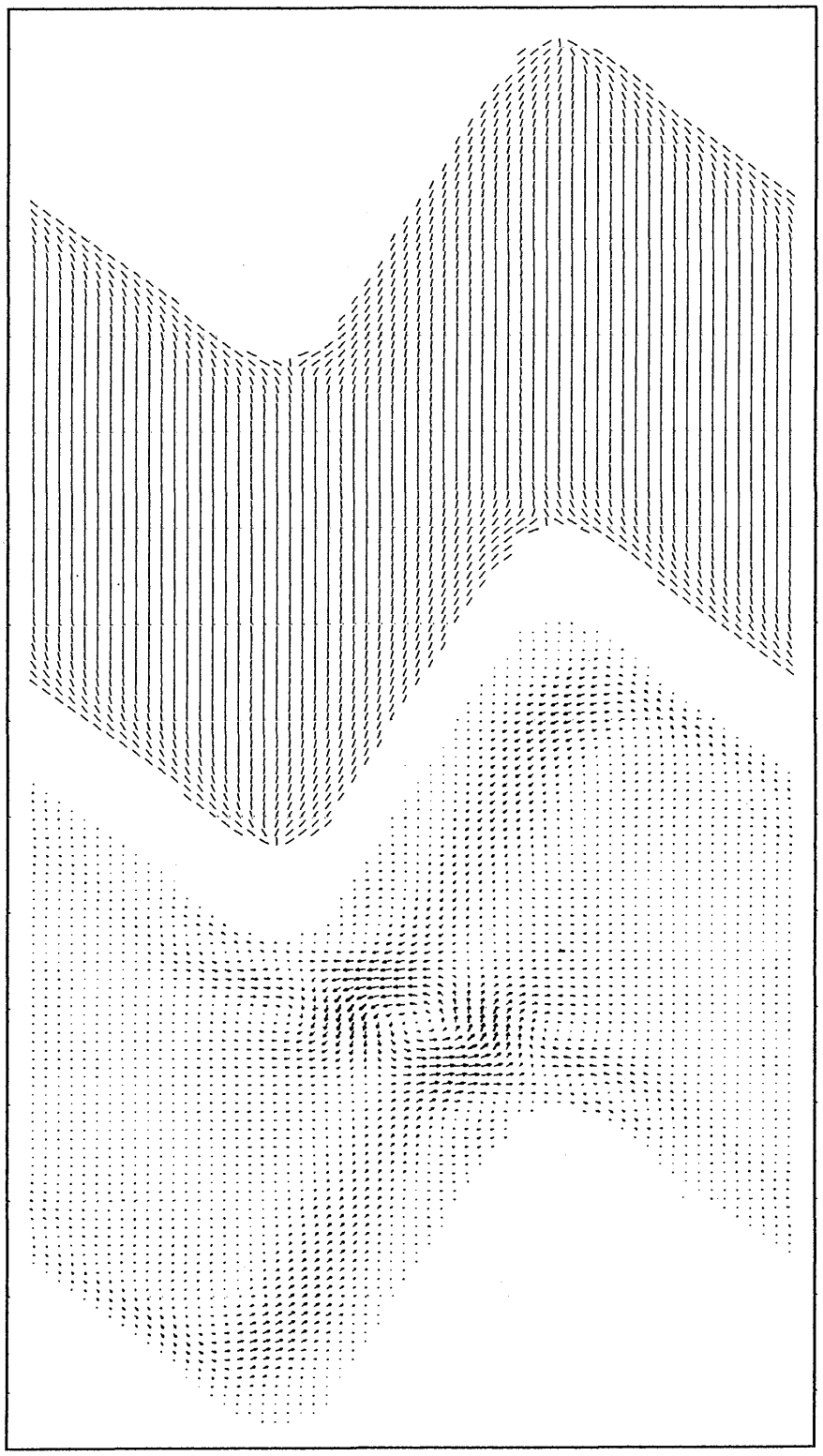

Figure 7.18: Director (top) and flow (bottom) fields for a ZBD cell of length 60 lu ($\approx$ 52 au) with nematic viscosities characteristic of MBBA shown in table (5.1) and an elasticity K set using $\bar{\omega} = 1.5$. ZBD characteristics are $h/w = 0.6$, $d/w = 0.92$ and $A = 0.5$. The bulk directors are aligned initially to 90° and the field was switched off at time $t = 0$, snapshot is at time $t = 140$.

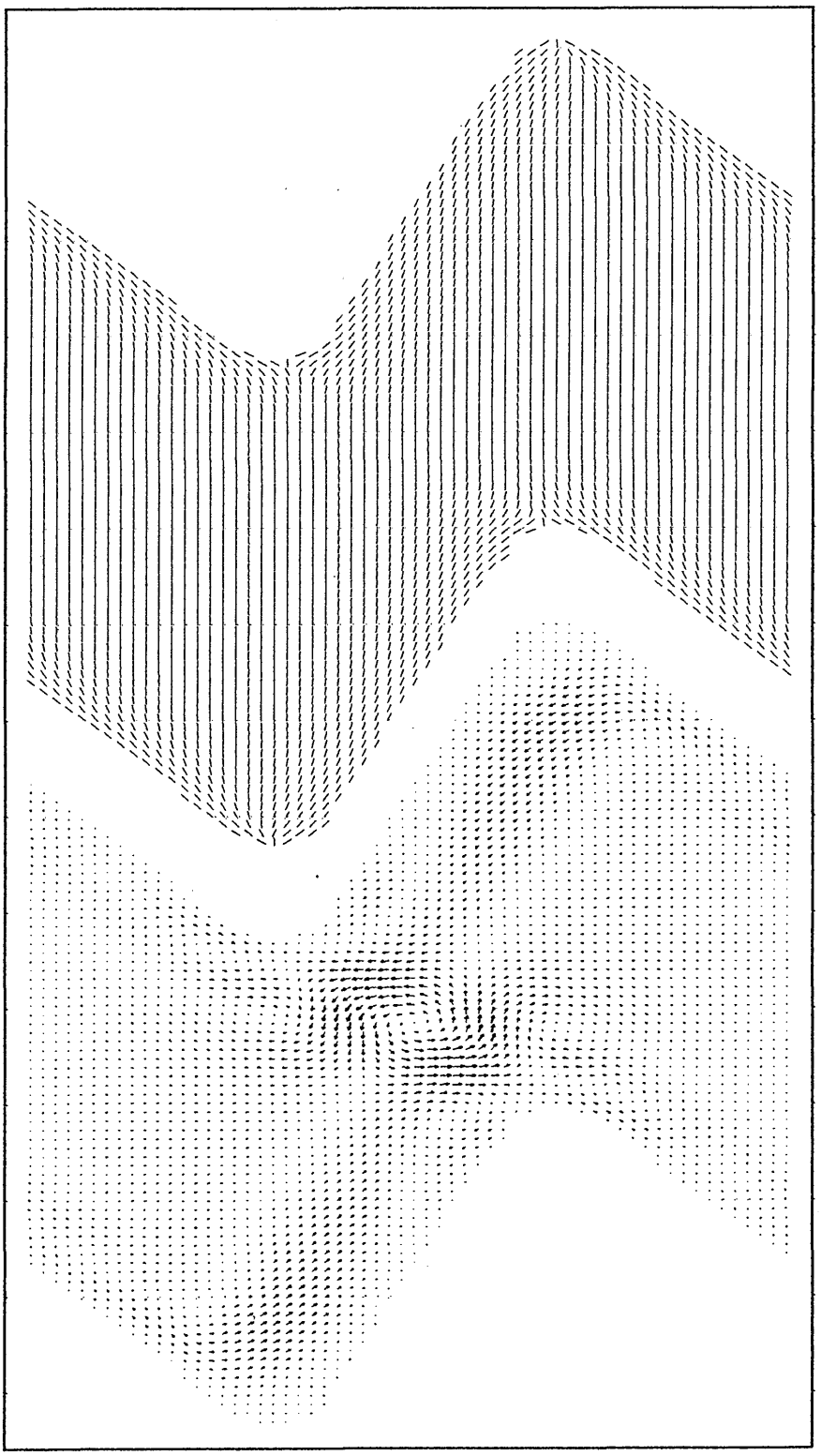

Figure 7.19: Director (top) and flow (bottom) fields for a ZBD cell of length 60 lu ($\approx$ 52 au) with nematic viscosities characteristic of MBBA shown in table (5.1) and an elasticity K set using $\bar{\omega} = 1.5$. ZBD characteristics are $h/w = 0.6$, $d/w = 0.92$ and $A = 0.5$. The bulk directors are aligned initially to 90° and the field was switched off at time $t = 0$, snapshot is at time $t = 160$.

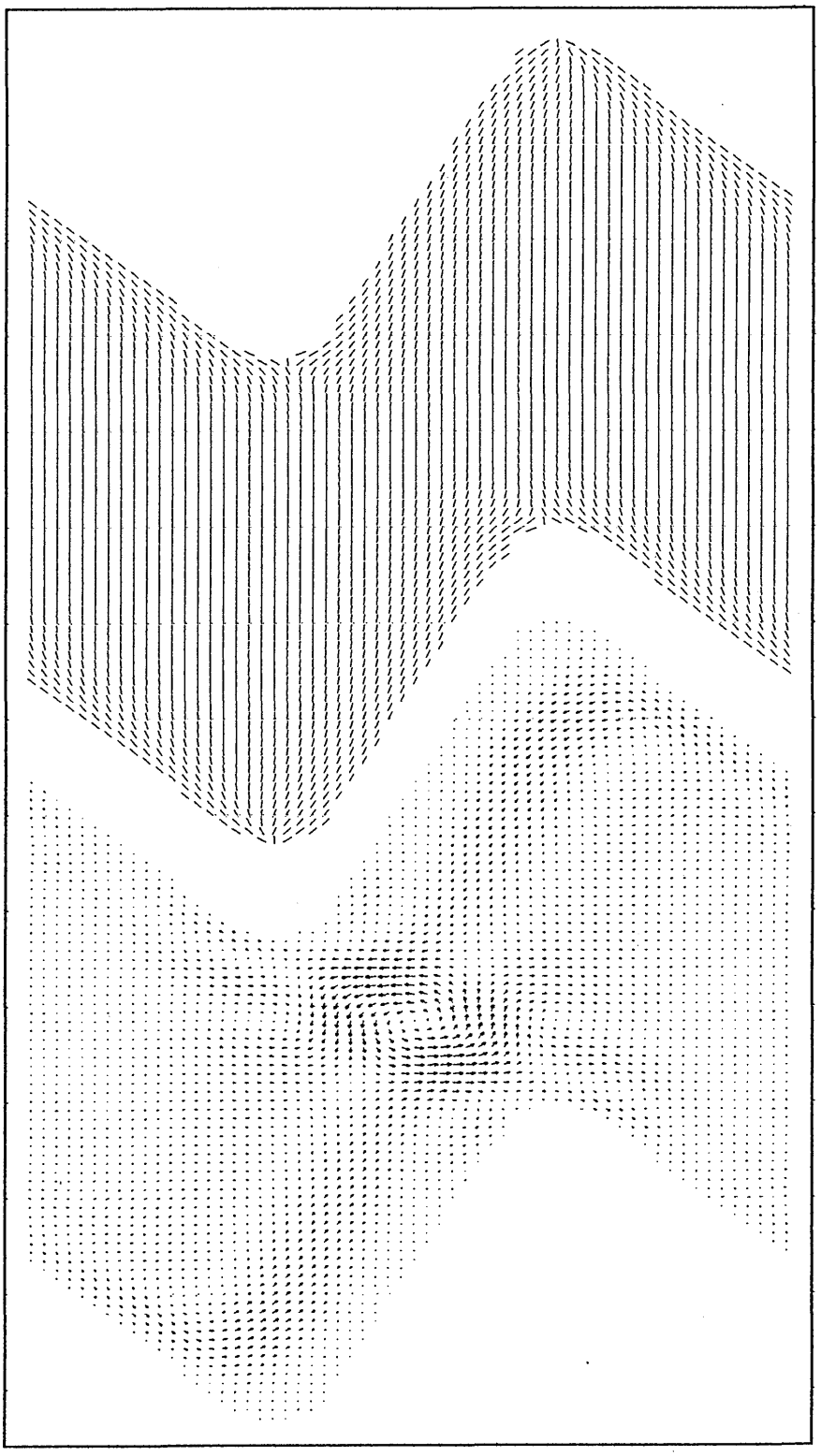

Figure 7.20: Director (top) and flow (bottom) fields for a ZBD cell of length 60 lu ($\approx$ 52 au) with nematic viscosities characteristic of MBBA shown in table (5.1) and an elasticity K set using $\bar{\omega} = 1.5$. ZBD characteristics are $h/w = 0.6$, $d/w = 0.92$ and $A = 0.5$. The bulk directors are aligned initially to 90° and the field was switched off at time $t = 0$, snapshot is at time $t = 180$.

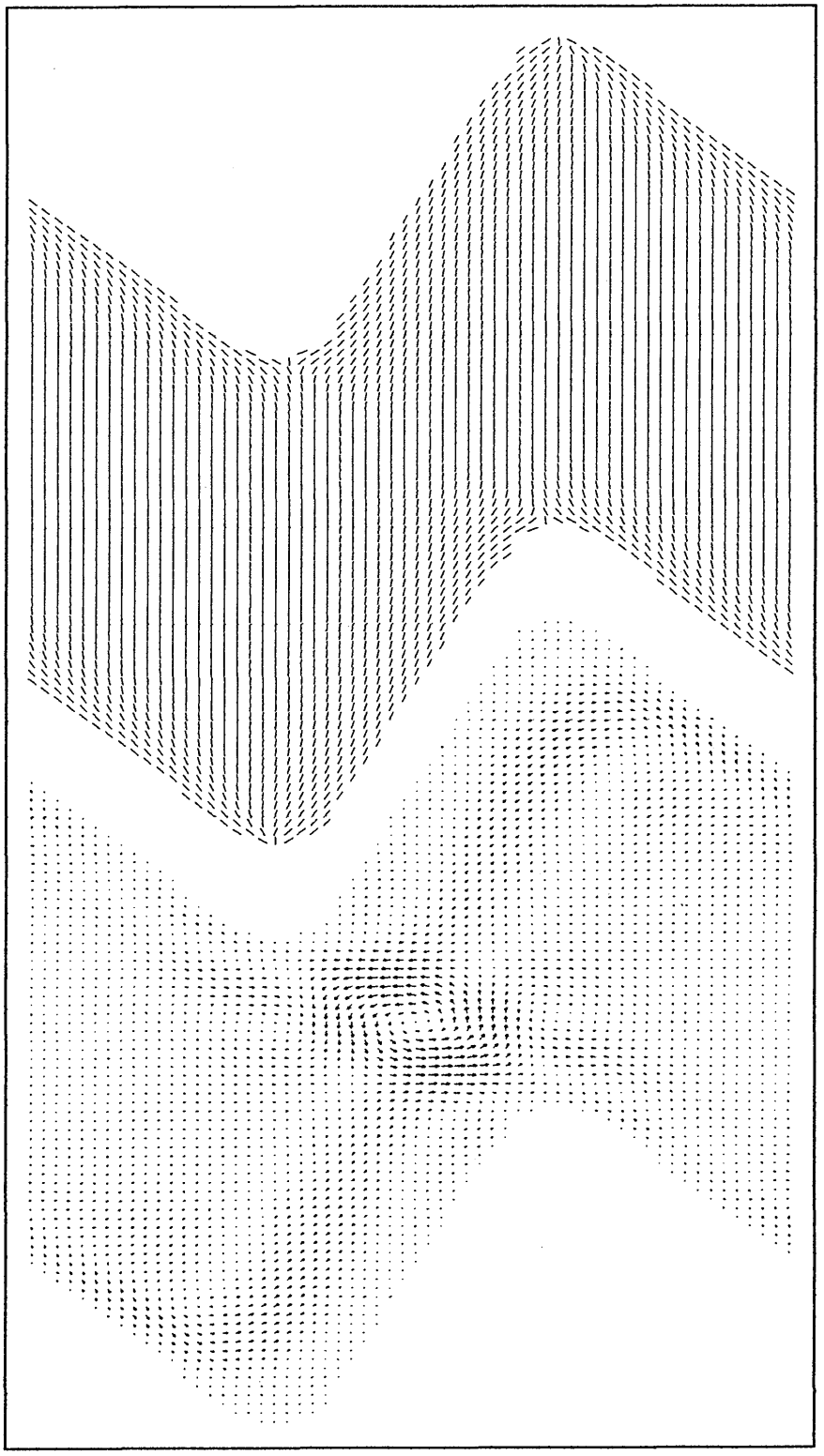

Figure 7.21: Director (top) and flow (bottom) fields for a ZBD cell of length 60 lu ($\approx$ 52 au) with nematic viscosities characteristic of MBBA shown in table (5.1) and an elasticity K set using $\bar{\omega} = 1.5$. ZBD characteristics are $h/w = 0.6$, $d/w = 0.92$ and $A = 0.5$. The bulk directors are aligned initially to 90° and the field was switched off at time $t = 0$, snapshot is at time $t = 200$.

Figures (7.11) to (7.21) show the director field relaxing towards the defect configuration with the defects occurring at the peak and troughs of the grating. The steady state director field conforms to the 90° tangential director field shown in figure (7.6).

The induced flow appears at the peaks and troughs of the grating wall as multiple (paired) recirculation regions. The trough recirculations push flow up the grating walls towards the peak, mainly along the "sharp" wall of the grating, eventually dissipating. The induced recirculations at the peaks are larger and eventually move away from the wall and into the bulk. Due to the small diameter to width ratio d/w of the ZBD cell, the flows from the adjacent opposed peaks converge and form a small singular recirculation region across the short part of the bulk.

The effect of the director field on the flow field is apparent however the effect of the induced flow on the director field is less obvious and appears to decay to rest without seriously re-effecting the director field. The overall maximum magnitude of the induced flow in this configuration was 0.004183 which, as we shall see later, is relatively small and therefore does not adversely affect the relaxation of the director field to the defect steady state. As the number of time steps increases and the director field relaxes towards the defect steady state the induced flow field decays away to rest.

The second time evolution sequence represents a steady state ZBD cell, aligned by a strongly orientating magnetic field to 0°. At time $t = 0$ the field is switched off and the initial 200 time steps of the relaxation are again observed. From figure (7.6) we know that this configuration should relax towards the smooth steady state.

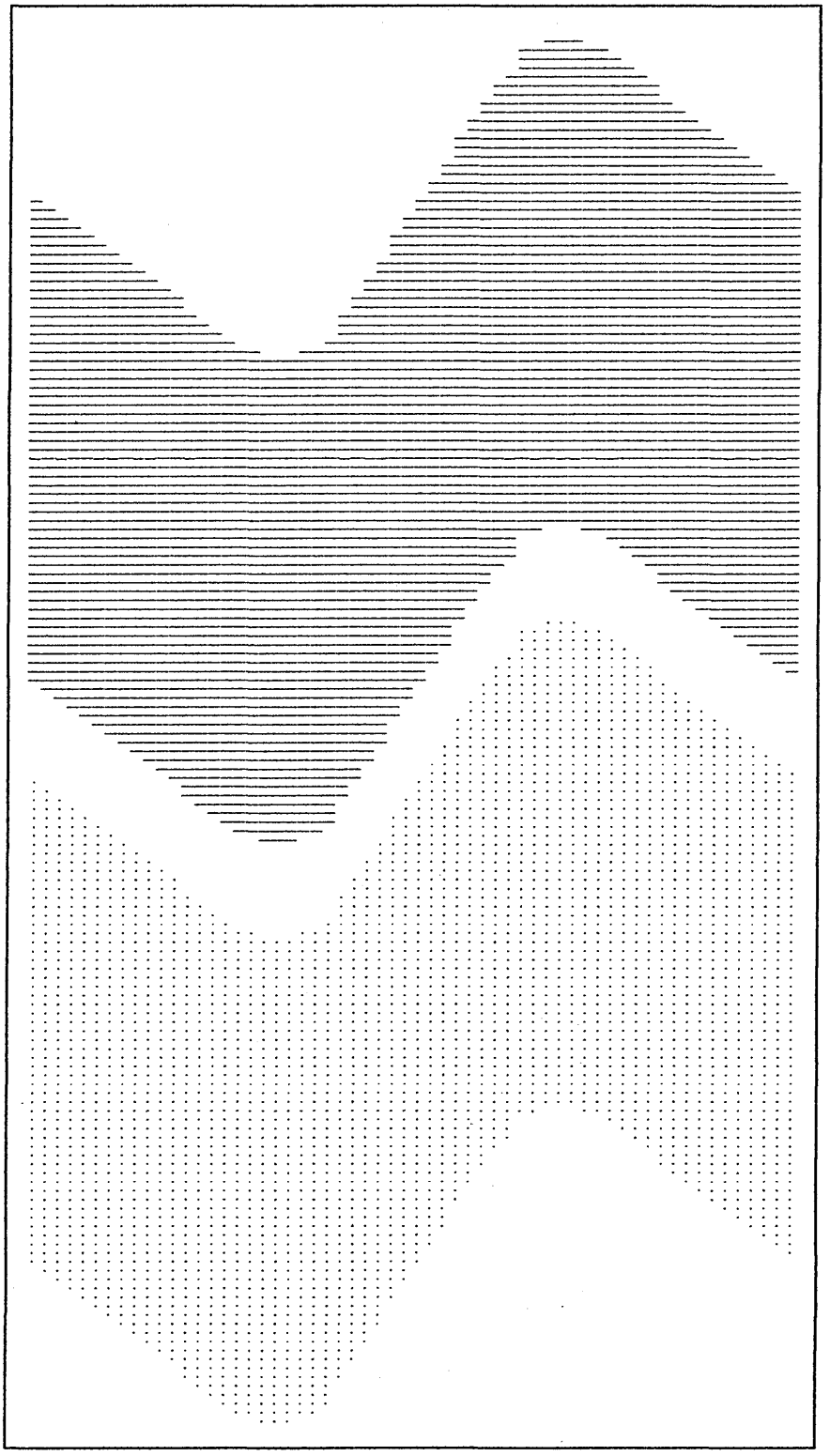

Figure 7.22: Director (top) and flow (bottom) fields for a ZBD cell of length 60 lu ($\approx$ 52 au) with nematic viscosities characteristic of MBBA shown in table (5.1) and an elasticity K set using $\bar{\omega} = 1.5$. ZBD characteristics are $h/w = 0.6$, $d/w = 0.92$ and $A = 0.5$. The bulk directors are aligned initially to 0^o and the field was switched off at time $t = 0$.

Figure 7.23: Director (top) and flow (bottom) fields for a ZBD cell of length 60 lu (?a 52 au) with nematic viscosities characteristic of MBBA shown in table (5.1) and an elasticity K set using $Q = 1.5$. ZBD characteristics are $h/w = 0.6$, $d/w = 0.92$ and $A = 0.5$. The bulk directors are aligned initially to 0° and the field was switched off at time $t = 0$, snapshot is at time $t = 20$.

Figure 7.24: Director (top) and flow (bottom) fields for a ZBD cell of length 60 lu (« 52 au) with nematic viscosities characteristic of MBBA shown in table (5.1) and an elasticity K set using Q — 1.5. ZBD characteristics are h/w = 0.6, djw = 0.92 and A = 0.5. The bulk directors are aligned initially to 0° and the field was switched off at time t = 0, snapshot is at time t = 40.

Figure 7.25: Director (top) and flow (bottom) fields for a ZBD cell of length 60 lu (« 52 au) with nematic viscosities characteristic of MBBA shown in table (5.1) and an elasticity K set using $Q = 1.5$. ZBD characteristics are $h/w = 0.6$, $d/w = 0.92$ and $A = 0.5$. The bulk directors are aligned initially to 0° and the field was switched off at time $t = 0$, snapshot is at time $t = 60$.

Pigllie 7.26i Director (top) and flow (bottom) fields for a ZBD cell of length 60 lu (« 52 au) with nematic viscosities characteristic of MBBA shown in table (5.1) and an elasticity K set using $u_{>} = 1.5$. ZBD characteristics are $h/w = 0.6$, $d/w = 0.92$ and $A = 0.5$. The bulk directors are aligned initially to 0° and the field was switched off at time $t = 0$, snapshot is at time $t = 80$.

Figure 7.27; Director (top) and flow (bottom) fields for a ZBD cell of length 60 lu (f» 52 au) with nematic viscosities characteristic of MBBA shown in table (5.1) and an elasticity K set using w = 1.5. ZBD characteristics are h/w = 0.6, d/w — 0.92 and A = 0.5. The bulk directors are aligned initially to 0° and the field was switched off at time t = 0, snapshot is at time t = 100.

Figure 7.28: Director (top) and flow (bottom) fields for a ZBD cell of length 60 lu (« 52 au) with nematic viscosities characteristic of MBBA shown in table (5.1) and an elasticity K set using $u_0 = 1.5$. ZBD characteristics are $h/w = 0.6$, $d/w = 0.92$ and $A = -0.5$. The bulk directors are aligned initially to 0° and the field was switched off at time $t = 0$, snapshot is at time $t = 120$.

Figure 7.29; Director (top) and flow (bottom) fields for a ZBD cell of length 60 lu (« 52 au) with nematic viscosities characteristic of MBBA shown in table (5.1) and an elasticity K set using $\mathcal{O} — 1.5$. ZBD characteristics are h/w = 0.6, d/w = 0.92 and A = 0.5. The bulk directors are aligned initially to 0° and the field was switched off at time t = 0, snapshot is at time t = 140.

Figure 7.30; Director (top) and flow (bottom) fields for a ZBD cell of length 60 lu 52 au) with nematic viscosities characteristic of MBBA shown in table (5.1) and an elasticity K set using u> = 1.5. ZBD characteristics are h/w = 0.6, d/w = 0.92 and A = 0.5. The bulk directors are aligned initially to 0° and the field was switched off at time t = 0, snapshot is at time t = 160.

Figure 7.311 Director (top) and flow (bottom) fields for a ZBD cell of length 60 lu *(fa* 52 au) with nematic viscosities characteristic of MBBA shown in table (5.1) and an elasticity K set using Q — 1.5. ZBD characteristics are h/w = 0.6, d/w = 0.92 and A = 0.5. The bulk directors are aligned initially to 0° and the field was switched off at time t = 0, snapshot is at time t — 180.

Figure 7.32: Director (top) and flow (bottom) fields for a ZBD cell of length 60 lu (?» 52 au) with nematic viscosities characteristic of MBBA shown in table (5.1) and an elasticity K set using Q — 1.5. ZBD characteristics axe h/w — 0.6, d/w = 0.92 and A = 0.5. The bulk directors are aligned initially to 0° and the field was switched off at time t — 0, snapshot is at time t = 200.

Figures (7.22) to (7.32) show the ZBD cell relaxing towards the smooth configuration conforming to the steady state 0^o tangential director field shown in figure (7.6).

Initially the induced flow moves down both sides of the grating wall however the peak recirculation regions observed in the previous simulation do not now appear. The flow appears to push away from the wall with a detached recirculation emerging close to the wall. Ultimately the flow forms a large recirculation region, flowing around the large part of the bulk.

The effect of the director field on the flow field is again apparent, however the induced flow again has little effect on the director field in that at all points in the simulation the director reorientates smoothly. There were no observed fluctuations in the director field which might indicate a strong influence from the velocity field. The maximum overall induced velocity magnitude for this simulation was 0.004019 which again is a relatively small being only marginally larger than the previous simulation. As the system evolves, the director field continues to relax towards the smooth steady state and the flow field again decays to rest.

The third time evolution sequence represents a ZBD cell that has initially been allowed to relax to one of its steady states. In this case we take the system considered in the last evolution sequence, therefore is is the smooth steady state with no defects at the grating wall that is produced. At time $t = 0$ a strongly orientating magnetic field in the 90^o direction is applied uniformly at all points in the cell.

The reaction of the nematic in the cell to the applied field is very quick, again, it appears that the flow modes are slaved to the director and so only the first 45 time steps of the evolution sequence are shown in 5 time step incremental snapshots. The magnetic field is applied continuously throughout the sequence ultimately pinning the director in the direction of the applied field.

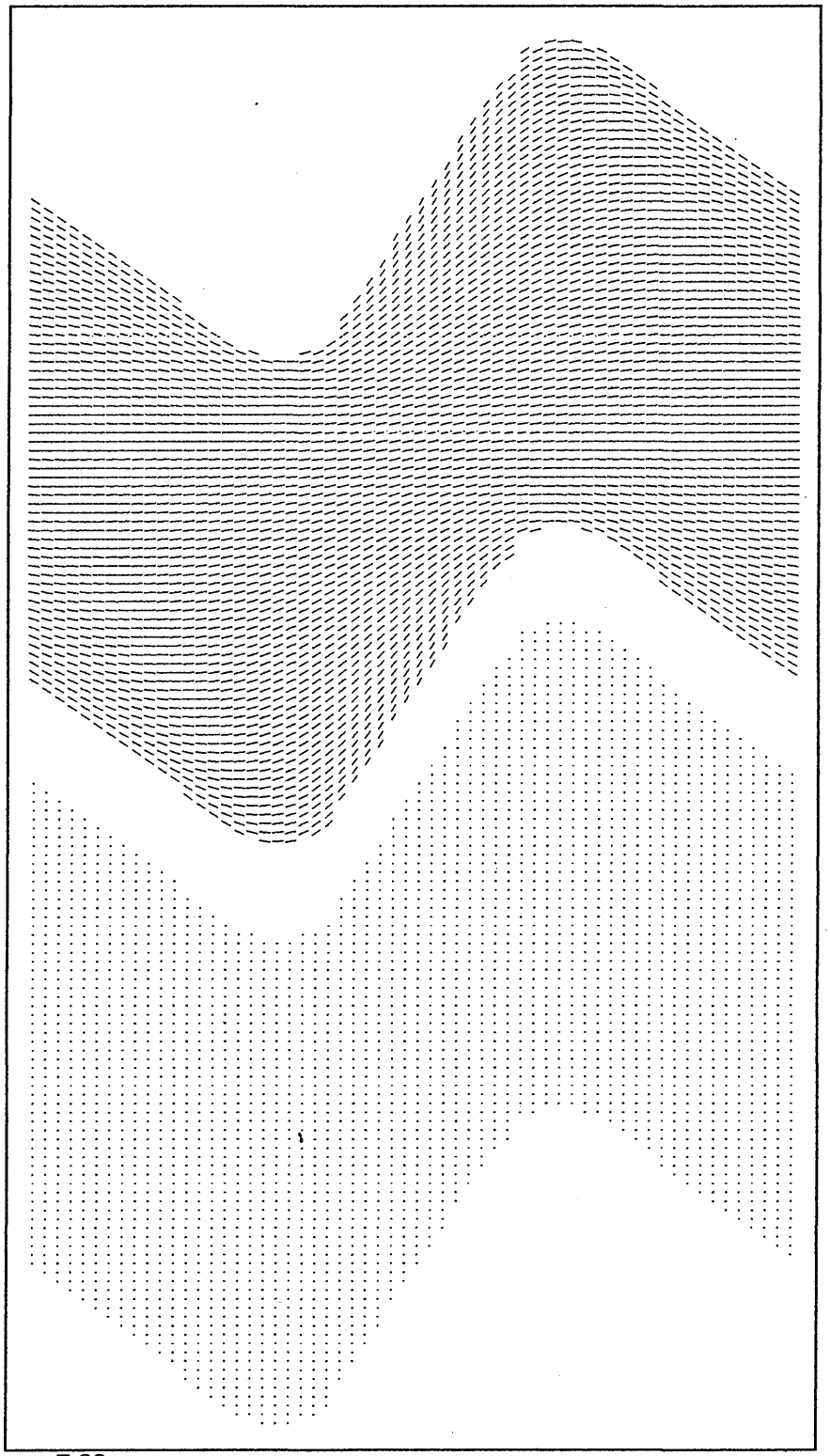

Figure 7.33: Director (top) and flow (bottom) fields for a ZBD cell of length 60 lu ($\approx$ 52 au) with nematic viscosities characteristic of MBBA shown in table (5.1) and an elasticity K set using $\bar{\omega} = 1.5$. ZBD characteristics are $h/w = 0.6$, $d/w = 0.92$ and $A = 0.5$. The bulk directors are aligned initially to the smooth configuration and at at time $t = 0$ a magnetic field of strength $H = 0.2$ ($\chi_a = 1$) is switched on in the direction of 90°.

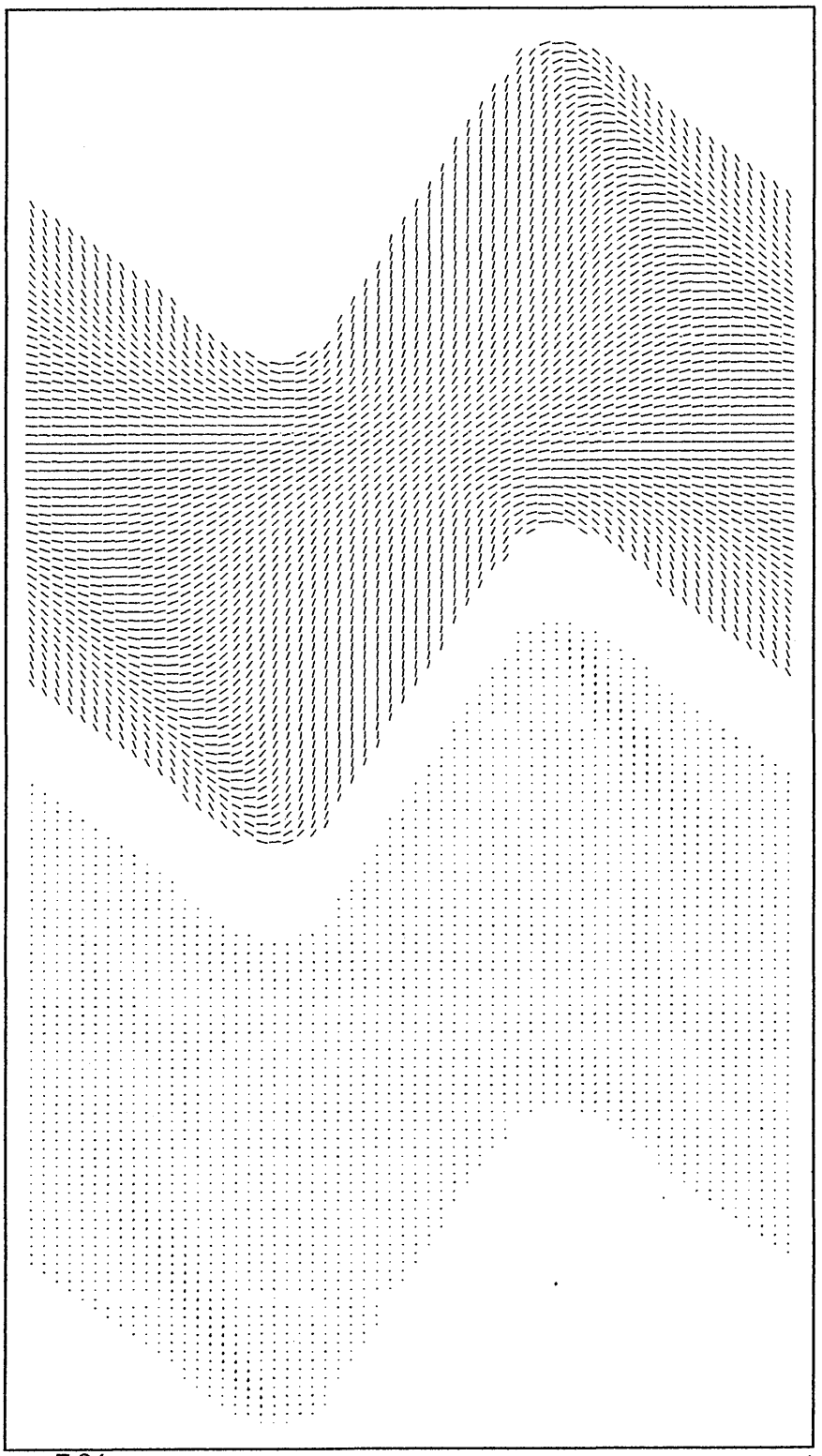

Figure 7.34: Director (top) and flow (bottom) fields for a ZBD cell of length 60 lu ($\approx$ 52 au) with nematic viscosities characteristic of MBBA shown in table (5.1) and an elasticity K set using $\bar{\omega} = 1.5$. ZBD characteristics are $h/w = 0.6$, $d/w = 0.92$ and $A = 0.5$. The bulk directors are aligned initially to the smooth configuration and at at time $t = 0$ a magnetic field of strength $H = 0.2$ ($\chi_a = 1$) is switched on in the direction of 90^o. Snapshot is at time $t = 05$.

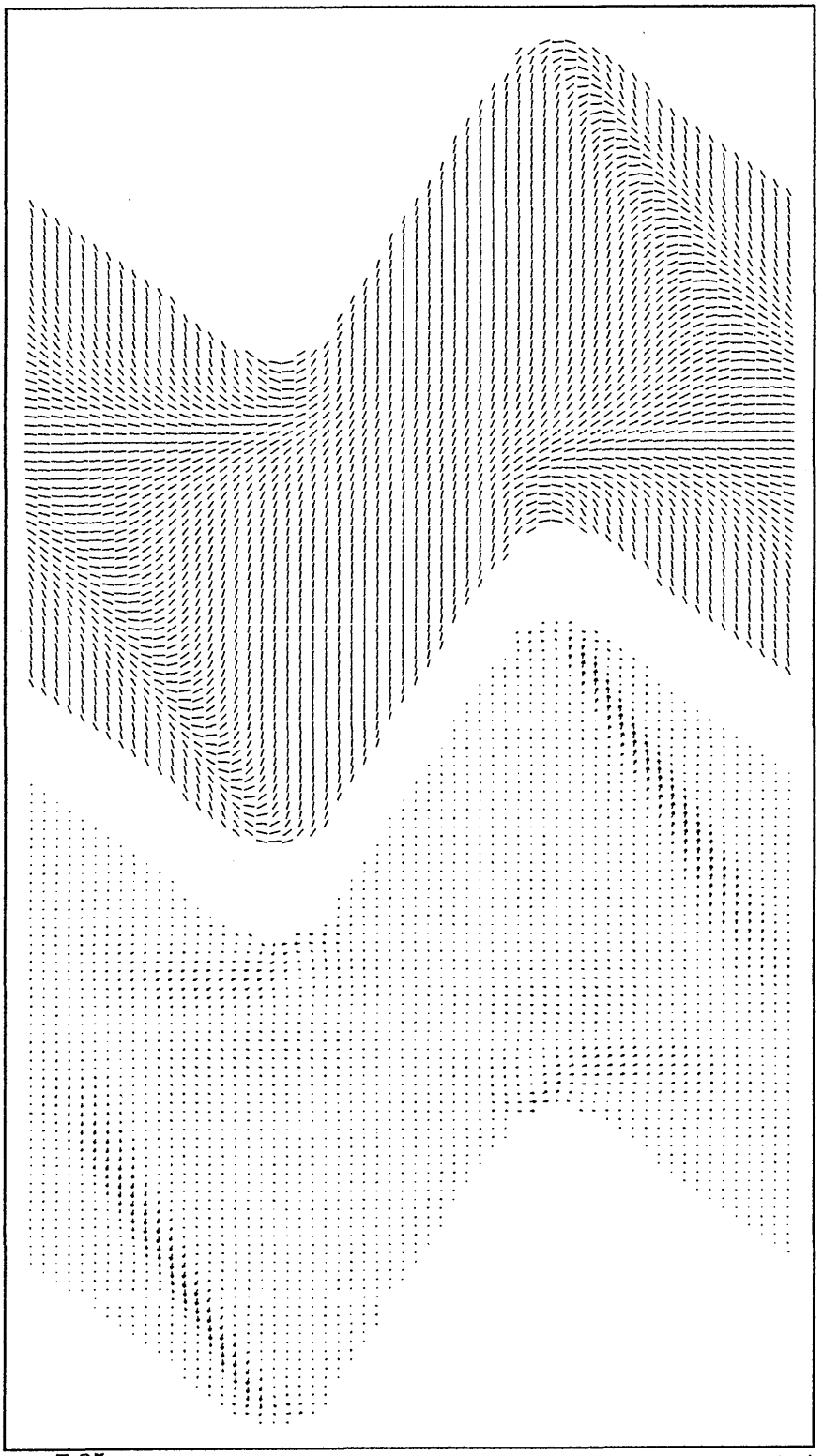

Figure 7.35: Director (top) and flow (bottom) fields for a ZBD cell of length 60 lu ($\approx$ 52 au) with nematic viscosities characteristic of MBBA shown in table (5.1) and an elasticity K set using $\bar{\omega} = 1.5$. ZBD characteristics are $h/w = 0.6$, $d/w = 0.92$ and $A = 0.5$. The bulk directors are aligned initially to the smooth configuration and at at time $t = 0$ a magnetic field of strength $H = 0.2$ ($\chi_a = 1$) is switched on in the direction of 90°. Snapshot is at time $t = 10$.

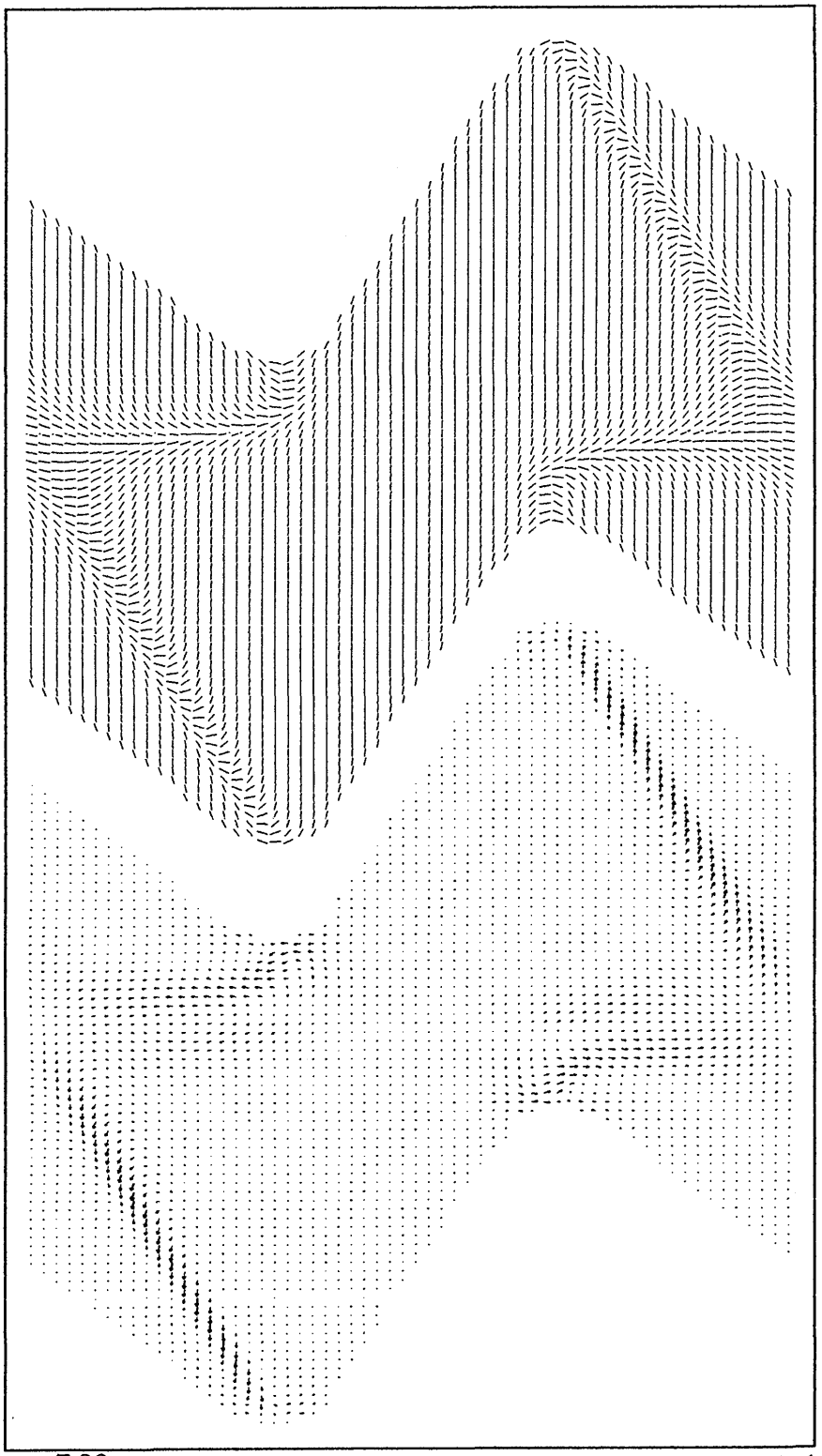

Figure 7.36: Director (top) and flow (bottom) fields for a ZBD cell of length 60 lu ($\approx$ 52 au) with nematic viscosities characteristic of MBBA shown in table (5.1) and an elasticity K set using $\bar{\omega} = 1.5$. ZBD characteristics are $h/w = 0.6$, $d/w = 0.92$ and $A = 0.5$. The bulk directors are aligned initially to the smooth configuration and at at time $t = 0$ a magnetic field of strength $H = 0.2$ ($\chi_a = 1$) is switched on in the direction of 90^o. Snapshot is at time $t = 15$.

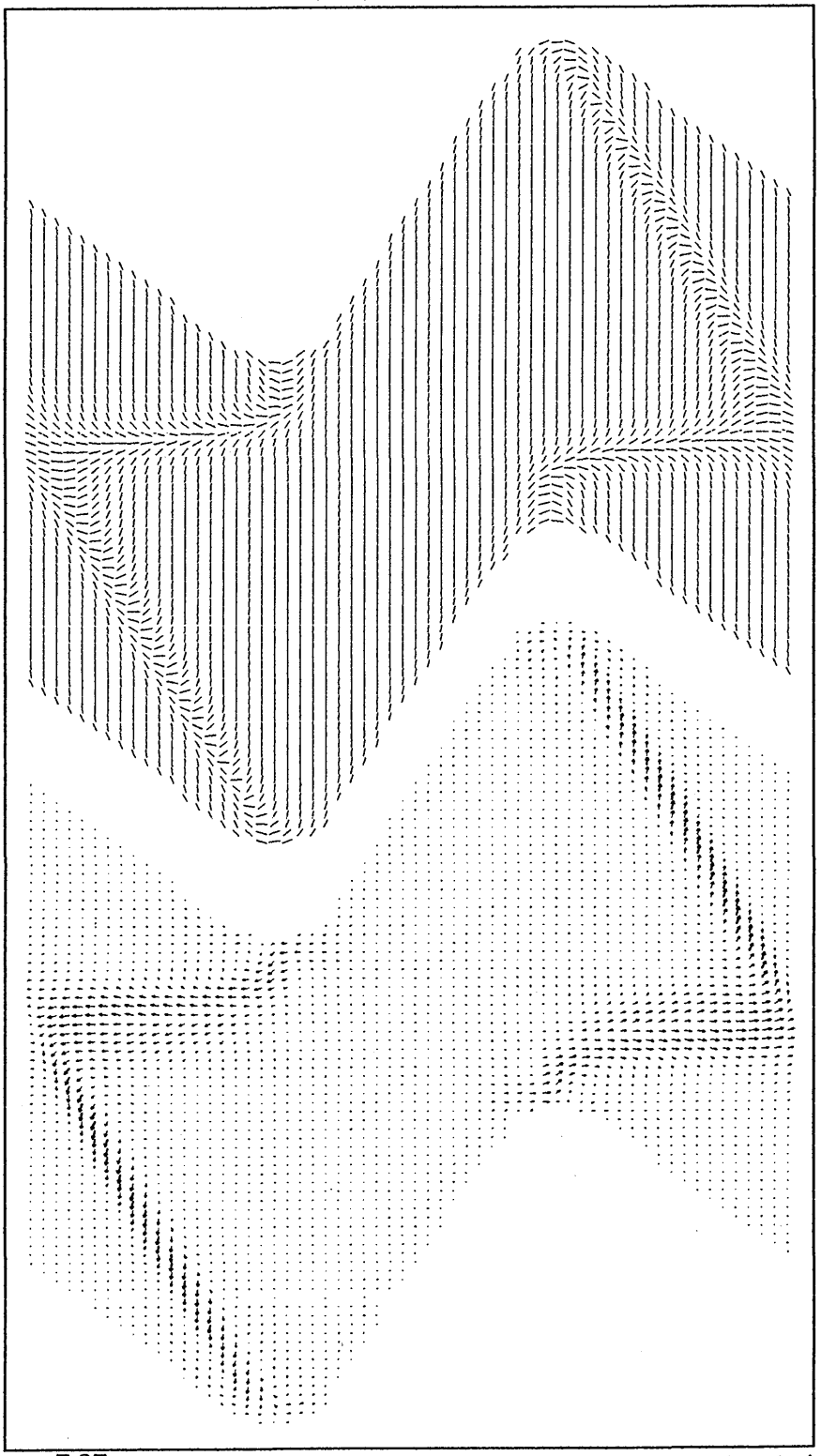

Figure 7.37: Director (top) and flow (bottom) fields for a ZBD cell of length 60 lu ($\approx$ 52 au) with nematic viscosities characteristic of MBBA shown in table (5.1) and an elasticity K set using $\bar{\omega} = 1.5$. ZBD characteristics are $h/w = 0.6$, $d/w = 0.92$ and, $A = 0.5$. The bulk directors are aligned initially to the smooth configuration and at at time $t = 0$ a magnetic field of strength $H = 0.2$ ($\chi_a = 1$) is switched on in the direction of 90°. Snapshot is at time $t = 20$.

Figure 7.38: Director (top) and flow (bottom) fields for a ZBD cell of length 60 lu *(fa* 52 au) with nematic viscosities characteristic of MBBA shown in table (5.1) and an elasticity K set using $Q = 1.5$. ZBD characteristics are $h/w = 0.6$, $d/w = 0.92$ and $A = 0.5$. The bulk directors are aligned initially to the smooth configuration and at at time $t = 0$ a magnetic field of strength $H = 0.2$ *(xa* = 1) is switched on in the direction of 90°. Snapshot is at time $t = 25$.

Figure 7.39; Director (top) and flow (bottom) fields for a ZBD cell of length 60 lu (« 52 au) with nematic viscosities characteristic of MBBA shown in table (5.1) and an elasticity K set using u> = 1.5. ZBD characteristics are h/w = 0.6, d/w = 0.92 and A = 0.5. The bulk directors are aligned initially to the smooth configuration and at at time (= 0 a magnetic field of strength H = 0.2 (xo —1) is switched on in the direction of 90°. Snapshot is at time t = 30.

Figure 7.40: Director (top) and flow (bottom) fields for a ZBD cell of length 60 lu *(fa* **52** au) with nematic viscosities characteristic of MBBA shown in table (5.1) and an elasticity K set using $Q = 1.5$. ZBD characteristics are h/w — 0.6, $d/w = 0.92$ and $A = 0.5$. The bulk directors **are aligned initially to the smooth configuration and at at time i = 0 a magnetic field of strength $H = 0.2$ *(xa* = 1) is switched on in the direction of 90°. Snapshot is at time $t = 35$.**

Figure 7.41: **Director** (top) and flow (bottom) fields for **a** ZBD cell of length 60 **lu** (« 52 au) with nematic viscosities characteristic of MBBA shown in table (5.1) and an elasticity K set using u> = 1.5. ZBD characteristics are h/w = 0.6, d/w = 0.92 and A = 0.5. The bulk directors are aligned initially to the smooth configuration and at at time t = 0 a magnetic field of strength H = 0.2 *(Xa* = 1) is switched on in the direction of 90°. Snapshot is at time t — 40.

Figure 7.42: Director (top) and flow (bottom) fields for a ZBD cell of length 60 lu (p» 52 au) with nematic viscosities characteristic of MBBA shown in table (5.1) and an elasticity K set using u = 1.5. ZBD characteristics are h/w = 0.6, d/w = 0.92 and A = 0.5. The bulk directors **are aligned initially to the smooth configuration and at at time t = 0 a magnetic field of strength H = 0.2 (Xa = 1) switched on in the direction of 90°. Snapshot is at time t —45.**

Figures (7.33) to (7.42) show the ZBD cell bulk directors reorientating towards the direction of the applied magnetic field. Due to the director orientations at the surface grating profile, some of the directors reorientate clockwise while other directors reorientate anti-clockwise. Ultimately this creates nematic domains within the bulk, separated by disclination walls and terminated at the wall by $\pm 1/2$ defects. As the time sequence progresses we can observe the disclination walls detaching from the grating profile and shrinking within the bulk until all the bulk directors are aligned in the direction of the applied field.

The formation of these defects and disclination walls produce a much larger flow field than in the previous relaxation cases. The overall maximum observed velocity magnitude in this case was 0.031897 which is approximately ten times as large as the flows that are produced in the relaxation cases.

The induced flow follows the disclination wall very tightly, flowing downwards into a trough and upwards away from a peak. Flow induced on the slopes of the grating is of the same order of magnitude as in the previous simulations and is effectively swamped by the induced flows due to the disclination walls. Moreover the induced flow is much larger in this simulation and the time required for the flow to decay to rest is much longer even though the director field is pinned by the magnetic field very quickly (within 50 time steps).

The final time evolution sequence represents a ZBD cell that has been allowed to reach the defect steady state. At time $t = 0$ a strongly orientating magnetic field is again applied this time in the direction 0^o. The magnetic field remains on for the duration of the simulation.

The reaction of the nematic cell is again rapid and hence only the first 45 time steps are displayed, again in snapshots of every 5 time steps.

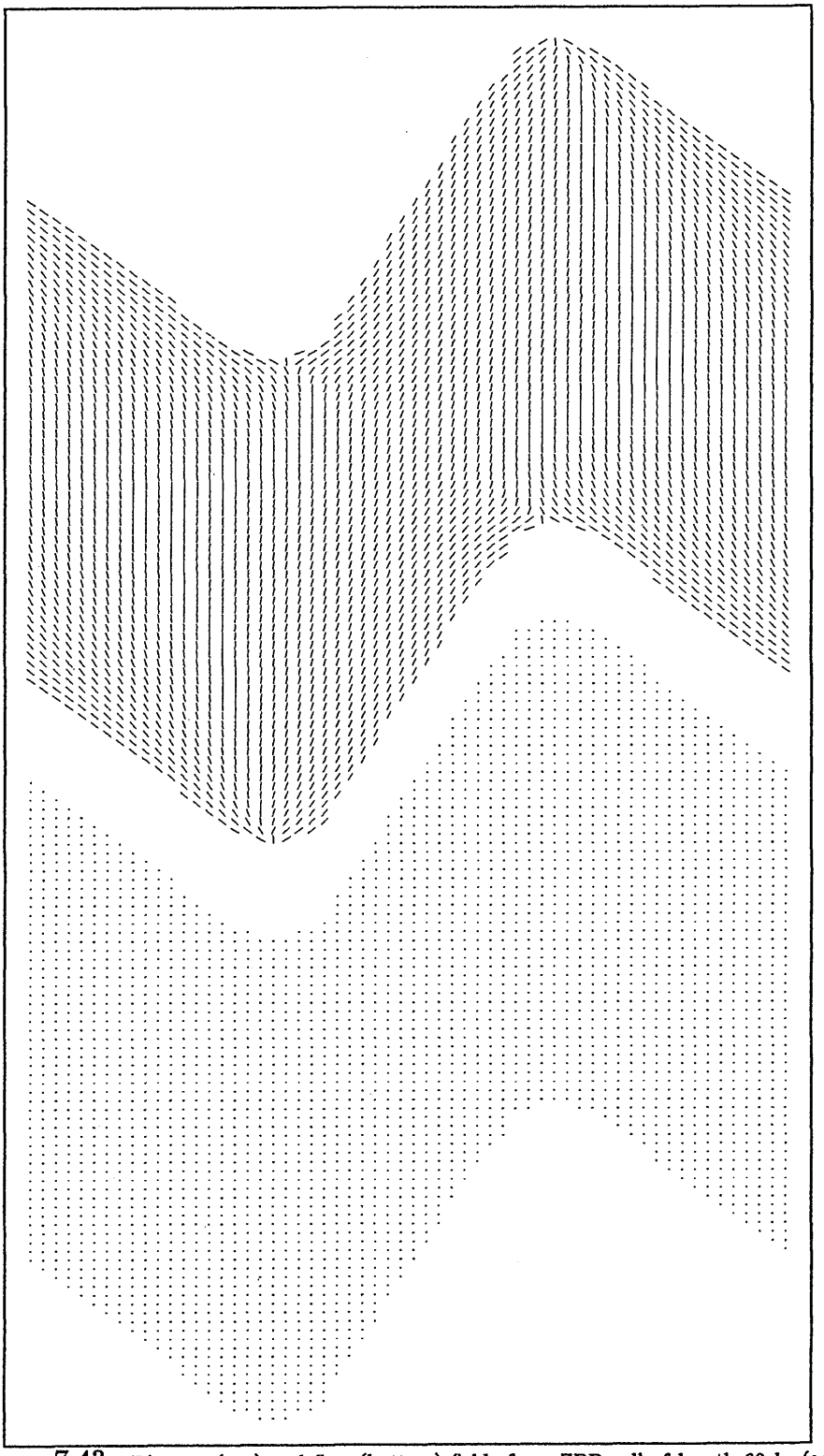

Figure 7.43: Director (top) and flow (bottom) fields for a ZBD cell of length 60 lu ($\approx$ 52 au) with nematic viscosities characteristic of MBBA shown in table (5.1) and an elasticity K set using $\tilde{\omega} = 1.5$. ZBD characteristics are $h/w = 0.6$, $d/w = 0.92$ and $A = 0.5$. The bulk directors are aligned initially to the defect configuration and at at time $t = 0$ a magnetic field of strength $H = 0.2$ ($\chi_a = 1$) is switched on in the direction of 0^o.

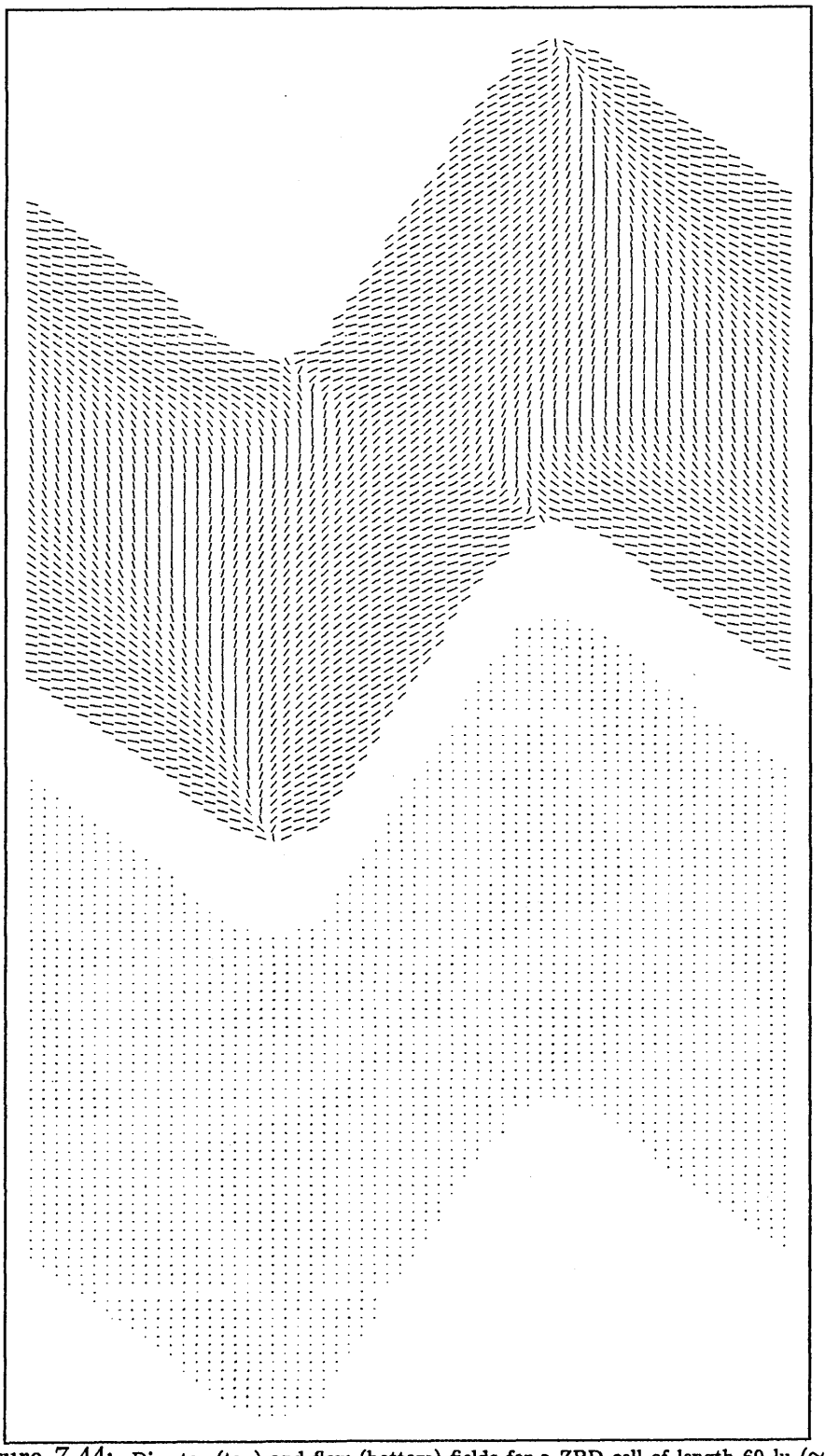

Figure 7.44: Director (top) and flow (bottom) fields for a ZBD cell of length 60 lu ($\approx$ 52 au) with nematic viscosities characteristic of MBBA shown in table (5.1) and an elasticity K set using $\bar{\omega} = 1.5$. ZBD characteristics are $h/w = 0.6$, $d/w = 0.92$ and $A = 0.5$. The bulk directors are aligned initially to the defect configuration and at at time $t = 0$ a magnetic field of strength $H = 0.2$ ($\chi_a = 1$) is switched on in the direction of 0^o. Snapshot is at time $t = 5$.

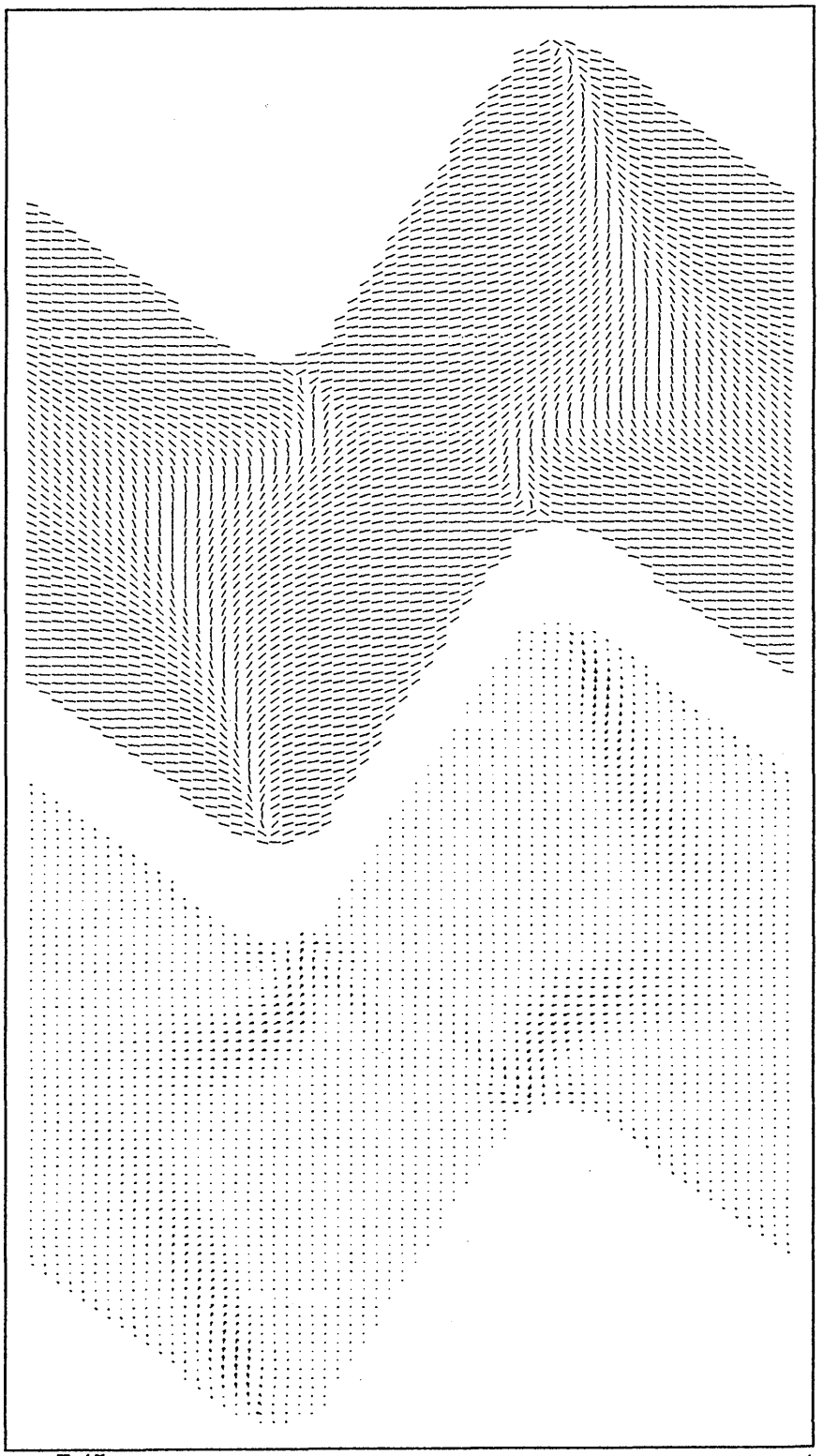

Figure 7.45: Director (top) and flow (bottom) fields for a ZBD cell of length 60 lu ($\approx$ 52 au) with nematic viscosities characteristic of MBBA shown in table (5.1) and an elasticity K set using $\bar{\omega} = 1.5$. ZBD characteristics are $h/w = 0.6$, $d/w = 0.92$ and $A = 0.5$. The bulk directors are aligned initially to the defect configuration and at at time $t = 0$ a magnetic field of strength $H = 0.2$ ($\chi_a = 1$) is switched on in the direction of 0^o. Snapshot is at time $t = 10$.

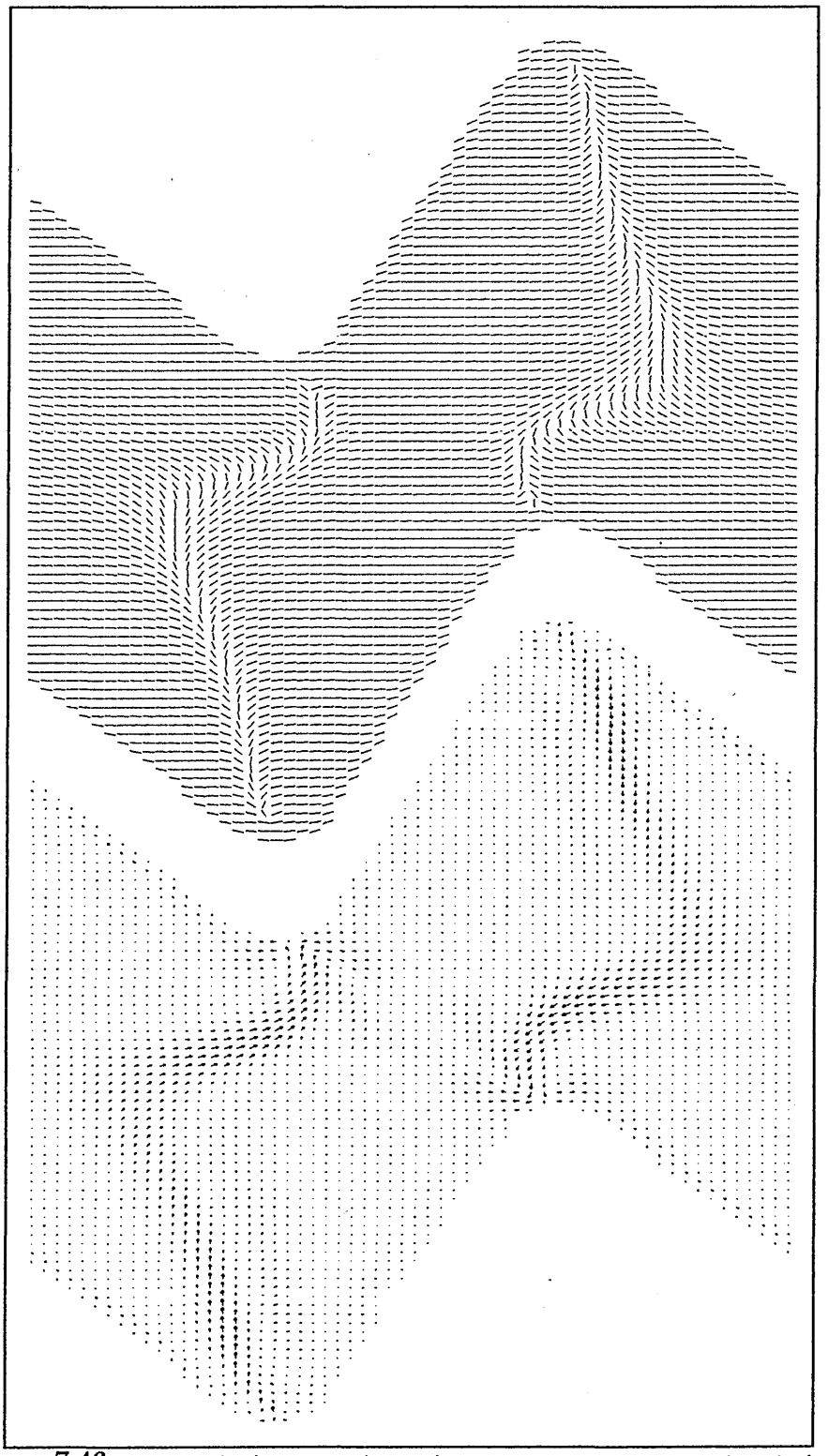

Figure 7.46: Director (top) and flow (bottom) fields for a ZBD cell of length 60 lu ($\approx$ 52 au) with nematic viscosities characteristic of MBBA shown in table (5.1) and an elasticity K set using $\bar{\omega} = 1.5$. ZBD characteristics are $h/w = 0.6$, $d/w = 0.92$ and $A = 0.5$. The bulk directors are aligned initially to the defect configuration and at at time $t = 0$ a magnetic field of strength $H = 0.2$ ($\chi_a = 1$) is switched on in the direction of 0^o. Snapshot is at time $t = 15$.

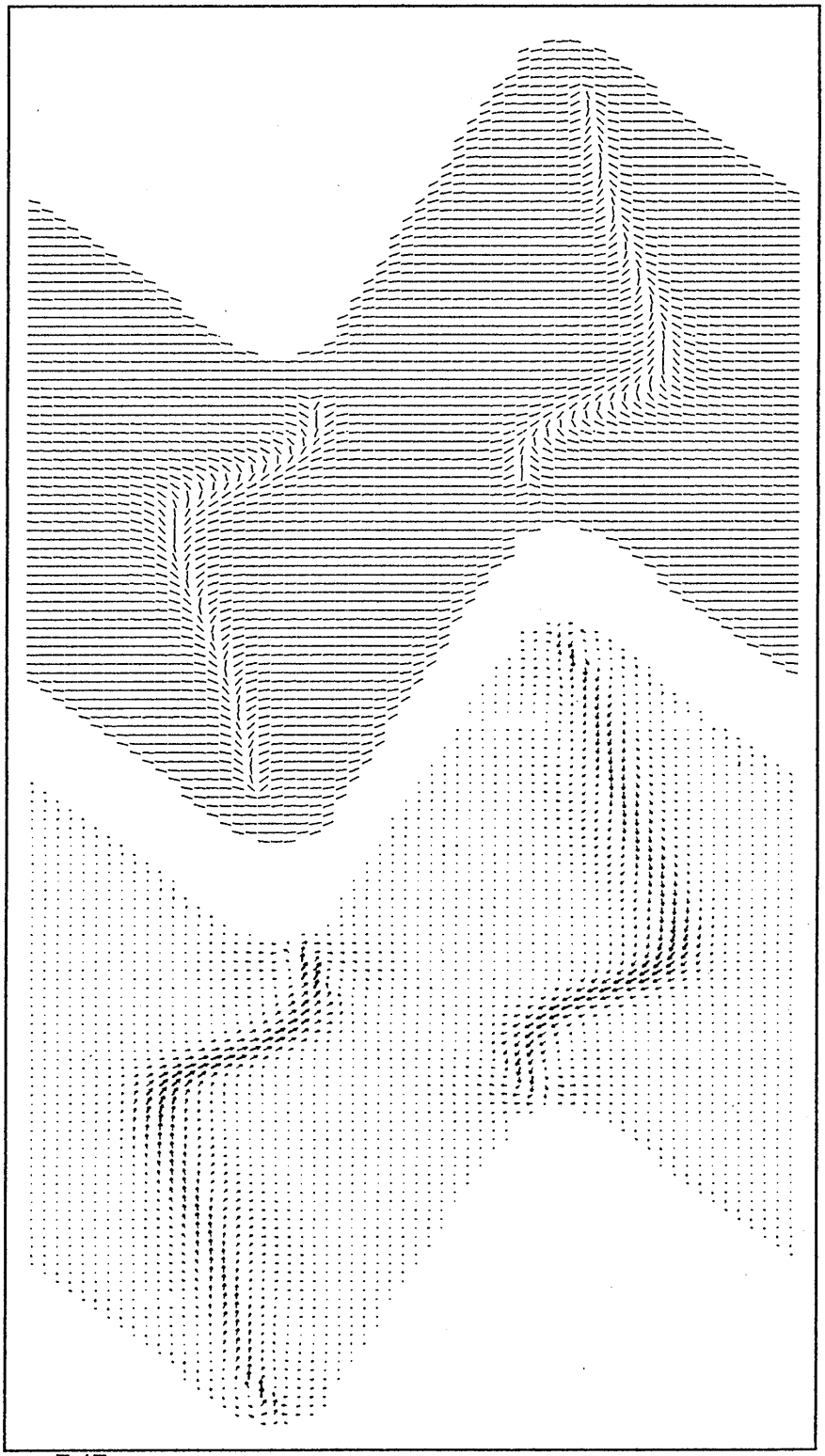

Figure 7.47: Director (top) and flow (bottom) fields for a ZBD cell of length 60 lu ($\approx$ 52 au) with nematic viscosities characteristic of MBBA shown in table (5.1) and an elasticity K set using $\bar{\omega} = 1.5$. ZBD characteristics are $h/w = 0.6$, $d/w = 0.92$ and $A = 0.5$. The bulk directors are aligned initially to the defect configuration and at at time $t = 0$ a magnetic field of strength $H = 0.2$ ($\chi_a = 1$) is switched on in the direction of 0°. Snapshot is at time $t = 20$.

Figure 7.48; Director (top) and flow (bottom) fields for a ZBD cell of length 60 lu (« 52 au) with nematic viscosities characteristic of MBBA shown in table (5.1) and an elasticity K set using Q = 1.5. ZBD characteristics are h/w = 0.6, d/w = 0.92 and A — 0.5. The bulk directors are aligned initially to the defect configuration and at at time t ~ 0 a magnetic field of strength H = 0.2 (xa = 1) is switched on in the direction of 0°. Snapshot is at time t = 25.

Figure 7.49: Director (top) and flow (bottom) fields for a ZBD cell of length 60 lu *(as* 52 au) with nematic viscosities characteristic of MBBA shown in table (5.1) and an elasticity K set using G = 1.5. ZBD characteristics are h/w = 0.6, d/w = 0.92 and A = 0.5. The bulk directors are aligned initially to the defect configuration and at at time t = 0 a magnetic field of strength H = 0.2 (xo = 1) is switched on in the direction of 0°. Snapshot is at time t = 30.

Figure 7.50: Director (top) and flow (bottom) fields for a ZBD cell of length 60 lu (« 52 au) with nematic viscosities characteristic of MBBA shown in table (5.1) and an elasticity K set using $Q = 1.5$. ZBD characteristics are $h/w = 0.6$, $d/w — 0.92$ and $A — 0.5$. The bulk directors are aligned initially to the defect configuration and at at time $t = 0$ a magnetic field of strength $H = 0.2$ (xo = 1) is switched on in the direction of 0°. Snapshot is at time $t = 35$.

Figure 7.51: Director (top) and flow (bottom) fields for a ZBD cell of length 60 lu (« 52 au) with nematic viscosities characteristic of MBBA shown in table (5.1) and an elasticity K set using u> = 1.5. ZBD characteristics are h/w = 0.6, d/w = 0.92 and A = 0.5. The bulk directors are aligned initially to the defect configuration and at at time t — 0 a magnetic field of strength H = 0.2 *(Xa* = 1) is switched on in the direction of 0°. Snapshot is at time t = 40.

Figure 7.52: Director (top) and flow (bottom) fields for a ZBD cell of length 60 lu (ft* 52 au) with nematic viscosities characteristic of MBBA shown in table (5.1) and an elasticity K set using u_i = 1.5. ZBD characteristics are h/w = 0.6, d/w = 0.92 and A = 0.5. The bulk directors are aligned initially to the defect configuration and at at time t = 0 a magnetic field of strength H = 0.2 (xa = 1) is switched on in the direction of 0°. Snapshot is at time t = 45.

Figures (7.43) to (7.52) show the ZBD cell director field reorientating from the defect state rapidly into the direction of the applied magnetic field. We again observe a much more intensive induced flow field than for the relaxation simulations. The overall maximum induced velocity magnitude for this simulation was 0.033202.

The flow again adheres to the positions of the disclination walls. However this time the velocity flows out from the troughs and onto the peaks. The realignment due to the applied magnetic field again occurs very quickly (around 50 time steps) and since the induced flow is of the order as the previous simulation the flow decay time is of a comparative length.

7.3 Discussion and Conclusions

In this last results chapter we have implemented for the first time an asymmetric wall geometry to study the predications of the model for the nemato-dynamics of the new ZBD device. The steady state bi-stability of the device was recovered by the model for both the tangential and the normal wall alignments. A geometrical argument was advanced to explain the bi-stability of the grating and the positioning of the defects on the grating wall for the defect steady state. This argument was supported by the simulation results under the condition that, in the case of strong anchoring, any defect formation at the wall, unless destroyed, remained static.

Our attention then turned to the induced flow in a ZBD cell which, to our knowledge, has not been simulated before. The overall maximum induced flows for the bi-

stability results suggested velocity maxima just prior the switching between the stable states.

Finally we considered, in a sequence of time snapshots, the effects on a ZBD cell of a strongly orientating applied magnetic field which was switched on or off. The size of the images meant that we can only present here the tangentially aligned wall profile ZBD cell. ¶

Interesting low velocity flow fields were observed for the 'field switching off' cases near the wall. Persistent recirculation regions lasting several hundred time steps formed, which ultimately decayed to rest. For the relaxation simulations the induced flow appeared to decay to rest without seriously re-affecting the director field which reorientated smoothly towards its steady state.

In the 'field switching on' simulations large flow fields were created by disclination walls in the bulk dominating over any flow fields induced at the walls. These flow profiles followed the direction of the disclination walls which terminated in wall defects. Since the magnetic field was applied either parallel or perpendicular, then the wall defects appeared at the peaks and troughs. Interestingly the disclination walls separated (shedded) from the grating profile and shrank in size within the bulk, until the strongly aligning applied field ensured all bulk directors were pinned in the direction of the field. The relatively large flow fields induced by the disclinations again appeared to impose a minimal effect on the director reorientations. Moreover the induced flow fields required a longer time to decay to rest than in the relaxation

¶see accompanying CD for animations of several ZBD geometrical setups.

simulations.

Although these results are qualitative they are highly informative and reveal several interesting features that would warrant further investigation. Unfortunately, due to the visual nature of these images the best appreciation of the LBE method and its predictive ability derives from watching time sequence animations of the ZBD cell. The CD provided with this thesis contains longer animations of the above images as well as for the normal aligned wall profile. In addition, several animations of simulated 'pulsed' systems are provided, where the ZBD cell experiences a magnetic pulse (of a specific duration) in one direction and then another. The system eventually reaches a pseudo-steady state when the pulsing is repetitive. Within these pulsed systems interesting director and flow fields are observed, which should help to inform both experiments and device design.

In summary it appears that useful observations about actual liquid crystal devices can be obtained from our nemato-dynamic model. The nature of the LBE models allows the configurational details of devices under simulation to be altered quickly and easily and the relatively short turn over times for the simulations allows results to be obtained quickly. We have developed a valuable tool, which, in conjunction with experimentation, can be used to assess/refine the performance of the ZBD device.

Chapter 8

Conclusions and Future Work

8.1 Summary

In this thesis we have established a mapping onto the macroscopic ELP equations of nemato-dynamics using the isotropic Lattice Boltzmann fluid modelling technique, enhanced with a second distribution. Having developed and implemented the model, validation exercises were performed. We shall briefly review the preceding chapters detailing the key developments and testing of our new Lattice Boltzmann derivative nemato-dynamic model.

In chapter 2 we considered the target governing continuum equations of nemato-dynamics onto which we aimed to tune the dynamics of a suitably modified LB technique. At the end of the chapter we reduced the three dimensional vectorial director equations of motion to a convenient scalar angle equation of motion in two

dimensions applicable to systems confined in the plane, $(2 \oplus 2)$.

Chapter 3 introduced the ideas and historical developments of the lattice models used to recover isotropic fluid dynamics. Taking a chronological approach we reviewed the development of key models and showed how an LG is mapped onto fluid dynamics (Chapman-Enskog expansion) as well as performing a pertinent literature review on LGs.

Extending the isotropic D2Q7 lLB hexagonal lattice model proposed by Higuera *et al* [53] to include next-nearest neighbours, we derived an isotropic D2Q13 lLB model that possessed the necessary link velocity isotropy up to 6^{th} order (an essential requirement for the anisotropic extensions). A full mapping of the new D2Q13 model onto isotropic hydrodynamics was presented along with a literature review of key LB papers. Chapter 3 concludes with a relevant discussion on the nature of the bounding and forcing mechanisms employed in the LG and LB models to derive flow.

A new scalar angle variable and associated evolution scheme was introduced in chapter 4 alongside the isotropic momentum scheme. The new distribution propagates in tandem with the isotropic momentum densities but undergoes its own LBGK collision step. The angle evolution scheme was shown to map onto the macroscopic ELP director equations of motion after insertion of suitable forcing terms which coupled in the effect of the flow field and an external bulk magnetic field upon the lattice fluid director. The momentum density evolution scheme was then enhanced so that the scheme mapped onto the modified Navier-Stokes equations (with an anisotropic

fluid stress tensor controlled through the 5 recovered Leslie viscosity coefficients $\alpha_2 ... \alpha_6$. Implementation details close the chapter.

Having introduced and implemented an anisotropic D2Q13 lLB model, suitable validation exercises were performed in chapter 5. The results from this chapter were encouraging, showing that not only did the isotropic D2Q13 model map correctly onto hydrodynamics but also that the anisotropic extensions mapped correctly onto known dynamics of an incompressible anisotropic fluid and gave simulation results in good agreement with said dynamics.

Chapter 6 proceeded to test the model for transient director and flow field effects in simple geometries. The well established magnetic Fréedericksz transition was successfully recovered and provided essential information about the sensitivity of the transition to the rate and magnitude of magnetic field increments. Several magnetically pinned equilibrium director field configurations, produced through a Fréedericksz transition were obtained and subsequently used to investigate the nature of the nematic transient phenomena of director kick-back with velocity back-flow. The effect of a magnetic coherence length on the subsequently induced kick-back and back-flow upon release of the pinned systems was shown.

Having performed tests on the new model in simple geometries in chapter 7 we subsequently used the model to study the dynamics of the recently developed Zenithly Bi-stable Display (ZBD) device. The asymmetric grating profile in these device cells produces a bi-stable steady state director field which has a potentially huge application in liquid crystal display industry. The bi-stability, due to device geometry,

was shown to be correctly recovered by the new model which moreover qualitatively demonstrated, for the first time, the types of flow field induced in the cell upon switching between the stable states. This success highlighted one of the advantages of the LB model: the complex grating was implemented quickly and relatively easily into the scheme, allowing the dependence of the resulting nemato-dynamics on the properties of the grating to be easily investigated. Chapter 7 produced some interesting results in terms of the induced flow-field and what appeared to be wall director orientation shedding.

8.2 Concluding remarks

In summary we have developed an isotropic lLB model and introduced into the scheme suitable algorithmic extensions that enable the ELP equations of nemato-dynamics to be recovered on the macroscopic scale. The implementation of these enhancements has provided insights into how to use a discrete lattice model to recover macroscopic nemato-dynamics. The validation results presented in chapter 5 seem to suggest that the main aim, a "proof of concept", of the thesis has been successfully achieved. Known steady-state solutions of the ELP equations of nemato-dynamics have been recovered to a high degree of accuracy by the model indicating, the suitability of LB scheme in recovering anisotropic fluid dynamics.

Chapter 6 provides evidence that the new model can produce meaningful insights into the transient (non-steady state) phenomena of nematics. The observed back-flow and kick-back in this section has produced interesting avenues of investigation.

The ability to observe 2D disclination affects even though the disclination singularity itself is forced off lattice and is not at present recoverable, is also promising and opens up a whole field of possibilities in terms of modeling formation, destruction and movement of nematic defects.

Chapter 7 highlighted the fact that we still retain all the key advantages of the LB technique, i.e. ease of implementation of complex geometries, inherent parallisation of the method and quick turn around times. It also produced interesting insights into the ZBD device itself not least the reasons for the bi-stability, defect information, induced flow-fields and wall director orientation shedding.

It should be stressed however that all results presented in the last two result chapters are basically qualitative and a more detailed investigation into any one of these areas would be an undertaking in itself. Moreover, whilst the model is very promising it is still in its infancy and there are issues that need resolving. It may be that the next level of refinement/simplification should aim at recovering a different formulation of the target dynamics; one which relies for orientation information upon a tensor order parameter, rather that the scalar angle, θ. Such an extension is an essential pre-requisite to any LB scheme which is extended to three dimensions. It is difficult to imagine a practical tool which does not simulate in three spatial dimensions with an unconfined director.

8.3 Future Work

Throughout the work presented in this thesis several interesting avenues of research have been noted that could be undertaken. In the following we indicate some of the key issues that still need to be considered and a general review of potential applications.

In terms of the theoretical background, the research has raised many insights into the use of a discrete model to recover anisotropic fluid dynamics. Within the scope of the current model we can recover four of the five viscosity coefficients that characterize a nematic. The methodology to recover the final viscosity coefficient is in place but requires a further enhancement to the isotropy of our underlying lattice, raising non-trivial bounding and forcing issues within the core LBE scheme. The method of producing a second order accurate boundary condition is still not a solved problem within the LBE community and as such would be an obvious refinement to all LBE models.

The most obvious consideration for further development/refinement to the anisotropic scheme is to describe the orientational information of the nematic in terms of a tensorial order parameter rather than a scalar angle. Recovery of a tensorial order parameter is a necessary requirement before any possible extensions to full three dimensional nemato-dynamics can be considered. Full classification of the simulated nematic in terms of the viscosities, elasticity and Ericksen Number for the director field and the Reynolds Number for the velocity field along with the time scales and "physical" size of the simulation are also important issues.

The nematic's response to an electric field is (generally) more complicated than to a magnetic field due to the electric dipole of the nematic being director dependent. Incorporating the electric field coupling into our scheme would allow for richer emergent physics and a wider range of potential applications.

Other possibilities include introducing a binary fluid with either one or both fluids being anisotropic or inclusion of objects (stationary or movable) within the nematic.

As can be seen the technique is applicable to many areas of interest and appears to have a promising future.

Appendix A

LBE body forced pressure gradient G_{CE}

Assuming a simple setup of a translationally invariant 'channel' which is periodic in the x-direction and bounded in the y-direction by non-slip walls. Suitable addition/subtraction of a constant forcing value Δ across all *bulk* node link distributions f_i at every time step results in a uniform Poiseuille flow profile at steady state.

Below we shall show by means of a Chapman-Enskog expansion of the link density distribution evolution equation, that application of the constant body force results in a constant pressure gradient G_{CE}.

Recalling the evolution equation (3.41) for the isotropic D2Q13 lLB algorithm,

$$f_i(\mathbf{r}+\mathbf{e}_i\delta, t+\delta) = f_i(\mathbf{r},t) + \sum_j \Omega_{ij}^{(\mathrm{iso})} f_j^{neqm} + F_i$$

where we have introduced the forcing term F_i, we perform a Taylor expansion in terms of the small spatial expansion parameter δ, retaining terms up to second order,

$$\begin{aligned}\delta\left[\partial_{t_0} + e_{i\alpha}\partial_\alpha\right] f_i^{(0)} + \delta^2\left[\partial_{t_1} f_i^{(0)} + \left(\partial_{t_0} + e_{i\alpha}\partial_\alpha\right) f_i^{(1)} + \tfrac{1}{2}\left(\partial_{t_0} + e_{i\alpha}\partial_\alpha\right)^2 f_i^{(0)}\right] \;=\; \\ \textstyle\sum_j \Omega_{ij}^{(\mathrm{iso})}\left[\delta f_j^{(1)} + \delta^2 f_j^{(2)}\right] + \delta\, F_i^{(1)} + \delta^2\, F_i^{(2)} + \mathrm{O}\left(\delta^3\right).\end{aligned} \tag{A.1}$$

The LBE methodology is in essence a relaxation towards equilibrium on the shortest time scale and inclusion of any forcing terms by definition 'forces' the relaxation away from equilibrium. We can therefore, on general grounds, argue that constant forcing contributions (i.e. no gradients) acting to force the system away from equilibrium are, like $f_i^{(1)}$, to be treated as $O(\delta)$ in the Chapman-Enskog expansion. Any forcing terms involving gradients emerge, therefore, at second order in δ or higher.

Taking into account the above argument, and the fact that we are introducing a constant forcing value Δ (i.e. vanishing gradients) we do not need any second order forcing contributions.

Extracting equation (A.1) to order $\mathrm{O}(\delta)$ results in

$$\partial_{t_0} f_i^{(0)} + e_{i\alpha}\partial_\alpha f_i^{(0)} = \sum_j \Omega_{ij}^{(\mathrm{iso})} f_j^{(1)} + F_i^{(1)}. \tag{A.2}$$

Now, we explicitly define the form of the forcing term as

$$F_i^{(1)} = \Delta\, t_\sigma e_{ix} \tag{A.3}$$

where Δ is the free forcing parameter used to set the magnitude of the flow. Therefore

$$\partial_{t_0} f_i^{(0)} + e_{i\alpha}\partial_\alpha f_i^{(0)} = \sum_j \Omega_{ij} f_j^{(1)} + \Delta\, t_\sigma e_{ix}. \tag{A.4}$$

The zeroth order velocity moment of the forcing term is odd and therefore zero. As such there is no forcing contribution to the continuity equation.

The first order velocity moment of equation (A.4) is

$$\partial_{t_0} \sum_i f_i^{(0)} e_{i\beta} + \partial_\alpha \sum_i f_i^{(0)} e_{i\alpha} e_{i\beta} = \sum_{ij} \Omega_{ij} f_j^{(1)} e_{i\beta} + \Delta \sum_i t_\sigma e_{ix} e_{i\beta}$$

which ultimately becomes

$$\partial_{t_0} (\rho u_\beta) + \partial_\alpha \Pi_{\alpha\beta}^{(0)} = c_s^2 \Delta\, \delta_{x\beta} \tag{A.5}$$

The extraction of terms of $O(\delta^2)$ from equation (A.1) recovers the viscosity term in the usual way. Therefore we have a constant body force (equivalent to $c_s^2\Delta$) in the plane of the channel appearing in the x-momentum equation only. As stated, there is no contribution to the second order forcing from equation (A.3) and the first order forcing in equation (A.3) will produce no error terms at second order.

Appendix B

$\sum_j \Omega_{ij}^{(1)} f_j^{(1)}$ approximation

Recalling the isotropic D2Q13 lLB link density equilibrium distribution function from equation (3.61),

$$f_i^{(0)} = \rho t_\sigma \left(1 + \frac{1}{c_s^2} e_{i\gamma} u_\gamma - \frac{1}{2c_s^2} u_\gamma u_\gamma + \frac{1}{2c_s^4} e_{i\gamma} e_{i\delta}\, u_\gamma u_\delta\right)$$

and neglecting terms of order $\mathrm{O}(\mathbf{u}^2)$ and higher leaves

$$f_i^{(0)} \approx \rho t_\sigma \left(1 + \frac{1}{c_s^2} e_{i\gamma} u_\gamma\right) \tag{B.1}$$

Now, recalling the first order extraction of the isotropic D2Q13 lLB evolution equation (3.47).

$$\left(\partial_{t_0} + e_{i\alpha}\partial_\alpha\right) f_i^{(0)} = \sum_j \Omega_{ij}^{(1)} f_j^{(1)}$$

Rearranging and expanding the brackets, gives

$$\sum_j \Omega_{ij}^{(1)} f_j^{(1)} = \partial_{t_0} f_i^{(0)} + \partial_\alpha f_i^{(0)} e_{i\alpha} \tag{B.2}$$

Replacing the full form of the equilibrium distribution function in equation (B.2) with the low order approximation form in equation (B.1) results in.

$$\sum_j \Omega_{ij}^{(1)} f_j^{(1)} \approx \partial_{t_0}\left(\rho t_\sigma + \frac{\rho}{c_s^2} u_\gamma t_\sigma e_{i\gamma}\right) + \partial_\alpha\left(\rho t_\sigma + \frac{\rho}{c_s^2} u_\gamma t_\sigma e_{i\gamma}\right) e_{i\alpha} \tag{B.3}$$

However we know from the summation properties of our first order extraction that

$$\begin{aligned} \partial_{t_0}(\rho) &= -\partial_\alpha(\rho u_\alpha) \\ \partial_{t_0}(\rho u_\gamma) &= -\partial_\alpha \Pi_{\alpha\gamma}^{(0)} \end{aligned}$$

Therefore equation (B.3) becomes

$$\sum_j \Omega_{ij}^{(1)} f_j^{(1)} \approx -\partial_\alpha(\rho u_\alpha) t_\sigma - \frac{1}{c_s^2}\partial_\alpha \Pi_{\alpha\gamma}^{(0)} t_\sigma e_{i\gamma} + \partial_\alpha(\rho) t_\sigma e_{i\alpha} + \frac{1}{c_s^2}\partial_\alpha(\rho u_\gamma) t_\sigma e_{i\alpha} e_{i\gamma} \tag{B.4}$$

Turning now to the zeroth order contribution to the momentum flux tensor, we recall the definition

$$\Pi_{\alpha\gamma}^{(0)} = \sum_i f_i^{(0)} e_{i\alpha} e_{i\gamma}$$

which in the low **u** order approximation reduces to

$$\Pi_{\alpha\gamma}^{(0)} \approx \sum_i \left\{\rho t_\sigma \left(1 + \frac{1}{c_s^2} e_{i\beta} u_\beta\right)\right\} e_{i\alpha} e_{i\gamma} \tag{B.5}$$

therefore, taking into account the velocity summation results in

$$\Pi_{\alpha\gamma}^{(0)} \approx c_s^2 \rho\, \delta_{\alpha\gamma} \tag{B.6}$$

Substituting equation (B.6) back into equation (B.4), and performing some algebra we are left with

$$\sum_j \Omega_{ij}^{(1)} f_j^{(1)} \approx \partial_\alpha(\rho u_\gamma) t_\sigma \left\{\frac{e_{i\alpha} e_{i\gamma}}{c_s^2} - \delta_{\alpha\gamma}\right\} \tag{B.7}$$

If we now define a new tensor of the form

$$Q_{i\alpha\gamma} = t_\sigma \left(e_{i\alpha} e_{i\gamma} - c_s^2 \delta_{\alpha\gamma} \right) \tag{B.8}$$

Equation (B.7) becomes

$$\sum_j \Omega_{ij}^{(1)} f_j^{(1)} \approx \frac{1}{c_s^2} \partial_\alpha \left(\rho u_\gamma \right) Q_{i\alpha\gamma} \tag{B.9}$$

During the second order Chapman-Enskog extraction of the D2Q13 evolution equation we derive terms that are higher order velocity moments of the term $\sum_j \Omega_{ij}^{(1)} f_j^{(1)}$. Equation (B.9) can be used to evaluate these expressions to an appropriate order.

Appendix C

Lattice approximations to $\nabla_\gamma f$ and $\nabla^2 f$

We may approximate $\nabla^2 f$ and $\nabla_\gamma f$ to second order in δ, using appropriate moments of the velocity vectors $\mathbf{e}_i$. Consider first a Taylor expansion of some function of position $f(\mathbf{r}+\mathbf{e}_i)$ about $f(\mathbf{r})$.

$$f(\mathbf{r}+e_{i\alpha}) = f(\mathbf{r}) + e_{i\alpha}\partial_\alpha f(\mathbf{r}) + \frac{1}{2}e_{i\alpha}e_{i\beta}\partial_\alpha\partial_\beta f(\mathbf{r}) \tag{C.1}$$

multiplying both sides by t_σ,

$$f(\mathbf{r}+e_{i\alpha})\,t_\sigma = f(\mathbf{r})\,t_\sigma + e_{i\alpha}\partial_\alpha f(\mathbf{r})\,t_\sigma + \frac{1}{2}e_{i\alpha}e_{i\beta}\partial_\alpha\partial_\beta f(\mathbf{r})\,t_\sigma \tag{C.2}$$

To derive the approximation to $\nabla^2 f(\mathbf{r})$ we perform a summation upon i giving

$$\sum_i f(\mathbf{r}+e_{i\alpha})\,t_\sigma = f(\mathbf{r})\sum_i t_\sigma + \partial_\alpha f(\mathbf{r})\sum_i t_\sigma e_{i\alpha} + \frac{1}{2}\partial_\alpha\partial_\beta f(\mathbf{r})\sum_i t_\sigma e_{i\alpha}e_{i\beta} \tag{C.3}$$

Performing the velocity summations

$$\sum_i f(\mathbf{r}+e_{i\alpha})\,t_\sigma = f(\mathbf{r})\,\mathrm{T}[0] + \frac{1}{2}\partial_\alpha\partial_\beta f(\mathbf{r})\,\mathrm{T}[2]\,\delta_{\alpha\beta} \tag{C.4}$$

and upon contraction of the delta function

$$\sum_i f(\mathbf{r}+e_{i\alpha})\,t_\sigma = f(\mathbf{r})\,\mathrm{T}[0] + \frac{1}{2}\partial_\beta\partial_\beta f(\mathbf{r})\,\mathrm{T}[2] \tag{C.5}$$

Which we invert to determine $\nabla^2 f(\mathbf{r})$,

$$\partial_\beta\partial_\beta f(\mathbf{r}) = \frac{2\left(\sum_i f(\mathbf{r}+e_{i\alpha})\,t_\sigma - f(\mathbf{r})\,\mathrm{T}[0]\right)}{\mathrm{T}[2]} \tag{C.6}$$

where we know for our D2Q13 lLB model $\mathrm{T}[2] = c_s^2 = 3/10$ and $\mathrm{T}[0] = 1$.

In order to approximate $\nabla_\gamma f(\mathbf{r})$ we multiply equation (C.2) by $e_{i\gamma}$ and again perform a summation over i.

$$\sum_i f(\mathbf{r}+e_{i\alpha})\,t_\sigma e_{i\gamma} = f(\mathbf{r})\sum_i t_\sigma e_{i\gamma} + \partial_\alpha f(\mathbf{r})\sum_i t_\sigma e_{i\alpha}e_{i\gamma} + \frac{1}{2}\partial_\alpha\partial_\beta f(\mathbf{r})\sum_i t_\sigma e_{i\alpha}e_{i\beta}e_{i\gamma} \tag{C.7}$$

Performing the velocity summations

$$\sum_i f(\mathbf{r}+e_{i\alpha})\,t_\sigma e_{i\gamma} = \partial_\alpha f(\mathbf{r})\,\mathrm{T}[2]\,\delta_{\alpha\gamma} \tag{C.8}$$

and contracting the delta function

$$\sum_i f(\mathbf{r}+e_{i\alpha})\,t_\sigma e_{i\gamma} = \partial_\gamma f(\mathbf{r})\,\mathrm{T}[2] \tag{C.9}$$

Which we again invert to determine $\nabla_\gamma f(\mathbf{r})$,

$$\partial_\gamma f(\mathbf{r}) = \frac{\sum_i f(\mathbf{r}+e_{i\alpha})\,t_\sigma e_{i\gamma}}{\mathrm{T}[2]} \tag{C.10}$$

where as stated $\mathrm{T}[2] = c_s^2 = 3/10$.

This method can therefore be used to approximate to second order, gradients and higher derivatives of any nodal macroscopic function, i.e. density, velocity, director etc.

Appendix D

Parts Integration of

$$\int \mathrm{d}^3\mathbf{r}\, \mathcal{E}_{\alpha\beta\gamma} r_\beta \partial_\theta \sigma_{\theta\gamma}$$

Recalling the form of the integration from equation (2.92) in chapter 2 :

$$\int \mathrm{d}^3\mathbf{r}\, \left(\mathcal{E}_{\alpha\beta\gamma} r_\beta \partial_\theta \sigma'_{\theta\gamma}\right)$$

Expanding the implied summation term $\partial_\theta \sigma'_{\theta\gamma}$ gives

$$\int \mathrm{d}^3\mathbf{r}\, \left(\mathcal{E}_{\alpha\beta\gamma} r_\beta \left(\partial_x \sigma'_{x\gamma} + \partial_y \sigma'_{y\gamma} + \partial_z \sigma'_{z\gamma}\right)\right) \tag{D.1}$$

and thus :

$$\mathcal{E}_{\alpha\beta\gamma} \int \mathrm{d}_z \mathrm{d}_y \left\{ r_\beta \sigma'_{x\gamma} - \int \sigma'_{x\gamma} \delta_{\beta x} \mathrm{d}_x \right\} \; + \; \mathcal{E}_{\alpha\beta\gamma} \int \mathrm{d}_z \mathrm{d}_x \left\{ r_\beta \sigma'_{y\gamma} - \int \sigma'_{y\gamma} \delta_{\beta y} \mathrm{d}_y \right\} +$$
$$\mathcal{E}_{\alpha\beta\gamma} \int \mathrm{d}_x \mathrm{d}_y \left\{ r_\beta \sigma'_{z\gamma} - \int \sigma'_{z\gamma} \delta_{\beta z} \mathrm{d}_z \right\}. \tag{D.2}$$

Regrouping equation (D.2) results in

$$\oint \mathbf{r} \times \left(\underline{\underline{\sigma}}' \cdot \mathrm{ds}\right)|_\alpha - \int \mathrm{d}^3\mathbf{r}\, \mathcal{E}_{\alpha\beta\gamma} \sigma'_{\theta\gamma} \delta_{\beta\theta} \tag{D.3}$$

upon contraction due to the Kronecker delta

$$\oint \mathbf{r} \times \left(\underline{\underline{\sigma}}' \cdot \mathrm{ds} \right) |_{\alpha} - \int \mathrm{d}^3\mathbf{r}\, \mathcal{E}_{\alpha\beta\gamma} \sigma'_{\beta\gamma} \tag{D.4}$$

and setting $\alpha = z$

$$\oint \mathbf{r} \times \left(\underline{\underline{\sigma}}' \cdot \mathrm{ds} \right) |_{z} - \int \mathrm{d}^3\mathbf{r}\, \left(\sigma'_{xy} - \sigma'_{yx} \right) \tag{D.5}$$

we can ultimately write

$$\int \mathrm{d}^3\mathbf{r}\, \left(\sigma'_{yx} - \sigma'_{xy} \right) + \text{surface terms.} \tag{D.6}$$

Bibliography

[1] C.M.Care, I.Halliday and K.Good, *J. Phys.: Condens. Matter*, **12**, pp 665-671 (2000).

[2] I.Halliday, L.A.Hammond, C.M.Care, K.Good and A.Stevens, *Physical Review E*, **64(1)**, pp 1208-1216 (2001).

[3] P.G. de Gennes and J.Prost, *The Physics of Liquid Crystals, Second Edition*, Oxford University Press (1993).

[4] S Chandrasekhar, *Liquid Crystals*, Cambridge University Press (1994).

[5] M.G.Clark and F.M.Leslie, *Proc. R. Soc. Land. A.*, **361**, pp 463-485 (1978).

[6] C.V.Brown,M.J.Towler,V.C.Hui and G.P.Bryan-Brown, *Liquid Crystals*, **27(2)**, pp 233-242 (2000).

[7] C.Z.Van Doorn, *J.appl Phys.*, **46(9)**, pp 3738-3745 (1975).

[8] U.Fisch, B.Hasslacher and Y.Pomeau, *Phys. Rev. Letts*, **56(14)**, pp 1505-1508 (1986).

[9] L.D.Landau and E.M. Lifshitz, *Fluid Mechanics, Volume 6 of a Course of Theoretical Physics*, Pergamon Press (1966).

[10] F.Reinitzer, *Monatsch Chem.*, **9**, pp 421 (1888).

[11] O.Lehmann, *Z. Physikal. Chem.*, **4**, pp 462 (1889).

[12] G.Freidel, *Ann. Physique*, **18**, pp 273 (1922).

[13] Edited by D.A.Dunmur, *Physical Properties of Liquid Crystals: Nematics*, EMIS Data Reviews Series, No.25. INSPEC. (2001).

[14] C.W.Oseen, *Trans. Faraday Soc.*, **29**, pp 883 (1933).

[15] H.Zöcker, *Trans. Faraday Soc.*, **29**, pp 945 (1933).

[16] F.C.Frank, *Disc. Faraday Soc.*, **25**, pp 19 (1958).

[17] A.Anzelius, *Uppsala Univ. Arsskr., Mat. Oct Naturvet*, **1**, (1931).

[18] J.L.Ericksen, *Arch. Rational Mech. Anal.*, **4**, pp 241 (1960).

[19] J.L.Ericksen, *Transactions of the Society of Rheology*, **5**, pp 23 (1961).

[20] F.M.Leslie, *Quart. J. mech. Appl. Math.*, **19**, pp 357 (1966).

[21] F.M.Leslie, *Arch. Rational Mech. Anal.*, **28**, pp 265 (1968).

[22] F.M.Leslie, *Advances in Liquid Crystals*, **4**, (1979).

[23] P.C.Martin, O.Parodi and P.S.Pershan, *Phys. Rev. A*, **6**, pp 2401 (1972).

[24] J.D.Lee and A.C.Eringen, *J. Chem. Phys*, **54**, pp 5027 (1971).

[25] J.D.Lee and A.C.Eringen, *J. Chem. Phys*, **55**, pp 4504 (1971).

[26] J.D.Lee and A.C.Eringen, *J. Chem. Phys*, **58**, pp 4203 (1973).

[27] H.Schmidt and J.Jahnig, *Annals of Physics*, **71**, 129 (1972).

[28] J.D.Lee and A.C.Eringen, *Liquid Crystals and Ordered Fluids*, **2**, pp 315 (1974).

[29] S. de Groot and P.Mazur, *Non-equilibrium thermo-dynamics*, Dover Publications (1984).

[30] X.He and L.S.Lou, *Physical Review E*, **55(6)**, pp 6333-6336 (1997).

[31] J. von Neumann. Univ. of Illinois press, 1966.

[32] J.Broadwell, *J. Fluid Mech.*, **7**, pp 367-370 (1964).

[33] J.Hardy,Y.Pomeau and O. de Pazzis, *J.Mathematical Physics*, **14**, pp 1746-1759 (1973).

[34] J.Hardy,O. de Pazzis and Y.Pomeau, *Physical Review A*, **13**, pp 1949-1961 (1976).

[35] G.R.McNamara and G.Zanetti, *Physical Review Letters*, **61(20)**, pp 2332-2335 (1988).

[36] U.Frisch, D.d'Humiéres, B.Hasslacher, P.Lallemand,Y.Pomeau and J-P Rivet, *Complex Systems*, **1**, pp 649-707 (1987).

[37] B.M.Boghosian and W.Taylor, *J. Stats. Phys.*, **81(1/2)**, pp 295-317 (1995).

[38] D.d'Humiéres, P.Lallemand, *Complex Systems*, **1**, pp 598-632 (1987).

[39] D.d'Humiéres, P.Lallemand and U.Frisch, *Europhysics Letters*, **2**, pp 291-297 (1987).

[40] S.Wolfram, *J. Stats Phys.*, **45(314)**, pp 471-526 (1986).

[41] M.Henon, *Complex Systems*, **1**, pp 475 (1987).

[42] J.P.Rivet. *C.R.Acad.Sci.*, 1987.

[43] S.Wolfram, *Nature Review Article*, **311**, pp 419-424 (1984).

[44] B.Hasslacher, T.Shimonura, G.D.Doolen and C.Fu, *Los Alamos Science Special Issue*, **1-2**, pp 175-200 (1987).

[45] S.P.Das, *Physica A*, **224**, pp 180-187 (1996).

[46] G.Zanetti, *Physical Review A*, **40(3)**, pp 1539-1548 (1989).

[47] F.J.Higuera and J.Jiménez, *Europhysics Letters*, **9(7)**, pp 663-668 (1989).

[48] R.Esposito, R.Marra and H.T.Yau, *Physical Review E*, **53(5)**, (1996).

[49] O.Tribel and J.P.Boon, *Int.J.Mod.Phys C*, **8(4)**, pp 641-652 (1997).

[50] F.de los Santos and P.L.Garrido, *Computer Physics Communications*, **121-122**, pp 321-323 (1999).

[51] R.Cornubert, D.d'Humiéres and D.Levermore, *Physica D*, **47**, pp 241-259 (1991).

[52] A.K.Gunstensen, D.H.Rothman, *Physica D*, **47**, pp 53-63 (1991).

[53] F.J.Higuera, S.Succi and R.Benzi, *Europhysics Letters*, **9(4)**, pp 345-349 (1989).

[54] B.Chopard, A.Masselot and A.Dupuis, *Comp. Phys. Comm.*, **129(1-3)**, pp 167-176 (2000).

[55] A.Károlyi and J.Kertész, *Comp. Phys. Comm.*, **121-122**, pp 290-293 (1999).

[56] L.P.Kadanoff, G.R.McNamara and G.Zanetti. *Complex Systems 1*, 1987.

[57] L.P.Kadanoff, G.R.McNamara and G.Zanetti, *Physical Review A*, **40(8)**, pp 4527-4541 (1989).

[58] G.R.McNamara, *Europhysics Letters*, **12(4)**, pp 53- 63 (1990).

[59] B.M.Boghosian and P.V.Coveney, *Computer Physics Communications*, **129**, pp 46-55 (2000).

[60] D.H.Rothman and J.M.Keller, *J.Stat.Physics*, **52**, (1988).

[61] E.Vives and A.Planes, *Physical Review A*, **38(10)**, pp 5391-5400 (1988).

[62] N.Angelescu, S.Romano and V.A.Zagrebnov, *Physics Letters A*, **200**, pp 433-437 (1995).

[63] Y.H.Qian, S.Succi and S.A.Orszag, *Annual Review of Computational Physics*, **3**, pp 195 (1995).

[64] A.K.Gunstensen and D.H.Rothman, *Europhysics Letters*, **18(2)**, pp 157 - 161 (1992).

[65] Y.H.Qian, D.d'Humiéres, P.Lallemand, *Advances in Kinetic Theory and Continuum Mechanics, Book in honour of H.Cabannes, edited by R.Gatignol and Soubbaramayer*, Spinger Verlag (1991).

[66] Y.H.Qian, D.d'Humiéres, P.Lallemand, *Europhysics Letters*, **17(6)**, pp 479-484 (1992).

[67] Y.H.Qian. *Gaz sur réseaux et cinétique sur réseaux appliquée à l'équation de Naiver-Stokes.* PhD thesis, University of Paris, (6) 1990.

[68] P.L.Bhatnagar, E.P.Gross and M.Krook, *Physical Review*, **94(3)**, pp 511-524 (1954).

[69] S.Chapman and T.G.Cowling, *The Mathematical Theory of Non-Uniform Gases*, Cambridge University Press (1970).

[70] C.M.Care. Lattice Boltzmann mesoscopic nemato-dynamics. in progress.

[71] S.Succi, E.Foti and F.J.Higuera, *Europhysics Letters*, **10(4)**, pp 443-438 (1989).

[72] J.M.V.A Koelman, *Europhysics Letters*, **15(6)**, pp 603-607 (1991).

[73] S.Hou, Q.Zou, S.Chen, G.D.Doolen and A.C.Cogley, *J. Comp. Phys.*, **118**, pp 329-347 (1995).

[74] E.G.Flekkøy, T.Rage, U.Oxaal and J.Feder, *Physical Review Letters*, **77(20)**, (1996).

[75] C.Sun, *Physics Review E*, **58(6)**, pp 7283-7287 (1998).

[76] G.Amati, S.Succi and R.Piva, *Int. J. Mod. Phys. C*, **8(4)**, pp 869-877 (1997).

[77] F.J.Alexander, S.Chen and J.D.Sterling, *Physical Review E*, **47**, pp 2249-2252 (1993).

[78] Y.H.Chen, H.Ohasi and M.Akiyama, *Physical Review E*, **50(4)**, pp 2776-2783 (1994).

[79] M.Soe, G.Vahala, P.Pavlo, L.Vahala and H.D.Chen, *Physical Review E*, **57(4)**, pp 4227 (1998).

[80] L.Vahala, D.Wah, G.Vahala, J.Carter and P.Pavlo, *Physical Review E*, **62(1)**, pp 507-516 (2000).

[81] G.R.McNamara A.L.Garcia and B.J.Alder, *Journal of Statistical Physics*, **81(1-2)**, pp 432 (1995).

[82] G.Vahala, P.Pavlo, L.Vahala and N.S.Martys , *Int. J. Mod. Phys. C*, **9(8)**, pp 1247 (1998).

[83] T.Ihle and D.M.Kroll, *Computer Physics Communications*, **129(1-3)**, pp 336 (2000).

[84] H.Sun, *Chinese Physics Letters*, **17(3)**, pp 305 (2000).

[85] D.M.White. *Lattice Bhatnagar-Gross-Krook studies of hydrodynamic and thermohydrodynamic internal pressure-driven flows.* PhD thesis, Sheffield Hallam University, 1999.

[86] A.K.Gunstensen, D.H.Rothman, S.Zaleski and G.Zanetti, *Physical Review A*, **43(8)**, pp 4320- 4327 (1991).

[87] I.Halliday and C.M.Care, *Physical Review E*, **53(2)**, pp 1602-1612 (1996).

[88] S.Hou, X.Shan, Q.Zou, G.D.Doolen and W.E.Soll, *J. Comp. Phys.*, **138**, pp 695-713 (1997).

[89] I.Halliday, S.P.Thompson and C.M.Care, *Physical Review E*, **57(1)**, pp 514-523 (1998).

[90] S.P.Thompson. *Investigation of the hydro-dynamics of a two component lattice BGK fluid.* PhD thesis, Sheffield Hallam University, 1998.

[91] Los Alamos Lattice Boltzmann Group, *Lattice Boltzmann Fluid Dynamics- a versatile tool for mulitphase.*, Los Alamos Science, No. 22 (1994).

[92] H.Chen, B.M.Boghosian and P.V.Coveney, *P. Roy. Soc. Lond Series-A Math.*, **456**, pp 2043-2057 (2000).

[93] M.Nekovee, P.V.Coveney and H.D.Chen, *Phys. Rev. E*, **62(6)**, pp 8282-8294 (2000).

[94] A.Lamura,G.Gonnella,J.M.Yeomans, *Europhysics Letters*, **45(3)**, pp 314-320 (1999).

[95] M.R.Swift, W.R.Osborn and J.M.Yeoman, *Phys. Rev. Letter*, **75(5)**, pp 830-833 (1995).

[96] A.Malevanets and J.M.Yeoman, *Faraday Discussion*, **112**, pp 1-12 (1999).

[97] Z.L.Yang, T.N.Dinh, R.R.Nourgaliev and B.R.Sehgal, *Int. J. of Heat and Mass Transfer*, **44**, pp 195-206 (2001).

[98] D.Grubert and J.M.Yeomans, *Computer Physics Communications*, **121-122**, pp 236-239 (1999).

[99] S.Succi, J.Wang and Y.H.Qian, *Int. J. Mod. Phys. C*, **8(4)**, pp 999-1008 (1997).

[100] S.Chen, H.Chen, D.Martinez and W.Matthaeus, *Phys. Rev. Letters*, **67(27)**, pp 3776-3779 (1991).

[101] D.O.Martinez, S.Chen and W.H.Matthaeus, *Phys, Plasmas*, **1(6)**, pp 1850-1867 (1994).

[102] P.B.Warren, *Int. J. Mod. Phys. C*, **8(4)**, pp 889-898 (1997).

[103] X.He, L.S.Lou and M.Dembo, *J. Stat. Phys.*, **87**, pp 115-136 (1997).

[104] P.A.Skordos, *Phys. Rev. E*, **48**, pp 4823-4842 (1993).

[105] D.R.Noble,J.G.Georgiadais and R.O.Buckius, *J. Stat. Phys.*, **81(1/2)**, pp 17-33 (1995).

[106] T.Inamuro, M.Yoshino and F.Ogino, *Phys Fluids*, **7(12)**, pp 2928-2930 (1995).

[107] Q.Zou, S.Hou and G.D.Doolen, *J. Stats Phys.*, **81(1/2)**, pp 319-334 (1995).

[108] S.Hess. *Pre-Print.* Institut für Theoretische Physik, Technische Universität Berlin, hardenbergstr. 36, D - 10623 Berlin, Germany, 1998.

[109] W.W.Beens and W.H.de Jeu, *Le Journal De Physique*, **44**, pp 129-136 (1983).

[110] T.Maruyama, G.G. Fuller, M.Grosso and P.L.Maffettone, *Journal of Non-Newtonian Fluid Mechanics*, **76**, pp 233-247 (1998).

[111] T.Tsuji, A.D.Rey, *Journal of Non-Newtonian Fluid Mechanics*, **73**, pp 127-152 (1997).

[112] W.Postze,I.Heynderickx, *J. Non-Newtonian Fluid Mechanics*, **58**, pp 173-190 (1995).

[113] S.Chono,T.Tsuji and M.M.Denn, *J. Non-Newtonian Fluid Mechanics*, **79**, pp 515-527 (1998).

[114] P.Pieranski and E.Guyon, *Solid State Communications*, **13**, pp 435 (1973).

[115] V.Fréedericksz and V.Zolina, *Trans Faraday Soc*, **29**, pp 919 (1933).

[116] G.Arfken, *Mathematical Methods for Physicists*, Academic Press (1970).

[117] D.J.Cleaver and M.P.Allen, *Physical Review A*, **43(4)**, pp 1918-1930 (1991).

[118] F.Brochard, L.Léger and R.B.Meyer, *J. Phys. (Paris)*, **36**, pp 209 (1975).

[119] D.W.Berreman, *Phys. Rev. Lett.*, **28**, pp 1683 (1972).

[120] G.Barbero, *Lett Nuovo Cimento*, **32**, pp 60 (1981).

[121] G.Barbero, *Lett Nuovo Cimento*, **29**, pp 553 (1980).

[122] I.Halliday, C.M.Care, S.P.Thompson and D.White, *Physical Review E*, **54(3)**, pp 2573-2576 (1996).

[123] Personal correspondence with J. Cliff Jones. Director of Research, ZBD Display Ltd, Malvern Hills Science Park, Geraldine Road, Malvern, Worcs, WR13 3SZ, UK.

[124] V.C.Hui. *Pre-Print.* DERA, Malvern, Worcestershire, WR14 3PS, U.K., 2000.